COMPUTATIONAL AND EXPERIMENTAL STUDY OF MULTIPHASE FLOW IN INCLINED PIPES

By

Ibrahim Ahmed

Thesis submitted in accordance with the requirements for the degree of Doctor of Philosophy

At the University of Leeds
School of Chemical and Process Engineering

MAY 2023

I, the candidate, Ibrahim Ahmed confirm that the work submitted is my own and that appropriate credit has been given where reference has been made to the work of others.

Acknowledgements

My gratitude to God Almighty, who has given me the strength, wisdom, and patience to cross many hurdles and overcome difficulties encountered in this PhD research work.

I want to express my deep appreciation to Dr Xiaoan Mao, my main supervisor, for his guidance, motivating moral support, understanding, advice and patience throughout the course of my PhD work. And, to my co-supervisor Late Dr Alan Burns, who taught and guided me on the use of Computation Fluid Dynamics simulation with ANSYS CFX and Fluent.

Special thanks to the laboratory technicians particularly Gurdev Bhogal from the Laser Laboratory of the Energy Building for his efforts, support, and useful suggestions, as well as Dr. Ben Douglas from the Physical Chemistry Laboratory 201 of SCAPE Building for assisting me with viscosity, density, and surface tension measurements.

Finally, I would like to express sincere appreciation to the Nigerian government through the Petroleum Technology Development Fund (PTDF) for providing the funding for my doctoral studies.

Dedication

In the memory of late Dr Alan Burns (Associate Professor of Fluid Dynamics)

Abstract

This work presents a computational and experimental investigation on the effects of liquid properties on multiphase flow in horizontal and upward inclined pipes. The overall aim of the research is to gain more insight into the effects of viscosity, density, and surface tension on multiphase flow behaviour. The computational part of the study simulated the drift velocity of an elongated gas bubble, commonly referred to as Taylor bubbles in a 2D domain.

The computational efficiency of 2D simulation makes it a preferred option for parametric studies, where different operational parameters are systematically varied to understand their impact on the flow behaviour. By simplifying the geometry to 2D, it becomes easier to explore a wide range of parameters and assess their effects. In this work, 78 simulations were run at six different pipe inclinations to study the effects of 13 different liquids. The simulation results show that liquid density alone has little or no influence on the Taylor bubble's velocity at all pipe inclinations, while the bubble's velocity is heavily influenced by liquid viscosity at all pipe inclinations. However, surface tension appears to show unique effects on the Taylor bubble, when the pipe inclination is less than 45^{O}, surface tension seems to have no effect on Taylor bubble's drift velocity, the effects of surface tension only become notable when the flow inclination is at 45^{O} or above. This behaviour has not been reported by previous researchers based on the review done, as no previous work has singled out one liquid physical property to study its effect while keeping the other properties constant.

Experimental study on the effects of liquid properties was also carried out to generate two-phase flow data using three different liquids, water, surfactant solution, and glycerol solution in a 19 mm ID pipe and 4m length. The experimental campaign was carried out in a horizontal and 15^{O} upward inclinations. Two-phase flow regime and slug frequency data were acquired using a high-speed camera, quick-action solenoid valves were used to collect liquid holdup data, and a differential pressure transducer was used to measure the pressure

drop across the flow section. The effects of liquid properties and variation of inclination angles on different flow parameters including flow regime, pressure drop, liquid holdup, and slug frequency were investigated and reported. Flow regime maps were also developed for all flow orientations investigated. The data generated would be a useful contribution to the gas/liquid flow database and could potentially be used to develop or improve multiphase flow correlations.

Table of Contents

List of Tables

List of Figures

List of Symbols

d	-	Pipe Diameter
Re	-	Reynolds number
μ	-	Viscosity
μ_G	-	Gas viscosity
ρ	-	Density
ρ_G	-	Density of gas
ρ_L	-	Density of liquid
v	-	Velocity
σ	-	Surface tension
g	-	Acceleration due to gravity
Fr_{SG}	-	Froude number of the gas phase
Ku_{SG}	-	Kutadelaze number
U_{SG}	-	Superficial velocity of gas
U_{SL}	-	Superficial velocity of liquid
U_m	-	Mixture velocity
L_S	-	Slug body length
H_S	-	Liquid holdup in the slug body length
L_f	-	Liquid film section length
H_f	-	Liquid holdup in the slug film lenght
U_t	-	Slug body translational velocity
U_S	-	Slug velocity
U_f	-	Liquid film velocity
U_{GP}	-	Gas pocket velocity.
C_0	-	Flow distribution coefficient
U_B	-	Drift velocity of a Taylor bubble in a stagnant liquid
U_B^v	-	Drift velocity of a Taylor bubble in a vertical pipe
U_B^h	-	Drift velocity of a Taylor bubble in a horizontal pipe
F_s	-	Slug frequency

U_{max} - Maximum velocity at the centre of pipe

U_{min} - Minimum velocity at the centre of pipe

E_L - In-situ liquid volume fraction

C_L - Input liquid volume fraction

Fr_m - Mixture Froude number

ρ_n - Non-slip mixture density

f_m - Mixture friction factor

f_n - No-slip friction factor based on the no-slip Reynolds number,

g_c - Dimensional conversion factor of gravity

Mo - Morton number

Eo - Eotvoss number

N_{vis} - Viscosity number

Chapter 1
Introduction

This chapter provides the background and importance of multiphase flows in section 1.1, while section 1.2 highlights the motivations that led to this study. Specific aims and objectives of the research is being summarised in section 1.3, and the contributions of the thesis to the wealth of research work are outlined in section 1.4. Finally, a breakdown of the thesis structure is given in section 1.5.

1.1 Background

Fluid flow is the backbone of almost all process industries and can be encountered in many areas of engineering and technology, either in one or more phases. Most fluid flow in petroleum production, power generation, and chemical industries consists of more than one phase. Hence this type of flow is called multiphase flow, derived from the word multi which means “more or many”. For the oil and gas industry, multiphase flow phenomena can be observed in various parts of the industry, from production to transportation, and processing.

In petroleum refining and chemical industries, most of the product separation processes take place in the distillation columns where there is a continuous flow of liquid and vapour, in and out of the column and its peripherals, the reboilers, and the condensers. Multiphase flow occurs not only inside these units but also in the piping system that connects the reboilers and the condensers to the distillation column. Similarly, multiphase flow is commonly found in other process equipment such as phase separators, chemical reactors, and boilers.

Current petroleum exploration technologies involve the tapping of hydrocarbons from reservoirs several miles away from the production site, the piping that connects the reservoirs to the production platform may come in a wide range of orientations; vertical, horizontal, and inclined. Such a typical offshore architecture is shown in Figure 1.1. Likewise, a wide range of variations is encountered for the pipe diameter, flow rate, and pressure drop. Therefore, there is a need to know the mixture behaviour inside these pipes to help engineers make an informed decision in designing and operating these production

facilities. This will minimise capital costs and ensure a safe and successful operation of the plant.

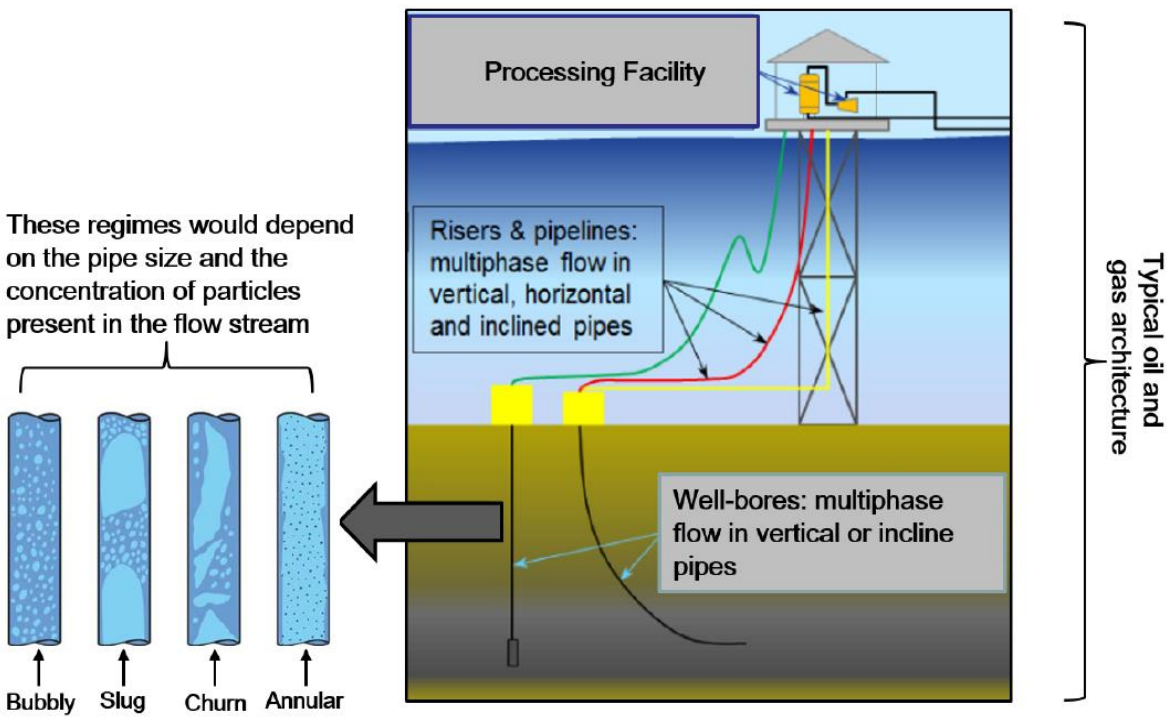

Figure 1.1 Schematic of an offshore oil/gas production facility (Gharaibah et al. 2015)

1.2 Motivation

Previously, most of the gas-liquid multiphase flow studies were conducted for low viscous liquids, predominantly water, and light oils. But with oil prices soaring to over $100 per barrel, many oil companies have started to pay more attention to the extraction of heavier oil, which has been almost ignored due to the lack of proper technology to exploit this resource as well as high production costs. Moreover, petroleum is a finite and non-renewable resource that is gradually being depleted. Figure 1.2 shows a global abundance of heavy and extra oil reserves, when combined with bitumen and oil sands, they make up over 70% of oil current known resources worldwide, which is more than twice the amount of conventional light crude oil. The exponential growth of the human population and the corresponding subsequent increase in demand for energy will inevitably exceed the available conventional reserves, and the next choice will be the unconventional reserves.

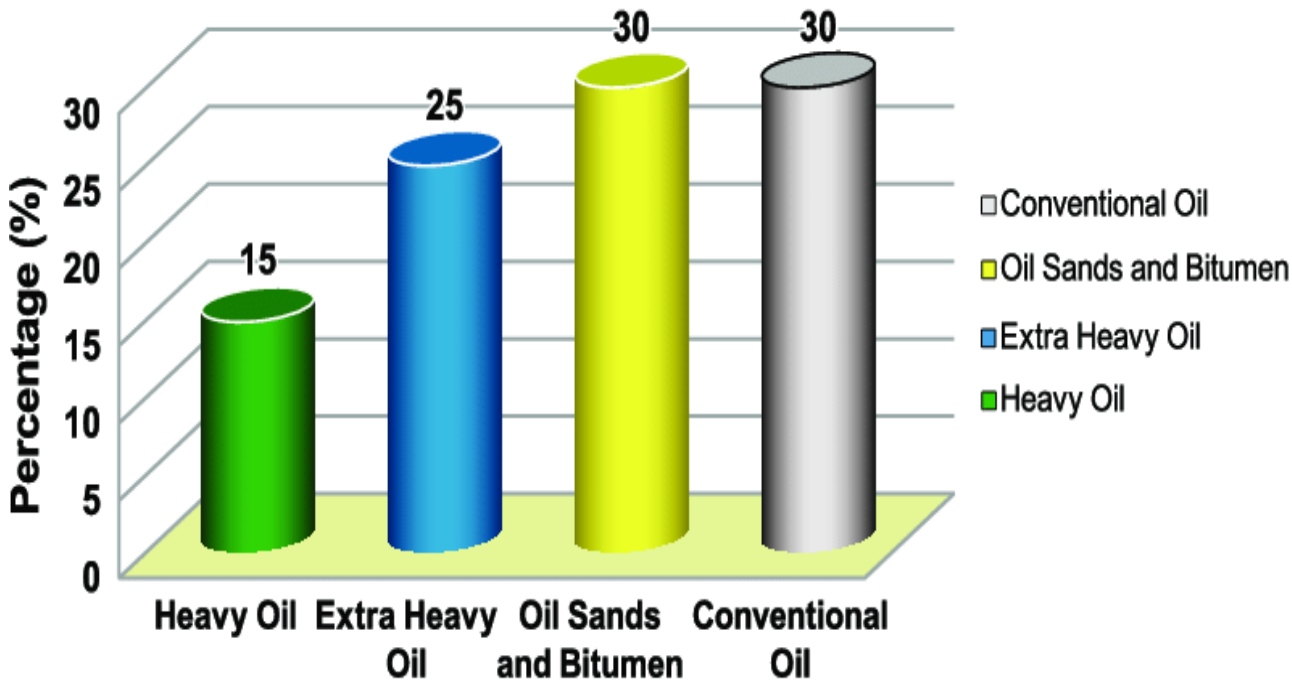

Figure 1.2 Total world oil reserves (Iskandar *et al*, 2016)

Extensive research on horizontal and vertical gas-liquid multiphase flow systems over the years has yielded several models and correlations for flow pattern transitions, pressure drop, and liquid holdup among others. In real situations, pipelines don't only follow vertical and horizontal layouts, commercial pipelines follow various terrains consisting of uphill and downhill inclined sections, making it impossible to apply the models and correlations that were developed for horizontal and vertical flow on the inclined sections. Therefore, pipe inclination adds another dimension of complexity to an already intricate flow phenomenon.

There are different types of flow regimes as will be discussed in the next chapter, slug flow is one of the most common flow patterns occurring on various types of multiphase flow, especially on the slightly upward inclined, horizontal, and vertical pipes. The hydrodynamics of slug flow is complicated and can be significantly influenced by several variables including gas and liquid flow rates, pipe diameter, inclination, and fluid properties such as density, viscosity, and surface tension. That is why this research will focus on

precisely understanding the influence of liquid properties on slug flow behaviour in inclined pipes, which is crucial for the optimal operation of the pipeline and downstream facilities.

1.3 Research Question

This study seeks to understand the influence of liquid properties on the behaviour of multiphase (gas/liquid) flow at different flow conditions, exploring to what extent the liquid properties (density, viscosity, and surface tension), as well as pipe inclination, alter the known hydrodynamic behaviour (flow pattern/map, pressure drop, etc) of multiphase flow.

1.4 Objectives

The key objective of this research is to improve the fundamental understanding of the hydrodynamic behaviour of multiphase gas-liquid flow in horizontal and inclined pipes. This is achieved via the following:

- Computational study of the effects of liquid properties (density, viscosity, and surface tension) on the drift velocity of a Taylor bubble in a pipe of 20 mm internal diameter (ID) at six different orientations from 0° (horizontal) to 75° under different conditions. These test conditions include varying the liquid's density from 870 to 1,050 kg/m3, the viscosity from 0.001 to 0.307 kg/ms, and the surface tension from 0.018 to 0.073 N/m.

- Using non-ionic surfactant and glycerol to experimentally study the effects of viscosity and surface tension on multiphase flow patterns, liquid holdup, pressure drop, and slug frequency, in horizontal and 15° upward inclined pipes. The study covers gas superficial velocity from 0.5 to 4m/s and liquid superficial velocity from 0.1 m/s to 0.8 m/s.

1.5 Structure of the Thesis

With the background and objectives of the research provided by this current chapter, the remainder of this thesis is divided into different chapters with each chapter focusing on a particular aspect of the work.

Chapter 2: This chapter contains a review of published works on two-phase flows in pipelines. The flow patterns and flow pattern maps for the horizontal, vertical, and inclined pipes are described. Emphasis is given to models available for predicting the liquid holdup, pressure drop, and slug characteristics and the current state of research activity into the potential applications of Computational Fluid Dynamics (CFD) in gas-liquid flow.

Chapter 3: In this chapter, both computational and experimental methodologies used in this work are extensively discussed. The first part of the chapter gives a general background to CFD, its applications, advantages, and analysis procedure, it went further to outline the numerical techniques used in the simulation aspect of this research. The second part of the chapter describes the experimental flow rig, the apparatus, experimental procedures, instrumentation, the properties of fluids used, and the technique for measurements of the liquid holdup, pressure drop, and slug frequency.

Chapter 4: This chapter presents a 2D simulation of the drift velocity of a single elongated gas bubble (Taylor bubble) in different liquids and pipe inclinations to study the effects of density, viscosity, and surface tension on the flow behaviour of the Taylor bubble, and their subsequent effects on slug flow. The simulation results were summarised in charts and results for air/water flow are compared to those found in the open literature.

Chapter 5: Presents the experimental results obtained in the experiments performed in a horizontal and 15O upward inclined pipe, key features of flow regimes, pressure drop, liquid hold up, and slug frequency are analysed and discussed.

Chapter 6: Brings together all the key conclusions from this work and outlines the recommendations for future research.

1.6 Contributions of the Thesis

- It provides an adequate detail on how each physical property of a liquid uniquely affects the drift velocity of a Taylor bubble and influences slug flow.
- It contributes to the understanding of the effects of viscosity and surface tension on the flow behaviour, liquid holdup, pressure drop, and slug frequency in a horizontal and inclined pipe multiphase flow.

Chapter 2
Literature Review

This chapter presents a review of the literature while addressing the primary aspects of fluid flow, starting from single-phase flow and its associated governing equations. Then multiphase gas-liquid flow patterns are briefly discussed to set a precedent for understanding slug flow. Distinguishing features of slug flow are discussed in depth while presenting a historical overview of previous works carried out by earlier researchers in these fields.

2.1. Single-Phase Flow Overview

The first step towards understanding multiphase flow is to comprehend the features of single-phase flow. Single-phase flow is relatively simpler and research in this field has developed and addressed the issues of pressure drop, flow behaviour, and fluid properties. Many correlations and formulas used in multiphase flow are derived from modifications of single-phase flow formulae.

Single-phase flow can either be laminar or turbulent, depending on many factors including fluid velocity, flow geometry, pipe roughness, temperature, fluid properties, etc. Laminar flow occurs in most cases because of low mass interaction between the fluid particles which flow as an individual layer (Shoham, 2006), this could be due to high viscosity and lower velocity making the flow maintain a uniform character throughout the pipe. In turbulent flow, on the other hand, the fluid particles do not flow in a clear path, this flow regime features a random 3D macroscopic movement of the fluid particles occurring mainly in low viscous fluids and high velocity. Thus, the nature of turbulent flow is characterised by a chaotic and fluctuating velocity field with time, which subsequently leads to the mixing of the fluid particles and fluctuation of the transported quantities such as energy and momentum (Bird et.al, 2007). The pressure drop in turbulent flow is more strongly influenced by the mass flow rate as compared to laminar flow, turbulent flow exhibits a stronger sensitivity to changes in mass flow rate due to the higher energy requirements

associated with maintaining turbulent motion. This means that increasing the mass flow rate in turbulent flow results in a larger increase in pressure drop compared to the same increase in laminar flow. Characterisation of turbulent flow is much harder than that of laminar flow, this is due to the randomness of mass transfer across the flow layers.

Some variables have been put forward to help analyse and better understand the turbulent flow, one of these variables is the eddy viscosity, which is also known as the turbulent viscosity. This is different from the actual absolute viscosity, which is a property of the fluid. Also, turbulent viscosity depends on the turbulence intensity and the pipe position, close to the pipe wall there exists a region called the laminar sublayer where eddy viscosity is negligible or much lower than absolute viscosity, but as the pipe centre or the turbulent zone is approached, the eddy viscosity increases and becomes much larger than the absolute viscosity (Bird et al., 2007). Sverdrup et al. (1942) have described this observation as a result of the exchange of momentum among particles of adjacent layers caused by turbulent eddies.

Osborne Reynolds put forward a dimensionless number called the Reynolds number for predicting turbulent flow regimes. This is defined as the ratio between inertial forces and viscous forces in the fluid. Expressing it mathematically in a circular pipe as:

$$Re = \frac{Inercial\ Forces}{Viscous\ Forces} = \frac{\rho v d}{\mu} \tag{2.1}$$

To characterise a flow based on the regime, Reynolds has shown through his experiments that in a circular pipe, laminar flow occurs when the ratio of inertial forces to viscous forces is less than 2000 (Re < 2000) while turbulent flow occurs when the ratio of inertial forces to viscous forces is greater than 2400 (Re > 2400). Values between 2000 and 2400 are regarded as transitional regimes, this flow regime is still one of the areas not yet fully explored in single-phase flow despite the extensive research in single-phase flow. For example, friction factor correlations are well-defined and accurate for turbulent and laminar flow, but most of the existent correlations for transient flow friction factors have low accuracies. The most widely used Colebrook friction factor fails to consider the effects of

the surface's uniformity which plays a major role. Furthermore, a completely turbulent flow regime hardly exists, for there exists a small region next to the pipe with laminar flow features (Bratland, 2009).

Single-phase flow can be described by a set of general equations. These are the continuity equation or mass conservation equation, and the momentum equation or Navier-Stokes equation. Together, they are collectively referred to as governing equations. For an incompressible flow (with constant density and viscosity), the governing equations can be written in Cartesian coordinates given as follows:

Continuity equation:

$$\frac{\partial u}{\partial x} + \frac{\partial v}{\partial y} + \frac{\partial w}{\partial z} = 0 \tag{2.2}$$

Navier-Stokes equation:

(2.3)

$$\rho\left(\frac{\partial u}{\partial t} + u\frac{\partial u}{\partial x} + v\frac{\partial u}{\partial y} + w\frac{\partial u}{\partial z}\right) = \rho g_x - \frac{\partial P}{\partial x} + \mu\left(\frac{\partial^2 u}{\partial x^2} + \frac{\partial^2 u}{\partial y^2} + \frac{\partial^2 u}{\partial z^2}\right) \tag{2.4}$$

$$\rho\left(\frac{\partial v}{\partial t} + u\frac{\partial v}{\partial x} + v\frac{\partial v}{\partial y} + w\frac{\partial v}{\partial z}\right) = \rho g_y - \frac{\partial P}{\partial y} + \mu\left(\frac{\partial^2 v}{\partial x^2} + \frac{\partial^2 v}{\partial y^2} + \frac{\partial^2 v}{\partial z^2}\right) \tag{2.5}$$

$$\rho\left(\frac{\partial w}{\partial t} + u\frac{\partial w}{\partial x} + v\frac{\partial w}{\partial y} + w\frac{\partial w}{\partial z}\right) = \rho g_z - \frac{\partial P}{\partial z} + \mu\left(\frac{\partial^2 w}{\partial x^2} + \frac{\partial^2 w}{\partial y^2} + \frac{\partial^2 w}{\partial z^2}\right)$$

Among the several purposes for these fundamental equations is obtaining the velocity field of the fluid particles. Thus, understanding them is vital as they are also applied in multiphase flow systems. For example, in a stratified two-phase gas-liquid flow, the momentum balance equation is directly obtained from these equations. Similarly, the Navier-Stokes equations are derived from Newton's second law of motion with a pressure term caused by viscosity. In addition, it can be applied to Newtonian fluids, both inviscid (zero viscosity) and viscous fluids.

Nevertheless, the presence of partial differential equations makes it impossible to solve these fundamental equations analytically. However, for most engineering problems, it is possible to numerically get an approximate computer-based solution to the governing equations. This is being addressed by Computational Fluid Dynamics (CFD) and is discussed in the next chapter.

2.2. Gas-Liquid Two Phase Flow Overview

As highlighted earlier, multiphase gas-liquid flow occurs in various units of process industries and the oil and gas transport pipelines. Thus, it is important to understand some parameters such as liquid holdup, gas/liquid volume fraction, and pressure drop, to accurately design and operate these equipment and pipelines. The complexity of multiphase flow systems has made it difficult to model, they have more flow parameters and variables than single-phase flow. Consequently, the empirical, exact-solution, and numerical simulation approaches are too complicated or almost impractical (Shoham, 2006). The common single-phase features such as velocity profile, boundary layer, and turbulence are not adequate to explain the behaviour of multiphase flow (Bertani et al, 2010).

Out of the several types of multiphase flows (Gas-Liquid, Gas-Solid, Liquid-Liquid, and Liquid-Solid), gas-liquid flows are known to be the most difficult ones. This complexity arises due to the mixture of certain unique features such as the compressibility of the gas phase along with the deformable interface of the liquid phase (Hewitt, 2011). Moreover, the random motion of complicated shapes presented by the gas-liquid interface makes quantifying the spatial distribution between the phases a complex task. This complexity increases especially with larger flow cross-sections (pipe diameter), longer lengths of pipes, and hostile topography (Brill, 2010).

Another multiphase complicating factor unique to gas-liquid flow is the influence that one of the flow phases has on the other, this leads to random fluctuations of local variables of each phase, such as velocity and pressure. Therefore, measuring an average value of the variables requires more complicated procedures for multiphase flow than for single-phase flow. One more phenomenon requiring much attention when talking about multiphase flow is turbulence, this is already a complex area for single flow and is still considered an

unsolved scientific puzzle (Kolev, 2012). The presence of more than one flowing phase mean multiphase flow turbulence is much harder to analyse and model. The larger number of terms to be modelled in the momentum equation enhances this complexity.

The problematic issues of multiphase flow increase when it comes to equipment and technology. For example, most flowmeters pose some uncertainties even for single-phase flow, let alone multiphase flow. This becomes more complicated when gas and liquid are mixed in the flow stream, and even one of the best flowmeters by Coriolis has accuracy problems (Meribout et al., 2020), as also other equipment like the differential pressure transducers. For single-phase flow, both the flow structure and the relationship between pressure and flow rate in the measurement devices are established and provide accurate results. However, those relationships are more complicated when two or more phases are present in the flow. This can be explained by the input of new parameters, such as the volumetric fraction of each phase and the phase's velocities. Nevertheless, solutions adapted from single-phase measurements are still being implemented (Paladino, 2005), while lots of efforts are being made toward the development of multiphase flow technologies.

2.3 Flow Patterns in Multiphase Systems

The composition of phases flowing in a multiphase system may vary over the cross-section of the pipe, where each phase will occupy a distinct volume fraction and velocity field. This motion of phases at different flow rates led to the phenomenon of "slip" between the phases (Abulencia and Theodore, 2009). Due to flow instabilities, whenever a gas-liquid stream flows co-currently in a pipe, the two-phase mixture may assume some different flow configurations relating to the interface between the phases, called flow patterns or flow regimes. The flow pattern largely depends on the pipe's orientation, flow velocity, the density difference between the two fluids, as well as the roles played by gravity.

An important factor in the application of two-phase gas-liquid flows is an understanding of how such flows behave within a pipe. Hewitt et al (1995) observed that the exact nature of the two-phase flow patterns depends on the relative mass ratios and velocities of the gas and liquid present as well as the pipe characteristics. Different flow patterns are believed to form as a result of the interaction between surface tension and gravitational forces (Ghajar, 2005).

Flow patterns can be considered as the several configurations that each of the phases flowing simultaneously in the can geometrically be set (Shoham, 2006). The key flow parameters that establish different flow regimes include the pipe's size and orientation (diameter and inclination), physical properties of the fluids (density, viscosity, and surface tension of the liquid and gas) as well as operating conditions (such as the gas and liquid's superficial velocities). (Ramdin, 2010).

2.3.1 Horizontal Pipes

Horizontal flow pattern prediction is much harder than vertical flows, Paladino (2005) has attributed this difficulty to the asymmetry caused by gravity, which acts perpendicularly to the pipe causing the phases to separate naturally due to their density differences. The denser component flows preferentially near the bottom of the pipe causing a separation of the flow, and energy transfer between the phases due to velocity difference leads to a more complex process (Carrizales et al., 2015). The flow patterns for horizontal and near-horizontal pipes are described as follows:

Stratified and Stratified Wavy Flow: In stratified flow, the two phases are separated by a clear horizontal interface, where the gas flows on the top while the liquid is on the bottom of the pipe, this flow pattern is associated with lower gas and liquid flow rates. Gravity is the main force behind stratification, a smooth gas-liquid interface is observed at low gas velocities which gives a stratified smooth regime. An increase in the gas flow rate leads to disturbances on the horizontal interface which tends to form waves and the flow pattern becomes a Stratified Wavy flow.

Slug Flow: At higher gas velocities, the gas-liquid interface that separates the two phases gets ruptured at some points of the flow leading to alternate flows of gas pockets and liquid slugs which can bridge the entire cross-sectional area of the pipe. The gas pocket is usually covered by thin droplets that can be observed inside the gaseous pocket, while gas bubbles are seen in the liquid structures. The liquid slugs traveling at a much higher speed can overrun the slow liquid film region. At the slug flow threshold, the gas bubbles become very

elongated and the entrained bubbles in the liquid escape to be part of the elongated gas bubble (Shoham, 2006).

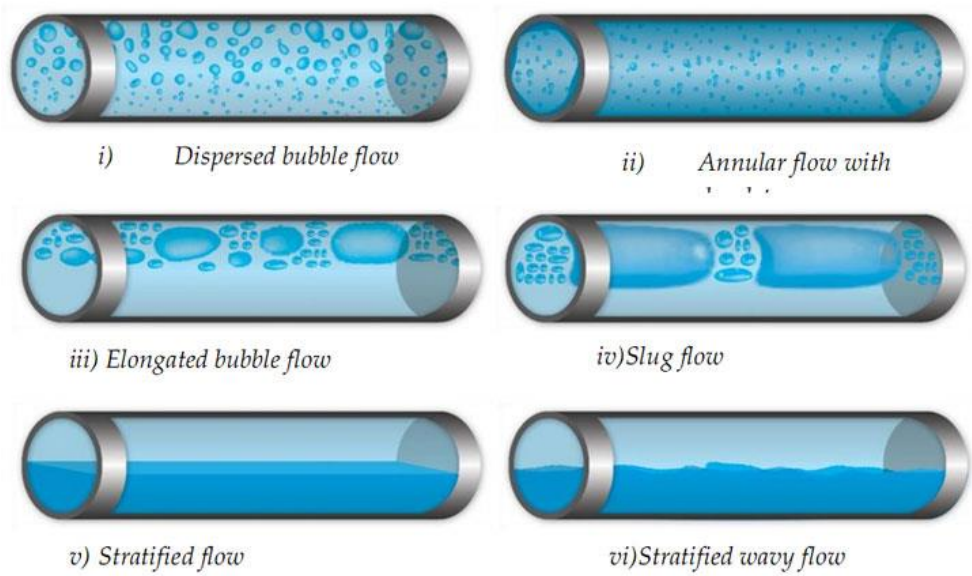

Figure 2.1: Flow regimes found in horizontal multiphase pipes (Abdalla, 2020)

Plug Flow: This flow regime usually occurs when there is a higher liquid volume fraction than the gas fraction, leading to the formation of bigger bubbles that flows near the top of the tube, the bubbles from in slug flow are usually shorter than the elongated gas bubbles in fully developed slug flows.

Annular Flow: Annular flow regime occurs at higher gas fractions and very high gas flow rates. In this case, a liquid film forms around the pipe walls pushed by the high gas velocity flowing at the core or centre of the pipe. Gravity also plays a role here making the film height bigger at the bottom of the pipe than at the top. The interface is unstable, and a considerable number of droplets are kept suspended in the gas core.

Dispersed-Bubble Flow: This occurs due to a higher volume fraction of the liquid as well as very high liquid velocities. The gas phase is uniformly dispersed as discrete gas bubbles in the liquid phase. Due to the high liquid flow rates, the dispersed bubbles are carried away by the liquid phase, and both phases flow at relatively the same speed (Ghajar, 2005).

2.3.2 Vertical Pipes

Flow schemes encountered in vertical systems are as follows:

Bubbly Flow: At low gas flow rates in a co-current vertical flow of liquid and gas, the gas phase tends to rise through the continuous liquid medium as small, discrete bubbles become fully dispersed within the liquid leading to a bubbly flow.

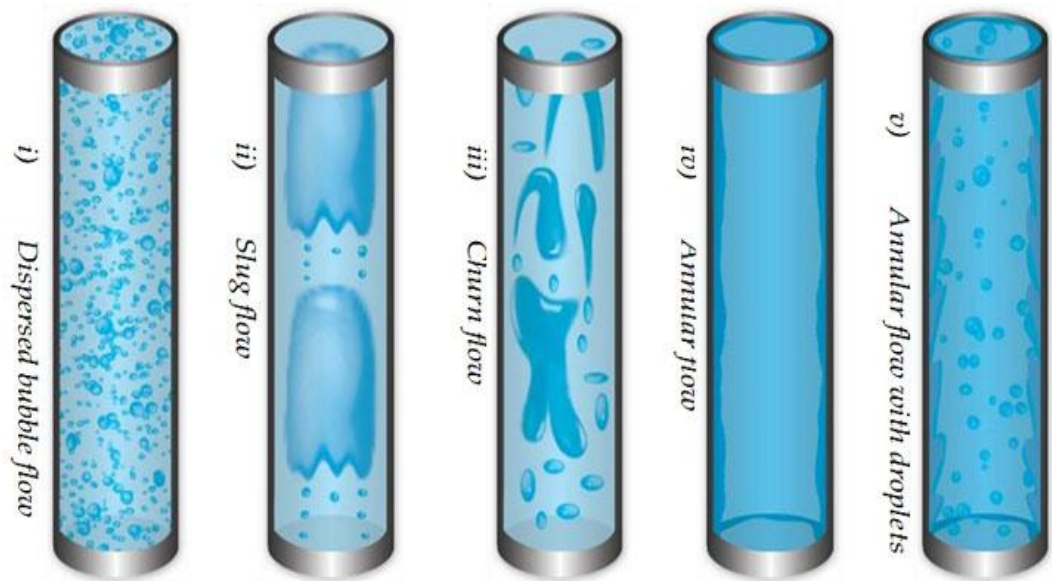

Figure 2.2: Flow regimes found in vertical multiphase pipes. (Abdalla, 2020)

Slug Flow: An increase in the gas rate, makes the smaller bubbles coalesce and turn into bigger bubbles. The bubbles can become large enough to occupy most of the cross-section of the pipe. These bigger bubbles which are often called “Taylor bubbles,” are separated by liquid slugs in the pipe giving rise to the name of the flow system slug flow.

Churn Flow: When the flow rates become much higher, the shear stress between the liquid film and the Taylor bubble also becomes higher, breaking down to give an oscillating churn regime.

Annular Flow: This occurs at very high gas flow rates and pushes the entire liquid away from the central section of the pipe to form a liquid film on the pipe wall, with some liquid entrained in the core) and the gas flows in the centre.

Wispy Annular Flow: Wispy Annular Flow occurs as the liquid flow rate increases and the concentration of droplets in the gas core also increases, this leads to the formation of large lumps or streaks (wisps) of liquid.

2.3.3 Inclined Pipes

Upward-inclined flow patterns are much like the flow patterns observed in vertical flow systems. These include bubbly flow, slug flow, churn flow, and annular flow. Figure 2.3: Multiphase flow regimes found in inclined pipes (Hernandez-Perez, 2008) However, with more than 20^{O} deviation from the vertical, churn flow is hardly present. For near-horizontal systems, stratified flow could be observed, whereas the bubbly flow pattern is sometimes absent. With more than 50^{O} deviation from vertical, bubbly flow never occurs according to Taitel et al. (1978).

In downward inclined multiphase flow, Barnea et al. (1982) found that an increase in the angle of inclination affects the interface shape varying from smooth for zero inclination to wavy stratified at higher inclinations, and nearly to axisymmetric annular flow for inclination angles approaching the vertical.

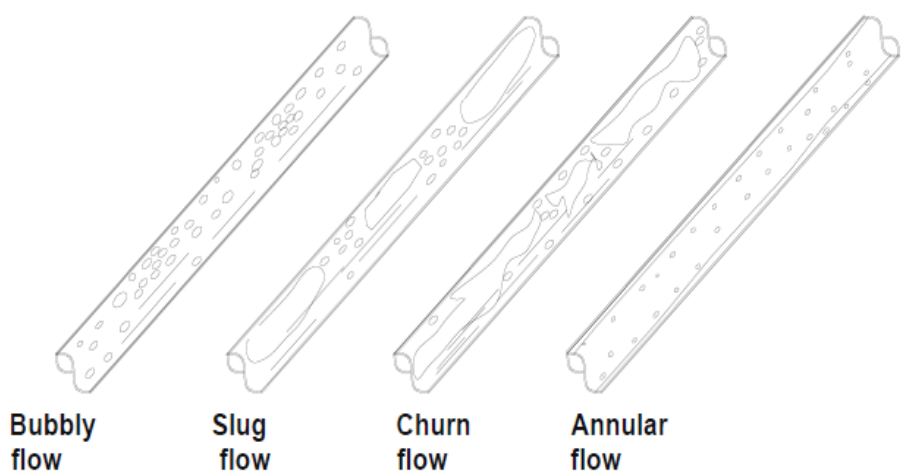

Figure 2.3: Multiphase flow regimes found in inclined pipes (Hernandez-Perez, 2008)

2.4 Flow Pattern Maps

Prediction of flow regimes has been done in literature by plotting the information on a flow regime map. A great deal of work has been carried out to generalise these plots for them to be applied to a wider range of fluid properties and flow geometries. Most of these maps are

plotted in terms of primary variables (such as the superficial velocity of the phases or mass flux and quality).

2.4.1 Flow Pattern Maps in Horizontal Pipes

Using several fluids in different pipe diameters, Baker (1954) developed the first flow pattern map for horizontal pipes. His plot involved mass fluxes of the phase and physical properties of the fluid like surface tension and density. Mandhane et al. (1974) experimented with smaller pipe diameters and established a flow regime map based on superficial liquid and gas velocities. This form of flow regime map is the most widely used now. Taitel and Dukler (1976) developed a theoretical, mechanistic flow pattern map which is also widely used after some modifications to the calculations of the interfacial friction factor.

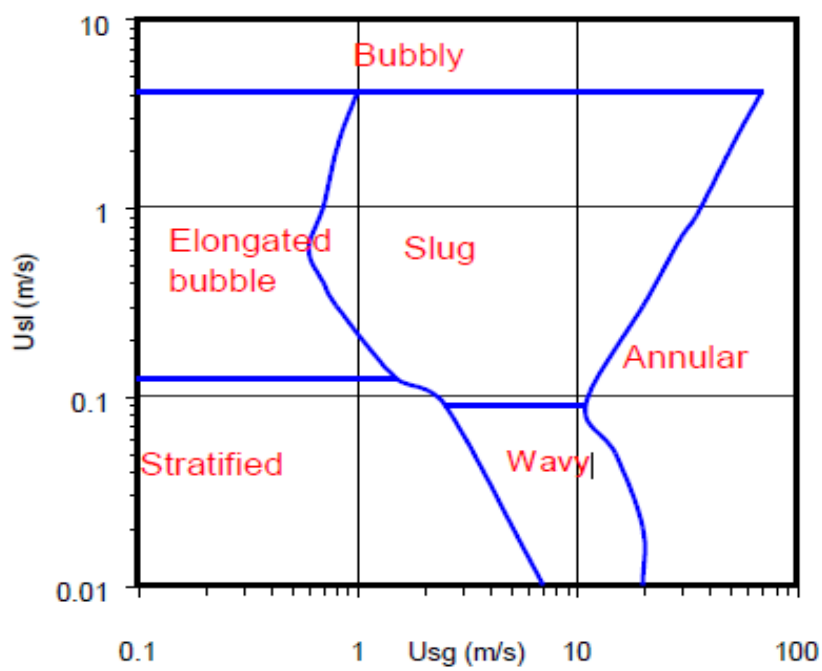

Figure 2.4: Flow pattern maps in horizontal pipes (Mandhane *et al,* 1974)

2.4.2 Flow pattern maps in vertical

Taitel et al. (1980) plot is the most widely acknowledged flow pattern map for vertical flow. Barnea et al. (1982) and Bilicki & Kestin (1987) have developed other flow patterns, specifically for downward flow in vertical pipes.

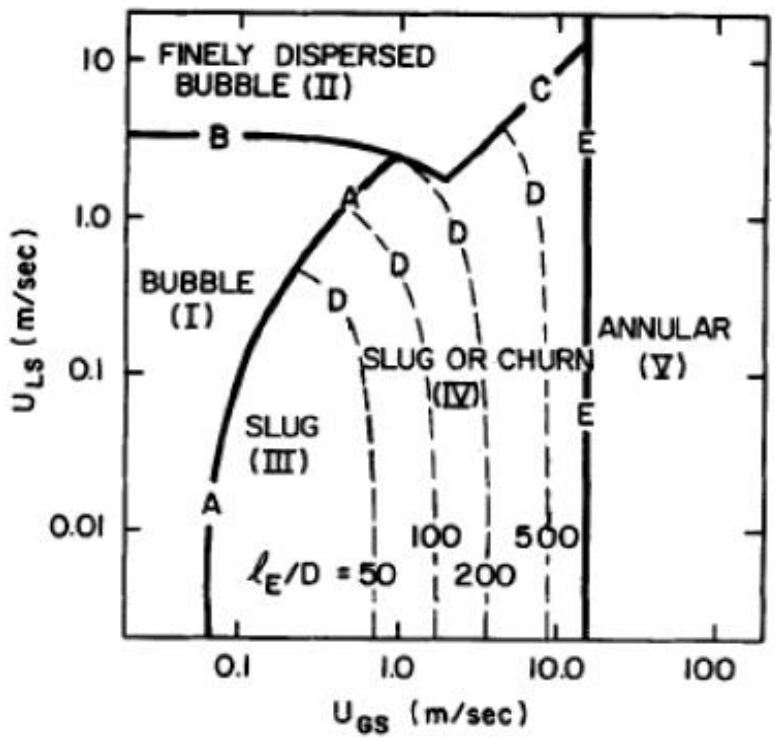

Figure 2.5: Flow pattern maps in vertical pipes (Taitel *et al,* 1980)

2.4.3 Flow pattern maps in inclined

One of the attempts was made by Gould et al. (1974), where flow pattern maps for horizontal and vertical systems and for the angular flow of up to 45^{O} inclinations are published. Subsequently, Mukherjee and Brill (1985) developed extensive data on two-phase inclined flow. Spedding and Nguyen (1976) compared the flow regime maps developed by others with air-water experimental data for conditions from vertically downward flow to vertically upward flow.

The major contribution in this area comes from the work of Weisman and Kang (1981), they observed that at high flow rates, the boundaries of flow patterns are usually not affected by pipe deviation, such as the transition from slug flow to dispersed bubbly flow or annular flow.

They observed that this process extends from vertical to horizontal, and they showed that for all angles of inclination, the transition to dispersed bubbly flow for all angles of inclination is given by:

$$\left[\frac{\left(-dp/dz\right)_L}{g(\rho_L-\rho_G)}\right]^{0.5}\left[\frac{g(\rho_L-\rho_G)d^2}{\sigma}\right]^{0.5}\geq 9.7 \tag{2.5}$$

Where $\left(-dp/dz\right)_L$ is the frictional pressure gradient of liquid flowing alone without any gas in the pipe.

This correlation for the transition to dispersed bubbly flow is quite similar to a previously developed correlation by Taitel *et al.* (1978) for vertical flow. Both of the correlations were observed at standard conditions for air-water systems at a mixture velocity of 3 m/s, for transition to dispersed bubbly flow. Weisman-Kang further gave a correlation for transition to annular flow for all angles of inclination as:

$$(Fr_{SG})(Ku_{SG}) = 25\left(\frac{U_{SG}}{U_{SL}}\right)^{0.625} \tag{2.6}$$

Where Ku_{SG} and Fr_{SG} are Kutadelaze number and Froude number respectively, based on gas superficial velocity.

One of the limitations of Weisman-Kang's correlation is that it did not differentiate between slug flow and churn flow but rather merged the two flow patterns together as intermittent flow. Their correlation for transition between bubbly and intermittent flow is given by:

$$\frac{U^2{}_{SG}}{gd} = 0.2\left[\frac{U_m}{gd}\right]^{1.56}(1-0.65\,cos\theta)^2 \tag{2.6}$$

Where U_{SG} is the superficial gas velocity and U_m, is the mixture velocity.

The last term, $(1-0.65\,cos\theta)^2$, accounts for the effect of inclination. Their stratified-wavy flow and separated-intermittent transitions are also given by the following respective correlations.

$$Fr_G{}^{1/2} = 0.25\left(\frac{U_{SG}}{U_{SL}}\right)^{1.1} \tag{2.7}$$

(2.8)

$$\left(\frac{\sigma}{gd^2\Delta\rho}\right)^{0.20}\left(\frac{dG_G}{\mu_G}\right)^{0.45} = 8\left(\frac{U_{SG}}{U_{SL}}\right)^{1.6}$$

Based on their findings, Weisman and Kang (1981) came up with a generalised flow pattern map for multiphase flow in inclined pipes.

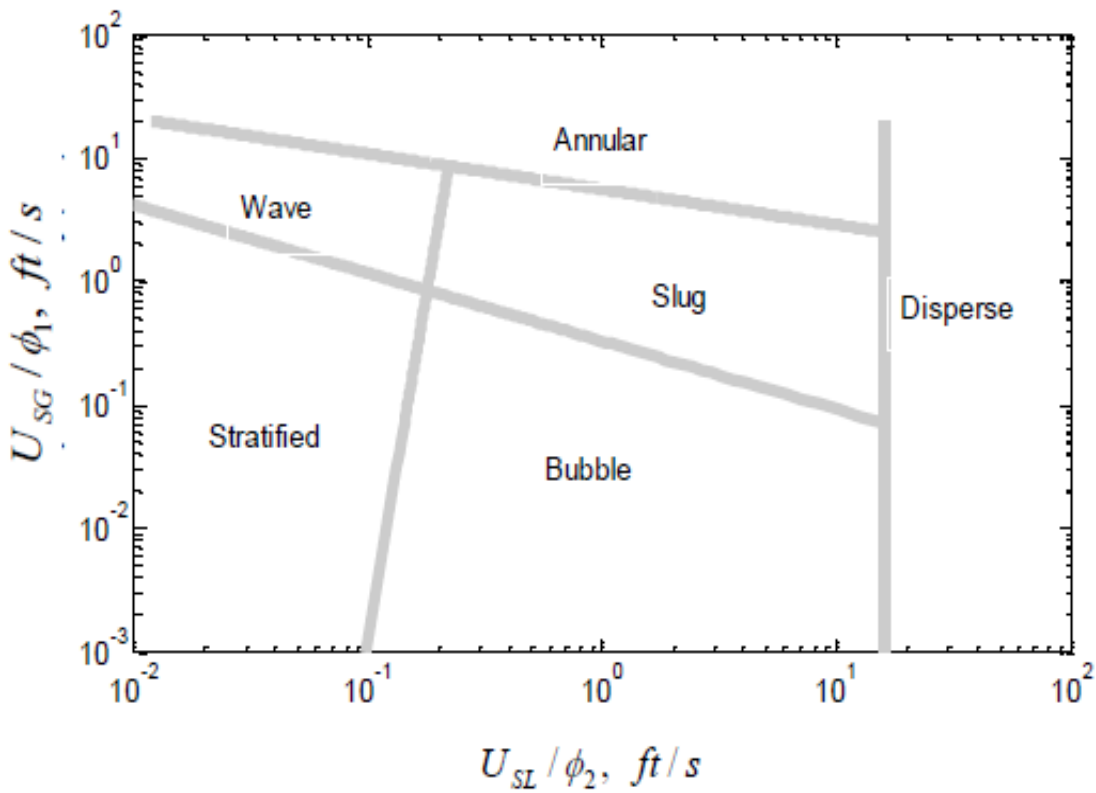

Figure 2.6: Generalized flow pattern map of Weisman and Kang (1981)

2.5 Slug Flow Overview

Slug flow is the dominant flow pattern in upward inclined pipes, it also commonly occurs in horizontal and vertical pipes over a wide range of gas-liquid flow rates. The slug flow can cause undesired consequences in process systems if not handled properly, hence this work will primarily focus on the slug flow regime. Slug flow can cause significant pressure

fluctuations, uneven arrival of gas and liquid at the processing facilities and causing flooding of the receiving tanks and knocking down gas-liquid separators in the oil and gas industry. Efficient oil-gas separators must be capable of handling the largest possible slugs without significant liquid carry-over in the gas stream, (Brill *et al*, 1981). Bratland (2010) has also reported that slug flow also leads to increases in hydrate deposits and corrosion of the facilities if the flow contains sand. The intermittent nature of slug flow also causes vibrations and high-pressure drops along the pipe. This increases the chance of damaging the pipe supports and bending as pointed out by Lu (2015).

In inclined and horizontal slug flow systems, gas flows in the topmost part of the pipe whereas liquid flows in the bottom due to gravity. The gaseous phase is mainly found in large bullet-shaped gas pockets (named Taylor bubbles), which alternate with flows of much faster liquid slugs (sometimes entrained with smaller gas bubbles) that bridge the entire cross-sectional area of the pipe separate them. The complex nature of slug flow is mainly attributed to its random nature and instability in a periodically steady-state condition, making it extremely complex to analyse the hydrodynamics variables associated with this kind of flow. A lot of experimental, computational, and mechanistic models have been carried out to improve understanding of the mechanism of slug formation, these studies have helped in achieving a well-defined time-averaged velocity profile at steady gas and liquid flow rates. Nevertheless, the components of phase velocities, mass flow rates, and pressure gradient present large variations over time at any pipeline cross-sectional area (Lu, 2015).

Dukler and Hubbard (1975) have set the precedence for unsteady gas-liquid hydrodynamics study, with their pioneering work on horizontal and near-horizontal tubes, where they created the concept of a slug unit to represent slug flow as a sequence of such with similar characteristics traveling at a constant translational velocity. They assume a homogeneous no-slip flow in the slug body, meaning that both gas and liquid in the slug body travel at the same velocity. With two additional parameters, slug frequency and liquid hold up, their model is capable of predicting various hydrodynamic parameters of slug flow such as translational velocity, film velocity as a function of time and distance, slug length, and

surface shape of the film region. They observed that the much faster slug body overrides and accelerates the slow liquid film in motion.

The film region is accelerated to the full slug velocity, which creates a mixing eddy region located at the front of the slug body. The pushing gas pocket sheds liquid behind at the same time that liquid from the film is picked up by the slug. A new film zone that decelerates over time is created. The rate of picking up and shedding is supposed to be the same for steady-state flow conditions thereby giving a constant slug length. Two types of losses along the different flow zones cause pressure drop, the increase in the velocity of the film to the slug body speed leads to acceleration pressure drop, and a wall friction loss within the slug body region (Cook and Newton, 1995).

Nicholson *et al* (1978) made the first attempt to extend the application of Dukler and Hubbard's model to the entire intermittent region by developing a mechanistic model for horizontal slug flow. They highlighted that the liquid holdup in the front of the film has not certainly been the same as that in the previous slug. Thus, the full length of the slug body is required to predict an average pressure drop. Through a comprehensive analysis of slug flow, Taitel and Barnea (1990) have developed a unified model that could work for all ranges of inclination. They introduced an interfacial shear stress term which was neglected in the previous model, to account for the gas-liquid interactions along the film zone. They developed two different methods to predict the pressure drop across a slug unit, by applying a force balance along two different zones. First, by applying it only to the liquid slug zone ignoring the pressure drop in the film region, the second option is by considering the entire unit which yields more accurate results.

Xiao et al (1990) adopted a uniform thickness along the film zone to avoid numerical integration, taking into account global pressure drop across the slug unit, and using the correlations for the slug length, translational velocity, and liquid holdup in the slug body as input parameters, they proposed an inclusive mechanistic model that combines slug flow models for horizontal and near-horizontal pipes.

2.5.1 Slug Flow Model

Slug Flow is one of the common flow patterns encountered during normal operating conditions in a multiphase pipeline. It is characterized by fast-moving liquid slugs with high values of liquid holdup alternating with large a gas bubble. The fast-moving liquid slugs keep prevailing over the slow-moving liquid films in the front, thereby making the flow very dynamic.

The fast-moving liquid slugs keep overriding slow-moving liquid films in front of them. Thus, a particle of liquid in the liquid film is continuously picked up by the front of the liquid slug. The particle is then accelerated to a much faster velocity before it decelerates as it travels along the liquid slug body. Finally, the particle is shed at the tail into the liquid film behind as the velocity approaches the film velocity once again. Bello (2017) has investigated the velocity distributions in the slug body and liquid film, he identified a significant drop in velocity magnitude immediately upstream of the slug nose, with the fastest velocities of the liquid in the axial direction appearing near the contact with the top surface of the pipe as it propagates downwards within the liquid phase.

The first comprehensive slug flow model was developed by Hubbard (1965), this was later improved by Dukler and Hubbard (1975). Since then, the two works remain the basis for modelling slug flow.

Figure 2.7 shows a basic model for slug flow, from the theory that a slug unit is composed of a slug body of and the gas pocket velocity U_{GP}. The model assumes that the quantity of liquid scooped up in the front of the slug is the same as the quantity of liquid shed behind, and so that means that the length of the slug body is always constant as it moves through the tube. To generate the slug flow equations, Hubbard (1965) used the complete liquid film and the gas pocket in the film zone as control volume. He then derived the continuity and momentum equations relative to the coordinate along which the translational velocity U_t moves.

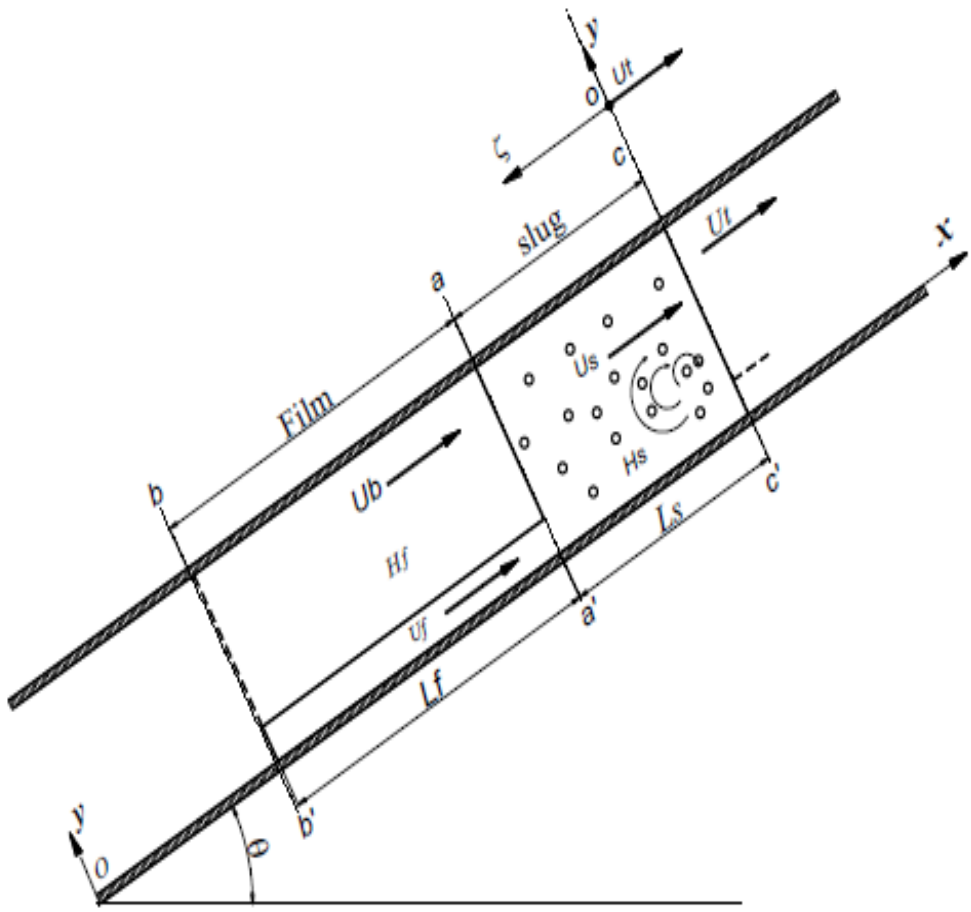

Figure 2.7: A simplified physical model of slug flow (Hernandez-Perez, 2008)

2.5.2 Slug velocity

To establish the speed with which the slug travels, Dukler and Hubbard (1975) carried out a liquid mass balance between the slug front and a point in the slug body where the slug velocity U_S, is fully accelerated. They came up with the following equation:

$$H_S(U_t - U_S) = H_f(U_t - U_f) \tag{2.9}$$

When arranged in another form:

$$U_t = (1 + C)U_S \equiv C_0 U_S \tag{2.10}$$

Whereas

$$C = \frac{H_f}{H_S}\left(\frac{U_t - U_f}{U_S}\right) \tag{2.11}$$

After performing a mass balance for both phases between the inlet and any slug unit, Dukler and Hubbard (1975) showed that the slug velocity is given as

$$U_S = U_m \equiv U_{SL} + U_{SG} \tag{2.12}$$

2.5.3 Slug Translational Velocity

Slug translational velocity, described as the velocity of slug units, is the summation of the maximum mixture velocity in the slug body and the drift velocity of the Taylor bubble. Nicklin *et al.* (1962) made the first attempt to study the motion of elongated bubbles. From a vertical flow experiment, they developed an expression for the calculation of the translational velocity of an elongated bubble in continuous slug flow as

$$U = C_0 U_m + U_B \tag{2.13}$$

Where C_0 is the flow distribution coefficient, U_m is the mixture velocity (defined as the sum of the liquid and gas superficial velocities; $U_{SL} + U_{SG}$) and U_B is the drift velocity of the Talor bubble in a stagnant liquid.

The Flow coefficient C_0 is defined as the ratio of the maximum to the mean velocity of a fully developed velocity profile. It is related to the contribution of the slug mixture to the translational velocity. Nicklin *et al.* (1962) assumed that the propagation velocity of the bubbles follows the maximum local velocity, U_{max}, in front of the nose tip, and based on that, the value of the constant C_0 can be expressed as

$$C_0 = {}^{U_{max}}/_{U_m} \tag{2.14}$$

Approximately, C_0 has a value of 2 for laminar flow and 1.2 for turbulent flow. The flow coefficient and drift velocity are both dependent on pipe inclination.

2.5.4 Taylor Bubble's Drift Velocity

The importance of drift velocity in slug flow cannot be overemphasised, it is one of the key components needed in calculating the slug interface velocity. Benjamin (1968) gave one of the best physical meanings that describes this phenomenon, by assuming a stagnant column of liquid in a horizontal pipe closed at both ends. If one of the ends is suddenly opened, gravitational force will drain the water out of the tube, while atmospheric pressure pushes air through the open to replace the drained liquid. The air bubble propagation speed through the liquid in the tube is what's called the drift velocity. The possibility for the bubble to drift ahead depends on the draining of the liquid, the higher the bubble potential, the faster it will move. Drift velocity is affected by the pipe's diameter, inclination as well as physical properties of the liquid, such as viscosity and surface tension (Gokcal, 2008).

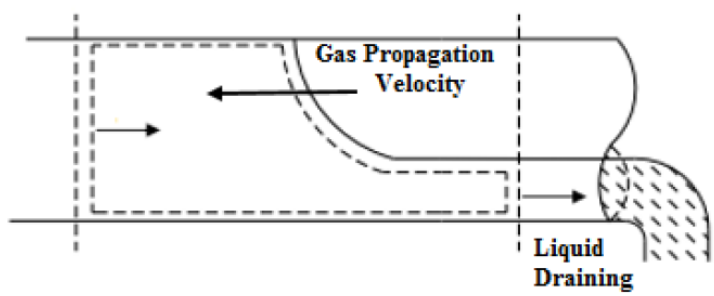

Figure 2.8 Propagation of gas pocket in draining horizontal pipe (Gokcal, 2008)

Earlier researchers such as Benjamin (1968), Zukoski (1966), Davies & Taylor (1950), Bendiksen (1984), Weber et al (1986), Hasan & Kabir (1989), etc, have all investigated the drift velocity for liquids with low viscosity at all sorts of pipe inclinations. Their observations show that the behavior of the drift velocity shows a convex parabolic trend with respect to inclination, while the bubble velocity increases from onset along the pipe until a steady value is attained. Later works such as Viana et al. (2003) used published data on the Taylor bubble rise velocity in a vertical pipe from 255 experiments to develop a generalised drift velocity correlation in terms of Froude number and Reynolds number for a fixed range of Eotvos number. Jeyachandra et al. (2012) extended the work of Gokcal et al. (2008) for different pipe diameters and viscosity ranges for horizontal and upward-inclined pipes. Using experimental data for water and viscous oils, they developed a new correlation

for Taylor bubble drift velocity at pipe inclination from 0^O to 90^O. Fabre et al. (2014) studied the effects of viscosity and surface tension on the shape and size of Taylor bubbles. Livinus et al. (2018) used a similar technique as Viana et al. (2003) by collecting multiple experimental data from open literature to develop a new generalised drift velocity correlation for Taylor bubbles at all pipe inclinations. However, all these models developed have shown various degrees of accuracy depending on the pipe orientation and the physical properties of the liquid.

There is a wide range of data for vertical flow; the standard formula for calculating drift velocity in a vertical system is given as

$$U_B^v = 0.35\sqrt{gd} \tag{2.15}$$

Zuber and Findlay (1965) put forward that the drift velocity in a horizontal flow exists due to the hydrostatic head difference between the liquid in the film and the liquid in the slug. This pressure difference causes the liquid in the slug to drain into the film. They postulated that for horizontal flows as well, there is a linear relationship between the drift velocity and the translational velocity U_t. This relationship was later proven by Benjamin (1968) who gave the formula as:

$$U_B^h = 0.54\sqrt{gd} \tag{2.16}$$

Weber (1981) proposed a method for calculating the drift velocity in a horizontal tube based on the drift phenomenon. In a horizontal pipe experiment with one closed end, Weber observed that when the pipe is initially filled with liquid, the liquid drains outs as a result of the hydrostatic pressure difference between the bottom and top of the pipe. A stretched-out gas bubble rushes through the pipe in the opposite direction to replace the liquid. The mechanism that causes the draining of the liquid as well as the movement of the gas bubble, is similar to the mechanism that causes the liquid on a horizontal surface to spread.

Weber (1981) proposed the following correlation for calculating drift velocity of low viscosity fluids in horizontal pipes:

$$U_B = \sqrt{gd}\left[0.54 - 1.76\left(\frac{\rho g d^2}{\sigma}\right)^{(-0.56)}\right] \tag{2.17}$$

Weber's correlation shows that the drift velocity is directly proportional; to pipe diameter, it becomes negligible for smaller pipes with less than 5mm in diameter. Kouba (1987) also developed the following expression for horizontal drift velocity, which also accounted for bubble entrainment in the liquid slug:

$$U_B = \sqrt{gd}\left[\frac{\frac{H_f}{H_S}cos\,\theta_f + \frac{2}{3}\left(\frac{sin^3\theta_f}{\pi H_s}\right) - 1}{1 - \frac{2H_s}{H_f}}\right]^{0.5} \tag{2.18}$$

Where θ_f is half the subtended angle by the liquid film height, shown in Figure 2.9.

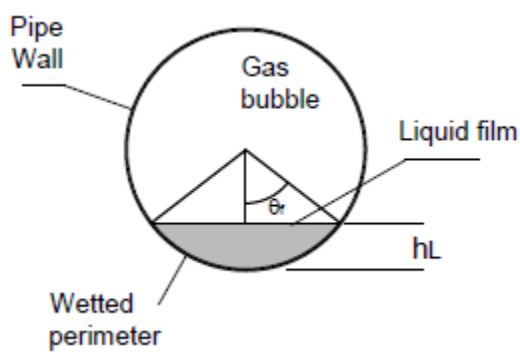

Figure 2.9: Cross section of a slug bubble (Kouba, 1987)

In an inclined multiphase flow, the angle of inclination also plays a role in the drift velocity. Bendiksen (1984) has proposed a practical formula for calculating drift velocity in inclined pipes which takes into account the angular influences.

$$U_B = U_B^h cos\theta + U_B^v sin\theta \tag{2.19}$$

Where U_d^h and U_d^v are the drift velocity for the horizontal and the vertical flow, and θ is the angle of inclination measured from the horizontal.

Hasan and Kabir (1988) also proposed the following relation for calculation drift velocity in inclined multiphase flow.

$$U_B = U_B^v \sqrt{sin\theta}(1 + cos\theta)^{1.2} \tag{2.20}$$

2.5.5 Slug Frequency

Slug frequency is a randomly occurring phenomenon due to the complexity of slug formation.

Hubbard (1965), and Gregory and Scott (1969) both defined slug frequency as the mean number of slugs per unit time. Gregory and Scott (1969) also developed a correlation for the prediction of slug frequency based on the experimental data generated by Hubbard (1965).

$$F_s = 0.0226 \left[\frac{U_{SL}}{gd}\left(\frac{19.75}{U_m} + U_m\right)\right]^{1.2} \tag{2.20}$$

Nydal (1991) checked the validity of Hubbard's correlation by comparing it with experimental data and found that there is a good fit with the original data range of $U_{SG} < 10\,{}^{m}/_{s}$ and $U_{SL} < 1.3\,{}^{m}/_{s}$.

Greskovich and Shrier (1972) also proposed a model similar to Gregory and Scott's correlation,

$$F_s = 0.0226 \left[\frac{U_{SL}}{U_m}\left(\frac{2.02}{d} + \frac{U_m^2}{gd}\right)\right]^{1.2} \tag{2.21}$$

Using a wider range of experimental data, Heywood and Richardson (1979) proposed the following correlation:

$$F_s = 0.0434 \left[\lambda_L \left(\frac{2.02}{d} + \frac{U_m^2}{gd}\right)\right]^{1.02} \tag{2.22}$$

Tronconi (1990) proposed a semi-mechanistic model for the slug frequency, this model assumed the slug frequency to be half the frequency of unstable waves:

$$F_s = 0.305Cw^{-1}\frac{\rho_G}{\rho_L}\frac{U_G}{h_g} \quad (2.23)$$

Where C_w is the wave velocity of the waves growing to become slugs, h_g is the height of the gas phase at the inlet, immediately upstream the point of slug initiation and U_G can be calculated from

$$U_G = \ U_{SG}/(1 - H_L) \quad (2.24)$$

Tronconi's correlation does not directly consider changes in slug frequency with the change in liquid flow rate, but indirectly accounts for this through the calculations of gas flow rate and height. Tronconi also hypothesized that there exists a linear relationship between critical waves frequency & slug frequency, this relationship is given as $f_w = C_w F_s$; with $C_w = 2$; This is in agreement with observations made by Dukler *et al.* (1985) and Kordyban (1985), where every second slug that originates from these waves becomes unstable and disappears.

Nydal (1991) claimed that, at high liquid rates, slug frequency weakly depends on U_{SG} and strongly depends on U_{SL}, he therefore proposed a correlation based on the liquid flow rate alone,

$$F_s = 0.088\ \frac{(U_{SL} + 1.5)^2}{gd} \quad (2.25)$$

Jepson and Taylor (1993) carried out an experiment with a 306 mm pipe diameter pipe. To investigate the effect of diameter, they compare their result with data obtained from Nicholson *et al.* (1978) for 25 and 51 mm pipes. Jepson and Taylor came up with a non-dimensional slug frequency correlation against the superficial mixture velocity:

$$F_s = \frac{U_{SL}}{d}(7.59 \times 10^{-3}U_m + 0.01) \quad (2.26)$$

Manolis *et al.* (1995) has proposed a new model based on Gregory and Scott (1969) by assuming $U_{min}, = 5\,{}^{m}/_{S}$ and modifying the Froude number to

$$Fr_{mod} = \frac{U_{SL}}{gd}\left[\frac{U_{m,min}^2 + U_m^2}{U_m}\right] \quad (2.27)$$

Zabaras (1999) also modified the Gregory and Scott correlation, to include the effect of pipe inclination.

$$F_s = 0.0226\left[\frac{U_{SL}}{gd}\left(\frac{19.75}{U_m} + U_m\right)\right]^{1.2}(0.836 + 2.75\,sin\theta) \quad (2.28)$$

Zabras tested this modified and reported that it worked very well for positive inclination angles up to 11^O to the horizontal.

Al-Safran (2016), has used the Poisson probability model suitable to model the slug frequency phenomenon. Theories and prediction methods of slug frequency for low viscous liquids in horizontal and near-horizontal pipes have been extensively studied by Al-Safran (2009), Hernandez et al (2010), Siddiqui et al (2015) etc. Their experimental investigation showed that slug frequency is independent of the pipe length, except only in certain slug flow sub-regimes where slug flow was observed to change with pipe length. The same can be said for low liquid flow rate and high gas flow rate, and for high liquid flow rate and low gas flow rate. Moreover, actual and superficial liquid velocity, pipe diameter, and the ratio of slip to mixture velocities were found to strongly correlate with slug frequency by Al-Safran (2009) and Hernandez et al (2010). Okezue (2013) and Siddiqui et al (2015) have both reported that for near-horizontal pipes, slug frequency increases with increasing the superficial liquid velocity, while on the other hand, frequency of the slugs decreases by increasing the gas superficial velocity, a trend they attributed to a higher void fraction.

Experimental works of Gokcal (2008), Hernandez et al (2010), Jeyachandra (2011), and Okezue (2013) on high viscosity oil for horizontal and inclined pipes showed that slug frequency increases with higher liquid viscosity, the same thing was observed for medium viscosity oil by Brito (2012). Inclination effects result in higher slug frequencies that when compared to horizontal flow, this phenomenon increases and attains a peak before decreasing at higher superficial gas velocities (Jeyachandra, 2011). Similarly, pipe diameter

also affects slug frequency, Zhao et al (2013) observed a higher slug frequency for smaller pipe diameters when compared to the larger pipe diameter.

There is still limited data on slug frequency in viscous liquids. More recent works on slug frequency include Baba et al. (2017) and Archibong-Esso et al. (2018). Using viscous oil, Baba et al. (2017) observed that viscosity has a strong influence on the slug frequency and proposed a new correlation incorporating the effect of viscosity on slug frequency for horizontal flow. Archibong-Esso et al. (2018) also investigated the effects of viscosity in two horizontal pipes of internal dimeters 0.0254and 0.0764m using test liquids with viscosities ranging from 1.0 to 4.0 Poise, they concluded that slug frequency increases with increase in oil viscosity and reduces with increase in pipe diameter. They attributed this reduction of slug frequency with the increased pipe diameter to the decrease in liquid height flowing across the cross-section of the pipe. They also observed a decreasing slug frequency along the pipe length due to slugs coalescing to form a more stable flow.

2.5.6 Slug Length

Slug flow experimental studies with air and water in horizontal and near-horizontal pipes have shown that slug length is affected by the superficial liquid and gas velocities. An increase in liquid superficial velocity leads to a decrease in slug length as a result of the increase in the liquid holdup, and on the other hand, an increase in the gas superficial velocity for the same liquid superficial velocity results in an increase in the slug length (Siddiqui et al 2015). Experimental studies carried out with high viscous oil by Gokcal (2008), and Al-Safran et al (2013) have indicated that slug length decreases with an increase in liquid viscosity. Furthermore, Gokcal (2008) claimed that the slug lengths observed in his tests are much shorter than 32D as proposed in the works of Taitel and Dukler (1980) and Barnea and Brauner (1985). Furthermore, an increase in the mixture velocities leads to a decrease in slug length in horizontal and near-horizontal pipes. (Jeyachandra, 2011).

Statistical analysis proves that viscosity of the liquid plays a significant role in slug length distribution, Al-Safran et al (2013) observed conspicuous deviation from the log-normal

distribution for low viscous liquids to a truncated positively skewed distribution. So far, most of the existing models in the literature tried could not satisfactorily predict slug length, Brito (2012) has likened this to the inability to consider all possible variables affecting slug lengths, such as pipe geometry, flow conditions, and fluid properties.

Abed and Ghoben (2015) explored the effects of gas and liquid superficial velocities on slug frequency and slug unit length in a horizontal pipe. Mohammed et al. (2016) used image processing techniques to measure the slug and velocity in a horizontal pipe. Baba et al. (2018) investigated slug length in high-viscosity oil-gas flow using air-water and air-oil systems in a horizontal pipe, their results showed that liquid viscosity has a significant effect on slug length. Using their experimental data, they carried out an assessment of existing prediction models and correlations in the literature and found some discrepancies, which can be attributed to the fluid properties used in developing those correlations.

2.5.7 Slug Liquid Holdup and Average Liquid Holdup

One of the most important parameters in co-current multiphase flow is a liquid holdup. The phases involved generally flow at different velocities because of gravitational effects and other factors. The lighter phase usually moves faster than the heavier phase, hence the likely hood of the heavier liquid being held back. This phenomenon has come to be referred to as liquid holdup. To determine in-situ flow rates, the holdup and velocity of each fluid need to be known. Slug liquid holdup is the fraction of liquid inside the slug body, several studies have been performed to predict this phenomenon mainly in horizontal and near-horizontal pipes. Earlier works such as Gregory et al (1978), Barnea & Brauner (1985), Gomez et al (2000), and Abdul-Majeed (2000) have all studied low viscous liquids while (Jeyachandra, 2011) and Kora et al. (2011) have focused on high viscous liquids.

Among the more recent works, Almutairi et al. (2020) studied the characteristics of two-phase flow in terms of liquid holdup and pipe inclination using experimental techniques, they developed an empirical correlation to predict the average liquid holdup based on dimensionless quantities, namely, the ratio of the gas-to-liquid superficial velocities and

gas-to-liquid density ratio. To gain more insight into the flow behaviour and pressure drop. Ribeiro et al. (2019) investigated the concurrent two and three-phase flow of oil, gas, and water in vertical pipes. Using MATLAB, developed an Artificial Neural Network (ANN) model for the prediction of multiphase pressure drop. Their models successfully predict two and three-phase flow pressure drop but reported low accuracies with total liquid holdup prediction.

Using experimental data from air-kerosene flow in inclined pipes, Chandrasekaran & Kumar (2018) developed data models by artificial intelligence techniques to predict multiphase flow and liquid hold at various inclinations of pipe flow. The model input variables include superficial velocities, densities, viscosities of the two phases, pressure, and temperature and the output variables are hold-up and flow pattern. Their models were successfully able to understand the complex relationship that exists in the multiphase fluid flow of air-liquid phases and extend it to predict different input scenarios.

Baba et al (2017) used advanced instrumentation to study the flow characteristics of highly viscous oils in a horizontal flow loop. Their results revealed that an increase in liquid viscosity has a significant effect on the flow pattern, pressure, and liquid hold. Archibong-Esso et al (2018) used viscous mineral oil to investigate slug liquid holdup in a horizontal pipe. Their experimental results show that slug liquid holdup is directly proportional to the viscosity and inversely proportional to the gas input fraction. They also developed a new empirical predictive correlation for estimating slug liquid holdup for highly viscous liquids. Although both correlations developed by Baba et al. (2019) and Archibong-Esso et al (2018) show an improved prediction performance for slug translational velocity and slug liquid holdup, the correlations did not consider the effects of pipe inclination.

Viscosity is shown to only have an effect on slug liquid hold up when the value goes up at higher mixture velocities. Meanwhile, slug holdup decreases when the oil viscosity increases for liquid medium viscosities between 0.108 Pa.s (108cP) and 0.166 Pa.s (166cP). This trend was explained by Brito (2012) as a result of more gas entrainment owing to the momentum exchange at the slug front; the amount of gas entrained in the liquid film

increases owing to the gas separation difficulties; less gas coalesces to the Taylor bubble. There are two methods widely used in the petroleum industry for the design of multiphase pipelines, these are from the works of Baker (1957) and Flanigan (1958). Using the Baker method, holdup can be calculated from the equation:

$$H_L = 1.61 {U_{SG}}^{-0.7}$$

Where U_{SG} is the superficial gas velocity in *ft/s*.

Following the works of Baker (1957) and Flanigan (1958), Guzhov *et al.* (1967) proposed a correlation for calculating the in-situ liquid volume fraction, E_L, from the input liquid volume fraction, C_L, the Froude number Fr_m and the mixture velocity, U_m. They carried out a series of experiments using a pipe inclined at an angle of 9^O to the horizontal to obtain a series of data. When E_L is plotted against C_L, they observed that all the plots converge at $C_L = E_L = 1$. They subsequently proposed an expression for the in-situ gas fraction that can be applicable for pipe inclinations up to 9^O from the horizontal.

$$E_G = 0.81\, C_G \left(1 - exp\left(-2.2\sqrt{Fr_m}\right)\right) \tag{2.30}$$

And since the total sum of hold ups for fluids present equals to unity, in-situ liquid fraction becomes:

$$E_L = 1 - 0.81\,(1 - C_L)\left(1 - exp\left(-2.2\sqrt{Fr_m}\right)\right) \tag{2.31}$$

Guzhov *et al.* (1967) claim that the above equations are applicable to Froude number up to 4.0, and for larger values of Froude number, E_L reduces to

$$E_L \approx 0.91 + 0.81 C_L \tag{2.32}$$

From the above equation, it is evident that the smallest value for in-situ liquid holdup in a pipe with inclination up to 9^O is 0.19. Figure 2.9 shows the plots for both Baker and Flannigan's correlations.

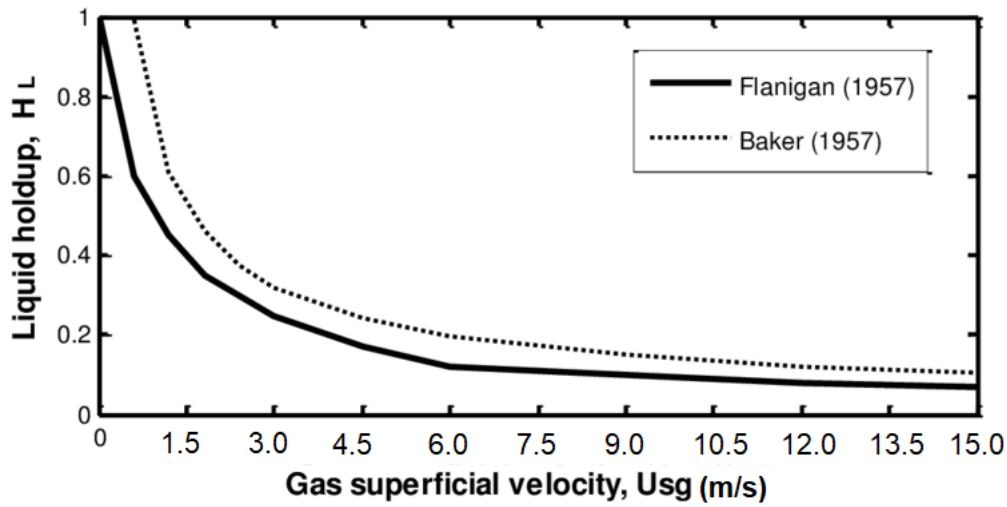

Figure 2.9: Baker and Flanigan correlations for liquid holdup adapted from Hernandez-Perez (2008) and replotted in SI Units

Improving on the works of Guzhov *et al.* (1967), Greskovich (1973) came up with an easier method. He proposed that it is only the intercept corresponding to $C_L = 0$ need to be measured in order to establish the whole line for a given Froude number, since straight lines were obtained by Guzhov *et al.* (1967) for a given mixture Froude number on a plot of E_L vs. C_L, all converges at $E_L = 1$.

He demonstrated that by passing gas through a pipe initially filled liquid and then took measurements of the liquid holdup after equilibrium is obtained. At this point, there is no liquid flow and thus presenting data for $C_L = 0$. Greskovich's experimental data set was cas carried out for pipe inclinations of 2^{O}, 6^{O} and 10^{O}. The result has revealed a significant inclination effect on the measured holdup, with values ranging from 0.13 to 0.22 for $Fr_m = 0.4$ and 0.32 to 0.41 for $Fr_m = 2.0$. Evidently, the findings of Greskovich (1973) have disagreed with the claim from Guzhov *et al.* (1967) that there is little effect of inclination angle on holdup.

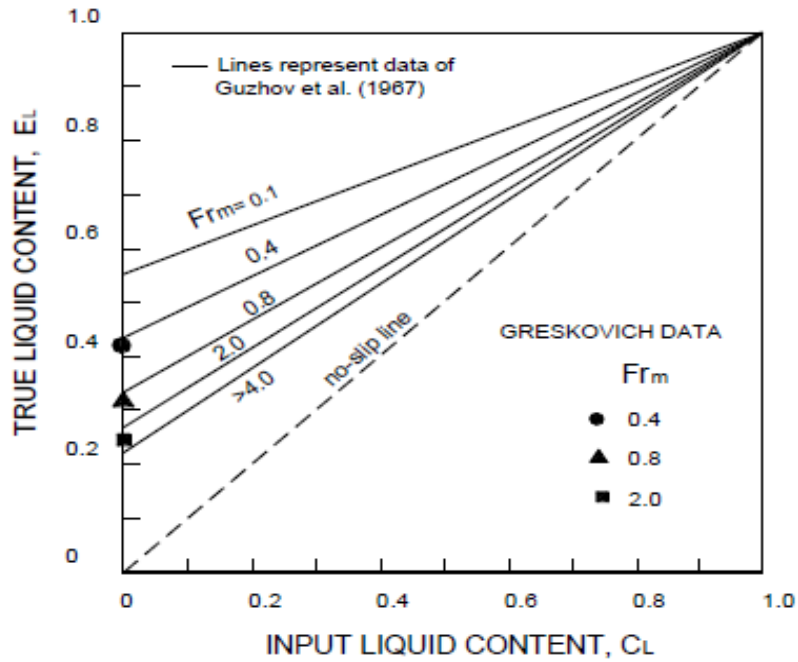

Figure 2.10: In-situ holdup plot of Guzhov *et al.* (1967), modified by Greskovich (1973)

Gregory (1974) investigated both Guzhov's correlation and the more popular Baker and Flanigan correlations, he found that Guzhov's correlation is unreliable at low values of liquid holdup (less than 0.25), while Baker and Flanigan's correlations are also subject to large errors.

Begss and Brill (1973) also carried out some experimental studies to come up with a correlation for the liquid holdup. Their correlation for inclined flow is a result of some modification for horizontal flow parameters; input volume fraction $\left(C_L = {U_{SL}}/{U_m}\right)$ and the mixture Froude number $\left(Fr_m = {U_m}^2/{gd}\right)$.

They divided the flow patterns detected in horizontal pipes into four groups: segregated flow, intermittent flow, transition flow, and intermittent flow. The segregated flow pattern includes wavy stratified flow, smooth flow, and annular flow, while the intermittent flow regime covers both slug flow and plug flow. The transition flow system encompasses the regions between stratified flows and intermittent flow patterns, whereas the distributed flow

regime comprises mist flow and bubbly flow. Their flow regimes are determined by following the conditions:

Segregated	$C_L < 0.01 \; and \; Fr < L_1$
	or $C_L > 0.01 \; and \; Fr < L_2$
Transition	$C_L < 0.01 \; and \; L_2 < Fr < L_3$
Intermittent	$0.01 < C_L > 0.4 \; and \; L_3 < Fr < L_1$
	or $C_L > 0.4 \; and \; L_3 < Fr < L_4$
Distributed	$C_L < 0.4 \; and \; Fr > L_1$
	or $C_L > 0.4 \; and \; Fr > L_4$

They further defined the four transition parameters as

$$L_1 = 316C_L^{0.302}$$

$$L_2 = 0.0009252C_L^{-2.4684}$$

$$L_3 = 0.1C_L^{-1.4516}$$

$$L_4 = 0.5C_L^{-6.738}$$

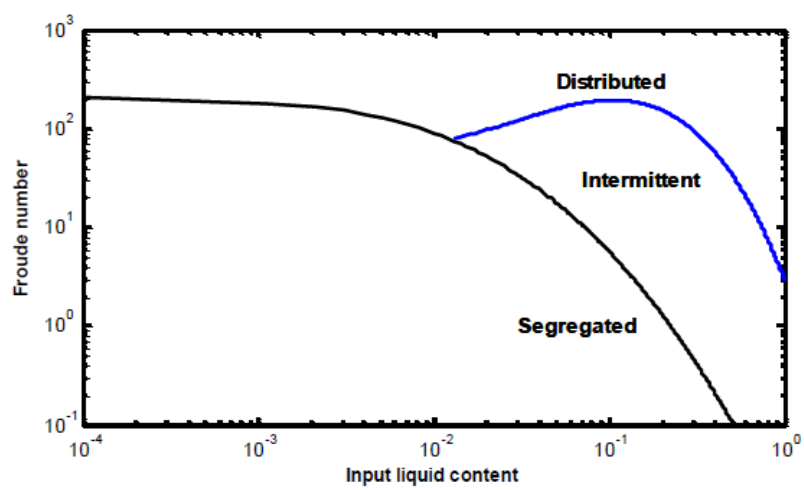

Figure 2.11: Beggs and Brill (1973) flow pattern map

Beggs and Brill came up with a correlation for estimation liquid holdup, H_L, in horizontal pipes as

$$H_{L(0)} = {aC_L^b}/{Fr^c} \tag{2.33}$$

Values of the constant parameters a, b, and c, depends on the nature of the flow, they were determined experimentally as

	a	b	c
Segregated	0.980	0.4846	0.0868
Intermittent	0.845	0.5351	0.0173
Distributed	1.065	0.5824	0.0609

When the flow pattern falls in the transition zone, they proposed that H_L can be estimated from a linear interpolation of H_L values calculated for the segregated and intermittent flow regimes. Thus,

$$H_{L,tran} = \left|\frac{(L_3 - Fr)}{L_3 - L_2}\right| H_{L,seg} + \left|\frac{(Fr - L_2)}{L_3 - L_2}\right| H_{L,int} \tag{2.34}$$

Other works on liquid holdup includes Mattar and Gregory (1974) who studied air-oil slug flow in an upward inclined pipe at inclination angles ranging from 0 to 10^O and obtained data for parameters such as bubble rise velocity and liquid holdup. They developed a correlation for liquid holdup as

$$H_L = 1 - \frac{U_{SG}}{1.3(U_{SG} + U_{SL}) + 0.7} \tag{2.35}$$

2.5.8 Liquid Film/Taylor Bubble Shape

Experimental investigations on Taylor bubbles have shown that the bubble shape change with the increase in mixture velocity. Rosa (2004) has observed a well-defined nose and tail at lower velocities, as the fluid velocity goes up, the nose points towards the centre of the pipe, and the tail is full of small gas bubbles. Taitel and Barnea's (1990) model matches well with the film profile for lower liquid viscosities, Cook (1995) suggests that the gas-liquid interaction in the stratified region must be taken into consideration. Further laboratory studies show that the liquid film height in the stratified zone increases for high liquid viscosity to become considerably larger and more aerated than for lower viscous liquids (Colmenares et al 2001). However, Marcano et al (1998) and Siddiqui et al (2015) have both

reported the existence of a thin film for high viscous oil flow at the top of the pipe due to the low drainage of the oil. There are still research gaps in numerical analysis to characterize the shape of this film.

2.5.9 Slug Flow Hydrodynamic Parameters Literature Review

One of the major gaps in the multiphase gas-liquid flow research area is the uncertainty of the existing correlations to calculate hydrodynamics of the high and medium viscosity liquids. Most of the current models were only tested for low viscous fluids in horizontal and near-horizontal pipes. Therefore, these models do not consider the combined effect of viscosity and higher pipe inclinations.

The drift velocity experiment with medium viscous liquid in long inclined pipes carried out so far only calculate drift velocity at one single location, such an experiment could explain how drift velocity behaves along the pipe length for medium viscosity liquids. However, for high viscous oils, tests have been conducted only for near-horizontal pipe angles and for vertical flow (Gomes, 2016). Thus, it is one of the motivations to generate a set of simulations and experimental data set that could be used to test the current correlations and models existing in the literature as well as contribute to expanding the understanding of slug flow phenomena.

2.6 Pressure Gradient

Existing studies in the literature have shown that pressure gradient is affected when inclination angle and viscosity change. One of the best models to predict pressure drop for high viscous liquids is Taitel and Barnea (1990). While Dukler and Hubbard's (1975) model is more suitable for low viscous liquids. An increase in liquid viscosity was reported to result in an increase in pressure gradient, this trend is more evident at higher superficial oil and gas velocities as shown by Gokcal (2008). In addition, the pressure gradient increases as liquid viscosity go up in the downward inclined flow. Moreover, the pressure gradient in inclined flow is lower when compared to horizontal flow due to the negating effect of the gravitational pressure gradient (Jeyachandra, 2011)

For upward inclined flows, a decrease in pressure gradient is observed at lower liquid velocities. An increasing trend is also observed for larger gas velocities according to Jeyachandra (2011). He explained that this phenomenon is due to the competing effects of the gravitational and frictional pressure gradients. Furthermore, a higher total pressure gradient when compared to horizontal flow could be explained by the additional effect of the gravitational pressure gradient.

The transition from one regime to another was reported to be one of the factors that lead to pressure drop in gas-liquid multiphase flow. To get an insight into the internal flow structure of the two-phase flow transition regime from stratified smooth to stratified way to slug flow, Bello (2017) used a non-intrusive optical technique – Particle Image Velocimetry (PIV) – to evaluate the velocity field of the liquid phase. He observed a significant increase in pressure drop along the pipe during the transition from stratified to slug flow, as the flow intermittency of the subsequent slug causes large fluctuations in liquid and gas flow rates and system pressure around the pipe.

2.6.1 Pressure Drop in Inclined Pipes

Pressure drop in an inclined pipe is determined by gravitational forces, acceleration forces, and shear stresses. The following momentum balance equation shows the three key components that determine the pressure gradient.

$$-\frac{dP}{dZ} = -\frac{dP_{fric}}{dZ} - \frac{dP_{acc}}{dZ} - \frac{dP_{grav}}{dZ} \tag{2.36}$$

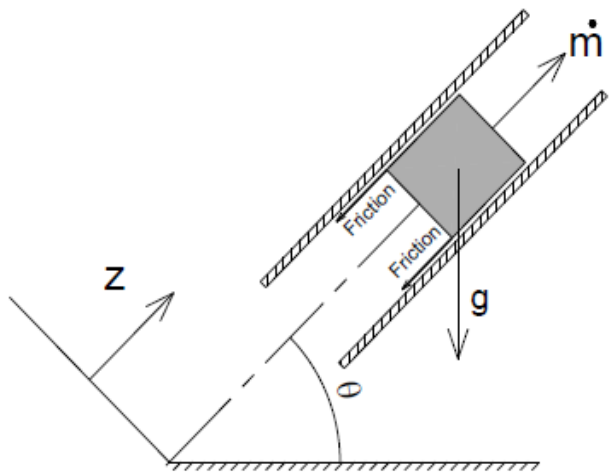

Figure 2.12: Forces acting on an inclined pipe (Abulencia and Theodore, 2009)

Beggs and Brill (1973) carried out extensive research on pressure drop in inclined multiphase flow. Based on the experimental data obtained from two pipes of internal diameters 1 and 1.5 inches, with a length of 90 feet, they came up with a correlation for pressure drop in inclined pipes for various angles, ranging from 0^O to 90^O in imperial units as:

$$\left(-\frac{dP}{dz}\right)_F = \frac{2f_m\rho_n u_m^2}{g_c d} \tag{2.37}$$

Where:

ρ_n is the non-slip mixture density; $\rho_n = \rho_l C_L + \rho_g C_g$,

f_m is the mixture friction factor; $f_m = f_n e^s$

f_n is the no-slip friction factor based on the no-slip Reynolds number,

while g_c is the dimensional conversion factor of gravity

To calculate the exponent s that appeared in the mixture friction factor, the two-phase friction factor needs to be determined first from the following expressions:

$$y \equiv {C_L}/{f^2_{L(\alpha)}}$$

For values of $y > 1.2$ s can be calculated from the formula (2.38)

$$s = \frac{ln\ y}{-0.0523 + 3.182(ln\ y) - 0.8725(ln\ \ y)^2 + 0.01853(ln\ y)^4} \quad (2.39)$$

And for $1.0 < y < 1.2$, s is given by

$$s = \ (ln2.2\ y - 1.2)1 < y < 1.2 \quad (2.40)$$

This shows that frictional pressure drop depends on the flow pattern as well as the angle of inclination. For gas-liquid phase flow in inclined pipes, they presented the correlation for total pressure drop as:

$$-\frac{dp}{dz} = \frac{g\ sin\theta}{g_c}\left(\rho_L H_L + \rho_G(1 - H_L)\right) + \frac{f_m U_m^2 \rho_n}{2 g_c d} \quad (2.41)$$

Although other works have been carried out, Beggs and Brill's correlation is still the best known. Other notable works in this field are Mattar and Gregory (1974) proposed the following model for estimating pressure drop:

$$\frac{\Delta P}{L} = \frac{\frac{g}{\rho_m g_c} sin\theta + 2\frac{f \rho_{mE} U_m^2}{g_c d}}{1 - \frac{\rho_m U_m U_{SG}}{g_c P}} \quad (2.42)$$

Where:

$$\rho_{mE} = H_L \rho_L + (1 - \rho_L)\rho_G \quad (2.43)$$

and

$$f = 0.0014 + \frac{0.125}{(Re)^{0.32}} \quad (2.44)$$

Few other works have been carried out for the determination of liquid holdup and pressure drop by using the mechanistic model. These include Hasan and Kabir (1988), Gomez *et al.* (2000), and Kaya *et al.* (2001). Hasan and Kabir (1998) used the flow pattern approach for vertical flow and modified it for deviation to inclined flow to come up with their model. They discovered that the flow rates are high for dispersed bubbly flow and annular flow. As a result of that, buoyancy influence is small and there is a negligible effect on pipe inclination. And for that reason, the models developed for vertical flow systems can be applied to inclined flow without the need for any modification.

For bubbly flow in vertical systems, Hasan and Kabir (1998) postulated that the in-situ velocity of the gas phase, U_G is the sum of the terminal rise velocity, U_∞, and the mixture velocity U_m, multiplied by the flow parameter C_O. That is:

$$U_G = {}^{U_{SG}}/_{\alpha} = C_O U_m + U_\infty \tag{2.45}$$

And liquid holdup H_L is given by:

$$H_L \equiv 1 - \alpha = 1 - \frac{U_{SG}}{C_0 U_m + U_\infty} \tag{2.46}$$

Gomez *et al.* (2000) and Kaya *et al.* (2001) followed a different approach for vertical systems, and came up with a slightly different formula:

$$H_L \equiv 1 - \alpha = 1 - \frac{U_{SG}}{C_0 U_m + U_\infty \sqrt{H_L sin\theta}} \tag{2.47}$$

Thus, the process of estimating pressure drop and liquid holdup in inclined flow will be similar to that of vertical flow. However, the values of two important parameters need to be known, flow parameter C_O, and the bubble rise velocity U_∞. C_0 has been reported to lie between 1.2 and 1.35. However, Kouba (1987) carried out and experiment analysis and concluded that C_0 can be as high as 1.8, depending on the conditions of flow (low superficial liquid and gas velocities). Zheng *et al.* (1994) also reported an experimentally determined value of C_0 as 1.20 for a wide range of slug flow conditions. Hence it is

established that in most cases, C_0 only varies between 1.2 and 1.25. The value of 1.2 represents the maximum velocity for fully developed turbulent flow. Both Hasan and Kabir (1988) and Kaya *et al.* (2001) adopted the value of 1.2 for the flow parameter C_O and assumed the bubble rise velocity in inclined systems to be the same as in vertical systems. Thus, the same formula with the similar values of parameters used in vertical flow can also be used to calculate liquid holdup in inclined pipes. Once liquid holdup is known, the total pressure gradient can be calculated by adding the frictional and accelerational components to the static head. And since the static head for an inclined pipe is $\rho_m sin\theta$. Hence the total pressure in inclined bubbly flow can be given as

$$-\frac{dp}{dz} = \frac{g\ sin\theta}{g_c}\left(\rho_L H_L + \rho_G(1 - H_L)\right) + \frac{f_m U_m^2 \rho_m}{2 g_c d} + \frac{f_m U_m}{g_c}\frac{dU_m}{dz} \tag{2.48}$$

However, the model presented above cannot be used directly for the estimation of pressure drop in slug flow, this is due to the difference in drift velocity between the bigger Taylor bubble in the slug and the smaller bubbles in the bubbly flow. Both Hasan and Kabir (1988) and Kaya *et al.* (2001) suggest that the easiest way to account for the difference in drift velocities in slug flow is to use some type of an average rise velocity for all gas bubbles, small and large. Therefore in-situ volume fraction in slug flow can be estimated as:

$$H_L \equiv 1 - \alpha_G = 1 - \frac{U_{SG}}{C_0 U_m + \bar{U}_{\infty\theta}} \tag{2.49}$$

As in vertical systems, the average rise velocity is given in terms of small bubble rise velocity, Taylor bubble rise velocity, and bubbly-slug transition velocity as

$$\bar{U}_{\infty\theta} = \bar{U}_{\infty T\alpha}(1 - e^{-U_t U_{SG}}) + \bar{U}_{\infty} e^{-U_t U_{SG}} \tag{2.50}$$

Where U_t is the superficial gas velocity for transition to intermittent flow.

The constant value of 1.2 can also be used for the flow parameter C_O, but the value of C_O might be affected by pipe inclination. The buoyancy force against drag force on the rising

bubble can be balanced by the formula for bubble rise velocity of volume V_b and of the projected area A_p.

$$U_b g \sin\theta(\rho_L - \rho_G) = {}^1/_2 C_{D\theta} U^2_{\infty T\theta} \rho_L A_{P\theta} \quad (2.51)$$

Where $C_{D\theta}$, is the drag coefficient for the bubble and $U_{\infty T\theta}$ is the bubble rise velocity in a pipe inclined by an angle, θ to the horizontal.

2.7 Chapter Summery

This chapter has discussed the fundamental concepts of both single and multiphase flow in pipelines, including flow patterns and flow regime map development. The literature survey studied in this chapter has revealed the following findings:

- The behaviour of two-phase (gas/liquid) flow is largely dependent on the physical properties of the fluids flowing through the pipe as well as the inclination and diameter of the pipe. The nature of the flow arises as a result of the interaction between the dispersed and continuous phases of the two-phase flow. Consequently, where there is a variation in the fluid properties, there are observable differences in the interfacial structure, flow regime, regime transitions, and the overall hydrodynamic behaviour.
- Most current models and correlations are derived based on data acquired from flow experiments using air and water, or other low viscous liquids. As a result of that, these models & correlations do not produce accurate results for more viscous liquids or when there is a very low surface tension between the gas and liquid. Therefore, there is a need to obtain more data over a wider range of fluid properties for model development and validation.
- Recently, there is an increased interest in viscous oils. Several multiphase flow research works have been carried out on viscous liquids to study some hydrodynamic parameters such as pressure drop, liquid holdup, slug frequency, and slug length. There still exist some considerable gaps especially for inclined multiphase flow, as much of these recent works are done for horizontal and vertical flow.

Chapter 3

Computational & Experimental Methodologies

This chapter discusses both the experimental and computational methodologies used in this work. The first part of the chapter highlights the concepts of Computational Fluid Dynamics (CFD) simulation, including its applications and advantages. It further delves deep into the various methods for carrying out two-phase flow models and the turbulent modelling approaches that will be used in this research. Three discretisation methods are also described, including the finite element, finite difference, and finite volume schemes. The discretisation method employed by the CFD code in this work to discretize each of the terms in the governing equations is also explained, including the strategies used to solve the resulting numerical equations such as the coupled solver and the Algebraic Multigrid method. The basic tools used for analysing the results are also given.

The second part of the chapter describes the experimental rig setup and equipment used to study the effects of viscosity and surface tension on pressure drop, liquid hold-up, and slug frequency, in horizontal and upward inclined pipes at 15^{O}. Glycerol and non-ionic surfactants were used to increase liquid viscosity and reduce surface tension, the experimental work was carried out on an inclinable rig in the Laser Laboratory of Energy Building, School of Chemical and Process Engineering (SCAPE).

3.1 CFD Basics and Applications

The invention and development of the digital computer has given rise to Computational Fluid Dynamics (CFD), a computer simulation-based tool, used by scientists and engineers to assess fluid handling system performances, including the fluid flow, heat transfer, and other complex phenomena such as combustion and chemical reaction (Versteeg and Malalasekera, 1996). CFD set up has two main steps; first and foremost, a set of mathematical equations are used to create a numerical model that expresses the flow or process. The second step involves obtaining a solution to these equations by using a

computer program (simulation software) that produces the flow variables through the flow domain.

At the beginning of the 1980s, computers developed into a sufficiently powerful tool for general application CFD software to become accessible. This has given CFD a wide acceptance and extensive usage in engineering fields to predict different aspects of fluid dynamics. It is also a powerful tool for design and analysis in the oil and gas industry. Earlier applications of CFD were in the aerospace, automotive, and nuclear industries (Bakker *et al.*, 2001). Additional improvement in CFD capabilities coupled with the rapid development in computing power has increased the usage of CFD applications to model intricate phenomena, such as evaporation, condensation, and two-phase flow in process engineering. Consequently, CFD has become part and parcel of a wide range of industries, such as petroleum, chemical, mechanical, mining, metallurgical, biomedical, and food industries. These industries now use CFD simulation to investigate the design of different equipment and gain information about various flow phenomena. In the chemical process industry, for example, CFD techniques are used in both design and optimisation of systems that involve heat exchange, mass transfer, drying, combustion, separation, reaction, mixing, and material processing multiphase systems.

Multiphase CFD models can be used to enhance the knowledge of complex multiphase interactions and provide specific information on 3-D transient flow, where it might not be feasible to carry out an experimental study. These models illustrate the potential of CFD to simulate and investigate complex flows in different industrial processes and a wide range of multiphase flow systems, even though a few limitations do exist.

3.1.1 Validation of CFD Models

One of the limitations of CFD simulations is the results accuracy, validation of CFD models is required to scrutinise the accuracy of the computational model. Validating CFD models is done by comparing the results obtained through CFD simulation with available experimental, theoretical, or analytical data. This has helped to produce more robust and accurate CFD models, establishing it as a reliable tool for industry and research.

Nevertheless, validation of CFD simulation data is not always possible due to a lack of available experimental or theoretical data in some cases.

3.1.2 Requirements for a CFD Procedure

The following information is required to deploy CFD analysis in process systems.

i. **A grid of points** is needed in the flow domain (geometry) to store the variables calculated by CFD.
ii. **Flow models** that describe the nature of the flow such as mass or heat transfer, turbulence models, and multiphase flow models.
iii. **Fluid properties** such as viscosity and density are required to be specified.
iv. **Boundary conditions** are needed to define the conditions at the flow domain boundaries and to allow the boundary values of all variables to be estimated.
v. **Initial conditions** must be given to guess the solution variables in a steady-state simulation or the initial state of the flow in a time-dependent transient flow.
vi. **Solver control parameters** manage the behaviour of the numerical solution processes; and
vii. **Analysis of the results** is done to study the information obtained from the simulation and verify that the solution is satisfactory against reliable experimental data or analytical correlations.

3.2 CFD Simulation Structure

The complete structure of CFD analysis can be classified into the following key steps.

3.2.1 Conceptualisation

The primary fundamental is the knowledge and understanding of the problem so as to select the right physical and computational model that describes the case. This step makes use of the necessary information for the simulation, such as the flow domain/geometry, flow specifications, fluid properties, as well as boundary, and initial conditions.

3.2.2 Geometry Construction

The geometry of the flow domain needs to be created to define the cell zones that store the simulation variables calculated by CFD. Flow geometry can be created by special software applications such as Gambit, SolidWorks, Design Modeller etc.

3.2.3 Mesh Generation

Meshing Generation is subdividing the flow domain into sufficiently small discrete cells. These cells are assigned to fix the positions of flow variables that need to be computed and stored. The accuracy of these variables increases from a coarse to a fine mesh. Thus, a fine mesh is mainly significant, especially in those regions where the accuracy of these flow variables is predicted to have large variations. However, a fine mesh requires more computational power and simulation time than a coarse mesh. Hence, it's critical when refining a mesh to optimize the mesh size with realistic computational resources and simulation time.

3.2.4 Flow Specification

This stage involves the definition of flow models, flow boundary conditions, as well as specifying the fluid's physical properties, and flow conditions.

3.2.5 Calculation of the Numerical Solution

At this stage, the CFD software uses the information provided by the user to carry out iterative calculations until a solution to the numerical equations describing the flow is reached. The time taken at this step depends on the complexity of the problem as well as mesh density.

3.2.6 Analysis of the Result

This is perhaps the most interesting step of CFD simulation, once the computational solution is obtained, the result needs to be analysed to bring out the simulation findings as well as the accuracy of the simulation. An unrealistic simulation result could arise from an incorrect definition or specification of one of the parameters mentioned in the previous sections. It could also be due to poor mesh quality, or even a conceptual error when the problem is not fully understood. Once the source error is identified and corrected, the

simulation can be set to run all over again as illustrated by Shaw (1992) in Figure 3.1 which demonstrates the flowchart of the CFD analysis process.

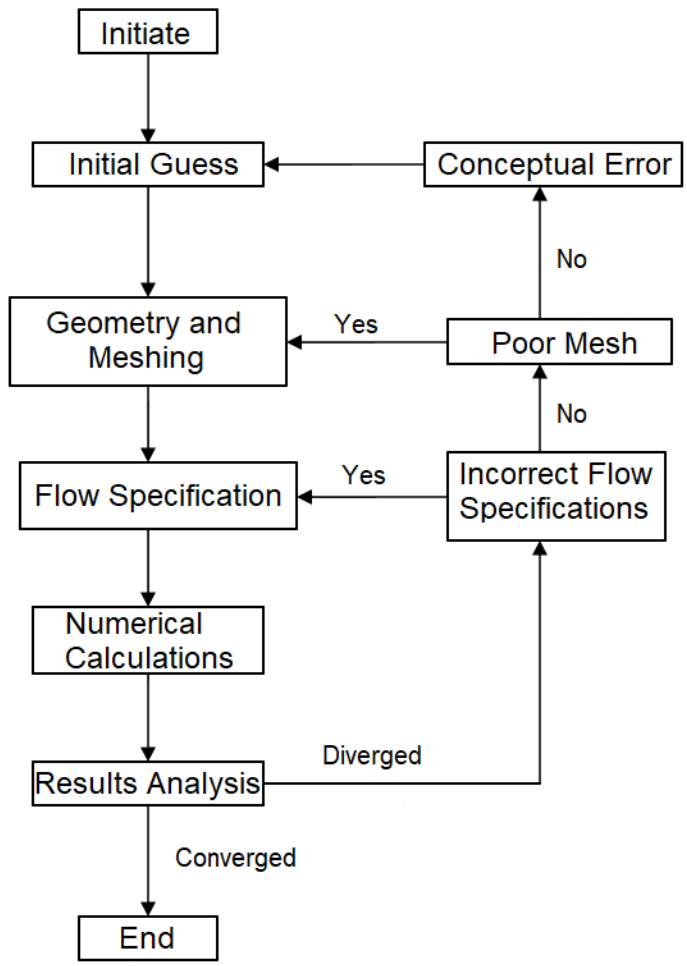

Figure 3.1: A flow diagram of the CFD analysis procedure (Shaw, 1992)

3.2 Benefits of CFD

CFD simulation has brought a tremendous benefit to research as well as the science and technology industry. Some of these benefits are:

i. CFD helps to study any system that are physically unsafe or experimentally challenging, such as the flows within a nuclear reactor.

ii. CFD can provide various information which could be difficult to obtain via experimentation due to inadequate of techniques or equipment, for example the hydrodynamics that occurs within an oil reservoir.

iii. CFD enables the flow behaviour visualisation within process equipment and systems, as it's now commonly used in industry as a flow visualisation tool.

iv. With CFD, the complex physical interactions taking place in a flow process can be modelled simultaneously.

3.4 CFD Codes: Open Source and Commercial

The increasing interest in CFD especially from the industry within the last three decades has led to the development of many CFD codes both open source and commercially available. These include CFX, FLUENT, PHOENICS, OpenFOAM, STAR-CCM, and many others to deal with the complex areas of fluid flow, heat transfer, mass transfer, and chemical reactions in industrial applications. Most of the available CFD codes are licensed commercial codes, OpenFOAM however, is free, open-source software. OpenFOAM is the leading free, open-source software for computational fluid dynamics (CFD), owned by the OpenFOAM Foundation and distributed exclusively under the General Public Licence (GPL). Irrespective of the different names and developers, a CFD package is made of three main components. These are, a pre-processor, a solver, and a post-processor. The three components act as a tripod stand without which the CFD application will not function. The pre-processor as the name implies is the first step which involves the creation of geometry and mesh. The solver is the second stage is where the numerical transport equations are discretized and solved based on the specified flow model, fluid properties, boundary conditions, initial conditions, and control parameters. The final step is the post-processor, where the output results of the simulation can be visualized and analysed.

3.5 Numerical Techniques

CFD governing equations usually come as partial differential equations (PDEs), such as Navier–Stokes equations which can neither be solved analytically nor directly using digital computers, even if the computer is capable of identifying and operating the differential

equations. Meanwhile, the PDEs have can be converted into numerical equations which include only numbers and no derivatives. The process of converting the PDEs to numerical format is what is referred to as Numerical Discretisation. There are three different methods of discretisation, these are finite element method, finite difference method, and finite volume method.

The finite element method involves the separation of the domain into small elements of subdomains, a simple variant of the dependent variables is then assumed over an individual element, and this variable variant is then calculated based on the values of the variable at the element nodes. The obtained set of equations for individual elements is then placed in a matrix and boundary conditions are applied to solve the equations in the matrix.

The Finite–difference method is obtained using the Taylor series to change the PDEs into derivatives of dependent variables, this produces a set of linear algebraic equations and the PDEs can be solved by one of the elimination approaches.

The finite volume method is the most widely used technique for numerical discretisation. The method involves the splitting of the spatial domain into finite control volumes covering many mesh elements that can be divided into sectors that belong to a different mesh element. The governing differential equations are then integrated over the specific control volumes to give a result that also ensures the accurate conservation of related properties in individual finite volumes. Each integral term is subsequently converted to a discrete term forming discretized equations at the nodal, or centroids points of the control volumes.

3.6 CFD Multiphase flow Models

Multiphase flow has particularly received special attention in the oil and gas industries as well as a wide range of other process industries. One of the widely used multiphase modelling techniques and the one employed in this work is dispersed multi-fluid modelling. (Ranade, 2002) has enumerated dispersed multiphase flow models into four different approaches:

i. Volume of Fluid (the Eulerian framework for both phases with interface forces reformulation based on a volumetric basis).

ii. Eulerian-Lagrangian (the continuous and dispersed phases are treated in the framework of Eulerian and Lagrangian respectively).
iii. Eulerian-Eulerian (both phases are treated within the Eulerian framework, not including explicitly the interface between phases), and
iv. Mixture (it treats both phases as continuous and dispersed as one mixture phase).

3.6.1 Volume of Fluid (VOF)

The volume of fluid (VOF) approach tracks the motion of an individual phase in each cell through the flow domain. When the two phases share the same control volume, they also share a set of conservation equations using mixture properties. Furthermore, if the control volume is occupied by one of the phases, its related properties are utilized. The approach helps in avoiding any unforeseen changes in the physical properties of the fluid through a thin interface. Thus, VOF becomes a model of choice when the shape and flow processes taking place close to the interface is an area of interest, it is appropriately used on most flow patterns in pipelines, such as stratified, slug, etc. Furthermore, the VOF model is able to simulate the profile deformation of the dispersed phase particles (i.e. droplets, bubbles) as a result of the surrounding fluid flow (Delnoij, 1999), thus the model can be applied to the flow around single objects such as droplets, bubbles, particles, etc., and dispersed multiphase flows which characterize the dispersed phase with extremely tiny fractions (Rashmi *et al*., 2009, De Schepper *et al*., 2008). However, a flow system characterized by a large fraction of the dispersed phase requires extensive computational power around every dispersed entity to determine the flow field.

There are several reasons why the VOF model is a useful tool for simulating fluid flow and interface dynamics. Here are some of the key benefits:

- Accurate representation of fluid interface: The VOF model can accurately track the interface between two immiscible fluids, even when the interface is highly curved or distorted.
- Flexibility: The VOF model can be used to simulate a wide range of fluid flow problems, including multiphase flow, free surface flow, and fluid-structure

interaction. It can also be used to simulate a variety of fluid types, such as Newtonian and non-Newtonian fluids.

- High computational efficiency: The VOF model is computationally efficient, which means that it can handle large and complex simulations without requiring significant computing resources.

Therefore, the VOF model is best suited to this work for its surface tracking ability of immiscible fluids with the interfacial position being a key point of interest in the hydrodynamics of the multiphase gas and liquid flow in this study.

3.6.1.1 VOF Governing Equations

Since the VOF approach shares the continuity equation by the two phases where the tracking of the interface is achieved by solving the equation for one of the phases. Therefore, the continuity equation is written for the liquid phase as follows:

$$\frac{\partial \alpha_l}{\partial t} + (U_i . \nabla)\alpha_l = 0 \tag{3.1}$$

In this study, the volume fraction equation is solved for the gas phase as the primary phase in the gas volume fraction is calculated based on the limitation of the total fraction being equal to unity as shown below:

$$\alpha_g + \alpha_l = 1 \tag{3.2}$$

Where α_g and α_l are the volume fraction of gas and liquid, respectively.

The momentum conservation equation can be expressed by the Navier–Stokes equation, which is shared by both phases and solved all through the domain as follows:

$$\frac{\partial}{\partial t}(\rho u_i) + \nabla .(\rho u_i u_j) = -\nabla p + \nabla .\left[\mu\left(\nabla u_i + \nabla u_j\right)\right] + \rho g_i + F_i \tag{3.3}$$

The first term on the right-hand side represents pressure, and the other terms represent diffusion and the body force of gravity. While the left-hand side corresponds to variation and convection

3.6.1.2 VOF Model Physical Properties

In the VOF model, the properties and variables of the different phases are presented as a mixture in cells or purely as one of the phases, these properties are found by the distribution of the volume fraction. That is the mixture of the two phases that are shown in the transport equations is calculated based on the fraction of each phase in the control volume. The density and viscosity in each cell are given as follows:

$$\rho_m = \alpha_l \rho_l + \alpha_g \rho_g = \alpha_l \rho_l + (1 - \alpha_l)\rho_g \tag{3.4}$$

$$\mu_m = \alpha_l \mu_l + \alpha_g \mu_g = \alpha_l \mu_l + (1 - \alpha_l)\mu_g \tag{3.5}$$

Where ρ_g, ρ_l, μ_g and μ_l are the density and viscosity of the liquid and gas phase.

3.6.1.3 VOF Interpolation near the Interface

The VOF algorithm generally solves the problem of updating the phase volume fraction field and provides a fixed grid, the velocity field, and the phase volume fraction as obtained in the previous time step (Zaleski, 2005). In a 2D domain, the interface is represented with a continuous, piecewise smooth line. A problem of this type can be reduced to the reconstruction of an approximation of the interface in each cell, with only a known volume fraction of each phase in the cell itself and in the neighbouring cells. The simple line interface calculation (SLIC) algorithms are the simplest VOF interface tracking schemes (Noh and Woodward, 1976). Figure (3.2–c) demonstrates the interface reconstruction by means of a SLIC algorithm.

Another VOF algorithm is the piecewise linear interface calculation (PLIC) algorithm (Li, 1995) which attempts to fit the interface through piecewise linear sections. PLIC is more accurate than SLIC, In the PLIC technique, the interface in the computational cell is approximated by a straight-line segment with a slope obtained from the interface normal. The computational cell is cut by the line segment in such a way that the fractional fluid volume equals the phase volume fraction value in that cell. The interface reconstruction by means of a second-order or PLIC algorithm is illustrated in Figure (3.2–b).

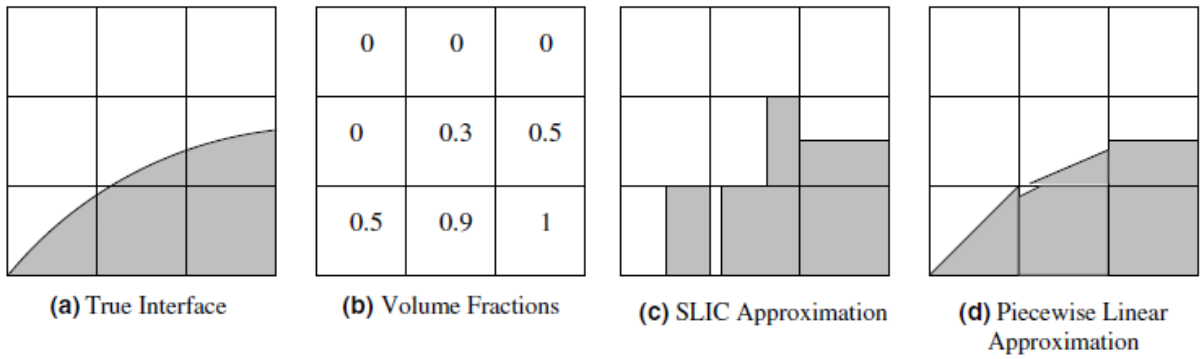

Figure.3.2: VOF interface reconstruction methods: The interface in (a) is reconstructed by VOF methods which stores volume fractions associated with the interface in each cell, as shown in (b). The interface is approximated by two interface reconstruction methods, SLIC in (c) and PLIC in (d). (Fluent 19.2 User's Guide, 2018).

The interface accuracy of VOF is improved further by the Compressive Interface Capturing Scheme for Arbitrary Meshes (CICSAM), based on Ubbink's research (1997). This technique is more appropriate when there is a high ratio of viscosity differences between the phases. It is also implemented in FLUENT as an explicit approach and provides the advantage of producing a sharp interface that is similar to that produced by a geometric reconstruction method.

3.6.2 Eulerian–Lagrangian (E–L) Approach

The Eulerian-Lagrangian approach considered the fluid continuum phase and then solved by time averaging of Navier–Stokes equations, just the way it is solved for a single-phase system. This approach also addresses a dispersed phase by using the equation of motion for each phase entity. Therefore, this method accurately captures dispersed fluid dynamics, such as particle-laden processes like chemical reactions, mass transfer, etc. Such a process can be sufficiently simulated manner and accounts for interaction between particles and size distribution in detail. However, an increase in the number of dispersed droplets, bubbles, or particles also means a proportionate increase in the computational costs. Consequently, this approach is limited to simulating two-phase flow with a low fraction of less than 10% of dispersed flow (Domgin *et al*., 1997; Jaworski and Pianko–Oprych, 2002).

3.6.2.1 Eulerian–Lagrangian Governing Equations

In the Eulerian-Lagrangian approach, the fluid phase movement is attained by calculating the average two-phase governing equations much like the Eulerian–Eulerian (discussed later). The continuity equation for one of the phases can be written as follows:

$$\frac{\partial}{\partial t}(\alpha_i \rho_i) + \nabla \cdot (\alpha_i \rho_i \vec{v}_i) = \sum_{j=1}^{n} \dot{m}_{ji} \tag{3.6}$$

While the momentum equation is expressed by the Navier–Stokes equation as:

$$\frac{\partial}{\partial t}(\alpha_i \rho_i \vec{v}_i) = -\nabla \cdot (\alpha_i \rho_i \vec{v}_i^2) - \alpha_i \nabla p - \nabla \cdot (\alpha_i \tau_i) + \alpha_i \rho_i \vec{g} + \alpha_i \rho_i (\vec{F}_i + \vec{F}_{lift,i} + \vec{F}_{vm,i}) \tag{3.7}$$

Where the stress tensor of the compressible fluid phase is identified as:

$$\tau_i = \alpha_i \mu_i (\nabla \vec{v}_i + \nabla \vec{v}_i^T) + \alpha_i (\lambda_i - \frac{2}{3}\mu_i) \nabla \cdot \vec{v}_i \mathrm{I} \tag{3.8}$$

The motion of the dispersed phase is presented by combining the force balance on the object that is expressed in the Lagrangian framework. Van Wachem *et al*. (2003) proposed the momentum balance equation in terms of particle acceleration as

$$m_d a_d = m_d g + V_d \nabla \cdot \tau_i - V_d \nabla P + \beta \frac{V_d}{\alpha_d} (\vec{v}_i + \vec{v}_d) \tag{3.9}$$

Where m_d, V_d, v_d and α_s are the mass, acceleration, velocity, and volume fraction of the dispersed phase respectively. While P and β are the local pressure and interface momentum transfer coefficients.

3.6.3 Eulerian–Eulerian (E–E) Approach

The Eulerian–Eulerian approach is based on the Eulerian framework, which assumes that all phases share the domain and may interpenetrate as they get moving all the way through it. Each phase can be described by phase velocity and volume fraction.

To effectively handle the coupling among the phases (closure), the interface forces such as drag, lift, and virtual mass must be specified. The continuum approach for the dispersed phase of the Eulerian–Eulerian approach has made the model more sufficient in terms of CPU time. When compared to other models, the Eulerian–Eulerian approach is very robust to modelling systems with high volume fractions of the dispersed phase, such as bubble column reactors, etc.

3.6.3.1 Eulerian–Eulerian Governing Equations

Governing equations of the Eulerian–Eulerian approach are derived by averaging all the conservation equations for each one of the phases as highlighted by the works of Drew (1983) and Lopez de Bertodano *et al*. (1990). Ranade (2002) has shown that the equation of volume average continuity for i^{th} interpenetrating phase as:

$$\frac{\partial}{\partial t}(\alpha_i \rho_i) + \nabla.\left(\alpha_i \rho_i \vec{v}_i\right) = \sum_{j=1}^{n} \dot{m}_{ji} \tag{3.10}$$

Where α, ρ, v are expressed as the macroscopic volume fraction, density, and velocity of phase (i) respectively, while m_{ji} is the mass transfer from the phase j^{th} to the phase i^{th}. The momentum equation of phase (i) is given by the Navier–Stokes equation as follows:

$$\frac{\partial}{\partial t}(\alpha_i \rho_i \vec{v}_i) = -\nabla.(\alpha_i \rho_i \vec{v}_i \vec{v}_i) - \alpha_i \nabla p - \nabla.(\alpha_i \tau_i) + \alpha_i \rho_i \vec{g} + \alpha_i \rho_i (\vec{F}_i + \vec{F}_{lift,i} + \vec{F}_{vm,i}) \tag{3.11}$$

where p, g, F_i, $F_{lift,i}$, and $F_{vm,i}$ are expressed as hydrodynamic pressure, gravity, external body force, lift force, and virtual mass force respectively, while τ_q represents the viscous stress tensor for i^{th} phase, which can be expressed by:

$$\alpha_q \mu_q (\nabla \vec{v}_q + \nabla \vec{v}_q^{T}) + \alpha_q (\lambda_q - \frac{2}{3}\mu_q) \nabla.\vec{v}_q I \tag{3.12}$$

In the Eulerian multiphase applications, the energy conservation equation can be expressed by the enthalpy equation of each phase as:

$$\frac{\partial}{\partial t}(\alpha_q \rho_q h_q) = -\nabla.(\alpha_q \rho_q h_q \vec{v_q}) - \alpha_q \frac{\partial P_q}{\partial t} + \tau_q : \nabla \vec{v_q} - \nabla \vec{q_q} + S_q + \sum_{p=1}^{n} (\vec{Q}_{pq} + \dot{m}_{pq} h_{pq}) \quad (3.13)$$

Where h_i, q_i, S_i, Q_{pq} and h_{pq} represent the specific enthalpy of phase i^{th}, the heat flux, the source term that takes into account sources of enthalpy due to chemical reaction or radiation, the intensity of heat exchange between the two phases, and the interphase enthalpy respectively.

3.6.3.2 Lift Force

In multiphase flow systems involving spherical objects (e.g. droplet, bubble, or particle), velocity gradients in the primary phase flow lead to a lift force on the particle. The lift force on large particles is considered to be more significant, so the enclosure of lift forces, is not suitable for very small particles and closely packed particles, although the Fluent model assumes that the inter-particle spacing is greater than the particle diameter.

In most situations, the lift force is not considered as significant as the drag force. Yet, the lift force is important in flow systems with two-phase separation, where both phases might be quickly separated. In such a case, it would be necessary to take into account the effect of lift force. The lift force is not included by default in multiphase system, but if it is required, the influence of lift force on dispersed phase *j* in a primary phase *i*, is obtained as:

$$\vec{F}_{lift,i} = \frac{1}{2} \rho_i \varepsilon_i \left| \vec{v}_j - \vec{v}_i \right| \times (\nabla \vec{v}_i) \quad (3.14)$$

where F_{lift} is the lift force that will be added to the right–hand side of the momentum Equation (3.11).

3.6.3.3 Wall Forces

Wall forces are considered one of the major forces which have an effect on bubbles the droplets, or particles as they approach the wall. Due to exerted force, the walls slow the drainage rate between the droplet or bubble and the wall. This in turn enhances the drainage rate on the other side. The net effect is the force that acts to drive the droplet away from the wall.

3.6.4 Mixture Model

The mixture model assumes the local equilibrium within small spatial length scales (FLUENT, 2005). It is one of the simplified multiphase flow approaches, it can be employed in the simulation of two phases with the same or different velocities. Therefore, the accelerating entities of dispersed fluid reach the terminal velocity after traveling a distance in which the length scale of the system has become greater (Chen *et al.*, 2005). In contrast to the Volume of Fluid model, the mixture model allows interpenetrating between the two phases, while the dispersed phase is characterized by a volume fraction equation. Each dispersed phase has its individual transport equation, which allows for the slip velocity between the phases (either continuous or dispersed).

The mixture model theory can be said to treat both phases dispersed and continuous as a single phase. This is regarded as the mixture phase where physical properties, like the density and viscosity of the mixture, are obtained based on each phase fraction. Additionally, homogeneous multiphase flows can be simulated by the mixture model when a strong coupling is employed between the phases, which flow nearly with the same velocity. The mixture model solves a minimum number of equations compared to other multiphase models discussed before, hence it also has a lower computational time than the other models. In the mixture model, none of the drag interphase forces such as the lift and virtual mass forces are calculated. This model is more suitable for industrial applications such as bubbly flows where the dispersed phase fraction remains low, sedimentation, and particle-laden flows with low loading.

3.6.4.1 Mixture Mode Governing Equations

The mixture continuity equation is obtained based on the average properties of the two-phase and can be written as:

$$\frac{\partial}{\partial t}(\rho_m) + \nabla.(\rho_m \overrightarrow{v_m}) = \dot{m} \tag{3.15}$$

where m, v_m, and ρ_m represents the mass transfer between phases, the mass–averaged velocity, and the mixture density.

The mass–averaged velocity and mixture density can be expressed by:

$$\vec{v}_m = \frac{\sum_{k=1}^{n} \alpha_k \rho_k \vec{v}_k}{\rho_m} \tag{3.16}$$

$$\rho_m = \sum_{k=1}^{n} \alpha_k \rho_k \tag{3.17}$$

Where α_k and ρ_k are the volume fraction and density of a corresponding phase.

The momentum equation for the mixture can be computed by the sum of individual momentum equations for all phases, which can be written as:

$$\frac{\partial}{\partial t}(\rho_m \vec{v}_m) + \nabla.(\rho_m \vec{v}_m^{\,2}) = -\nabla p + \nabla.\left[(\mu_m(\nabla \vec{v}_m + \vec{v}_m^{\,T})\right] + \rho_m \vec{g} + \vec{F} + \nabla.(\alpha_g \rho_g (\vec{v}_g - \vec{v}_m)^2 + \alpha_l \rho_l (\vec{v}_l - \vec{v}_m)^2) \tag{3.18}$$

where F and μ_m are the body force and the mixture viscosity, which is expressed by:

$$\mu_m = \sum_{k=1}^{n} \alpha_k \mu_k \tag{3.19}$$

Where α_k and μ_k are the volume fraction and viscosity of a corresponding phase.

The energy equation for the mixture takes the following form:

$$\frac{\partial}{\partial t}\sum_{k=1}^{n}(\alpha_k \rho_k E_k) + \nabla.\sum(\alpha_k \vec{v}_k(\rho_k E_k + p)) = \nabla.(k_{eff} \nabla T) + S_E \tag{3.20}$$

Where k_{eff} is the effective conductivity which can be obtained by the sum of each phase, thermal conductivity (k_i) and the turbulent thermal conductivity (k_t).

The first term on the right–hand side represents the conduction term due to energy transfer which is obtained by the expression below and S_E is any other volumetric heat sources.

$$E_k = h_k - \frac{p}{\rho_k} + \frac{\upsilon_k^2}{2} \tag{3.21}$$

The above expression is for a compressible phase, for an incompressible phase; $E_k = h_k$, where h_k is the sensible enthalpy for phase k. The continuity equation and the volume fraction equation for secondary phase p can be obtained as:

$$\frac{\partial}{\partial t}(\alpha_p \rho_p) + \nabla.(\alpha_p \rho_p \vec{\upsilon}_m) = -\nabla.(\alpha_p \rho_p \vec{\upsilon}_{dr,p}) \tag{3.22}$$

3.7 Direct Numerical Simulations (DNS)

Direct Numerical Simulation as the name implies is the process of solving the governing equations directly. For any type of fluid flow, it is possible to theoretically find out the entire turbulent flow fields for three dimensions without having to resort to any type of modelling. DNS method churns out a lot of data including the time history associated with all the flow variables at each point in the domain. Nevertheless, the DNS technique is the best way to understand the fundamentals of fluid flow dynamics, especially turbulence phenomena. Consequently, this has assisted in the development and evaluation of existing models used in mainstream CFD codes.

However, the DNS techniques are not suitable for real-world engineering problems. This is mainly due to the excessive mesh sizes that are required to resolve all scales of motion in the three spatial dimensions (Fluent, 2018). Furthermore, setting up boundary conditions and initialisation are both significant stages and yet very complicated to carry out using the DNS concept. (Ranade, 2002). Additionally, the simulation would have to be transient with very small-time steps. And obviously, more computational resources are needed to solve the highly dispersed phase fraction, and usually turbulent and multiphase flows are above the capabilities of even modern computers.

3.8 Treatment of Turbulence in Multi–fluid Flows

Multiphase flow dispersions encountered in chemical and process industries are mostly turbulent in nature and are therefore classified based on the fluctuation of velocity fields.

These deviations combine transported quantities such as momentum, energy, as well as species concentration, and cause them to fluctuate. These high-frequency fluctuations become extremely expensive in terms of computational process time for DNS to simulate them directly. Alternatively, the instantaneous governing equations can be ensemble-averaged, time-averaged, or otherwise controlled to remove the small scales of Large Eddy Simulation (LES), leading to reformulating a set of equations, which can then be developed and become computationally less expensive to solve. However, modifying such equations brings in additional unidentified variables, and turbulence models, which are required to find these variables in terms of known quantities.

3.9 Large Eddy Simulations (LES)

The Large Eddy Simulations (LES) approach implicitly assumes that the relevant scales in turbulent flows can be divided into the large and small–scale (also called sub-grid) components as shown in Figure (3.3). The method is built on the assumption that such separation does not significantly affect the evolution of large–scale turbulent motions, which are usually much more energetic than the small–scale motions. Consequently, these large–scale turbulent motions contribute more to the transport of conserved quantities. Therefore, LES focuses more on simulating these large–scale motions than small–scale motions, even though the latter is considered to be more general in character and thus easier to be modelled.

LES requirements for time step sizes and mesh resolution are less restrictive unlike in the DNS approach. Despite the numerous advantages of LES, they still have some shortcomings just like DNS. These include the difficulties in specifying boundary conditions and generating a huge amount of information that is not useful for practical purposes (Bakker and Oshinowo, 2004).

The computational limitations of the DNS or LES methods have restricted their applicability to flows of practical interest in chemical process industries. However, the latest advances in modelling have given rise to a hybrid method that combines RANS modelling with LES. This is known as Detached Eddy Simulation (DES). And ultimately, DES

reduces to RANS in near-wall regions and changes back to LES in regions away from the walls (Constantinescu and Squires, 2003). Consequently, this leads to a significant reduction in computational demands, while providing more accurate flow features when compared to RANS.

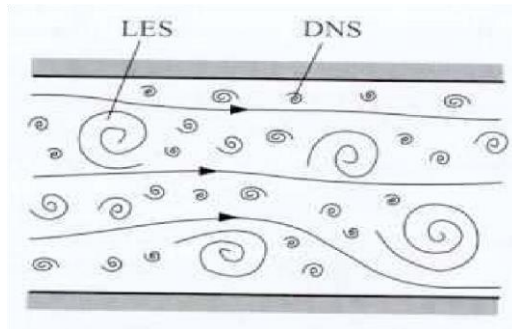

Figure 3.3: Schematic representation of scales in turbulent flows (Ferziger and Peric, 2002)

3.10 Turbulence Models Based on RANS

In RANS approach, the instantaneous value of any flow variable is decomposed into a mean and a fluctuating component, mathematically:

$$\phi = \overline{\phi} + \phi' \tag{3.23}$$

Where ϕ is the Instantaneous value, $\overline{\phi}$ is the Time averaged mean, and ϕ' is the Fluctuating component. The mean value can is found by averaging over an appropriate time interval, where the Reynolds averaging obeys the following properties:

$$\overline{\overline{\phi}} = \overline{\phi} \quad \text{and} \quad \overline{\phi'} = 0 \tag{3.24}$$

Where the over bar describes time averaging.

Equation 3.23 is substituted in the basic governing equations for the flow Instantaneous flow variable such as the velocity of a phase and followed by time-averaging, subject to the conditions listed in Equation 3.24 to yield governing equations for the mean quantities. The equation can be simplified to a new averaged equation that features an extra term which consider the turbulent transport of the instantaneous variable. Resolving the smaller spatial

and temporal scales is not needed in the RANS–based approach as the fluctuation of time-averaged quantities takes place at much larger scales. The variation of fluid velocity with time is shown in Figure 3.4 and demonstrates a comparison between the RANS-based approach with the DNS and LES approaches.

Considerably less computational power is required for RANS approach as compared to the DNS or LES techniques. Nonetheless, the technique of time-averaging the basic governing equations leads to the introduction of new terms which results in a closure difficulty. The new equations might be integrated as apparent stress gradients and heat/mass fluxes associated with turbulent motion (Ranade, 2002). Governing equations for these new expressions can be theoretically derived. However, the obtained equations would also introduce more unknown terms. Thus, it is needed to establish a turbulence model that can these unidentified terms to known ones in order to complete the set of governing equations. Several turbulence models have been developed within the last three decades, these models have been tested in simulations and sown different degrees of success.

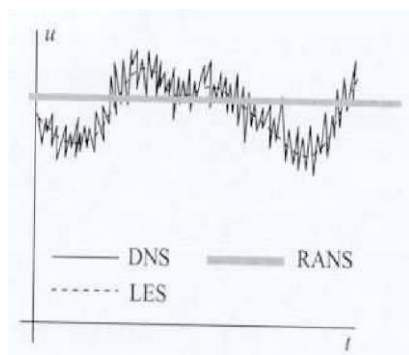

Figure 3.4: Comparing DNS, LES, and RANS (Ranade, 2002)

3.11 Other Turbulent Models

Main turbulent models in most of the CFD codes are the k–ε, k−ω, and the k–ε RNG.

3.11.1 k−ε Model

The k–ε model is generally the most utilized turbulence model in the simulation of turbulence eddies. The k–ε model is defined by a semi-empirical model, based on model transport equations for the turbulence kinetic energy (k) and turbulence dissipation rate

(ε). The transport equation for turbulence kinetic energy (k) is derived from the explicit equation, whereas the equation of dissipation rate (ε) is obtained using a physical hypothesis, bearing little resemblance to its mathematically exact counterpart. Both turbulence kinetic energy k and turbulence dissipation rate ε are obtained from the following form of transport equations (Fluent, 2018):

$$\frac{\partial}{\partial t}(k\rho_k)+\frac{\partial}{\partial x_i}(k\rho_k U_k)=\frac{\partial}{\partial x_j}\left[\left(\mu+\frac{\mu_t}{\sigma_k}\right)\frac{\partial k}{\partial x_i}\right]+G_k+G_b-\rho\varepsilon-Y_M+S_k \tag{3.25}$$

and

$$\frac{\partial}{\partial t}(\varepsilon\rho_k)+\frac{\partial}{\partial x_i}(\varepsilon\rho_k U_k)=\frac{\partial}{\partial x_j}\left[\left(\mu+\frac{\mu_t}{\sigma_\varepsilon}\right)\frac{\partial \varepsilon}{\partial x_i}\right]+C_{1\varepsilon}\frac{\varepsilon}{k}(G_k+C_{3\varepsilon}G_b) - C_{2\varepsilon}\rho\frac{\varepsilon^2}{k}+S_\varepsilon \tag{3.26}$$

G_k and G_b are the turbulence kinetic energy created as a result of the mean velocity gradients and buoyancy respectively. Y_M presents the involvement of the fluctuating dilatation incompressible turbulence to the total dissipation rate. S_k and S_ε are utilized to define the source terms, while the turbulent viscosity, μ_t is calculated using the combination of k and ε as given below:

$$\mu_t=\frac{C_\mu\rho k^2}{\varepsilon} \tag{3.27}$$

Where C_μ is an empirical constant. In turbulence layers, diffusion and the production terms are equal to zero, thus $C_{2\varepsilon}$ is a constant appearing in the equation (3.4). However, the decay measurement of turbulent kinetic rate (k) might be used to find $C_{2\varepsilon}$ directly, which has been shown to lie within the range of 1.8−2. C_μ is equal to 0.09 for local equilibrium shear layers. Launder and Spalding (1974) has recommended the values of these empirical model constants $C_{1\varepsilon}$, $C_{2\varepsilon}$, $C_{3\varepsilon}$, C_μ, σ_k, and σ_ε as 1.44, 1.92, 1.3, 1.0, and 1.3, respectively for a dispersed multiphase system.

3.11.2 RNG k−ε Model

Renormalisation Group (RNG) is a mathematical technique for analytical derivation. The RNG model is developed from the instantaneous Navier–Stokes equations, using analytical derivation, which generated dissimilar constants to those in the standard *k*–ε model. Moreover, additional terms and functions also are produced in the transport equations for *k* and ε. The impact that is caused by small-scale turbulence is usually recognized by a random forcing function in the Navier– Stokes equations (Hjertager *et al*., 2002).

$$C_1^o = C_1 - \frac{\mu(1-\mu/\mu_o)}{1+\beta\mu^3} \tag{3.28}$$

$$\mu = \left[2\left\{\left(\frac{\partial U_x}{\partial x}\right)^2 + \left(\frac{\partial U_y}{\partial y}\right)^2 + \left(\frac{\partial U_z}{\partial z}\right)^2\right\} + \left\{\left(\frac{\partial U_x}{\partial x}\right) + \left(\frac{\partial U_y}{\partial y}\right) + \left(\frac{\partial U_z}{\partial z}\right)\right\}^2\right]^{0.5} \tag{3.29}$$

The empirical constants of this model recommended by Fluent (2018), are 1.42, 1.68, 0.0845, 0.72, 0.72, 4.377, and 0.012 corresponding to $C_{1\varepsilon}$, $C_{2\varepsilon}$, $C_{3\varepsilon}$, σ_k, σ_ε, μ_o, and β, respectively.

3.11.3 k−ω Model

The k−ω model is based on transport equations that are expressed by two terms, these are the turbulence kinetic energy (k) and the specific dissipation rate (ω). The k and ω can also be evaluated as the ratio of ε and k. The turbulence kinetic energy k and specific dissipation rate ω are calculated from the given transport equations Fluent (2018) as:

$$\frac{\partial}{\partial t}(k\rho_k) + \frac{\partial}{\partial x_i}(k\rho_k U_k) = \frac{\partial}{\partial x_j}\left[\left(\mu + \frac{\mu_t}{\sigma_\varepsilon}\right)\frac{\partial k}{\partial x_i}\right] + G_k + G_\omega - \rho\omega - Y_M + S_k \tag{3.30}$$

$$\frac{\partial}{\partial t}(\omega\rho_k) + \frac{\partial}{\partial x_i}(\omega\rho_k U_k) = \frac{\partial}{\partial x_j}\left[\left(\mu + \frac{\mu_t}{\sigma_\varepsilon}\right)\frac{\partial \omega}{\partial x_i}\right] + C_{1\varepsilon}\frac{\varepsilon}{k}(G_k + G_{3\omega}G_\omega) \tag{3.31}$$

$$- C_{2\omega}\rho\frac{\omega^2}{k} + S_\omega$$

Additional terms have been included for both k and ω equations since the k–ω model was developed, this has improved the accuracy of the model for predicting free shear flows. The terms G_k, and G_ω in equations (3.8) and (3.9), expresses the turbulence kinetic energy that is generated due respectively to the mean velocity gradients and buoyancy, Y_M presents the compressible turbulence to the all dissipation rate due to the contribution of the fluctuating dilatation whereas S_k and S_ω are terms of user-defined source, while the turbulent viscosity, μ_t is calculated by involving k and ω as shown below.

$$\mu_t = \frac{C_\mu \rho k}{\omega} \tag{3.32}$$

The values of empirical constants of $C_{1\varepsilon}$, $C_{2\varepsilon}$, $C_{3\varepsilon}$, σ_k, and σ_ε, are given as 1.44, 1.92, 0.09, 1.0, and 1.3 respectively (Fluent, 2018).

3.12 Numerical Simulation

3.12.1 Initial Conditions

Initial conditions are required and must be specified for all the flow variables before the CFD code can carry out a simulation and obtain unique solutions for the governing equations. Furthermore, the initial conditions must be taken carefully into consideration in order to provide a desired ultimate solution and avoid numerical complexities. Gravity force is mainly used to initialize the initial pressure field, resulting in the pressure drop at the fluid phase being equal to the atmospheric pressure. There are two main techniques used in the existing CFD codes to initialize the solution (Fluent, 2018). These are:

- **Initialize the whole flow field:** Initializing the flow field provides the simulation with a starting condition that is physically realistic and consistent with the problem being solved, this ensures numerical stability and reduces simulation time.
- **Patch value in selected zone cell for chosen flow variables:** patch initialisation is a technique used in CFD simulations to initialize a part of the flow field with different initial conditions than the rest of the domain, this is done by assigning initial values to the cells or nodes on a specific region or patch of the computational domain. Patch

initialisation is necessary when solving a fluid flow problem with different boundary conditions or when simulating a complex geometry.

3.12.2 Boundary Conditions

Boundary conditions are used to set the flow and thermal variables on the system boundaries under consideration. There are two types of boundary conditions for two-phase simulations, these are:

i. inlet and outlet boundary conditions
ii. wall boundaries

Inlet and Outlet Boundary Conditions

To obtain reliable solutions for the simulation, appropriate specifications of inlet and outlet boundaries are required. There are different boundary conditions for the inlet and outlet, these include velocity inlet, mass flow inlet, and inlet and outlet pressure. The velocity inlet is mainly used to define the velocity as well as other phases' scalar properties at the inlet boundary, such as turbulent parameters, volume fraction, etc. While on the other hand, the outlet boundary condition is mainly described using outflow and pressure outlet.

In the simulation aspect of this work, the velocity inlet condition is specified at the pipe inlet, the physical velocity of two phases is defined and the volume fraction of the secondary phase is also defined. While at the outlet of the pipe, the pressure outlet condition is specified due to the convergence improvements, and to avoid backflow problems. Atmospheric pressure condition is used at the pipe outlet in this situation.

Wall Boundaries

The boundaries of a simulation domain can be set with different terms depending on the situation, such as a periodic axis or asymmetry, and can be used to bound fluid and solid regions. The boundary condition can be specified as a no-slip wall in the case of viscous flows, rather than being described as a tangential velocity component in terms of the rotational or translational motion of the wall boundary, or by describing shear (slip wall).

3.13 Turbulence Parameters

When modelling a two-fluid flow using the k–ε model as the turbulence model, two turbulence properties are needed for the two phases. CFD codes give three combinations to identify these values as follows:

a. Turbulence intensity (I) and length scale (l)
b. Turbulence intensity and viscosity ratio (μ_t/μ)
c. Turbulence intensity and hydraulic diameter

The turbulent intensity term can be calculated as:

$$I = 0.16\,\mathrm{Re}^{-1/8} \tag{3.33}$$

The turbulence intensity usually has a value between 1–10%, but sometimes goes higher than 10%. The above equation 3.33 is the best practice for predicting the value of turbulent intensity. Contrastingly, turbulent length scales in fully developed pipe flow are limited by the flow path length since turbulent eddies cannot be greater than the conduit length. However, the turbulence length scale can be taken as between 5–10% of the pipe diameter or can be approximated using the following equation:

$$l = 0.07\ \mathrm{D} \tag{3.34}$$

Where D expresses the pipe diameter and 0.07 is an empirical constant based on the maximum value of the mixing length in a fully developed turbulent (Fluent, 2018).

The turbulent kinetic energy and dissipation rate can be calculated as follows:

$$k = \left(IU_{inlet}\right)^2 \tag{3.35}$$

$$\varepsilon = C_{\mu}^{3/2}\frac{k^{3/2}}{l} \tag{3.36}$$

The turbulent intensity (I) and turbulent length scale (l) can be found from Equations (3.33) and (3.34), respectively, U_{inlet} is the mixture velocity at the inlet and C_{μ} is an empirical constant given by 0.09.

3.16 Numerical Solver

Available CFD codes are mainly based on two types of solvers, coupled solver, and segregated solver. The governing equations for momentum, mass, and energy are solved simultaneously in the coupled solver, while in the segregated solver, the equations of transport governing are solved sequentially. For both formulations, governing equations of additional scalars are calculated sequentially.

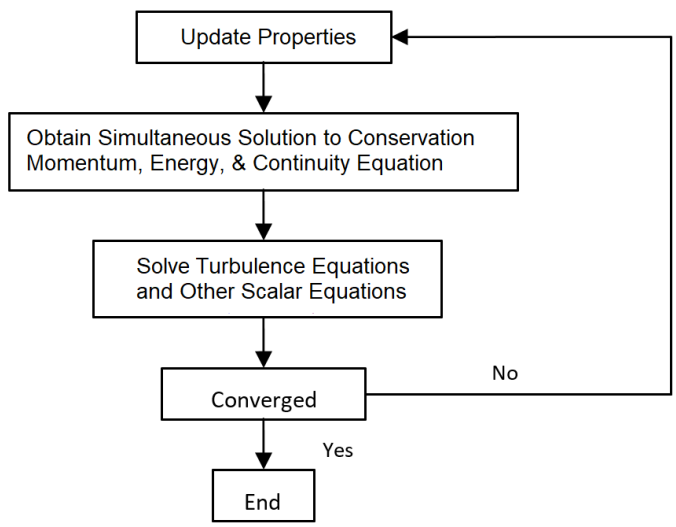

Figure 3.5: Fluent coupled solver

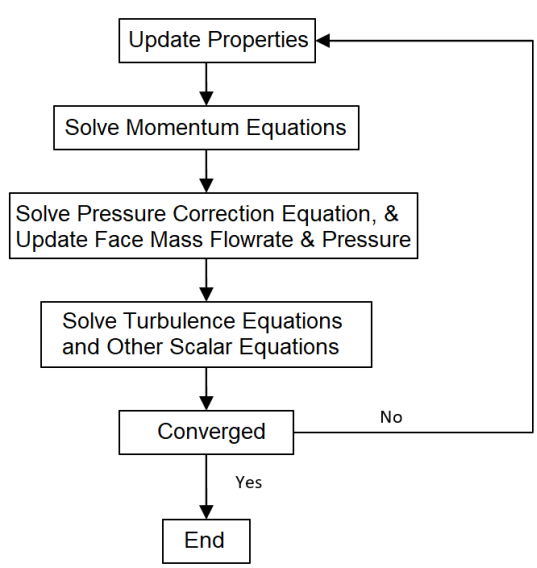

Figure 3.6: Fluent segregated solver

The segregated solver is mostly suited for incompressible and mildly compressible flows. Before simulations converge to a solution, several iterations of the solution loop have to be performed, this is due to the non-linear nature of the governing equations. The performance of each solver is determined using discretisation schemes specification, the segregated solver is also commonly used for multiphase flow modelling.

Figures 3.5 and 3.6, show the flow charts of both coupled and segregated numerical solvers, including the steps of each. The segregated solver, therefore, is often utilised for multiphase modelling and has been used in this work to study the multiphase study of bubbles in inclined pies.

3.15 Discretisation

As has been discussed in section (3.7), a finite volume method is utilized by most of the CFD codes to convert the governing equations to algebraic equations and then solved numerically. The finite volume approach includes the combination of governing equations relating to each control volume, leading to discrete equations that preserve each quantity based on the control volume. Discretisation of these partial differential equations can be shown more simply by using the generic transport equations of a scalar qϕtity as written in the following form (Ferziger and Peric, 2002):

$$\frac{\partial}{\partial t}(\rho\phi) + \nabla \cdot (\rho U\phi) = \nabla \cdot (\rho\Lambda\nabla\phi) + S_{\phi} \tag{3.37}$$

Where Λ presents the scalar diffusivity of scalar ϕ, while S_{ϕ} describes the source term.

Available CFD codes as FLUENT provide different options of algorithms that can be used in conjunction with first and second-order upwind, power law, third order MUSCL (Monotone Upstream-centered Scheme for conservation laws), and QUICK (Quadratic Upstream Interpolation for Convective Kinetics) schemes. Discretisation schemes such as the first and second-order upwind, as well as QUICK, are used for momentum, turbulence, and phase volume fraction. The first-order upwind scheme usually gives a stable solution,

with less computation time compared with higher-order discretisation schemes, however higher discretisation schemes give more accurate results.

3.16 Under Relaxation

Discretisation equations in a finite volume have a linear form that can be written as:

$$x\phi = y + \sum_i x_i \phi_i \tag{3.38}$$

Where x and y are linearized constants. The equation is solved iteratively for ϕ until convergence is achieved. Controlling the difference in consecutive values of ϕ is necessary to prevent the calculation from fluctuations. This can usually be achieved using an under-relaxation factor, which minimizes the change of ϕ attained throughout the consecutive iterations. Modifying equation 3.38 leads to:

$$\phi_{new} = \phi_{old} + \alpha \Delta\phi \tag{3.39}$$

$$\Delta\phi = \left(y + \sum_i x_i \phi_i \right)_{new} - \phi_{old} \tag{3.40}$$

Where α refers to under-relaxation factor, which has a value ranging from 0.1 to 1.

3.17 Pressure Velocity Coupling

Pressure velocity coupling is needed in the CFD solver to develop an equation for pressure from the continuity discrete equation. There are different techniques based on the pressure velocity algorithm, these include SIMPLE, SIMPLEC, and PISO. The SIMPLE (semi-implicit pressure linked equation) algorithm employs the relationship between velocity and pressure corrections to impose the mass conservation in consequence to get the pressure, it is broadly utilized in existing CFD codes. The velocities are usually calculated by a segregated solver, and coupled with the phases. The equation of pressure correction is derived based on total volume continuity and is solved. Subsequently, the pressure and velocities are adjusted to assure the satisfaction of the continuity constraint (Fluent, 2018). PISO (Pressure–Implicit with Splitting of Operators) is another scheme that is one of the

SIMPLE algorithm categories is the scheme. PISO scheme is derived from the higher degree of the approximate relation among the velocity and pressure corrections. Unlike the SIMPLE algorithm, PISO can do two further corrections, these are skewness and neighbour correction. The advantage of using this algorithm is that it allows a fast convergence rate and sufficient accuracy without a loss (Fluent, 2018). Therefore, the simulation done in this work has used the PISO scheme for pressure velocity coupling.

3.18 Experimental Rig Overview

The two-phase experimental flow rig was designed, fabricated, and commissioned for the works of Bello (2017), located in the laser lab of the University of Leeds's Energy Building, the rig has a robust capacity for generating the entire range of two-phase flow patterns in a pipe with variable inclinations from -30^o (downward) to +30^o (upward), and capabilities for liquid fraction and pressure drop measurements. The experimental rig is comprising of liquid and gas circuits, a two-phase mixing section where gas and liquid can be thoroughly mixed, flow measuring instrumentation and a test section pipe made of a transparent acrylic pipe, The enter piping section and other accessories are mounted on a rotating platform, capable of being rotated between -30^o to 30^o (upward and downward directions).

The design of the piping loops, the two-phase mixing sections, the metering and controlling systems of the gas and liquid flow rates, and the appropriate instrumentation were assembled to primarily achieve the objectives of Bello (2017) using air and water. A change of liquid from normal water to surfactant solution or glycerol required some small recalibration, this is appropriately done and will be discussed later in this chapter. A schematic diagram of the experimental rig set-up is shown in Figure 3.7, while Figure 3.8 shows a detailed view. The various components of the flow rig are discussed in the following sections.

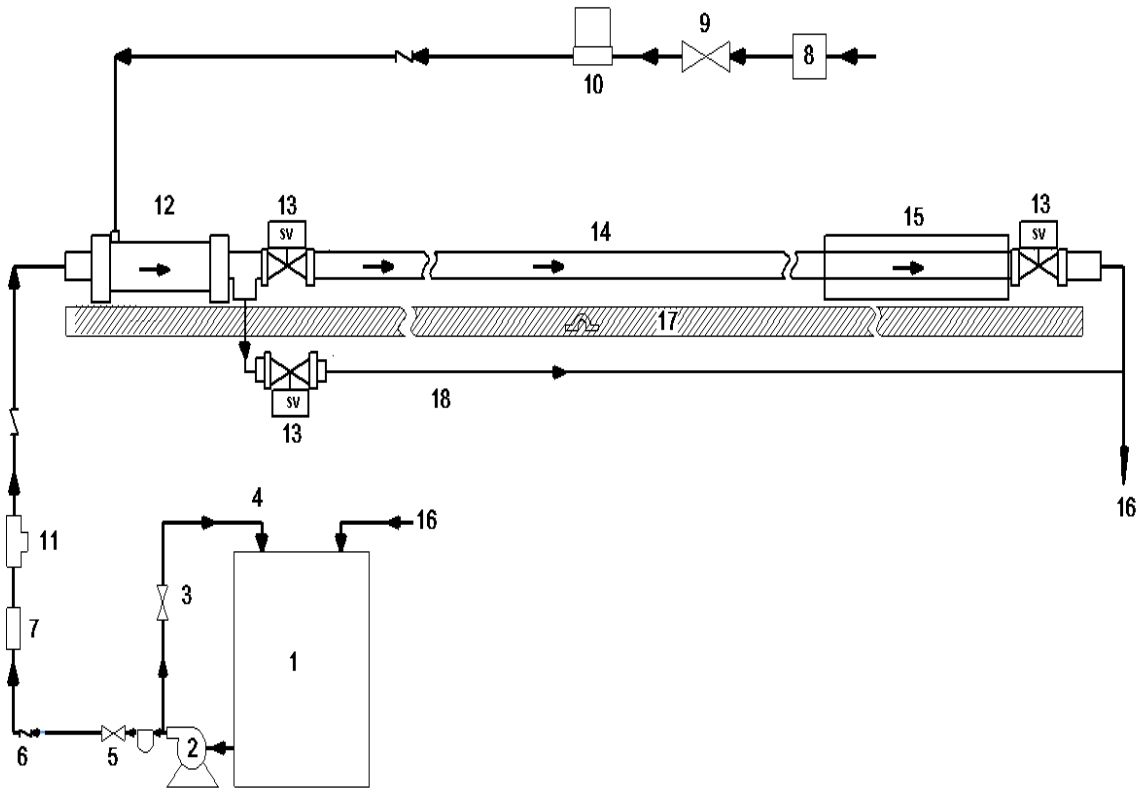

KEY

1	Water Tank	10	Air mass flowmeter
2	Centrifugal pump	11	Turbine flow meter
3	Gate valve	12	Air-water flow mixer
4	By-pass line	13	Quick stop solenoid valve
5	Ball valve	14	Test pipe (L = 3.8 m, ID = 19 mm)
6	Check valve	15	Visualisation box
7	Rotameter	16	Return line to tank
8	Pressure regulator	17	Pipe bed
9	Ball valve	18	Test pipe by-pass line

Figure 3.7: Schematic diagram of an experimental flow rig circuit as used by Bello (2017).

Figure 3.8: Photographic view of the experimental flow rig

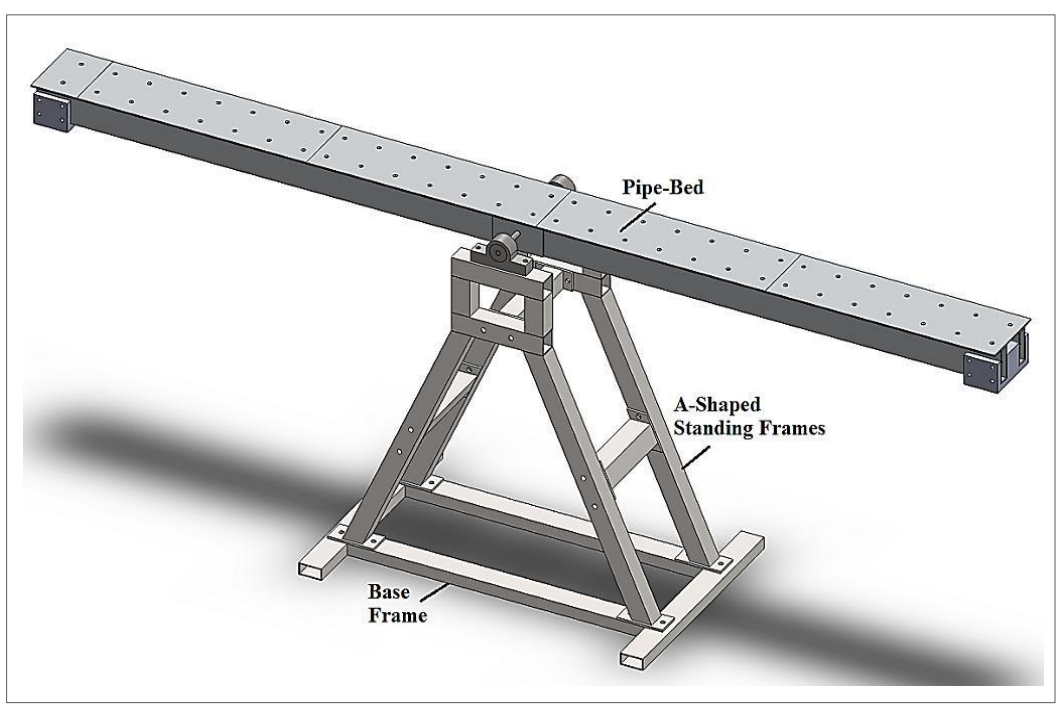

Figure 3.9: Model of the experimental flow rig: pipe bed and support structure.

3.18.1 Liquid Flow System

The rig has originally been designed with compressed air and purified water as the working fluids. A 350-litre capacity tank is initially provided as a purified water reservoir, which also serves as an air-water separation tank. The seesaw rig is equipped with a centrifugal pump capable of producing a maximum flow rate of 60 L/min which is more than enough volumetric throughput required for the experimental work. Control valve and by-pass flow valves are installed downstream of the pump to regulate the liquid flow rate. Liquid flowrate into the test section is measured by a rotameter before entering the mixing chamber, to cover the required experimental range of superficial water velocities. The rotameter gives a precise volumetric flow rate of the liquid before entering the mixing chamber, where the water is thoroughly mixed with compressed air from the laboratory air supply.

Figure 3.10: A narrower100 litre tank, replacement to the 350-litre tank.

The 350-litre tank was replaced with a smaller but taller tank of 100 litres, the smaller volume means less amount of glycerol will be required as well as less quantity of surfactant will be required to make the viscous solution. The narrower tank shown in Figure 3.10 provides enough space for the two-phase air-liquid mixture from the test section to be separated by gravity, where the air can leave through the holes provided on the lid of the tank. A flexible hose connecting the rig to the tank allows the rig to be rotated to any angle of interest within the range of 0^O to 30^O inclinations for both upward and downward flow orientations. A check valve is fitted to prevent a backflow and copper tubing was used for connecting, the pump, valves, and flow meters.

3.18.2 Gas Supply System

The flow rig uses compressed air provided by the university laboratory compressed air reservoir. The compressed air passes are supplied via copper tubes fitted with a 200 regulator and filter-drier assembly which removes foreign objects from the airflow as well as unwanted condensation produced by the compressor, while the regulator enables control over the air pressure inlet to the set-up at the same time providing added air pressure consistency, avoiding pressure oscillations in the rig. The compressed air flow from the regulator to the mixing unit via the flow meters is controlled with the aid of check and control valves. Fine adjustment of the airflow rates entering the system is achieved by the combined action of the check valve and a ball valve in series. The gas flow rate is accurately controlled by a mass flow rate controller as shown in Table 3.2.

3.18.3 Two-Phase Mixing Section

The gas-liquid mixing chamber is the essential part of the flow rig, this is where both air and water can be introduced into the two-phase mixing chamber where proper mixing of the gas and liquid will be achieved before entering the testing pipe. It is essential to thoroughly mix the two phases before they are introduced into the test section, thorough mixing minimizes flow unsteadiness and allows a multiphase flow to develop within the shortest length of the test pipe.

Different mixer designs have been reported suitable for two-phase mixing by previous researchers. Mixer design influences the appearance of a particular flow pattern, Aziz and Govier (1972) studied the issue of mixer design and inlet pipe geometry on two-phase flow was and found that the design of a mixing section or a mixer affected the flow pattern only up to a certain distance and provided a sufficient calming length after which no special mixing device was required. Therefore, the mixing unit on this rig was adopted from the design is the work of Al-Aweet (2008), built with an annular mixing section, with the aim of providing the required time for the two-phase flows to develop and to achieve the much-needed flow stability.

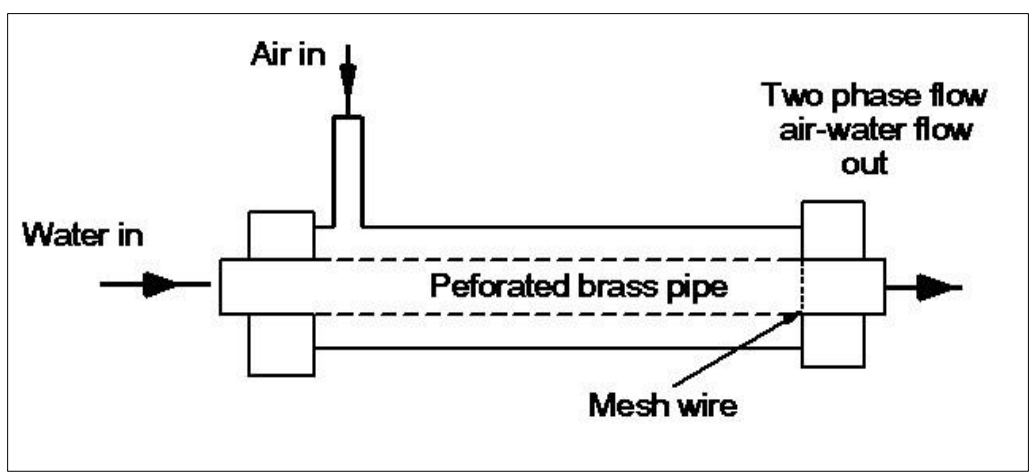

Figure 3.11: Schematic of air-water mixing unit

Figure 3.12: Photographic view of the air-water mixer

Figure 3.11 and Figure 3.12 shows the schematic diagram of the mixing unit and a photograph of the mixer setup is shown in respectively. The mixing section was made using PVC pipe and a brass annular pipe with about 100 holes with a diameter of 1.0 mm each on the wall of the central brass pipe. Gas is introduced from one side of the mixer and water is fed from the rear of the mixing section directly into the annulus through a distributor, thus creating a more even circumferential mixing action.

3.18.4 Test Section

The test section comprises of key components such as the test pipe with a visualisation section, flow measuring instruments, liquid hold-up, and pressure drop measurements. To achieve a fully developed flow, a necessary sufficient calming length is needed. Mandhane et al. (1974) reported that a calming length is similar to a hydrodynamic entry length for a pipe flow and is necessary in order to observe a fully developed flow pattern profile. The right calming length had been an issue of debate among different investigators, previous researchers have used different L/D ratios for experimentation. Different values of L/D ratios were used in the two-phase flow studies, Table 3.1 summarises these values from the works of Crawford et al. (1985), Oshinowo and Charles (1974b), Golan (1968), Yamazaki and Yamaguchi (1979) and Nguyen and Spedding (1977).

Table 3.1 Different calming length used in multiphase flow, (Bhagwat, 2011)

Author	Pipe Diameter, D(mm)	Calming Length, (L)
Crawford and Weinberger (1985)	25	50D
Oshinowo (1971)	25	60D
Golan (1968)	38	40D
Yamazaki & Yamaguchi (1979)	25	50D
Nguyen (1975)	45	44D
Present Study	19	150D

The listed comparison of calming lengths indicates that the calming length used in the present set-up is in good agreement with other investigations, thereby giving confidence in

the ability of the experimental rig to study multiphase flow behaviour. The test pipe is made of a transparent acrylic pipe with a 19 mm internal diameter and a length of 3.8 m, of which 3.2 m is calming length (over 150D) and 1.0 m for flow visualisation. This enables clear visualisation of the flow behaviour as it develops through the pipe length. A sufficient calming length of 3.2 m was provided to ensure that the flow has fully developed before passing through a visualisation box.

The flow visualisation box is made of Perspex with a section tube 80 mm x 60 mm and 350 mm long and filled with the same liquid being used in the experiment helps cancel the distortion caused by the curvature of the pipe and provides clear images of two phases passing through. The air and water mixture leaving the test section can drain back to the tank where the gas and liquid are separated by gravity. Figure 3.13 shows a photograph of the flow visualisation box used in this study.

Figure 3.13: Photographic view of the flow visualisation box

A standard ⅜" nominal air compressor hose was used to bring air to the inlet of the test area, while the liquid is provided via 1-inch nylon reinforced flexible clear PVC tubing. Gas and liquid are brought into the testing area via reinforced flexible tubing. PVC tubing

is also used in the return line from the exit of the test section to the 100-litre reservoir tank. Two ball valves are placed at the exit of the test section to prevent backflow into the test branch during experimentation.

3.18.5 Rotating Bed Support

A rigid frame structure was designed and fabricated to support a rotating bed which could be rotated between 0º and 30º in upward and downward directions. The two-phase flow mixing unit, the test pipe and the measuring instruments of the experimental flow rig were all mounted and underpinned on this rotating platform. Shown in Figure 3.9 the rig support is made of two major parts, vertical "A-shaped" support frames holds the surface platform called the "pipe bed".

The A-shaped vertical frames were intended to support the pipe bed. They include two vertical supports made from 80 mm x 80 mm box section, three "cross braces" made out of a 100 mm x 50 mm box section and a "base frame" made out of a 100 mm x 50 mm box section. The vertical supports were braced up together by the three cross braces and fastened to the base frame for a firmer grip to the base foundation. The pipe-bed assembly is mounted on the A-shaped frames and made to rotate freely about the shaft axis. The angular setting of the rig is achieved by rotating the pipe bed using an inclinometer attached to it and a cantilever mechanism for positioning and locking up.

Bello (2017) adapted the design of from the work of Acklam (2010) and made up of two parallel aluminium box sections (100 mm x 50 mm) which are 4.2 m long. The tubes are joined together at the top by aluminium plates (300 mm x 6 mm) to form the flat surface and at the bottom reinforced with metal blocks. The pipe-bed aluminium tubes have a hole drilled through the centre, to allow the steel shaft to be inserted. The design is such that the pipe bed can rotate about the axis of the shaft.

3.19 Instrumentation and Data Collection

Table 3.2 summarises all the key instruments used in this work for flow measurement along with their accuracy ranges and uncertainties.

Table 3.2: Range and accuracies of equipment and instrumentations

Measuring Device/Instrument	Range	Tolerance
Pedrollo Water Pump CP0.37 kW	60 L/min, H14 m	± 5 %
PVC-U variable area flowmeter TROGFLUX VA meter	100-1000 l/hr	± 2 %
Honeywell Pressure gauge	16 bar Max.	± 1 %
Air Flowmeter– Omega FMA1700/1800 Series	0 – 100 L/min	±1.5% of FS
Air Filter & Regulator	8 bar Max.	± 5 %
Gas ball flow meter		± 0.6 % of FS
OMEGA 2-WaySolenoid Valves SV6000 Series – NO	15 Bar	± 10% (voltage)
PX409 Series Wet-Wet Differential Pressure Transducers	0 – 170 mbar	0.08 %
RS Temp. gauge including digital display	0 – 100^{o} C	± 0.5%

3.19.1 Flow rate measurements

Two flow rig is already equipped with devices to measure and control of the flow rates of both air and water prior to entering the test section. A PVC-U variable area flowmeter (plastic tube) flow meter - TROGFLUX VA meter controls the water flow. The air metering system is made up of a mass flowmeter (Omega FMA1700/1800 Series) with an accuracy of ±1.5% and two ball valves in series that can give an accuracy of up to ±0.6%. A digital thermometer was used to measure the liquid temperature, to make sure that the flow temperature is constant at room temperature during the experimental runs. The rig was refitted with a quick action solenoid valve for liquid holdup measurement and a digital pressure transducer which sends live pressure data to the computer for analysis.

3.19.2 Pressure Drop Measurements

Multiphase pressure drop depends on several factors, among which are the pipe geometry, mass flux, pipe orientation, the phase properties, the volume fraction of each phase, as well as flow direction and flow regimes. An extensive background review on the pressure drop in multiphase flows is reported by Hewitt (1982). In most cases, the pressure drop in inclined flow has been calculated using horizontal or vertical two-phase flow correlations, as there is no method for performing the pressure drop calculations which is accurate for all flow conditions. Many authors have suggested empirical modifications to the homogeneous models to take account of the two-phase nature of the flow. Most of the widely utilized and frequently preferred correlations of the models mentioned are reviewed by Mahmud (2012).

A provision was made on the rig for a transducer to be fitted at the two-phase mixing chamber and over the length of the test section. In the experiment, an Omega-Wet/Wet Differential Pressure Transducer with a range of 0-175 mbar will be connected to the inlet and outlet of the test pipe via a constant diameter and equal length flexible tubes as shown below.

In this work, pressure drop measurements were carried out by pressure transducers at the two-phase mixing chamber and over the length of the test section respectively, using a differential pressure transducer (Omega-Wet/Wet Differential Pressure Transducer series) operating within the range of 0-170 mbar.

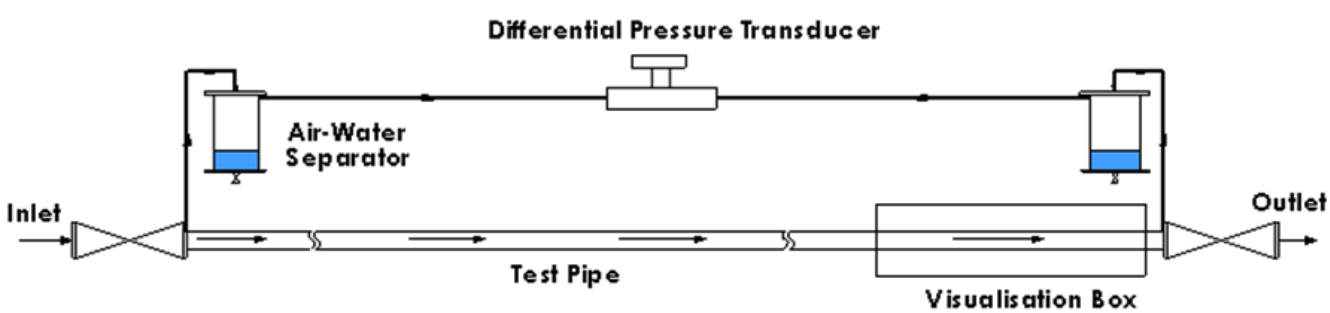

Figure 3.14: Schematic layout for differential pressure measurement

A constant diameter and equal length flexible tubes were used to connect the transducer sensors to the inlet and outlet of the test pipe as shown in Figure 3.14, the equal length is needed to ensure equal pressure measurement from both ends. The flexible tubes were connected to small gas-liquid separators of transparent plastic cylinders, which ensures that no liquid or droplets enters. The Omega PX409 is equipped with a USB cable and can be plugged in directly to a computer where the pressure drop data can be viewed, saved, and plotted.

Figure 3.15: USB enabled Omega PX409 series differential pressure transducer

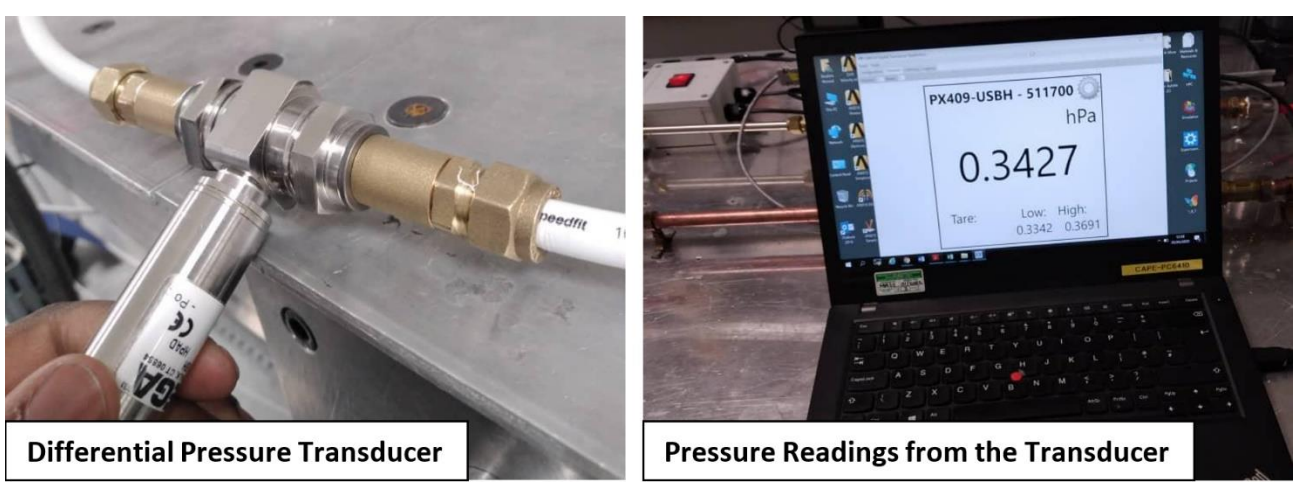

Figure 3.16: Omega PX409 series wet/wet differential pressure transducer connected to the computer showing pressure readings

The transducer is made with rugged stainless steel, equipped with a micro-machined silicon sensor providing a very stable and exceptional high accuracy of ±0.08% and a broad compensated range of -29 to 85°C. It also comes with a high-speed USB that connects directly to the computer, the transducer software was downloaded from the Omega website for data logging and charting.

In this work the transducer was set to record 5 samples per second over of 3 minutes for each experimental run. A total of 900 samples was taken for each run, from where the average pressure drop is calculated.

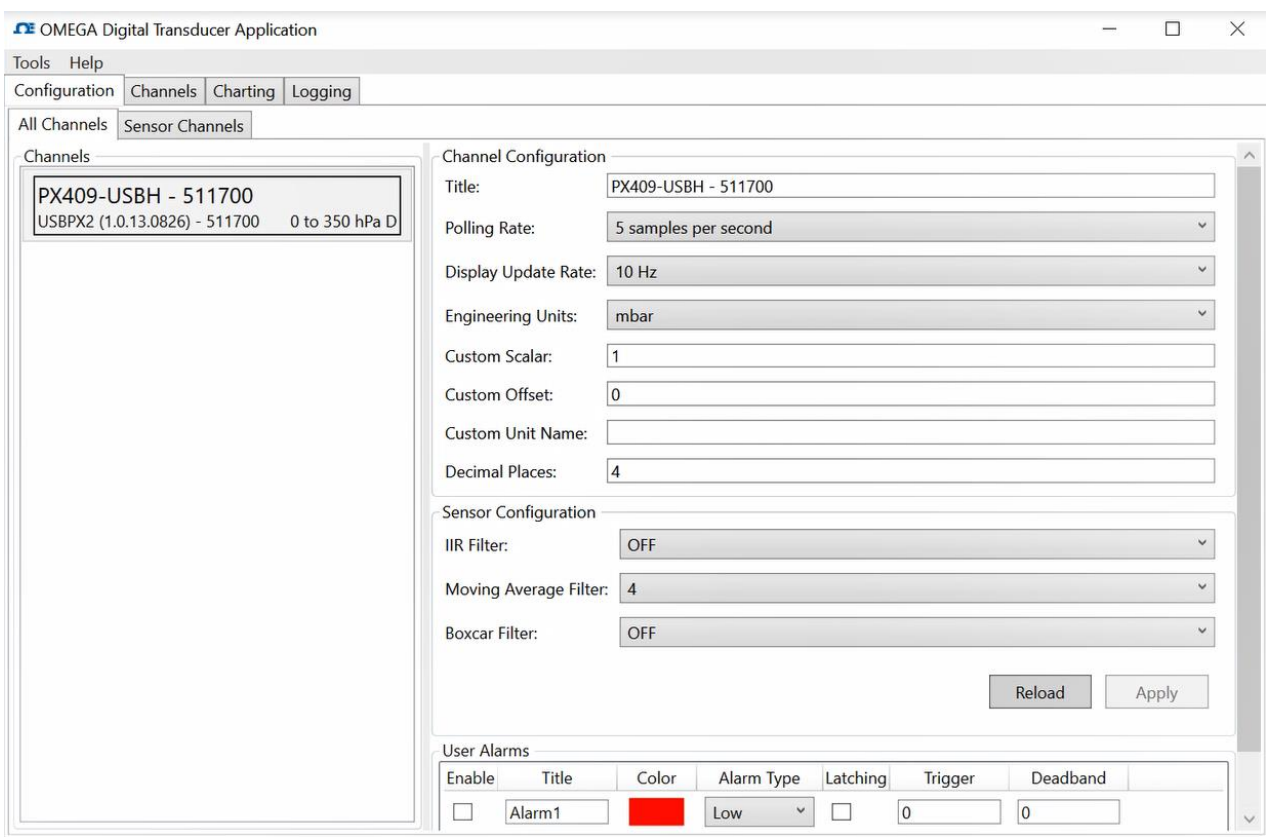

Figure 3.17: Configuring the transducer

A channels window displays pressure data from the transducer, each channel has configurable user alarms, three data filters, tare, resettable low/high indication, and sample rates ranging from 30 minutes to 1000Hz.

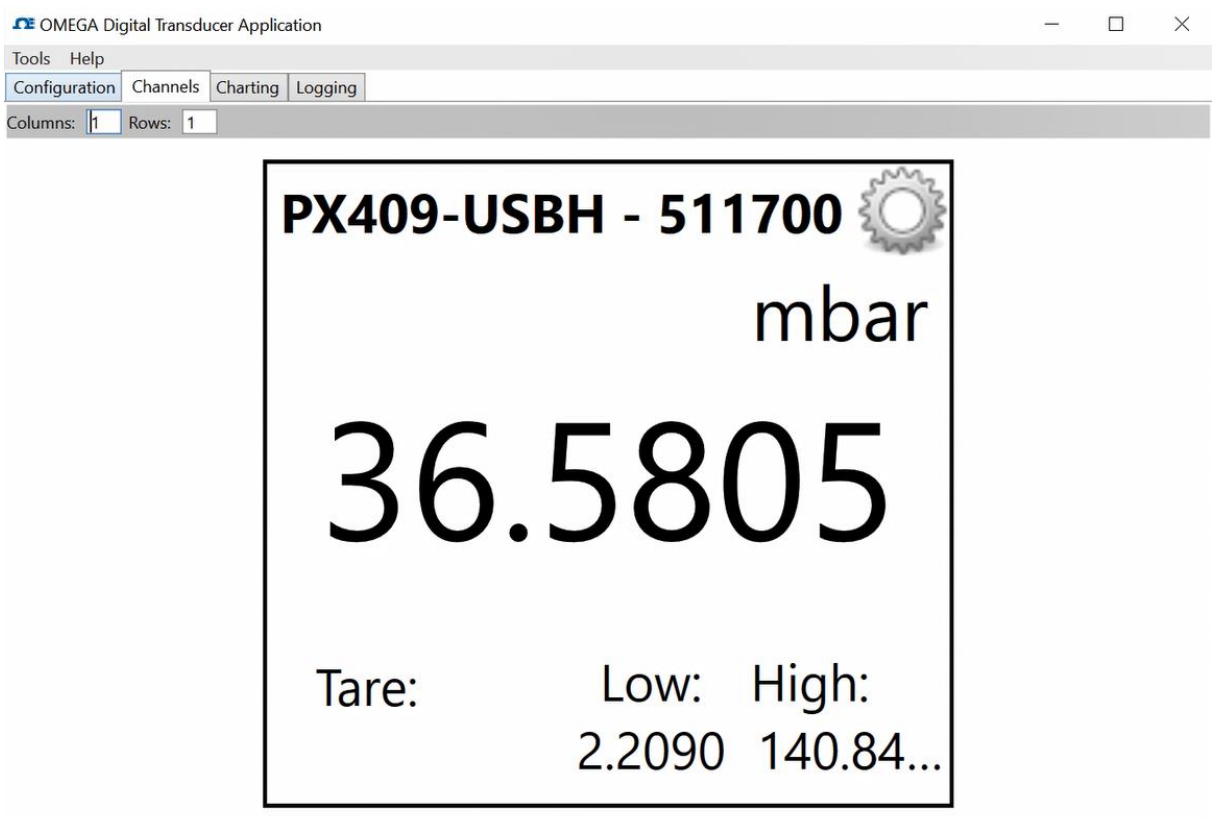

Figure 3.18: Transducer software channels window

A charting window allows data display in graphed in real time. The Y axis is configurable to allow simultaneous graphing of multiple engineering units, outputs of the graphical plot can be saved as a picture file.

A logging window shows live statistical data display, including the transducer information, the start/stop time, the number of samples taken, the current reading, and the High/Low readings. The logging window was used to capture data for later analysis in either in a .csv or .xls format which can both be exported to Microsoft excel for analysis.

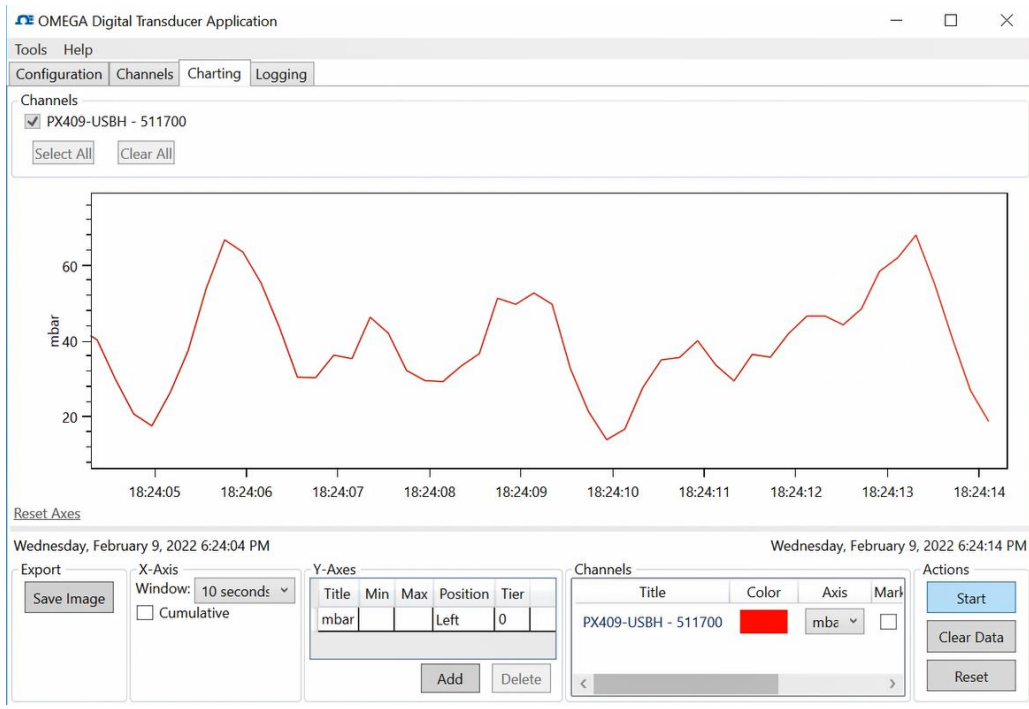

Figure 3.19: Transducer software charting window

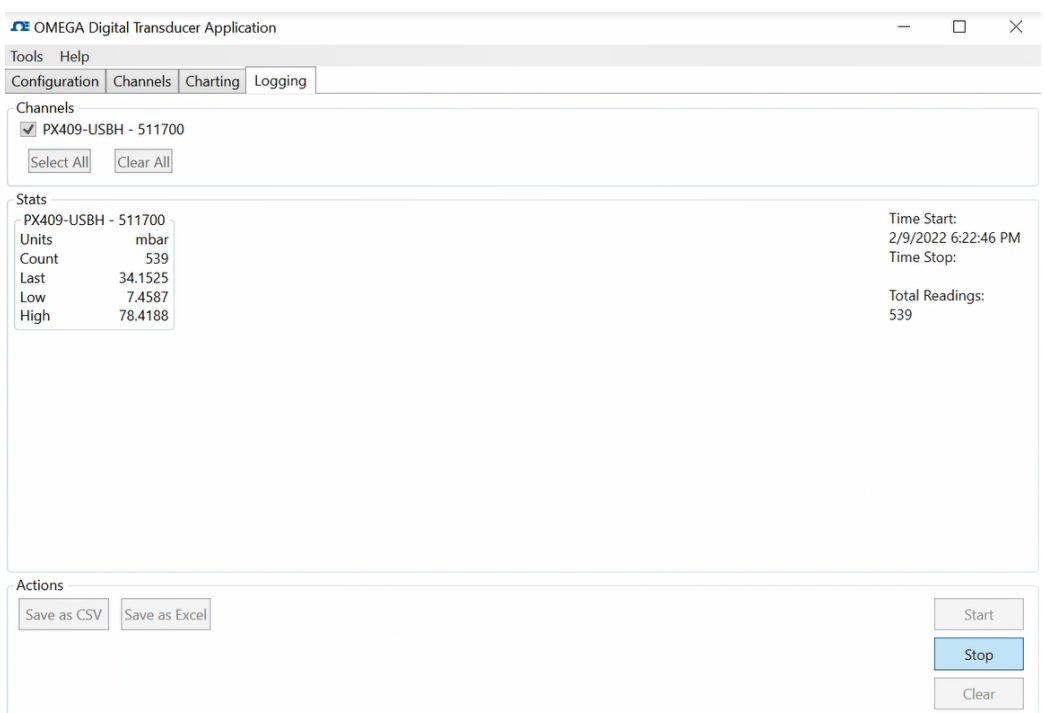

Figure 3.20: Transducer software data logging window

3.19.3 Liquid Holdup Measurement

The liquid holdup is one of the important factors to consider in the study of concurrent two-phase flows. This is the fractional percentage of the element of pipe which is occupied by liquid at the same instant. Experimentally, the liquid hold-up is determined by several techniques such as the resistivity or capacitance probes, or by trapping a segment of the flow stream between quick action closing valves and then measuring the volume of liquid trapped. In this project, the latter method of trapping a section of the flow stream is adopted for the liquid hold-up measurement. Two synchronous quick action solenoid valves were used to trap the two-phase flow mixture and collect the trapped residual liquid in the test section.

The two solenoid valves are both normally open (NO) and were installed at the inlet and outlet of the test section. When the solenoid valves were triggered, the two NO valves would be closed, thus trapping a volume of the two-phase mixture inside the test section. A drainage valve is then opened to let the liquid drain via a tap and collected in a measuring cylinder to measure the volume of liquid held. Compressed air was used to ensure maximum removal of liquid from the test section. A check valve was used to prevent the backflow of the two-phase mixture into the exit line.

The use of quick-opening solenoid valves is one of the standard methods of the liquid holdup, this technique has been adopted and proven by some previous researchers including Salehi et al. (2018), Bello (2017), and Mathure (2010).

3.19.4 High-Speed Video System

A high-speed video camera equipped with an LED lighting system was used to visualize and capture the flow patterns. The high-speed video observations were carried out with the aid of a Photron FASTCAM high-speed system that provides a broad range of high-performance features including ultra-high-speed recording, high light sensitivity, and short exposure times.

The high-speed digital camera was operated with full (1024 x 1024) megapixel resolution images at 125 frames per second (fps) to record the videos of the flow patterns for 60 seconds (1 minute) for each experimental run. The recordings were transferred from the camera in a slow-motion format to PC storage for analysis. A multi-LED 24 high power LEDs, 84 Watt, 24 Volt (7,700 Lumen total) light system was used to illuminate the photo viewing section to obtain a clear view of the flow in the test pipe. A schematic diagram of the experimental set-up and the camera configuration is shown in Figure 3.21.

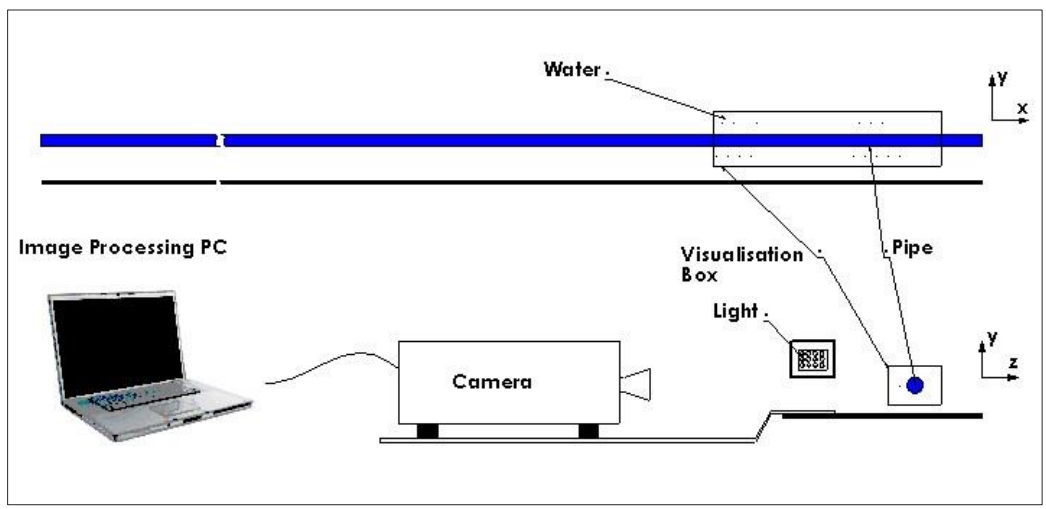

Figure 3.21: High-speed video camera schematics.

3.20 Setting Up the Rig

A consistent experimental procedure was developed to ensure that the experimental data obtained from the set-up was of the highest accuracy all through the experimental range. The flow pattern was observed and recorded for every set input of air and water mass flow rate. An experimental program and test matrix were designed to provide data on gas-liquid two-phase flow behaviour, predominantly across the slug flow regime. Experimental test conditions were determined for each programmed test matrix to be studied, this is then proceeded with to establish the corresponding gas and liquid flow rates. Once a particular inlet flow condition has been set, the conditions are maintained until the experiment is completed and all the data is captured. The procedure is repeated until the entire matrix of the inlet flow conditions is fully covered.

Before the main experiment, the rig was tested to ensure that there are no leakages. This was done by pumping the test liquid at room temperature and atmospheric pressure with the centrifugal pump from the water reservoir and passing through a regulator valve to maintain a constant liquid flow rate, while the overflow was returned to the liquid tank through a by-pass pipe, controlled by a manual valve. Compressed air was also supplied at room temperature from the university laboratory air compressor line and passed through a pressure regulator to maintain a constant gas flow rate. The same liquid as the test liquid was also filled into the visualisation section, which is made up of a transparent rectangular box, this is to reduce image distortion caused by the curvature of the pipe and to provide cooling against the heating effect of the illumination. The experiments were conducted at preselected gas and liquid flow rates at pipe inclination angles of 0^{o} and $+15^{o}$. A digital inclinometer was used to set the pipe's angle of inclination. For each experimental run, pressure drop data was collected for 180 seconds, a visual recording of the flow was taken for 60 seconds, while the liquid holdup measurement was taken 3 times and averaged.

Figure 3.22: Digital inclinometer used to measure the rigs inclination

A systematic approach was used to capture data with sufficient accuracy. The airflow rate was adjusted by small increments within the range of 0.5 to 5.0 m/s using the two control valves placed in series. While the water flow rate was kept constant at a pre-selected value. The superficial velocities of gas and liquid were used as control variables. The superficial liquid velocity was in the range of 0.1 to 1.0 m/s with increments of 0.1 m/s. After the flow is fully developed and stabilized, all data were then taken simultaneously: flow visualisation video is recorded for one minute and converted to AVI format for processing. It takes an average of 10 minutes to complete the recording and conversion, during this period, pressure drop data was captured at the rate of 5 data samples per second for three minutes, giving a total of 900 pressure drop readings and saved in an excel file for processing. Liquid holdup measurement was also taken three times and averaged to find the liquid holdup at the given flow conditions. This process was repeated for all the flow matrices using the three working fluids investigated.

Figure 3.23: Flow visualisation and pressure drop logging station

3.21 Experimental Matrix

Table 3.3 shows the test matrix with different combinations of the investigated superficial liquid velocity and superficial air velocity in the experimental rig, where X*ij* represents the experimental value obtained at a gas velocity *i* and liquid velocity *j*.

Table 3.3: Experimental test matrix (X*ij* represents the experimental value obtained at a gas velocity *i* and liquid velocity *j*)

U_{SL} (m/s)	U_{SG} (m/s)							
	0.5	**1**	**1.5**	**2**	**2.5**	**3**	**3.5**	**4**
0.1	X11	X21	X31	X41	X51	X61	X71	X81
0.2	X12	X22	X32	X42	X52	X62	X72	X82
0.3	X13	X23	X33	X43	X53	X63	X73	X83
0.4	X14	X24	X34	X44	X54	X64	X74	X84
0.5	X15	X25	X35	X45	X55	X65	X75	X85
0.6	X16	X26	X36	X46	X56	X66	X76	X86
0.7	X17	X27	X37	X47	X57	X67	X77	X87
0.8	X18	X28	X38	X48	X58	X68	X78	X88

3.22 Measurement of Physical Properties

In addition to water whose physical properties are well known, two other liquids were used in the experiment to study the effects of surface tension and viscosity. These are a glycerine-water solution, and a non-ionic surfactant solution. The key physical properties of these solutions need to be known, this includes the viscosity, density, and surface tension. The listed physical properties were appropriately measured as described below.

3.22.1 Viscosity Measurement

Anton Paar's rotational viscometer was used to measure the liquid viscosities based on the Searle technique of rheology measurements. The viscometer is equipped with a cup containing the sample and the cup is matched with a so-called measuring bob that is placed in the substance under test.

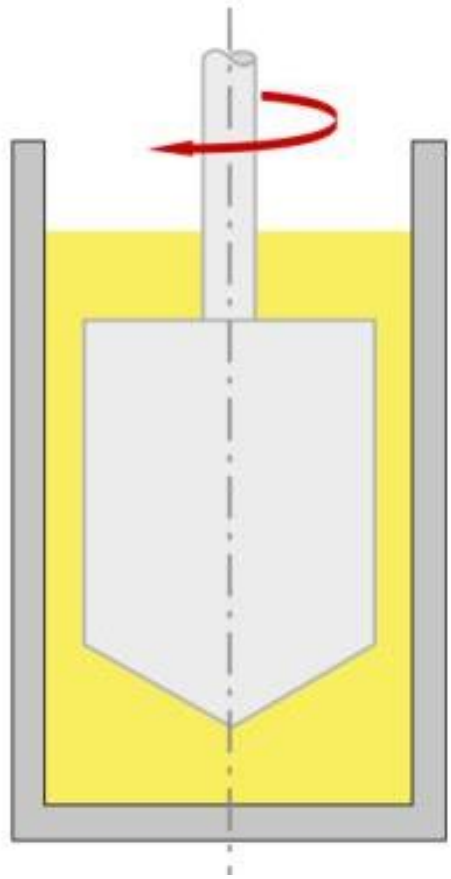

Figure 3.24: Searle principle: The instrument's motor turns the measuring bob inside an immovable vessel filled with sample

A motor drives the bob inside the fixed cup at a set temperature, the rotational speed of the bob is pre-set and produces a certain motor torque that is needed to rotate the measuring bob. This torque must overcome the viscous forces of the tested substance and is, therefore, a measure of its viscosity. Precisely defined geometries of the bob and its cup permit the computation of shear rate as well as shear stress and, consequently, absolute viscosity values. This data is presented in Appendix C.

3.22.2 Surface Tension Measurement

Surface tension is an important parameter in this experimental work its measurement is mandatory, surface tension measurements are done using either force or optical Tensiometer. Surface tension arises from cohesive forces between the liquid molecules. In

the bulk, molecules are interacting equally with each other in all directions. However, at the surface, molecules don't have the same neighbours on all sides. Thus, a net inward force pulls the molecules toward the bulk. This gives rise to a property called surface tension. How high the surface tension is, is dependent on the type of molecular interactions present.

In this work, the Goniometer KSV CAM200 was used to measure the surface tensions of the working liquids. An automated dispenser with disposable tips was used for different test liquids. A high-speed camera is used to capture the drop shape throughout the entire process. The frame interval can be set from 10ms-1000s. The contact angle measuring range is ~4-180° with an accuracy of ±1°. Attension Theta software was used to perform curve fitting image analysis to determine contact angle measurements. Data and images were exported for further analysis, shown in Appendix E.

3.22.3 Density Measurement

Density is defined as the measure of mass per unit volume. In this work, the mass of the liquid was weighted using a scale balance in a controlled environment. The weighted mass is then poured into an empty graduated cylinder to obtain the volume of the sample. The known mass of the sample is then divided by the obtained volume to get the density of the liquid. This was repeated for all the samples used as working liquids in the experimentation.

3.22.4 Rotameter Calibration

Rotameter is the commonly name for a variable area flowmeter which is inherently a volumetric flow measurement device. It is equipped with an indicator which floats at a steady value when the forces on it are equal. The main forces are the weight of the float (downward) and the drag force of the fluid (upward). Other forces are the difference in pressure over the float and the buoyancy force of the displaced fluid, which increases with pressure. The static equilibrium of the float is defined by the weight of the float, the drag, and the buoyancy force on the float. Ideally, a rotameter is designed and calibrated at the same temperature and pressure, and with the same process fluid for which it will be used. This ensures that the density of the liquid is the same.

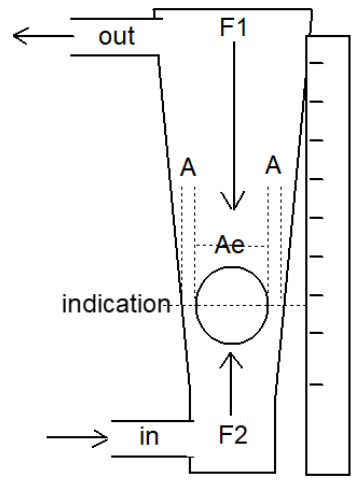

Figure 3.25: Rotameter schematics

The TROGFLUX VA rotameter fitted to the rig is designed for ordinary water at standard temperature and pressure. Switching the working fluid with a different liquid such as glycerol or surfactant solution will not give an accurate flowrate due to the difference in their physical properties such as viscosity to an extent, and most especially density. Options available are either to replace the flowmeter or recalibrate the rotameter. The latter option was taken, and whenever there is a switch in working liquid, the rotameter is recalibrated.

Figure 3.26: TROGFLUX VA rotameter on the rig

This was simply done with the use of a stopwatch and a measuring cylinder. At each indicated level of the rotameter, a certain volume of liquid was collected over a period. The volume collected was divided by the time taken to establish the actual volumetric flow rate. This was done at different levels of the rotameter flow indicator and for all the liquids. The collected data was plotted on the same graph. The graphical plot of actual flowrate against the rotameter flowrate for all the liquids is shown in Appendix E, the plot was used to deduce the correct required translational velocities of the working liquids.

3.38 Chapter Summary

This chapter has reviewed Computational Fluid Dynamics (CFD) methodologies and their capabilities for modelling multiphase flow. Furthermore, an overview of the available CFD codes, turbulence models, and related issues of modelling two-phase flow was introduced. This follows with a detailed description of the dispersed multi-fluid flow modelling (Eulerian–Eulerian, Volume of Fluid, and Eulerian-Lagrangian), including the governing equations that have been used in each method.

In the second part of the chapter, the experimental rig setup and equipment used were extensively described, some modifications and adopted methodologies was also highlighted. Detailed methodology and procedures undertaken to acquire the experimental data are described in sections. An overview of the experimental facility is given in Section 3.18, while Section 3.19 gives further information on some key equipment for data collection.

Chapter 4

Taylor Bubble Simulation in a 2D Pipe

This chapter explains the key steps taken to simulate the effects of liquid properties (density, viscosity, and surface tension) on the behaviour of elongated gas bubbles (Benjamin bubbles and Taylor bubbles). The effects of these properties on drift velocity are studied in horizontal and inclined 2D pipes using the commercial CFD package, ANSYS Fluent (Version 19.0). Water and 12 other simulated liquids are used together with air at six different pipe inclinations, giving a total of 78 simulations as shown in a simulation matrix of Table 4.1. Two-dimensional simulations are computationally cheaper to run although less informative or accurate than 3D. However, results from these 2D simulations provided enough information on how individual properties of liquid influence gas-liquid flow behaviour. Other than water, the simulated liquids shown in Table 4.1 are achieved by editing the properties of water in Fluent Database.

Table 4.1: 2D simulation matrix for an elongated gas bubble in a pipe filled with different liquids

Pipe Inclination	Liquid												
0	Water	D-1	D-2	D-3	V-1	V-2	V-3	V-4	V-5	ST-1	ST-2	ST-3	ST-4
15	Water	D-1	D-2	D-3	V-1	V-2	V-3	V-4	V-5	ST-1	ST-2	ST-3	ST-4
30	Water	D-1	D-2	D-3	V-1	V-2	V-3	V-4	V-5	ST-1	ST-2	ST-3	ST-4
45	Water	D-1	D-2	D-3	V-1	V-2	V-3	V-4	V-5	ST-1	ST-2	ST-3	ST-4
60	Water	D-1	D-2	D-3	V-1	V-2	V-3	V-4	V-5	ST-1	ST-2	ST-3	ST-4
75	Water	D-1	D-2	D-3	V-1	V-2	V-3	V-4	V-5	ST-1	ST-2	ST-3	ST-4

4.1 Problem Description

The flow geometry for the 2D drift velocity simulation is similar to Benjamin's (1968) work on the inviscid potential flow theory to determine the drift velocity in a horizontal pipe, where a horizontal pipe filled with liquid is initially closed at all ends, when one end of the

pipe is suddenly opened, there is a simultaneous draining of the liquid accompanied by propagating air in the shape of an elongated bubble. However, in this simulation, the pipe is closed at both ends with the gas bubble initially trapped at one end of the pipe, as shown in Figure 4.1.

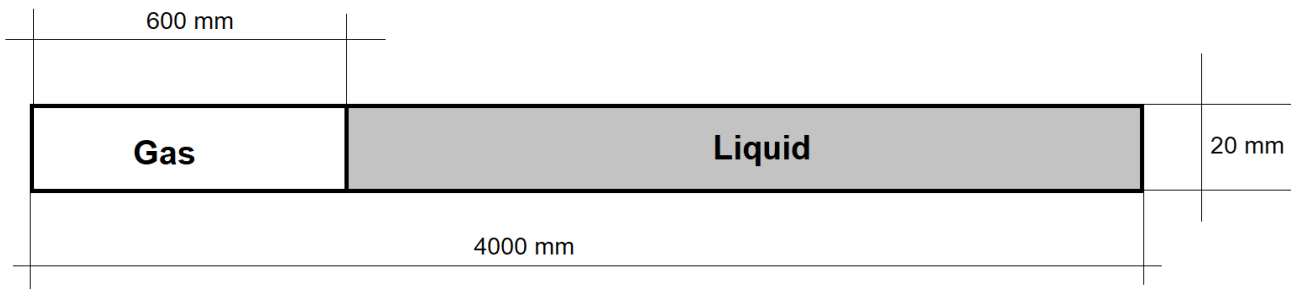

Figure 4.1: Flow geometry for the 2D horizontal pipe

The pipe is fully closed in all sides, there is no inlet or outlet boundaries, the driving force for the trapped gas bubble in the horizontal case is typically the pressure difference between the gas phase and the liquid phase. This pressure difference arises due to the difference in density between the gas and liquid phases. As the pipe orientation changes from horizontal to inclined, gravity also plays a role in causing the gas bubble to drift from one end of the pipe to the other end. The time it takes the trapped gas bubble to drift from end of the pipe to the other end is obtained at all pipe inclinations from 0^{O} to 75^{O}.

4.2 Geometry & Meshing

A rectangular geometry according to the dimensions shown in Figure 4.1 was created using the design modeler of the ANSYS workbench, the dimensions of the flow geometry are based on the dimensions of the pipe on the inclinable multiphase experimental rig. The geometry was meshed using the ANSYS meshing tool in the workbench. Meshing is the discrete representation of the flow geometry into smaller cells over which the partial differential equations can be approximated. Meshing is an integral part of the numerical solution and must satisfy some criteria to ensure that a valid and accurate solution is obtained. The better the mesh quality, the more an accurate result is obtained from the simulation. The ANSYS Workbench mesh generating tool offers the capability to create grids from geometry in multi-blocks, structured, unstructured, hexahedral, tetrahedral,

hybrid grids and more formats combined with boundary conditions. However, as this geometry is in 2 dimensions, a simple quadrilateral mesh was used. The required precision of the final solution dictates the mesh quality, as non-sufficiently refined mesh gives results with large error margins. However, a higher quality mesh also comes at the CPU cost among other factors to be considered. For a highly refined mesh, where the number of cells per unit area is maximum, the CPU time required will be relatively large. Simulation time is generally proportional to the number of elements since calculations must be done on each cell.

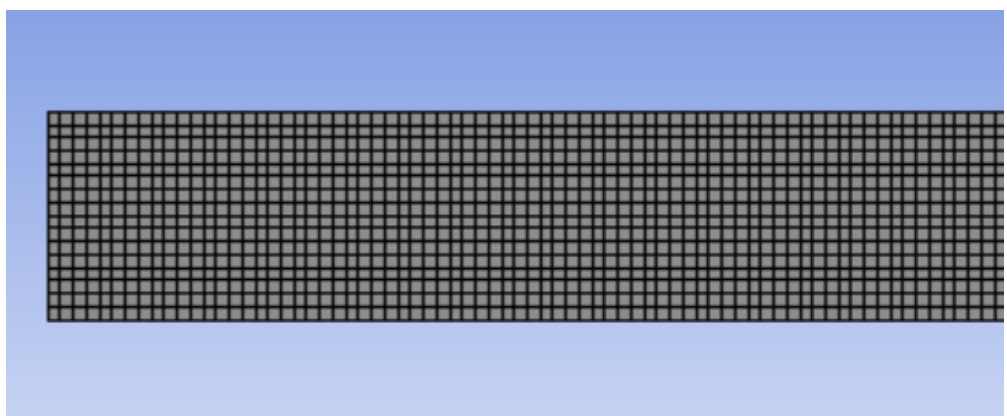

Figure 4.2: Geometry and mesh view for a 20mm 2D horizontal pipe

The flow geometry was uniformly meshed with grid spacing ($\Delta x = \Delta y$), with n number of cells. Details of the mesh are summarised in Table 4.2 below, and a sample is shown in Figure 4.2.

Table 4.2: Details of the different meshes used in this study

Mesh	**Grid spacing, (m)**	**Number of Cells, *n***
Mesh-1	0.00200	15,000
Mesh-2	0.00175	20,580
Mesh-3	0.00150	28,000
Mesh-4	0.00125	38,400
Mesh-5	0.00100	60,000

4.3 Mesh Independence Analysis

A mesh independence analysis is a process of investigating, whether the simulation results are independent of the underlying mesh or not. It is done by running several simulations with different mesh resolutions and then checking the changes in results between one mesh and another. To start with, a robust mesh independence analysis was carried out, six different meshes were tested to get an optimum mesh for the main simulations. The denser the mesh, the more accurate the result will be, but also the more computational resources in terms of the number of cores needed as well as simulation time.

4.3.1 Boundary & Initial Conditions

Boundary conditions are critical components of any CFD simulation, as they specify the flow properties on the computational domain boundaries. In this problem, all the perimeters of the geometry were set as walls with no-slip condition, thereby making it a closed pipe as shown in Figure 4.3. Patching is one of the methods of selecting a section of the geometry and assigning some unique additional features or properties at the initial conditions of the simulation. To fill the geometry with liquid and assign a section of gas pocket, the geometry was patched using coordinate points that correspond to the geometry in Figure 4.1. The left end of the pipe was filled with gas (up to the 600 mm length) using the patching feature of ANSY Mesh, while the remaining 3400mm of the pipe (600mm to 4000mm) was patched with water. At the start of the simulation, the liquid drains to the other side of the pipe, while at the same time, the gas pocket propagates through the liquid region due to the pressure difference.

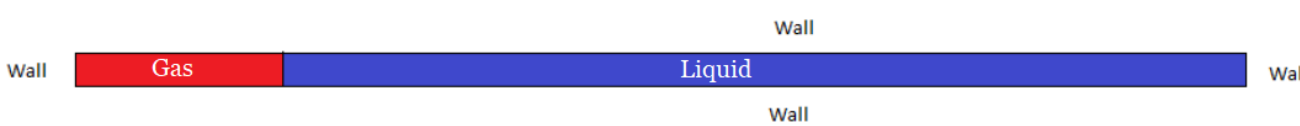

Figure 4.3: Boundary and patching at the initial condition

The pressure difference is primarily caused by the difference in hydrostatic pressure between the gas and liquid phases. The hydrostatic pressure in a fluid depends on its density and height. The gas bubble, being less dense than the liquid, experiences a lower hydrostatic pressure compared to the surrounding liquid. This pressure difference creates a driving force

that tends to push the gas bubble in the direction of lower pressure. As a result, the gas bubble moves along the horizontal pipe, driven by the pressure difference.

4.3.2 Governing Equations

The volume of fluid (VOF) model implemented in Ansys Fluent was applied to capture phase distributions. As discussed in Chapter 3, the VOF model is a surface tracking method applied on a fixed Eulerian grid used to model two or more immiscible fluids and where the interface between the fluids is of interest. A single set of conservation equations is shared by the phases in the VOF model, and the volume fraction for each of the phases is tracked throughout the domain. The interphase between the liquid phase α_l and the gas phase α_g is tracked by solving the conservation equation for the volume fraction of the secondary phase.

$$\frac{\partial(\alpha_g \rho_g)}{\partial t} + \nabla \cdot \left(\alpha_g \rho_g \mathrm{u}\right) = 0 \tag{4.1}$$

The volume fraction is solved only for the secondary phase and the volume fraction for the primary phase is obtained using the following constraint.

$$\alpha_l + \alpha_g = 1 \tag{4.2}$$

The phase volume fraction has a value of 0 or 1 when a control volume is filled with liquid or gas, and a value between 0 and 1 if an interface is present in the control volume.

- **Continuity Equation:**

$$\frac{\partial(\rho)}{\partial t} + \nabla \cdot (\rho u) = \sum_n S_n \tag{4.3}$$

where ρ, u, t, S, and n are the density, velocity, time, mass source and the fluid type respectively. The mass source for this set up is zero based on initial assumption of no mass transfer.

- **Momentum Equation:**

The key assumptions made in the VOF this model are the flow is unsteady, immiscible liquid pair, isothermal, no mass transfer, and no phase change. Thus, a single set of momentum equations is shared by the two fluids.

$$\frac{\partial(\rho u)}{\partial t} + \nabla \cdot (\rho u \cdot u) = \nabla p + \nabla \cdot [\mu(\nabla u + \nabla u^T)] + \rho g + F \quad (4.4)$$

where ρ, u, t, p, μ, g, and F are the density, velocity, pressure in the flow field, viscosity, acceleration due to gravity and the body force respectively.

The properties appearing in the momentum equations are volume-fraction-averaged properties, the body force F represents the contribution of surface tension. The continuum surface force (CSF) model proposed by Brackbill et al. (1992) was used. The model is dependent on the surface tension coefficient, σ, and the curvature of the interface, *k*.

$$F = \sigma k \frac{\rho \nabla \alpha_g}{1/2(\rho_l - \rho_g)} \quad (4.5)$$

The curvature, *k*, is defined in terms of the divergence of the unit vector normal to the wall, $\hat{n}$.

$$k = \nabla \cdot \hat{n} \quad (4.6)$$

$$\hat{n} = \frac{n}{|n|} \quad (4.7)$$

where n is the surface normal, expressed as the gradient of the volume fraction of the gas phase, α_g.

$$n = \nabla \alpha_g \quad (4.8)$$

4.3.3 Solution Method

Having extensively discussed the numerical methods and techniques behind the CFD software in Chapter 3, the numerical methods chosen to solve the physical problem of the drift velocity is summarised in this subsection. The double-precision option of ANSYS Fluent was used for all simulations, and gravitational force acting in the downward direction was included in all calculations. Gas was set as the primary phase in the VOF model, while the liquid was set as the secondary phase. The PISO scheme was used for the pressure/velocity coupling. This is due to its ability to handle unsteady flow phenomena,

such as bubble deformation and vortex shedding at the tail end of the Taylor bubble. PISO is also numerically stable even for large time step size. For pressure interpolation, the PRESTO scheme was selected for its use of collocated grid arrangement: This means that

the pressure and velocity variables are stored at the same locations in the computational domain. This simplifies the implementation of boundary conditions and reduces the computational cost of the simulation. The Green-Gauss Cell-Based method for gradient computation was used for its consistency with the continuity equation, it satisfies the conservation of mass principle. This is important for ensuring the overall accuracy of the simulation. For spatial discretisation of pressure, the Body Force Weighted (BFW) method was used. The BFW method is relatively simple to implement and does not require any additional computational cost beyond the standard discretisation of the pressure equation.

Table 4.3: Summary of Discretisation Scheme

Variable	**Scheme**	**Advantage**
Pressure-Velocity Coupling	PISO	Numerical stability, accuracy, flexibility, and efficiency.
Pressure	PRESTO	Improved accuracy, collocated grid arrangement, and ease of implementation.
Gradient	Green-Gauss Cell-Based method	Accuracy, consistency, flexibility, efficiency, and ease of implementation.
Volume Fraction	Geo-Reconstruct	More realistic representation of the geometry of the domain, reducing computational cost, and improving the overall accuracy of the simulation.
Momentum	Second Order Upwind	Improved accuracy, stability, consistency, computational efficiency, and compatibility with turbulence models.
Turbulent Kinetic Energy		
Turbulent Dissipation Rate		

A Second-Order Upwind Discretisation was set for momentum, turbulent kinetic energy, and turbulent dissipation rate. This method is based on the idea of using a higher-order discretisation scheme that takes into account the direction of the flow to improve the accuracy of the solution. The second-order upwind discretisation method is also more stable than other higher-order schemes such as the central differencing scheme, which can be prone to numerical oscillations and instability. Furthermore, this discretisation method is compatible with a variety of turbulence models including the k-epsilon model used in this work.

Geometric Reconstruction (Geo-Reconstruct) was used for discretisation of volume fraction, this improves the accuracy of the solution by reconstructing the geometry of the domain from discrete data points, thereby maintaining high-quality meshes that conform well to the geometry of the domain. This is important for accurate simulation of the flow and minimizing numerical errors. Since there is no heat loss or gain in the flow, the Energy Equation was turned off so that the computational efforts will only be used to solve the momentum and the continuity equations.

4.3.4 Fluid properties

The relevant properties of the two fluids (air and water) used in the simulation are as given the Table 4.4 below:

Table 4.4: Properties of air and water used in simulations at 20^{O} C

Fluid	Density (kg/m3)	Viscosity (kg/ms)	Surface Tension (N/m)
Air	1.224	0.000018	0.072
Water	999.98	0.001	0.072

4.3.5. Solver controls

The simulations in this work are carried out under time-dependent conditions, and the main controlling factor in a time-dependent solution scheme is the time step. A small-time step gives a smoothly converging solution, and a large-time step is likely to lead to too much change causing the solution to diverge. The velocity and cell size are other factors that together with the step determine the convergence of the solution as well as the

computational time, these parameters are put together mathematically to form a dimensionless number called the Courant Number. The Courant number is a mathematical condition necessary for achieving a stable convergence when solving a partial differential equation using a numerical method. The equation involves spatial coordinate, time, and velocity. Mathematically, the Courant number C is given as:

$$C = Ux\frac{\Delta t}{\Delta x} + Uy\frac{\Delta t}{\Delta y} \leq 1 \quad (4.9)$$

Where Ux= velocity in the x axis, Uy = velocity in the y axis, Δt = time step, Δx and Δy are the spatial differential distance in the x and y direction respectively.

The larger the velocity, the lower the time step should be set in order to keep the Courant number less than 1 and get an accurate convergence. The higher the resolution of the mesh, the lower the Δx value, and the smaller the time step (Δt) in the Fluent should be, otherwise convergence will not be achieved as the courant number will exceed 1. This was the case with some of the meshes where the simulations lead to runtime errors. The only variable that can be controlled from Equation 4.9 are the mesh density and time step size. Therefore, different time step sizes were used for meshes to ensure that the Courant number is less than 1. Table 4.5 shows the effect of times step size *(Δt)* on Courant number (CFL) on a bubble with drift velocity *(U_D)* of 0.185168 in a mesh size *(Δx)* of 0.00125.

Table 4.5: Effects of times step size on CFL number

CFL	***U_D (m/s)***	***Δt (s)***	***Δx (m)***
0.148134	0.185168	0.001	0.00125
0.296269	0.185168	0.002	0.00125
0.592538	0.185168	0.004	0.00125
0.888806	0.185168	0.006	0.00125
1.185075	0.185168	0.008	0.00125

Inside each time interval iterations are carried out to calculate the transport equations for that time step. If the time step is small enough to get convergence, fewer iterations per time

step are required. For this iteration process to converge, it may be necessary to control the change of the variables from one iteration to the next. This is achieved under relaxation factors. Under relaxation factors of 0.3, 0.7, and 0.8 respectively were applied on pressure, momentum, and turbulence kinetic energy parameters as recommended by Fluent.

4.3.6 Simulation Runs

The High-Performance Computing services of Leeds University were fully utilised, and all simulations in this research were performed using ANSYS Fluent 19.2 on ARC2, ARC3, and ARC4. Each of the mesh independence cases was run on 24 cores, with simulation time ranging from one week to four weeks depending on the mesh density. A job submission script was created for each case with a varying time step size of 0.01s to 0.0001s, and time steps varying from 20,000 to 60,000, depending on the mesh resolution, ensuring that the simulation is run to completion. The simulation is assumed to be completed when the Taylor bubble nose touches the other end of the pipe. A maximum of 100 iterations per time step was set with a convergence criterion of 10^{-9} for all scaled residuals. The results were saved after every 50-time steps for post-processing with CFD post.

4.3.7 Mesh Independence Results & Analysis

The mesh independence simulation was designed to provide a general overview of how each mesh behaves with regard to flow characteristics and phase distribution. At time equals zero, the two phases are initially separated as shown in Figure 4.4 *(a)*. When simulation starts, falls along the gas side of the pipe while the gas propagates along the pipe's length as shown in Figure 4.4 *(b)*.

(a) Initial conditions t=0

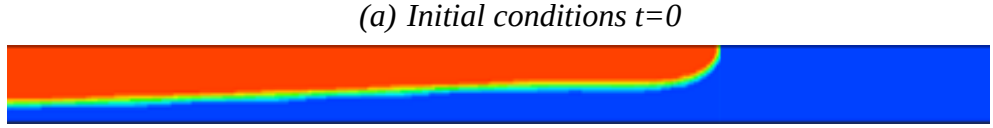

(b) Simulation in progress t=x

Figure 4.4: Contours of phase fraction for liquid and gas at the initial condition (a) and during the simulation (b)

The drift velocity is the time taken by the front of the elongated gas bubble to travel between two fixed points. In this work, the drift velocity was calculated from the contours of the phase fraction by tracking the instantaneous position of the bubble's nose along the pipe. Multiple points were marked along the pipe's length at 0.1m intervals and the time taken for the bubble to travel between two points was measured to obtain the bubble's instantaneous velocities using the following formula:

$$U_B = \frac{x_2 - x_1}{t_2 - t_1} = \frac{0.1}{t_2 - t_1} \tag{4.10}$$

Where, x_1 and x_2 are the previous and current positions of the bubble's nose, while and t_1 and t_2 are their respective times as shown in Figure 4.5.

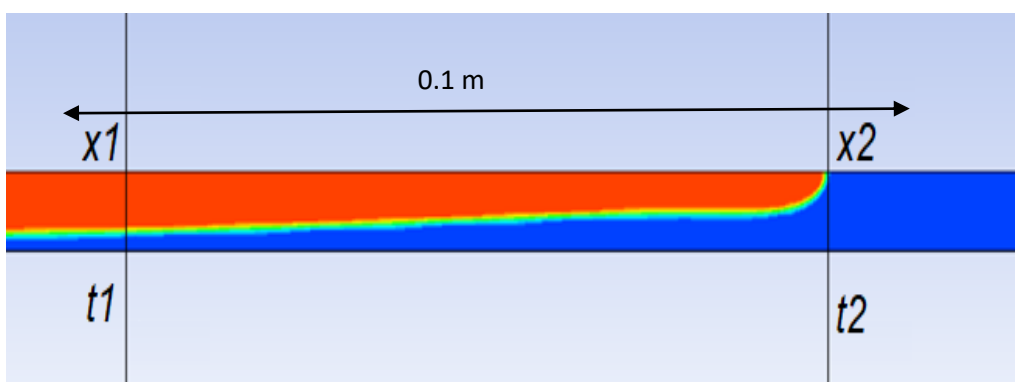

Figure 4.5: Drift velocity measurement in a horizontal pipe from ANSYS simulation

Performance data of the six different meshes were summarised in a graphical representation of the Displacement-Time plot (Figure 4.6) and Velocity-Time Plot (Figure 4.7) of the bubble. The displacement-time graph shows little difference in performance among the 5 different meshes, a notable difference is however seen in the velocity-time plot, where the average bubble velocity varies from **0.179 m/s** to **0.185 m/s**. The simulated value of the drift velocity obtained from one mesh is compared to the value obtained from the next denser mesh. The percentage deviation is calculated and summarised in Table 4.4.

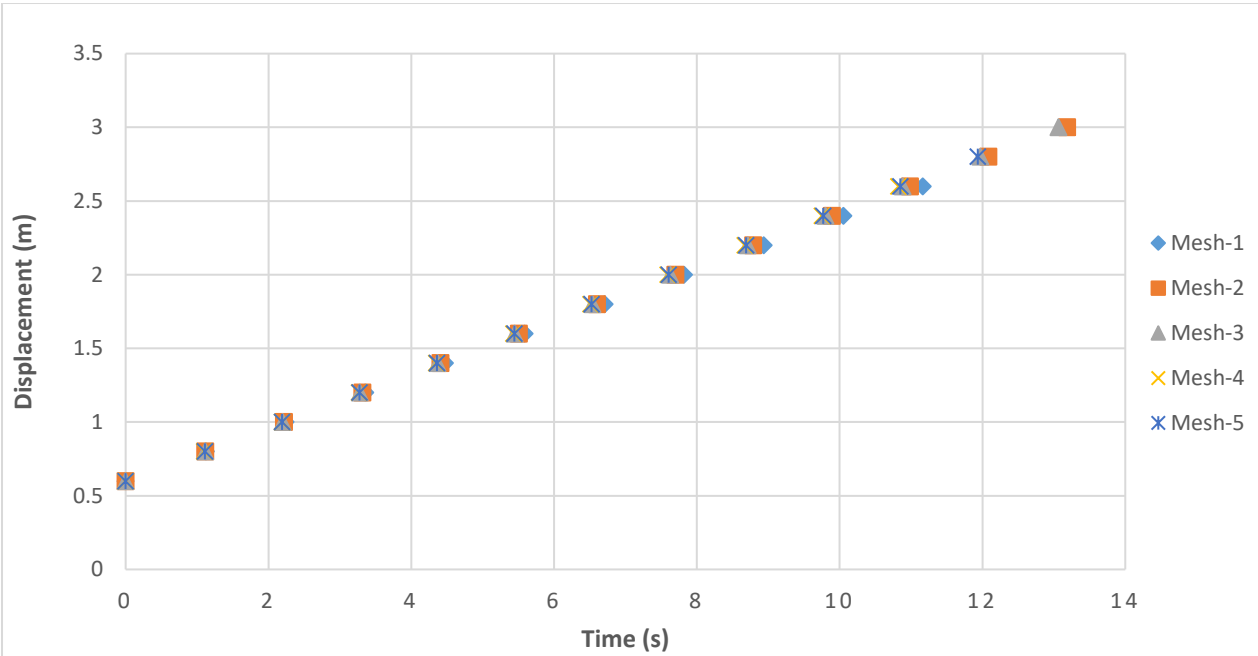

Figure 4.6: Displacement-Time plot for an elongated air bubble in horizontal pipe of water.

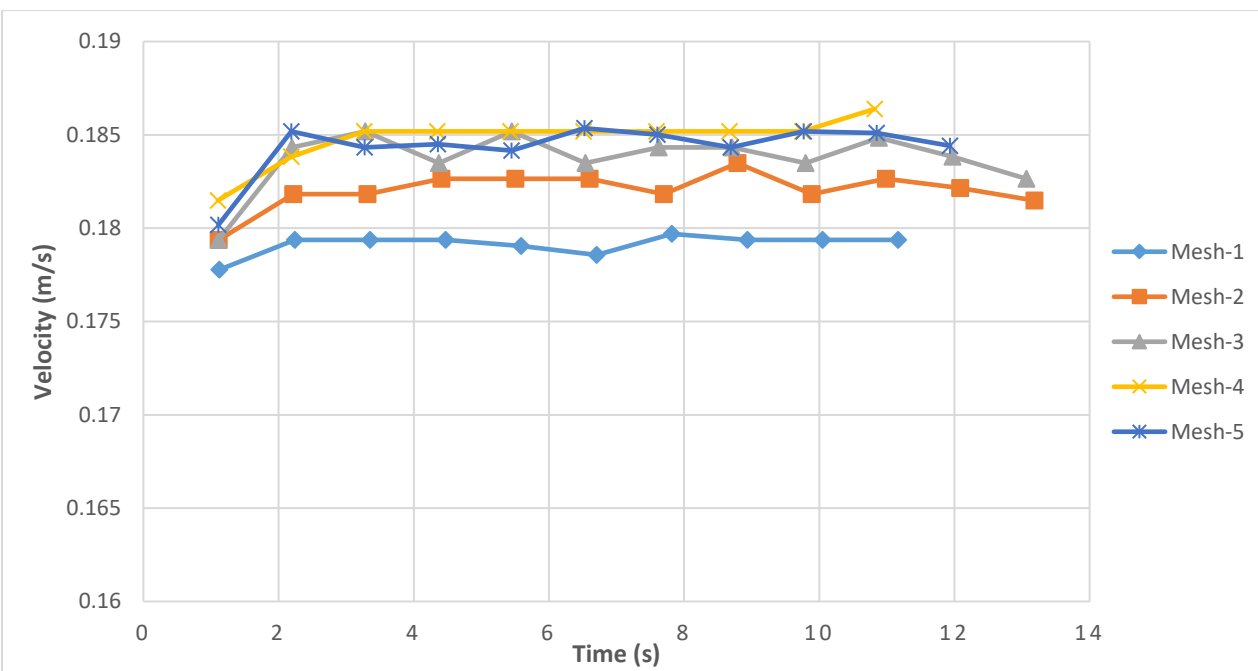

Figure 4.7: Velocity-Time plot for an elongated air bubble in horizontal pipe of water.

Table 4.6: Mesh performance analysis

Mesh	Simulated U_B	% deviation from next mesh
1	0.17928	1.6399
2	0.18227	0.9951
3	0.18410	0.5746
4	0.18517	0.0108
5	0.18519	-

Table 4.6 shows that the percentage deviation for the simulated value of U_B decreases with increasing mesh refinement. Approximately, the value of U_B obtained from mesh-1 is 1.64% less than the value obtained using mesh-2, while mesh-4 provides a U_B value of 0.18517 which is just 0.01% less than the value of 0.18519 obtained from mesh-5. Therefore, mesh-4 was selected as the optimum mesh for further simulations.

4.4 Simulation Runs with Different Liquids at Different Inclinations

Having selected mesh-4 with a grid size of 0.00125m, 12 more liquids were tested at pipe inclinations of 0^O, 15^O, 30^O, 45^O, 60^O, and 75^O as already presented in Table 4.1.

The additional liquids used were also water but with one of its properties modified (either density, viscosity, or surface tension) while the rest of the properties are kept constant. These liquids shown in Table 4.7 are not real liquids, but simulated liquids achieved by changing editing the properties of water in Fluent Database. As this research is more towards multiphase flow applications in the oil and gas industry, the modified property for the liquids were all the known properties of different brents crude oils (viscosity, density, and surface tensions). Table 4.5 shows the list of all the liquids used and their physical properties. Air was used as the gas in all the simulations.

Each of the above liquids was used in the simulation at six different pipe inclinations, giving a total of 78 simulation runs that took about six months to complete on the HPC.

Table 4.7: Properties of different liquids used in the simulations

S/N	Liquid	Density (Kg/m3)	Viscosity (Kg/m.s)	Surface Tension (N/m)
1	Water	998.2	0.001	0.073
2	D-1	870	0.001	0.073
3	D-2	920	0.001	0.073
4	D-3	1,050	0.001	0.073
5	V-1	998.2	0.0021	0.073
6	V-2	998.2	0.0049	0.073
7	V-3	998.2	0.0107	0.073
8	V-4	998.2	0.0886	0.073
9	V-5	998.2	0.307	0.073
10	ST-1	998.2	0.001	0.054
11	ST-2	998.2	0.001	0.032
12	ST-3	998.2	0.001	0.025
13	ST-4	998.2	0.001	0.018

4.5 Simulation Results and Analysis

The behaviour of elongated gas bubbles under a downward-facing surface is an interesting topic in many industrial operations other than the oil and gas industry, these include certain heat transfer equipment and electrolytic cells. The computational studies carried out on the elongated gas bubble drift velocity across various densities, viscosities, and surface tensions have yielded both expected outcomes and new interesting information.

4.5.1 Bubble's Shape and Flow Profile

Figures 4.8 and 4.9 show that liquid viscosity and pipe inclination result in bubble deformation. When the viscosity increases, the bubble remains un-deformed with a blunt nose leading to a lower drift velocity. Less viscous liquids and high angles of inclinations show high bubble deformation with a trail of smaller bubbles flowing behind the elongated

bubble, the motion of these smaller gas bubbles creates turbulence in the liquid. This subsequently affects fluid mixing, mass transfer rate, and temperature homogenisation. The highly viscous liquids analysed also leave a thick film between the penetrating gas bubble and the pipe walls. The thickness of this film tends to increase as liquid viscosity goes up, and this varies along the pipe.

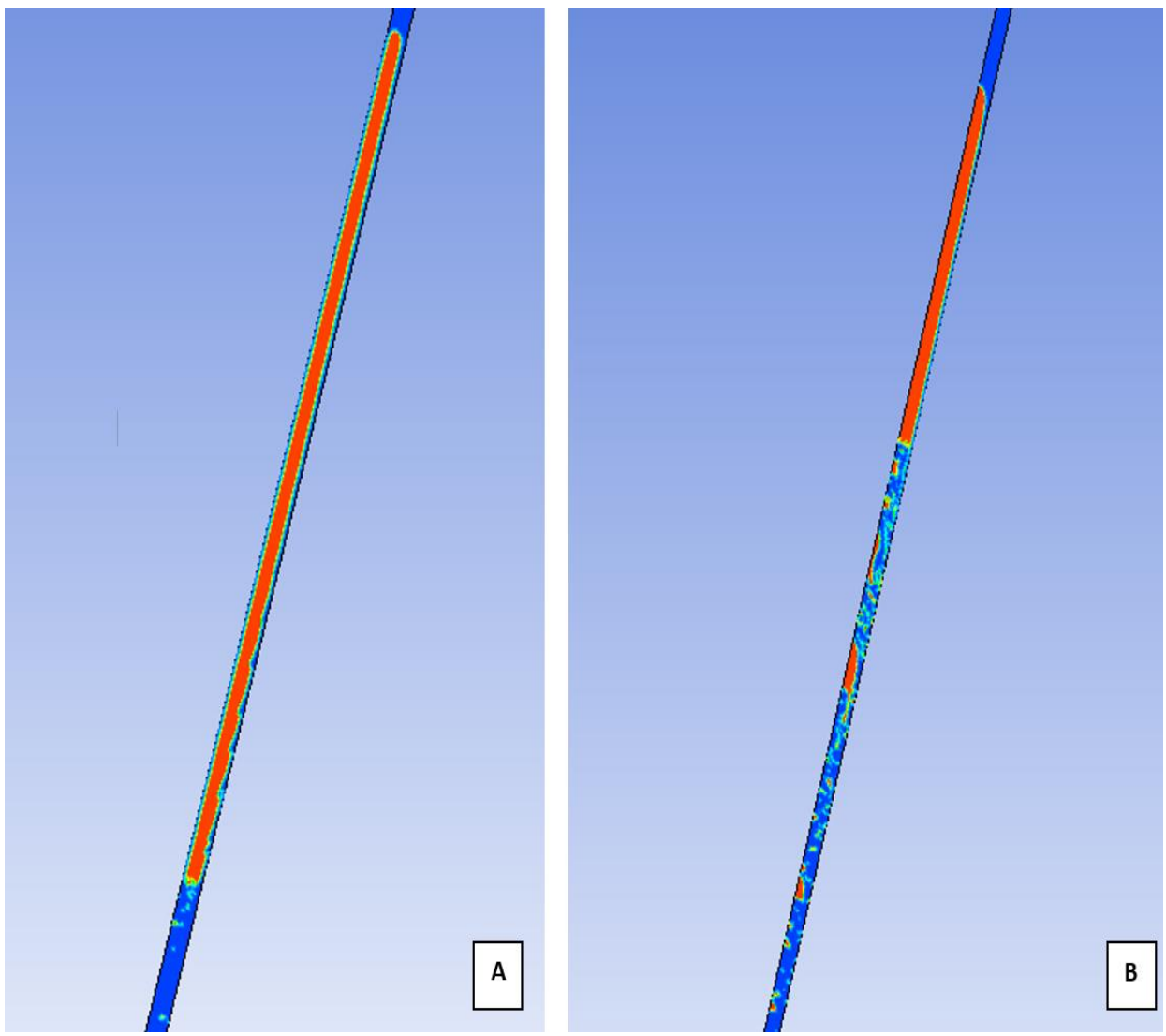

Figure 4.8: Effects of viscosity on bubble length fragmentation. Less fragmented Taylor bubble in V-5 (A), compared to a very fragmented Taylor bubble in a V-1 (B), for a pipe inclined at 75^{O}.

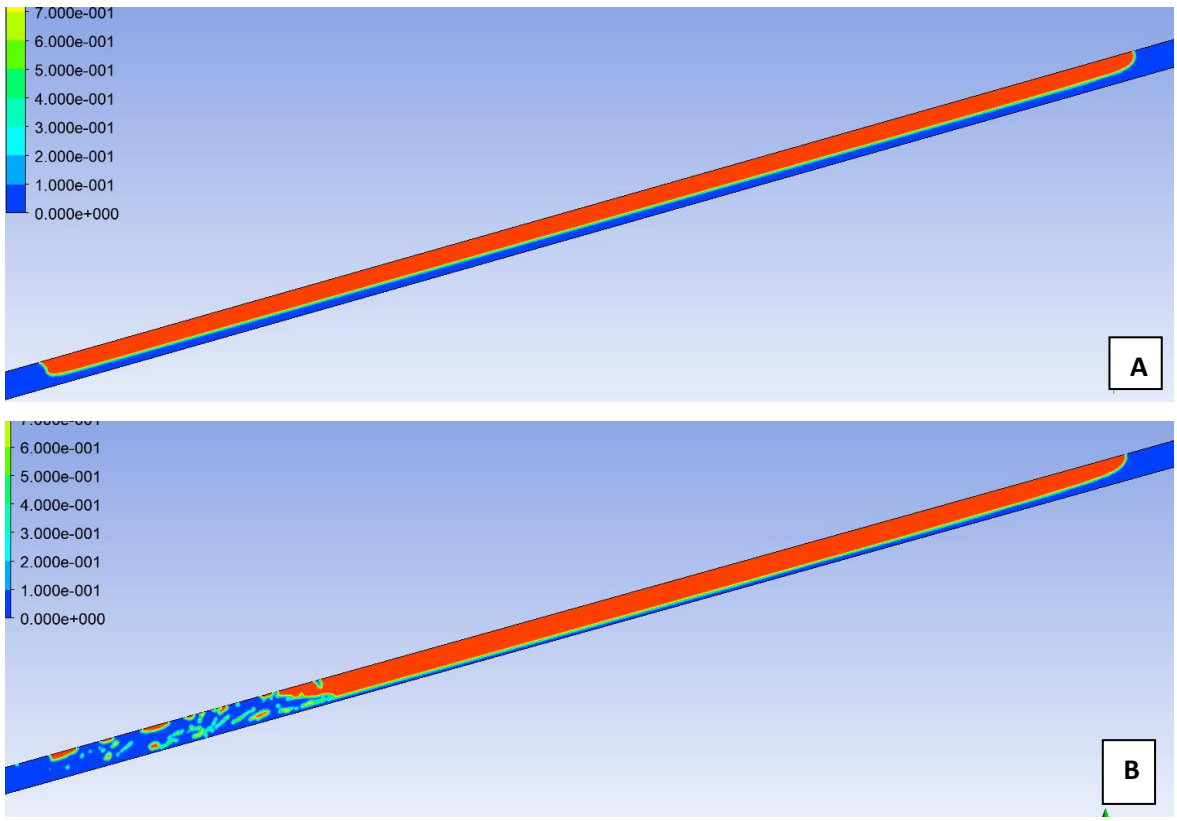

Figure 4.9: Effects of viscosity on bubble length fragmentation. Less fragmented Taylor bubble in V-5 (A), compared to a very fragmented Taylor bubble in a V-1 (B), for a pipe inclined at 15^{O}.

The simulation results have also shown that density alone has little or no effect at all on the behaviour of the elongated gas bubble. The displacement time-plots from Figures 4.10A, 4.11A, 4.12A, 4.13A, 4.14A, and 4.15A showed almost an identical behaviour of the bubble as it drifted through the pipe at different inclinations, the average drift velocity is almost the same across all tried densities at a given pipe inclination. Interestingly, surface tension also shows little effect at lower inclinations, as shown in Figures 4.10B, 4.11B, and 4.12B. However, the effects of surface tension become notable as the pipe's angle inclination increases to 45O upwards, this is depicted in Figures 4.13B, 4.14B, and 4.15B. This feature has never been reported by previous researchers based on the review done so far, as no previous work has singled a physical property to study its effect while keeping the others constant.

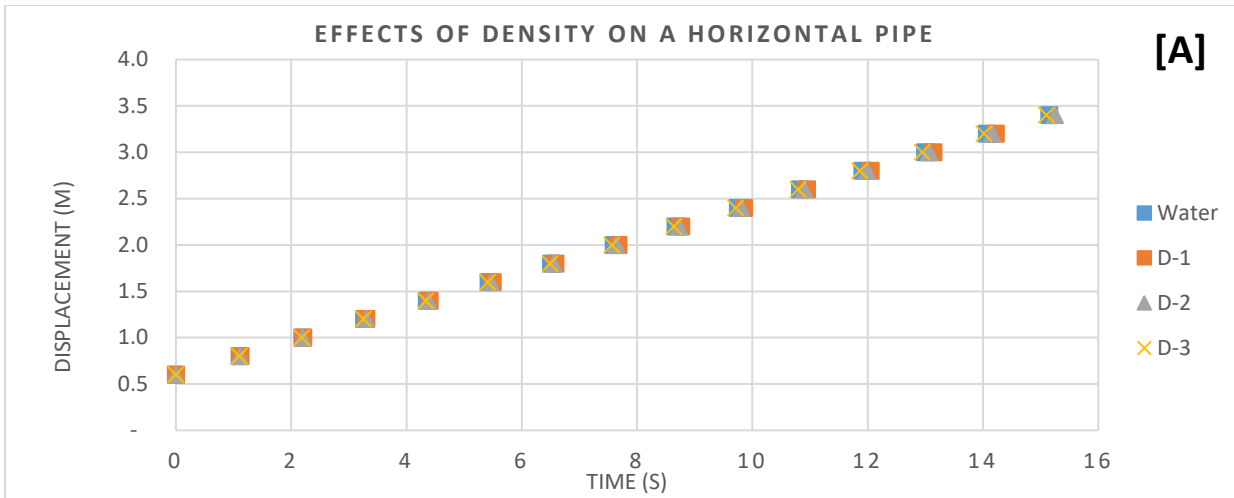

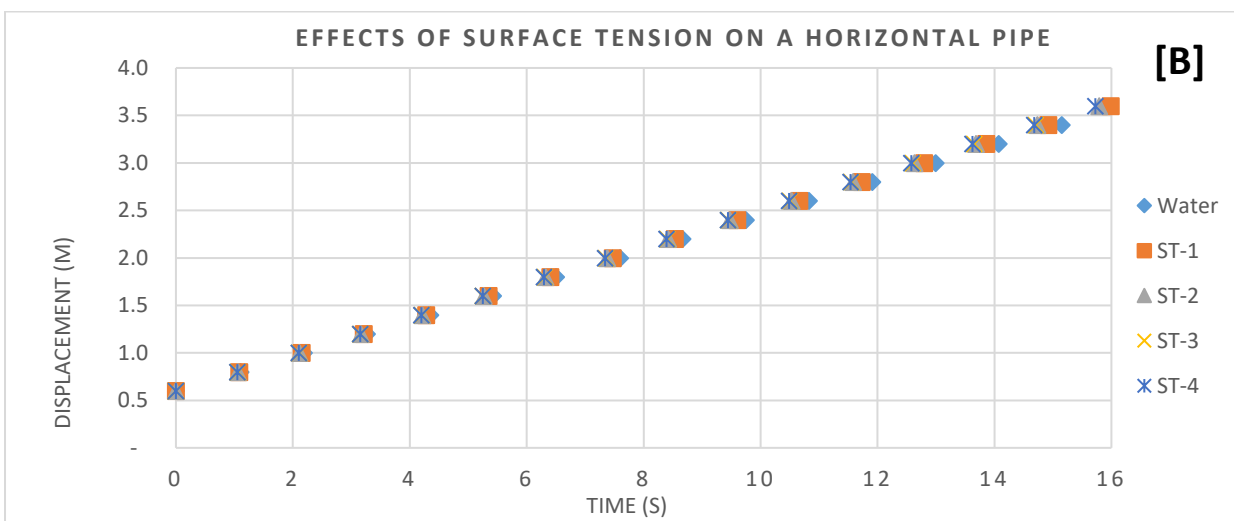

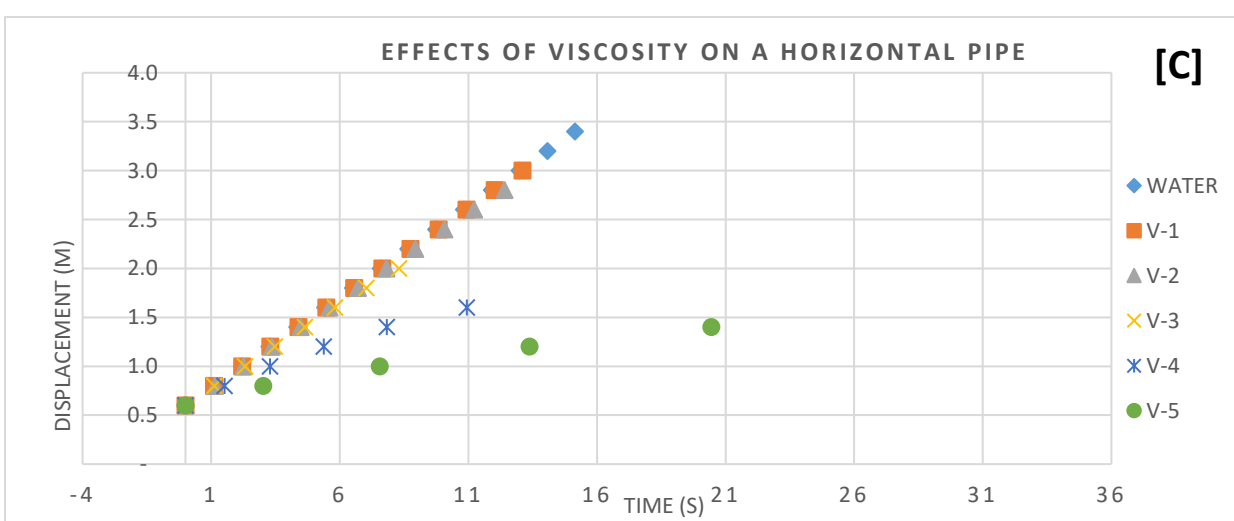

Figure 4.10: Disp.-Time plot for a horizontal pipe showing the effects of density [A], surface tension [B], & viscosity [C]

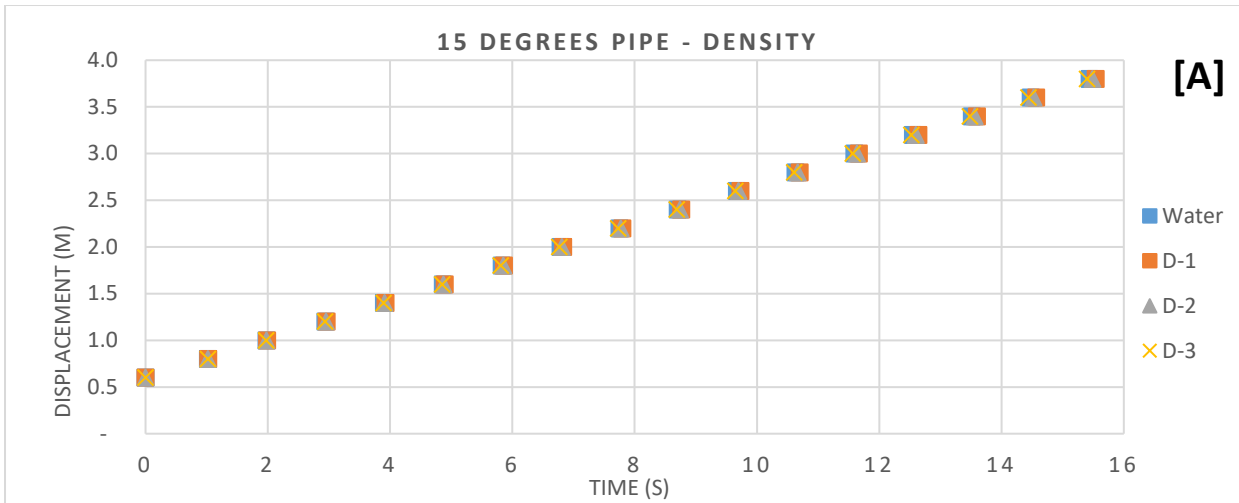

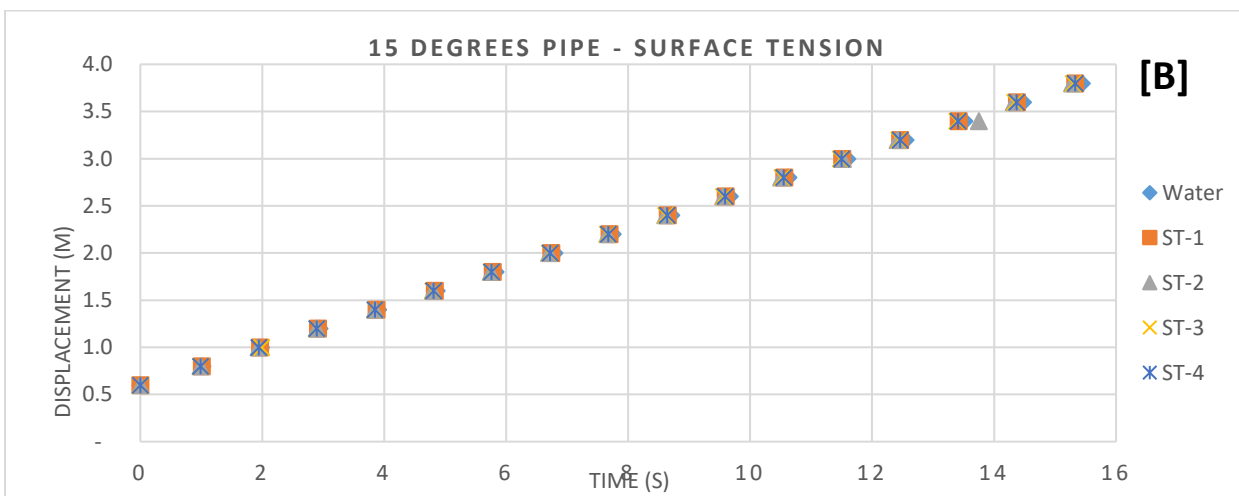

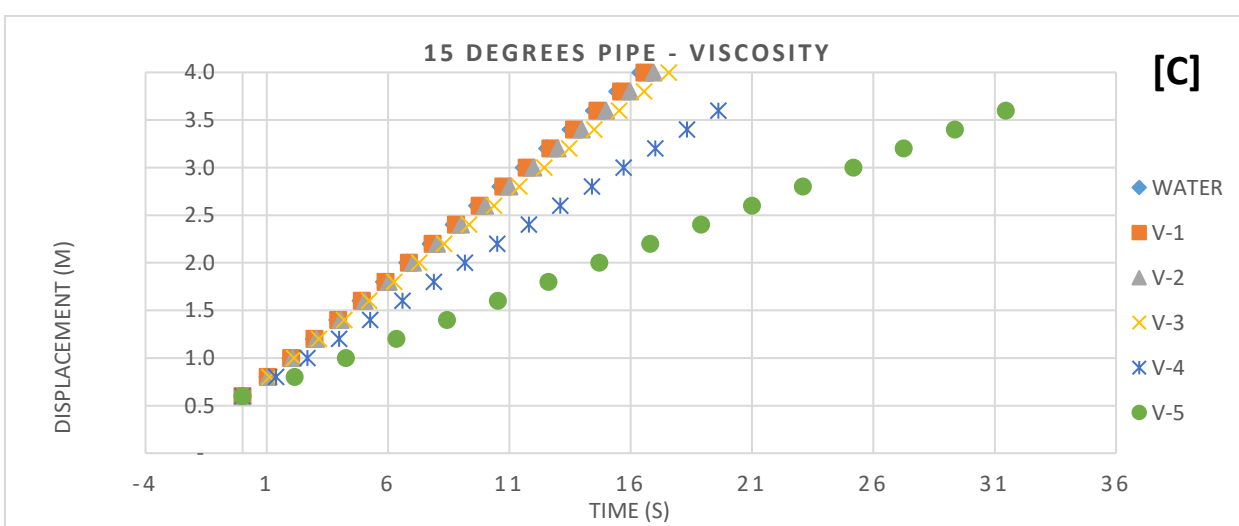

Figure 4.11: Disp.-Time plot for a 15^{O} inclined pipe showing the effects of density [A], surface tension [B], & viscosity [C]

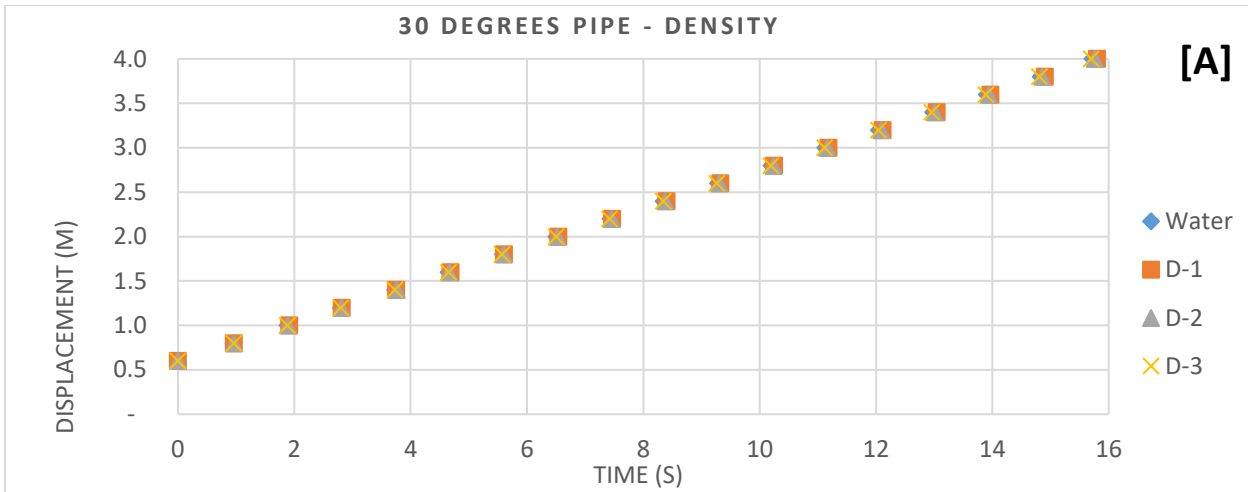

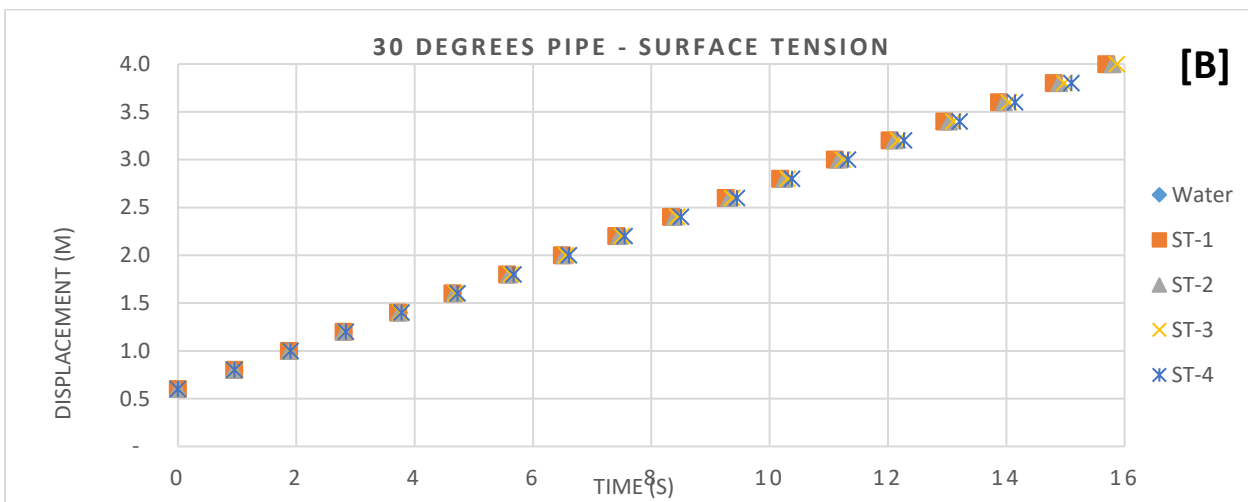

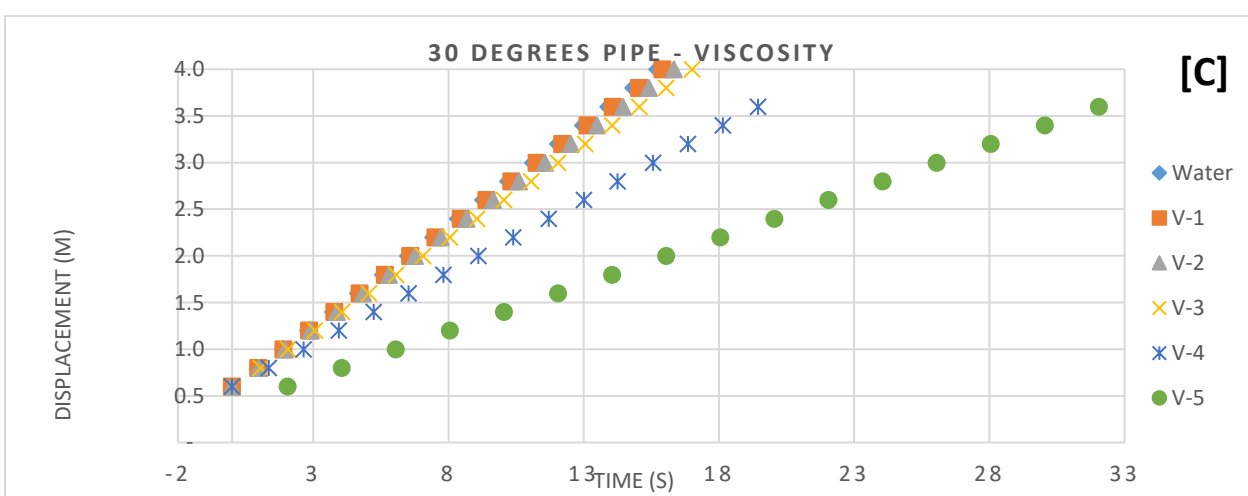

Figure 4.12: Disp.-Time plot for a 30^{O} inclined pipe showing the effects of density [A], surface tension [B], & viscosity [C]

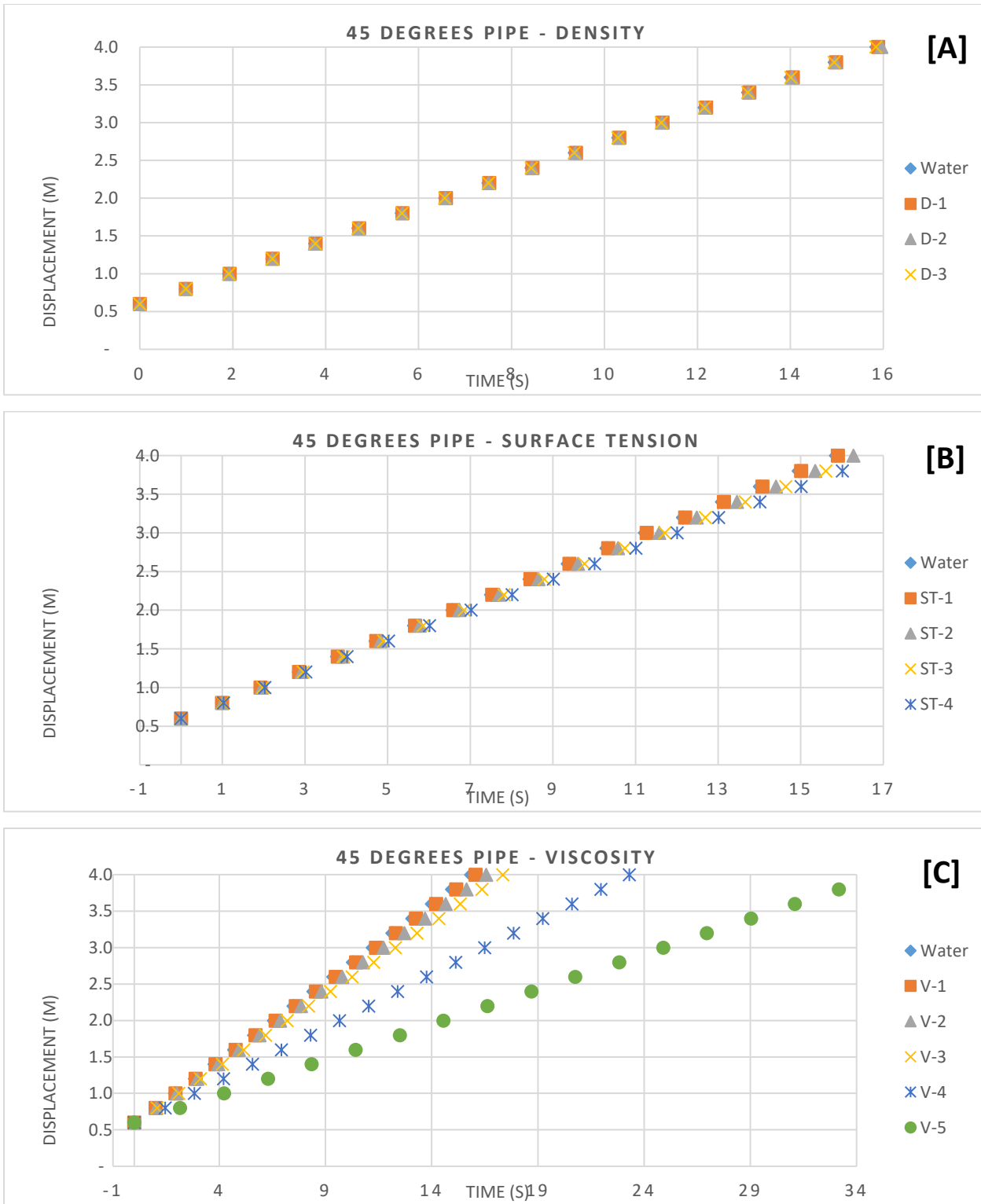

Figure 4.13: Disp.-Time plot for a 30^{O} inclined pipe showing the effects of density [A], surface tension [B], & viscosity [C]

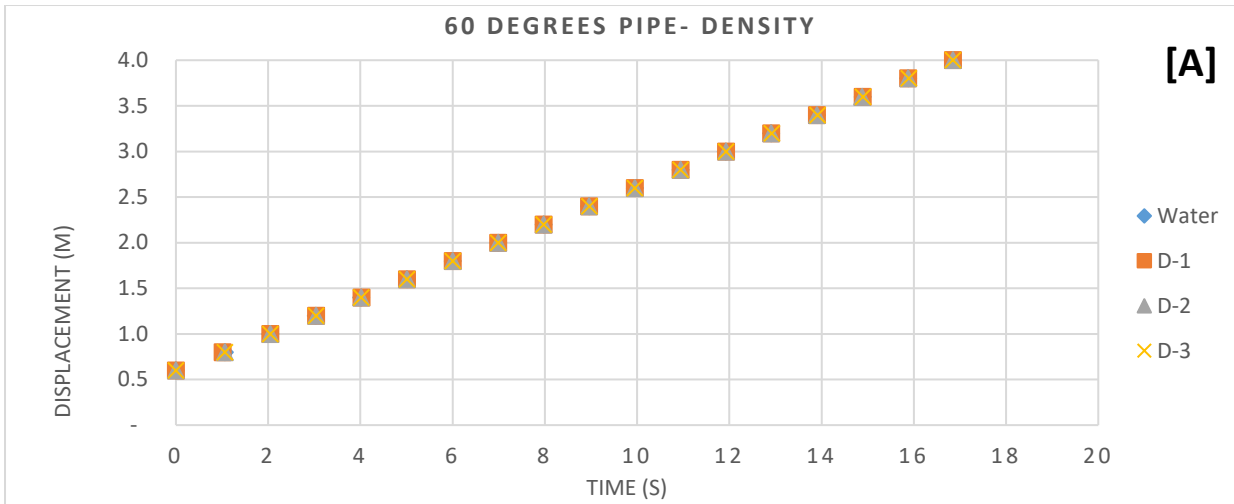

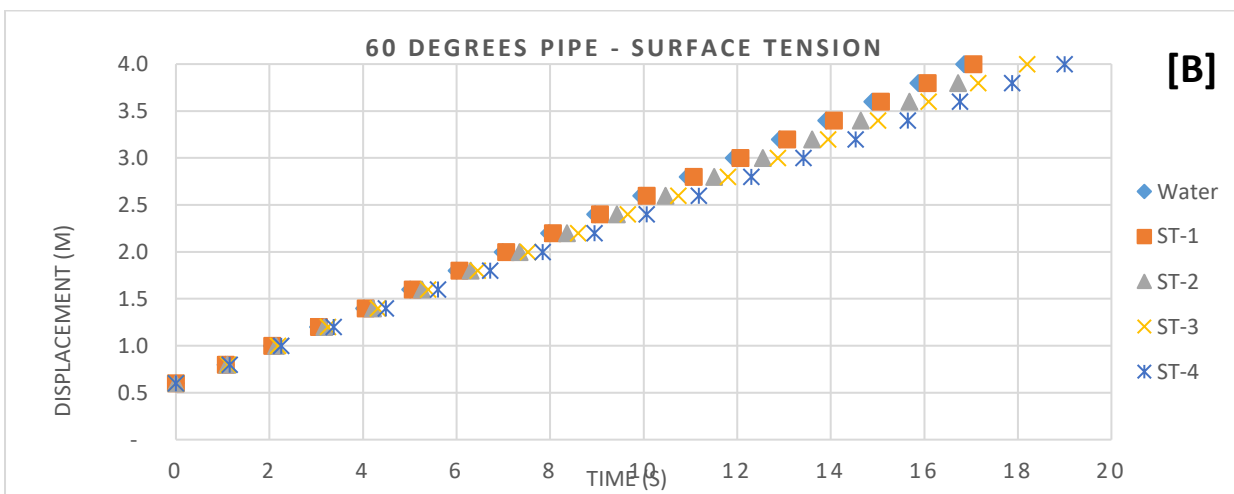

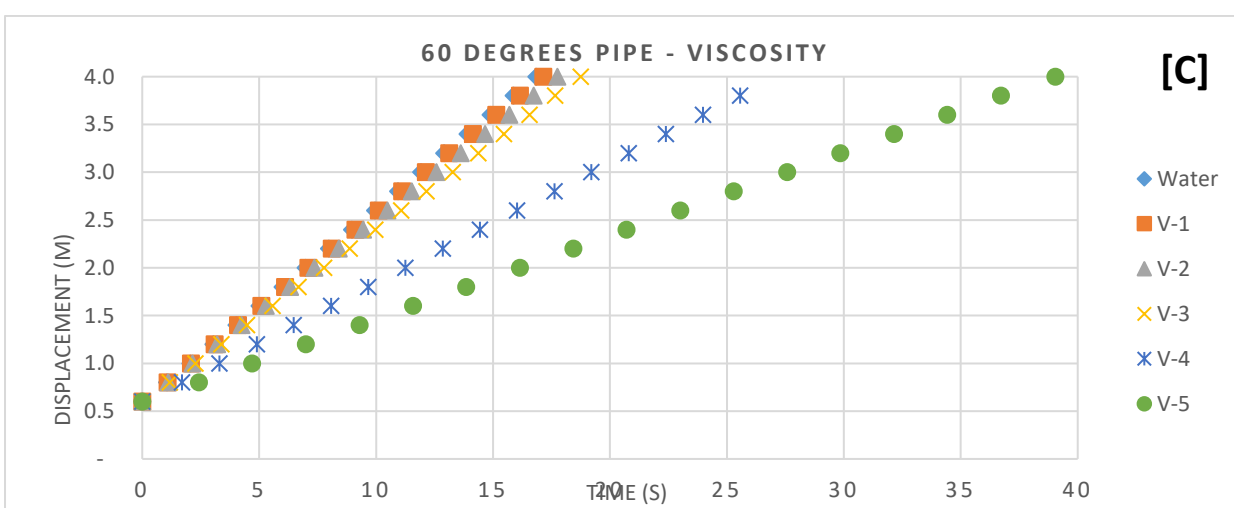

Figure 4.14: Disp.-Time plot for a 30^{O} inclined pipe showing the effects of density [A], surface tension [B], & viscosity [C]

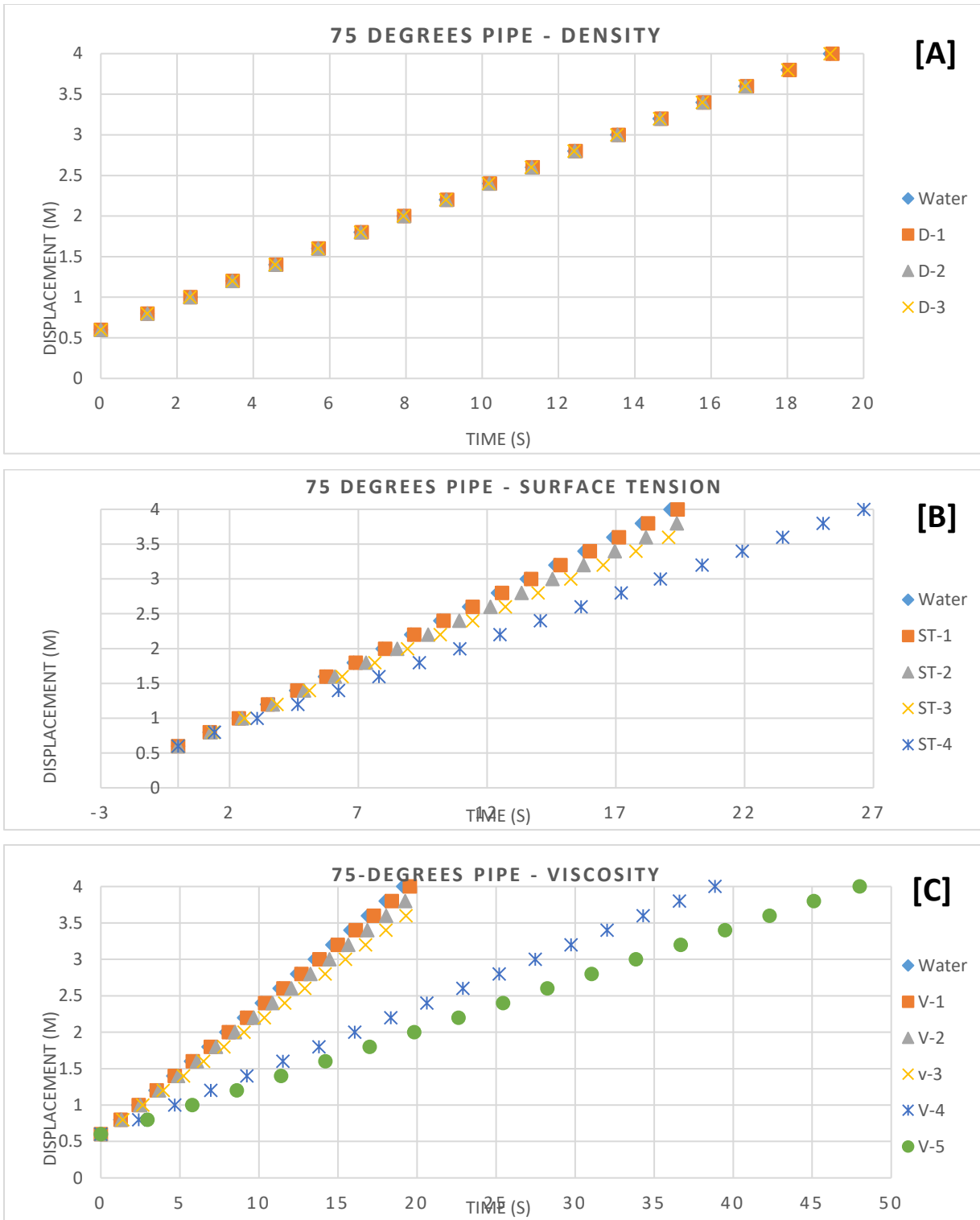

Figure 4.15: Disp.-Time plot for a 30^{O} inclined pipe showing the effects of density [A], surface tension [B], & viscosity [C]

The conspicuous effects of surface tension on pipe inclination as the raises towards vertical has shown that surface tension is much dependent on gravity, and surface tension is one of the key variables that influence change of flow regime. Viscosity on the other hand, from Figures 4.10C, 4.11C, 4.12C, 4.13C, 4.14C, and 4.15C shows a high influence on both the behaviour and velocity of the bubble at all inclinations starting from horizontal to vertical.

4.5.2 Bubble's Drift Velocity

The Taylor bubble is the underlying foundation of slug flow, and the drift velocity of a Taylor bubble is highly important being one of the components needed to calculate the slug's interface velocity. The drift velocity can be affected by the pipe geometry and the physical properties of the liquid, particularly the viscosity as well as the surface tension at the interface between the liquid phase and the gaseous phase. The simulation results have shown the drift velocity to go up as the inclination angle gradually increases from the horizontal, an action that increases the gravitational potential of the bubble resulting in a stronger driving force that enables the bubble to penetrate faster through the fluid. This potential driving force reaches a peak at an inclination angle where the gravitation potential is at its maximum value. The point where this peak value is attained can be anything between 30^0 and 50^0 inclinations depending on the liquid (as shown by the parabolic curves in Figures 4.16, 4.17, and 4.18). Further increase in inclination leads to a reduction in the area available for drainage. Consequently, resistive forces for the bubble to penetrate effectively into the liquid are created, thereby reducing the drift velocity, this leads to a Taylor bubble having the lowest velocity when the pipe is inclined at 90^O as reported by earlier researchers including Zukoski (1966) and Alves (1992). The Taylor bubble drift velocity is relatively low in a vertical pipe because of the buoyancy force acting on the bubble. In a vertical pipe, the buoyancy force of the bubble is directed opposite to the direction of flow. This causes the bubble to rise slowly, while the liquid flows downwards at a faster rate.

4.5.2.1 Effects of Density

As it has been observed in the previous section, difference alone has little or no effect on both the shapes of the bubble and its flow profile. Thus, liquids Water, D-1, D-2, and D-3

are all expected to behave very much like water as shown in Figure 4.16, depicting a parabolic curve on how the bubble's potential rose from about 0.186 m/s at the horizontal position, reaching a maximum of 0.22 at 30^0. From this peak, the bubble loses its potential and falls to a low velocity of 0.179 at 75^0. This is approximately the case for all Water, D-1, D-2, D-3, and water. Density effects on multiphase flow are only prominent in liquid-liquid systems where slight density differences can lead to density stratification. However, in gas-liquid multiphase flow with a density difference of almost 1000 kg/m^3, the effects of density become hardly noticeable.

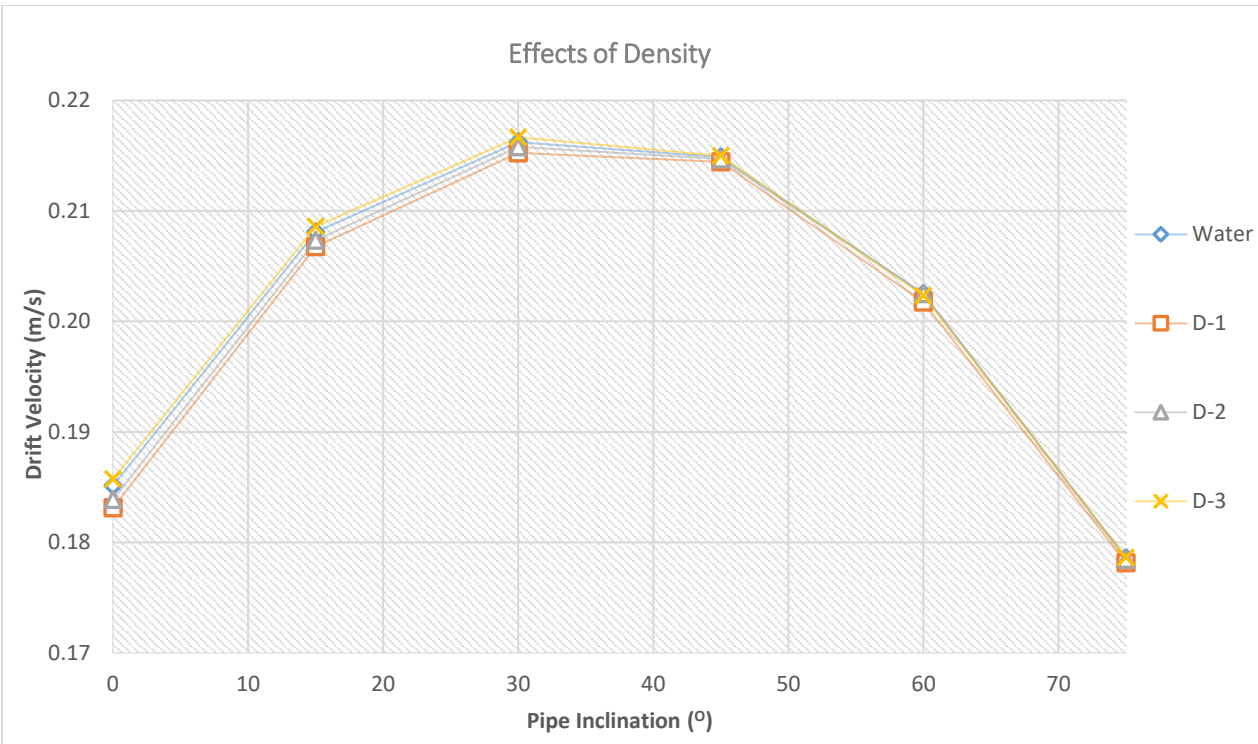

Figure 4.16: Effects of density on the drift velocity of a Taylor bubble

4.5.2.2 Effects of Surface Tension

The effects of surface tension on drift velocity seem to be negligible when the pipe is in a horizontal position and at lower angles of inclination. An increase in the pipe's inclination angle leads to a larger drainage area for the liquid and increases the bubble's gravitational potential. Thus, increasing the drift velocity. The behaviour of the bubbles at inclinations less than 30^0 appears to be identical for all the liquids tested, Water, ST-1, ST-2, ST-3, and

ST-4 as shown in Figure 4.17. 30^0 inclination is the point at which the drift velocity attains its maximum speed, and from this point, the velocity decreases and each of the liquids exhibits a unique behaviour. Thus, a decrease in surface tension has increased the frontal area of contact with the pipe walls leading to an increase in frictional drags that eventually lowers the bubble velocity, as particularly observed with liquids ST-3 and ST-4.

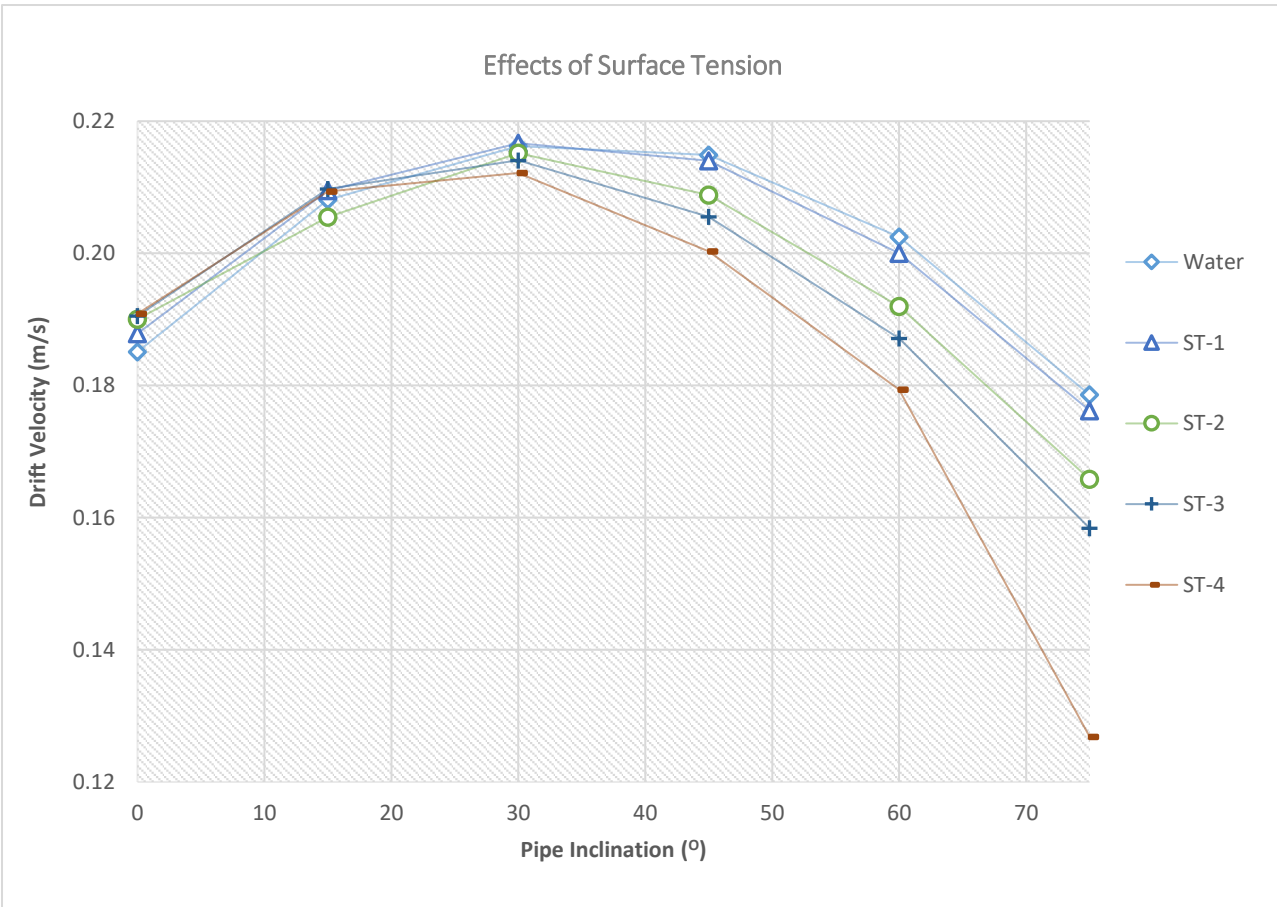

Figure 4.17: Effects of surface tension on the drift velocity of a Taylor bubble

4.5.2.3 Effects of Viscosity

Taylor bubble drift velocity for an inclined viscous flow is found to display a similar convex parabolic trend with respect to the angle of inclination. The velocity goes up as the inclination angle increases until a maximum is reached, and then it starts dropping to its lowest value (for vertical flow). However, the simulation results have shown that the attained maximum value range depends on the viscosity of the liquid. Low viscous liquids

such as Water, V-1, V-2, and V-3 follow a neat parabolic curve attaining maximum velocities in the regions around 30^0 to 45^0 pipe inclination as shown in Figure 4.18. However, highly viscous liquid such as V-4 and V-5 quickly attains maximum velocities at regions between 15^0 and 30^0 and the velocity immediately begins to reduce afterward on a slower decline.

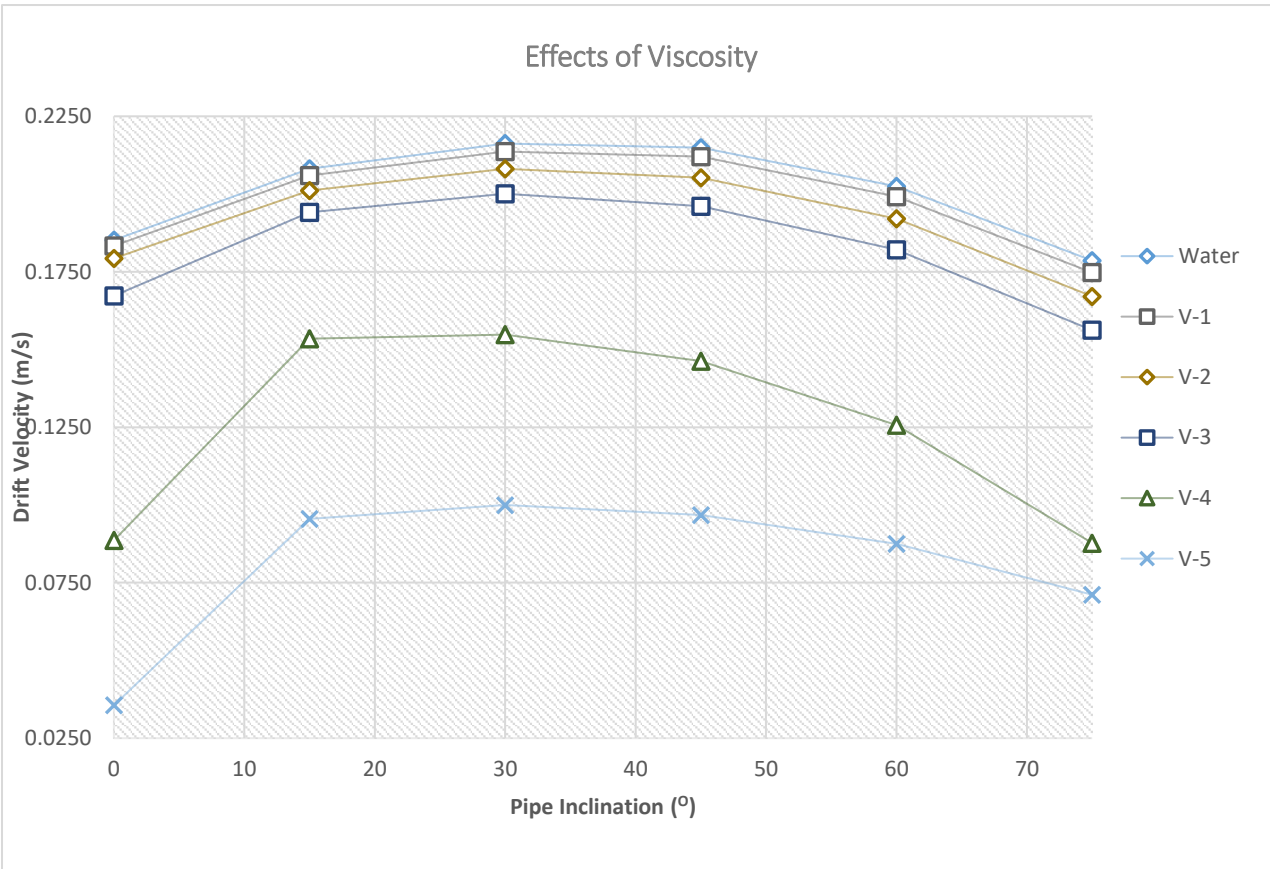

Figure 4.18: Effects of viscosity on the drift velocity of a Taylor bubble

In a nutshell, it can be said that the bubble speed is less dependent on inclination for viscosity-dominated conditions, as slow drainage of fluid was constantly observed around the bubble nose. Similarly, on a horizontal pipe, the simulation has revealed that the drift velocity decreases over a short period of time along the pipe shown in Figure 4.19, this behaviour can be attributed to the increased frictional losses which become higher when the height of the liquid layer beneath the bubble increases. It can be likened to the tube draining

experiment in the literature, using the same fluid in tubes of decreasing diameter, where a certain smaller size will not drain, i.e. the bubble velocity is zero in the horizontal tube. Nevertheless, an almost steady constant velocity along the pipe was observed for most of the liquids at all inclinations as depicted by Figures 4.20, 4.21, 4.22, 4.23, and 4.24.

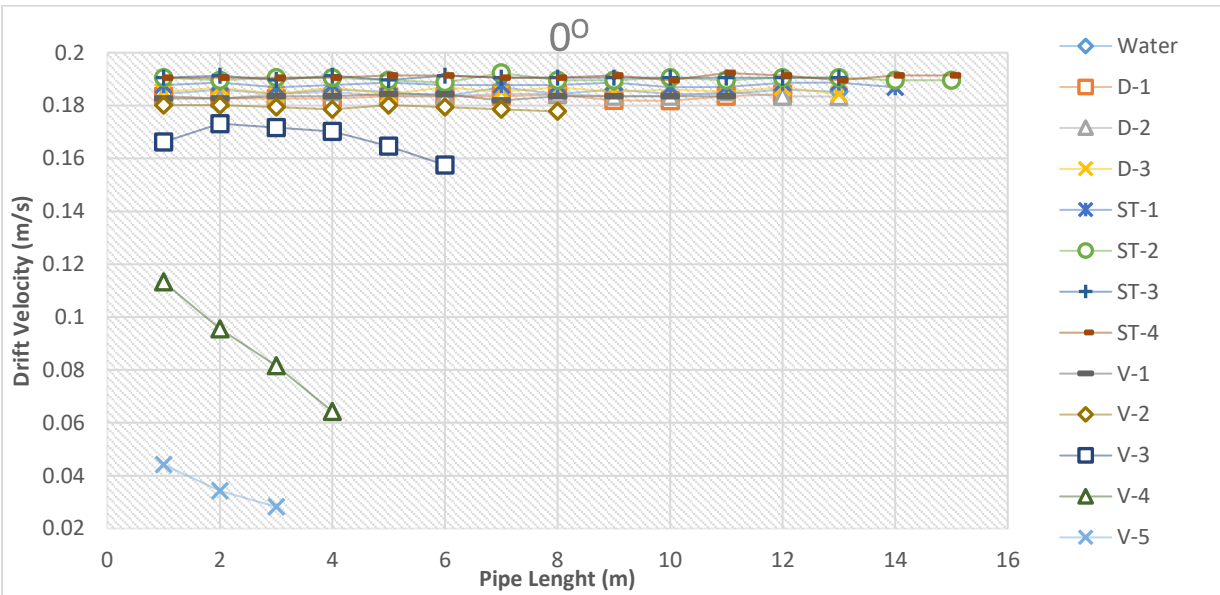

Figure 4.19: Drift velocity of a Taylor bubble in a horizontal pipe

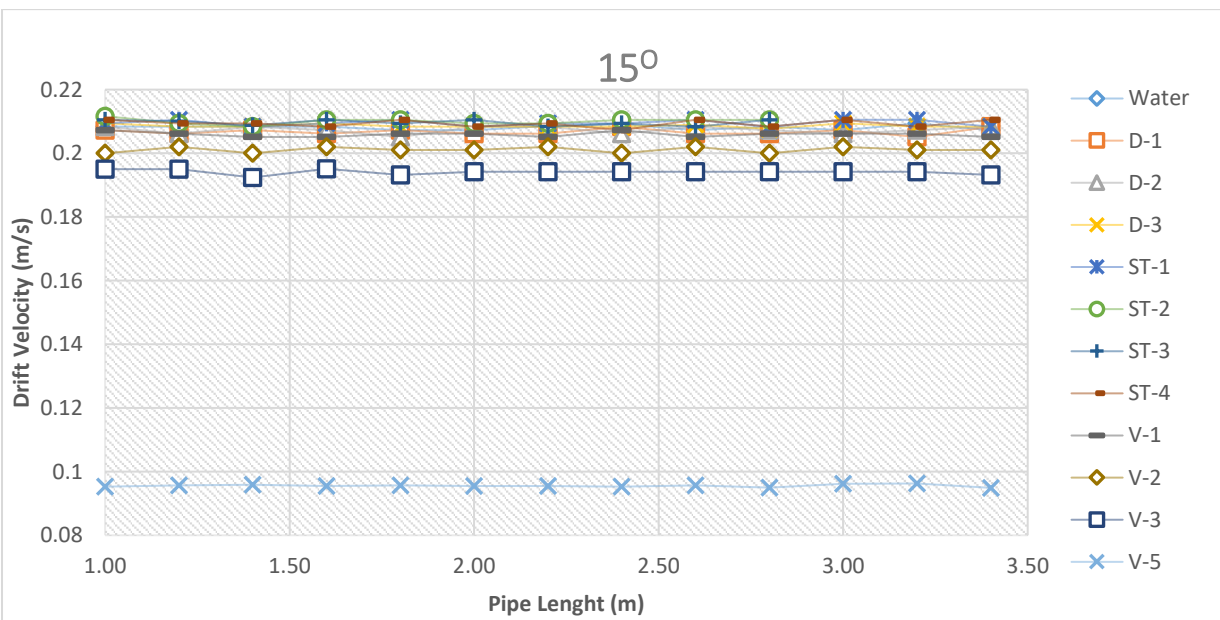

Figure 4.20: Drift velocity of a Taylor bubble in a pipe inclined at 15°

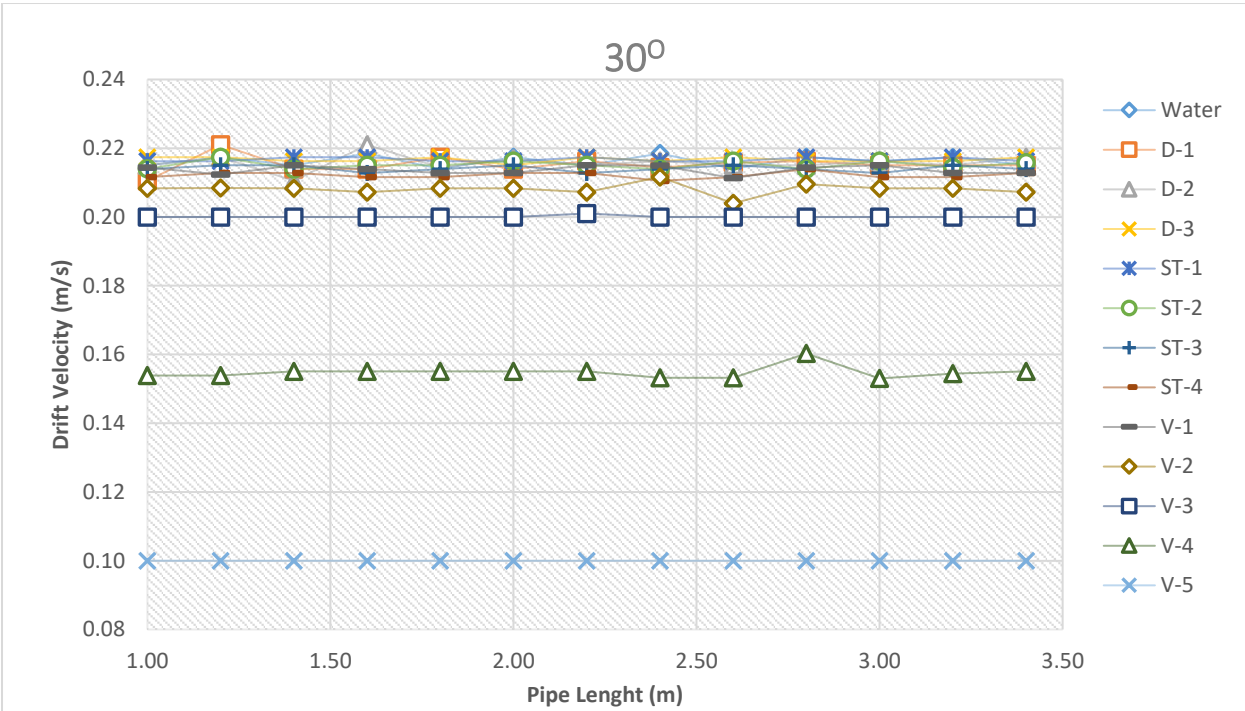

Figure 4.21: Drift velocity of a Taylor bubble in a pipe inclined at 30^{O}

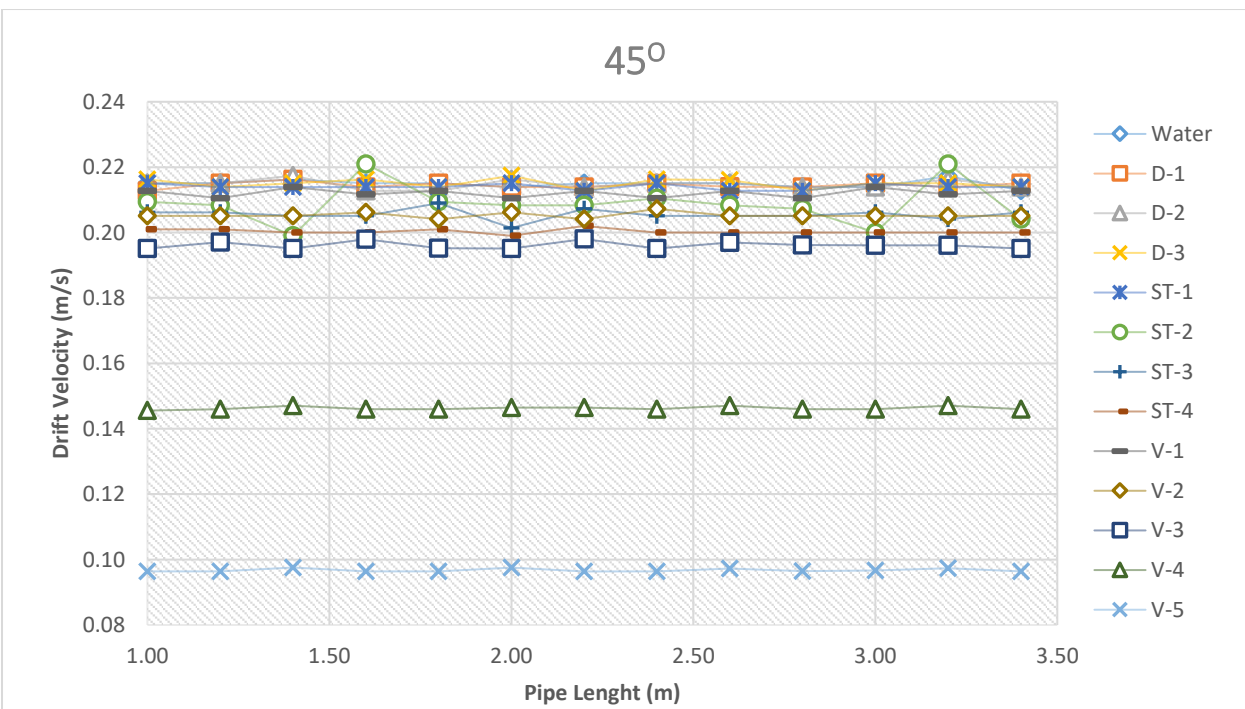

Figure 4.22: Drift velocity of a Taylor bubble in a pipe inclined at 45^{O}

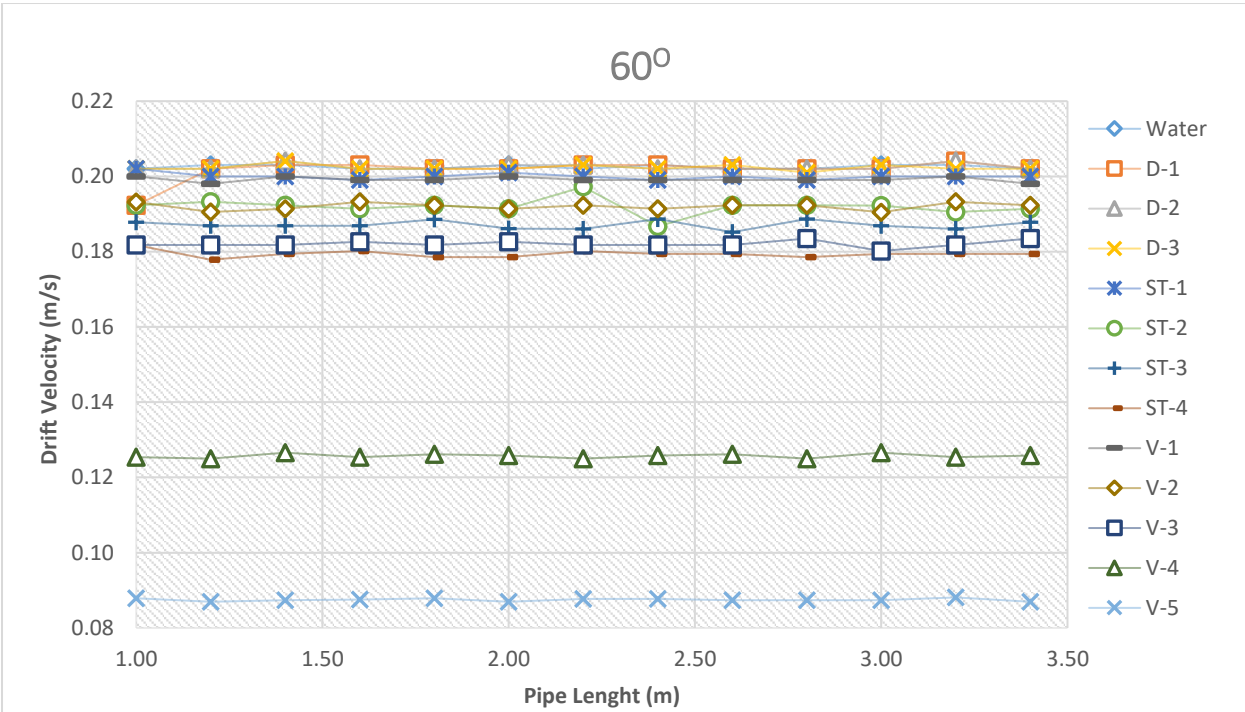

Figure 4.23: Drift velocity of a Taylor bubble in a pipe inclined at 60^{O}

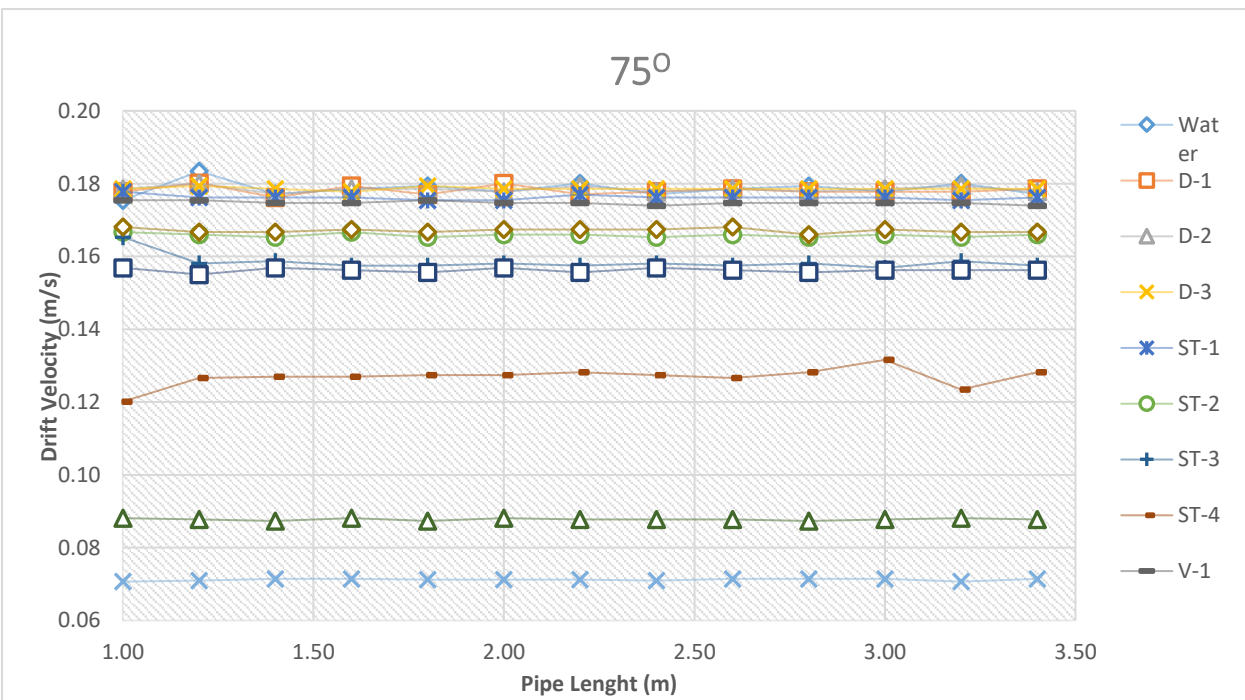

Figure 4.24: Drift velocity of a Taylor bubble in a pipe inclined at 75^{O}

4.5.3 Dimensionless Analysis

Multiphase flow parameters are usually analysed in terms of dimensionless numbers for more generality and applicability. Most common among these dimensionless numbers are the Froude Number, the Eotvoss Number, Viscosity Number and the Morton Number. These dimensionless groups are expressed in terms of the flow parameters and fluid properties including the liquid viscosity μ, surface tension σ, liquid density ρ_l, gas density ρ_g, pipe diameter D, drift velocity U_B and acceleration due to gravity g.

- *Morton Number:* The Morton number is a dimensionless number that characterises the relative importance of buoyancy forces compared to viscous forces in a fluid flow. It is defined as the ratio of the buoyancy force to the viscous force:

$$Mo = \frac{g\mu_L^4(\rho_l - \rho_g)}{\rho_L^2\sigma^3} \tag{4.11}$$

  When the Morton number is small, it indicates that the viscous forces dominate over buoyancy forces, and the fluid flow is considered to be viscously dominated. On the other hand, when the Morton number is large, it indicates that buoyancy forces dominate over viscous forces, and the fluid flow is considered to be buoyancy dominated.

- *Eotvoss Number*: The Eotvoss number is a dimensionless number that describes the relative importance of surface tension forces compared to gravitational forces in a fluid system. It is used to determine whether surface tension forces or gravitational forces dominate in a particular fluid system. It is defined as:

$$Eo = \frac{g(\rho_l - \rho_g)D^2}{\sigma} \tag{4.12}$$

  When the Eotvoss number is small, it indicates that gravitational forces dominate over surface tension forces, and the fluid behaviour is primarily governed by gravity.

On the other hand, when the Eotvoss number is large, it indicates that surface tension forces dominate over gravitational forces, and the fluid behaviour is influenced by surface tension effects.

- *Froude Number:* The Froude number is a dimensionless number that describes the ratio of inertial forces to gravitational forces in a fluid. It is defined as:

$$Fr = \frac{U_D}{\sqrt{gD\left(\frac{\rho_l - \rho_g}{\rho_l}\right)}} \tag{4.13}$$

The Froude number helps to determine whether a fluid flow is dominated by inertial forces (high Fr) or gravitational forces (low Fr). When the Froude number is less than 1 (Fr < 1), it indicates that the flow is subcritical and dominated by gravity, resulting in tranquil or subcritical flow conditions. When the Froude number is greater than 1 (Fr > 1), it indicates that the flow is supercritical and dominated by inertial forces, resulting in rapid or supercritical flow conditions.

- *Viscosity Number:* The viscosity number is a dimensionless number that describes the ratio of inertial forces to viscous forces in a fluid. It is used to characterize the behaviour of viscous flows, particularly the flow of non-Newtonian fluids. The viscosity number is defined as:

$$N_{vis} = \mu\left(gD^3(\rho_l - \rho_g)\rho_l\right)^{-0.5} \tag{4.14}$$

Among the above-listed dimensionless groups, only the Froude number depends on the drift velocity. And therefore, the Froude number is used in carrying out further analysis in this work and also comparison with available data from previous works. Figures 4.25, 4.26, and 4.27 shows a plot of the Froude number *Fr* against the pipe's angle of inclination.

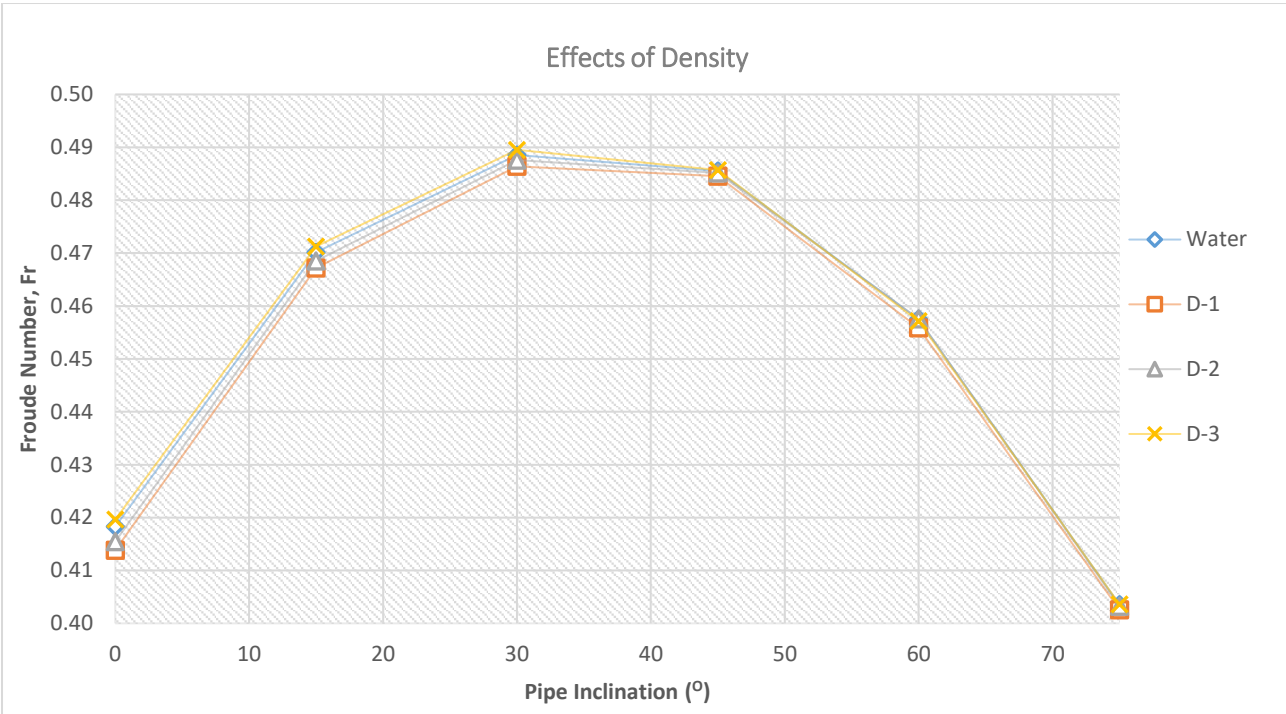

Figure 4.25: Effects of density on the Froude Number of a Taylor bubble

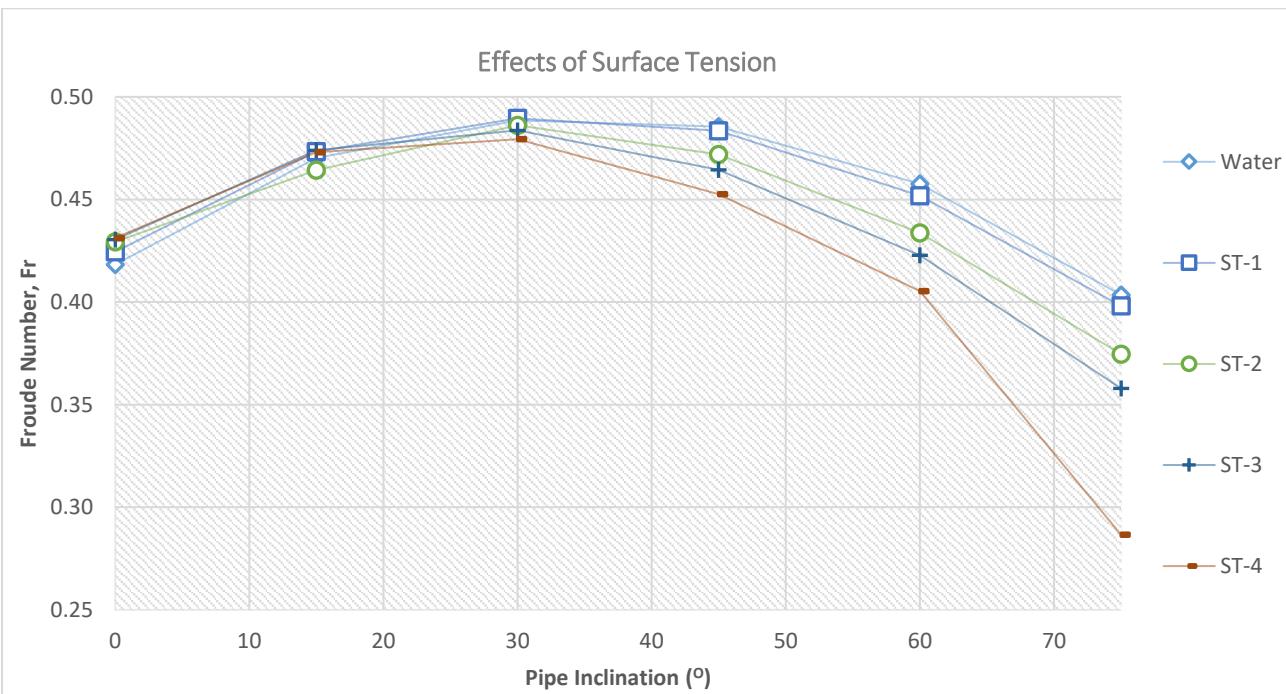

Figure 4.26: Effects of surface tension on the Froude Number of a Taylor bubble

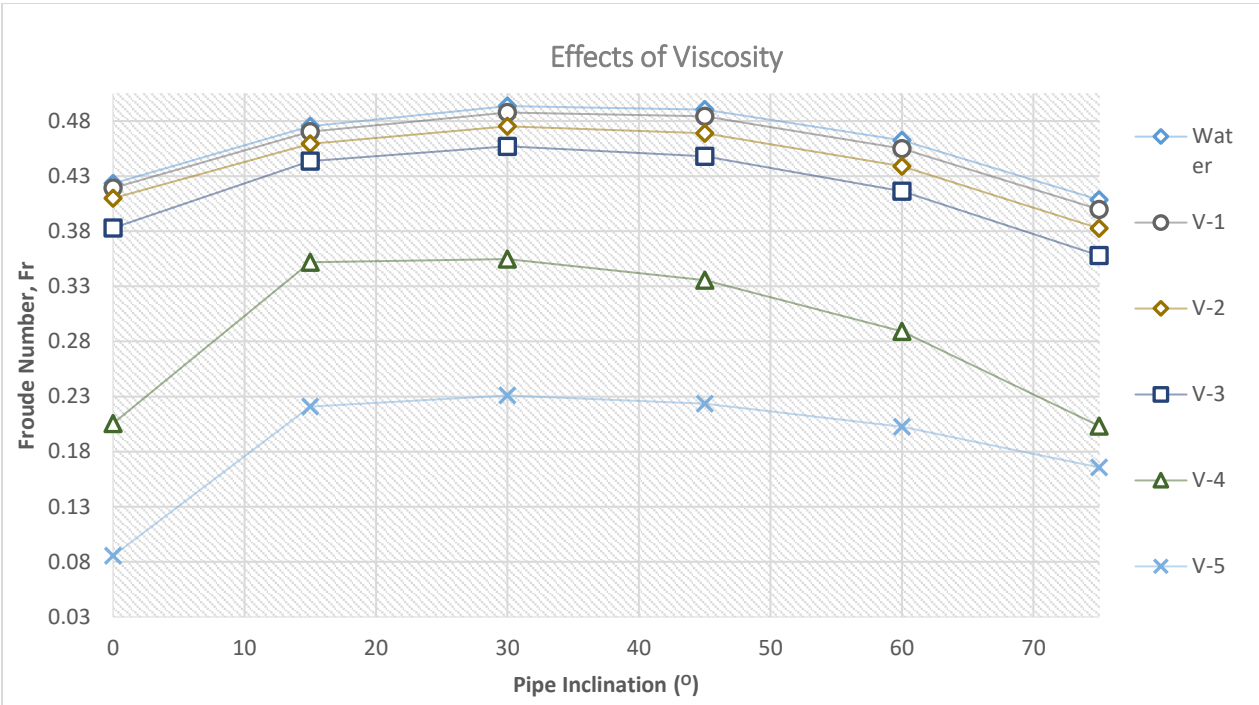

Figure 4.27: Effects of viscosity on the Froude Number of a Taylor bubble

The plotted values of Froude number against pipe inclination are similar to the plotted values of drift velocity against pipe inclination. Therefore, the generated simulation data can be safely used to develop a unified drift velocity correlation for a Taylor bubble and be used in slug flow predictions.

4.6 Validation of Simulation Results

Although some of the simulations carried out in this work cannot be exactly replicated in the real world, especially where simulated liquids were used to have a single property of the liquid modified, simulation results from air-water flows can be validated by comparing with previous research works. A lot of work has been carried out to study the drift velocity of a Taylor bubble in different pipe sizes as a function of pipe inclination. Some of the notable works include Zukoski (1966), Bendiksen (1984), and Alves (1993). Experimental results from these works have been generalised to obtain the drift velocity in the form of a dimensionless Froude number as a function of pipe inclination.

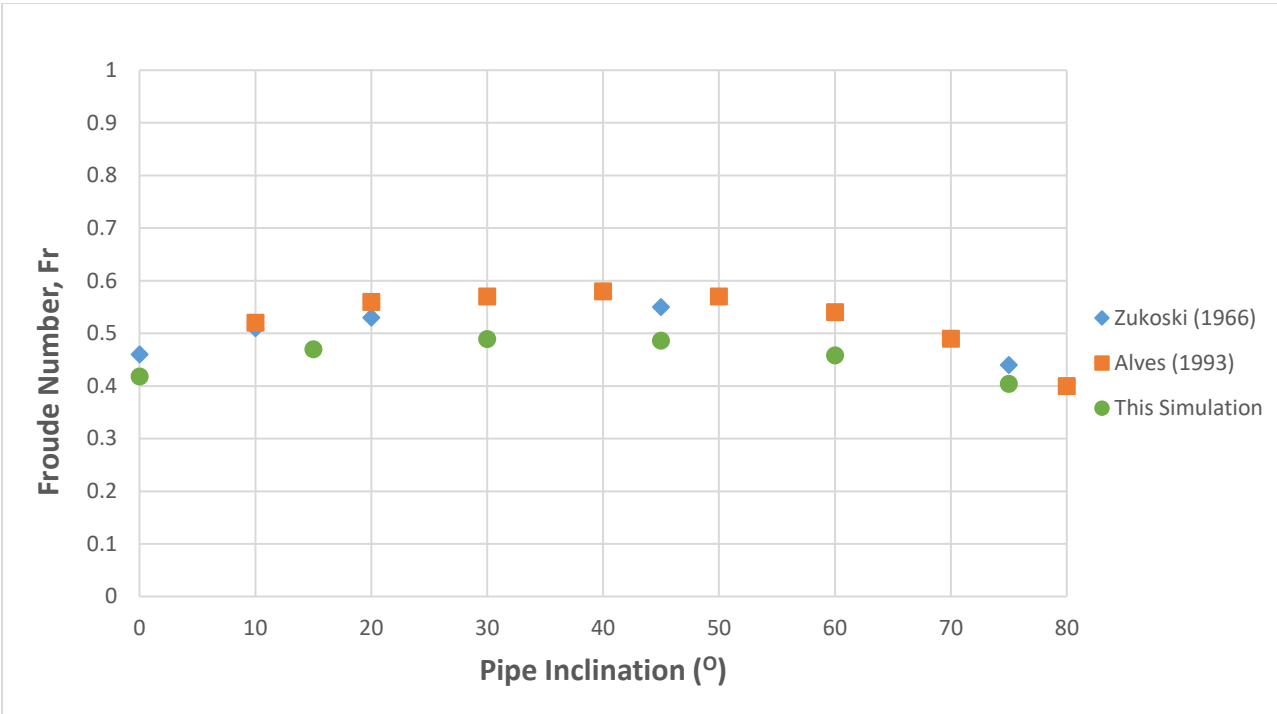

Figure 4.28: Froude number vs. pipe inclination comparison of the CFD simulation result with experimental results for air-water Taylor bubble flow

Figure 4.28 shows plotted values of the Froude number vs. pipe inclination from the works of Zukoski (1966), Alves (1993), and this simulation results for air-water Taylor bubble flow. The 2D simulation has perfectly captured the trend with accuracy levels from 86 to 95% at some points. The underestimation of the experimental results at some points (with up to 14% at 30^{O} inclination) can be attributed to the use of a two-dimensional geometry which simplifies the flow domain. Nevertheless, despite these limitations, the 2D simulations used in this work have provided very good and acceptable results as compared to experimental results.

4.7 Chapter Summary

In this chapter, CFD simulation with ANSYS Fluent was used to study the effects of viscosity, surface tension, and density on the behaviours of an elongated gas bubble in horizontal and upwards inclined pipes up to 75° in a 2D pipe. The simulation results have

shown distinguishing effects of the liquid properties on the Taylor bubble's velocity as it freely drifts in a stagnant pipe filled with different liquids. Liquid density has displayed little or no effect on the bubble. At the same time, surface tension only shows the effect when the pipe's inclination reaches 45°. Viscosity, however, has been shown to play a key role in the behaviour of the bubble, at all inclinations. With both drift velocity and its generalized form of dimensionless quantity, the Froude number rises steadily until a maximum velocity is attained at a range between 25° and 50°, depending on the liquid properties. As the pipe inclination increases, the drift velocity increases and peaks at an inclination around 30-50° then it decreases again (refer to Figures 4.16 to 4.18). For the air-water system, a dimensionless drift velocity plotted against pipe inclination was compared with experimental results from Jukoski (1966) and results from the correlation developed by Alves (1993), a very good match was obtained between the data set produced by the simulation and both the experimental correlation data set.

Chapter 5

Experimental Data and Analysis

This chapter focuses on the results obtained from the experimental work, including the flow data acquisition process, descriptive analysis of the flow regimes observed from flow visualisation techniques, pressure drop, liquid holdup and slug frequency analysis. Due to laboratory constraints, the simulated work in this research could not be experimentally replicated. The experimental rig was initially designed for a continuous gas-liquid flow, not a single bubble flow. Also, the laboratory ceiling height could only accommodate a maximum of 15^{O} upward inclination.

Therefore, a different set of experimental campaign was deigned to study the effects of liquid properties, on the above-mentioned hydrodynamic parameters of multiphase flow. All the experiments were performed with atmospheric pressure at the end of the pipe and ambient temperature. The objective of the experimental campaign is to improve the understanding of the effects of viscosity and surface tension in multiphase flow behaviour.

5.1 Physical Properties of the Fluids Used

The main experiments were carried out with three different liquids whose properties are described in Table 6.1. The experimental work carried out follows the experimental matrix presented in Table 3.3.

Table 5.1 Fluid properties of the working fluids for the experiment.

Fluid	**Air**	**Tap water**	**Surfactant Solution**	**Glycerol Solution**
Density at 20°C [room temp.]	1.22 kg/m3	999 kg/m3	1,017.60 kg/m3	1,155.40 kg/m3
Viscosity at 20°C [room temp.]	0.018 mPa·s	0.98 mPa·s	1.002 mPa·s	7.622mPa·s
Surface tension at 20°C [room temp.]	-	72.0 mN/m	36.76mN/m	66.06mN/m

5.2 Flow Regimes Data Collection and Visualisation

Flow regimes are very important elements of research in multiphase flow systems, they play vital roles in understanding the hydrodynamic behaviour of flow, characterisation of multiphase flow, and the estimation of pressure drop. Thus, flow regime investigations provide process system designers and operators the opportunity to predict and choose the proper flow pattern that would help them achieve the intended operational objective, such as the minimisation of pressure losses during multiphase flow transportation through long-distance pipelines.

In this study, flow regime data for air-water, air-glycerol solution, and the air-surfactant solution was collected in the form of still pictures and videos for horizontal (0°) pipe and upward inclined pipe at 15O. The flow regime data collection was achieved using a visualisation system that includes a highspeed camera, a two-way LED lighting system, and a computer system with a high-capacity data storage drive. More details about specifics related to the visualisation system were discussed in Chapter 3.

5.3 Analysis of Flow Regimes Observed

The high-capacity data storage drive provided hundreds of hours of video recordings which were critically analysed using video motion analysis methods such as slow-motion playback, frame-by-frame playback, instant replay, etc. Classification of most of the flow regimes was easy because their specific morphology was “self-evident”, the flow regime was seen to have changed with changing inclination angle and test liquids. The flow regimes observed include stratified smooth flow, stratified wavy flow, stratified frothy, elongated bubble flow, slug flow, bubbly flow, and churn flow (refer to Figure 5.8 for the plot of these in a flow regime map).

Stratified smooth flow: This flow regime features a tranquil motion of the liquid and gas phases separated by a distinct smooth layer with minimal mixing between the two phases. In stratified smooth flow, a well-defined interface separates the liquid phase and the gas phase. The liquid phase occupies the lower portion of the pipe, while the gas phase occupies the upper portion. Each phase retains its distinct identity and flows independently within its respective regions.

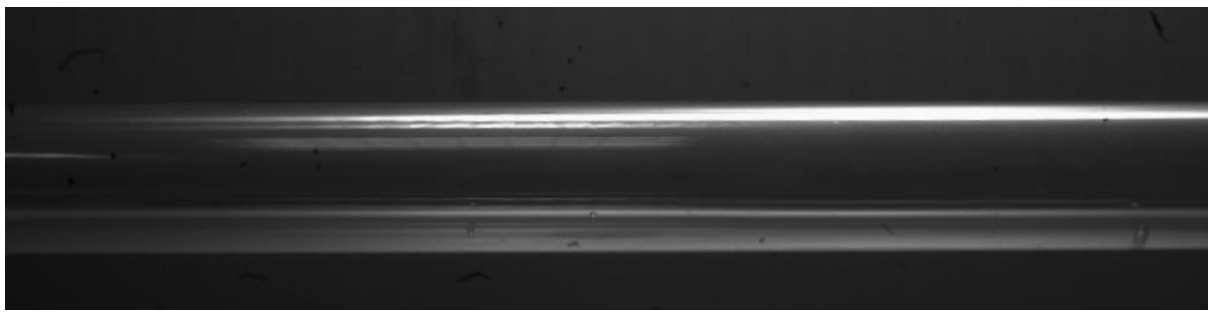

Figure 5.1: Stratified smooth flow observed in air-water flow in a horizontal pipe at U_{SG} = 0.5 m/s and U_{SL} = 0.1 m/s

In smooth stratified flow, the combined effects of gravity and density variation in the vertical direction cause the lighter fluid to always flow above the heavier fluid. This separation of layers under the influence of gravity usually occurs in horizontal or near-horizontal pipe flows at very low gas and liquid velocities. The fluids are not only not subjected to gravitational force as they flow, but other forces such as static forces, buoyancy, viscosity, density, and surface tension. These forces are mostly dominant in the liquid phase, while dynamic components like frictional and inertia forces increase progressively and become dominant at higher gas flow rates. This flow regime is relatively stable and exhibits little or no interfacial instabilities or fluctuations. The interface between the liquid and gas phases remains relatively constant along the pipe length, except for minor waviness or ripples caused by small disturbances.

In this study, the stratified smooth flow was only observed in horizontal pipe at the lowest superficial liquid velocity U_{SL} = 0.1(m/s) and 0.2 (m/s) with a corresponding low-to-medium superficial gas velocities U_{SG} = 0.5 to 2.5 (m/s) depending on the liquid properties as shown in the flow regime map in Figure 5.8. The flow is relatively calm and the interface between the two phases remained smooth through the gas increase.

Stratified wavy flow: This type of flow pattern is characterised by a distinct interface between a continuous liquid phase and a continuous gas phase, with the interface exhibiting wavy or undulating behaviour. These waves are typically caused by interfacial instabilities or disturbances, such as flow rate variations. Various shapes and sizes of waves were

observed, ranging from small ripples to large amplitude waves propagating downstream along the pipe. The propagation speed of the waves depends on the flow conditions and the properties of the fluids. The flow structure consists of alternating regions of liquid-rich and gas-rich regions. The liquid phase tends to accumulate in the troughs of the waves, while the gas phase accumulates in the crests.

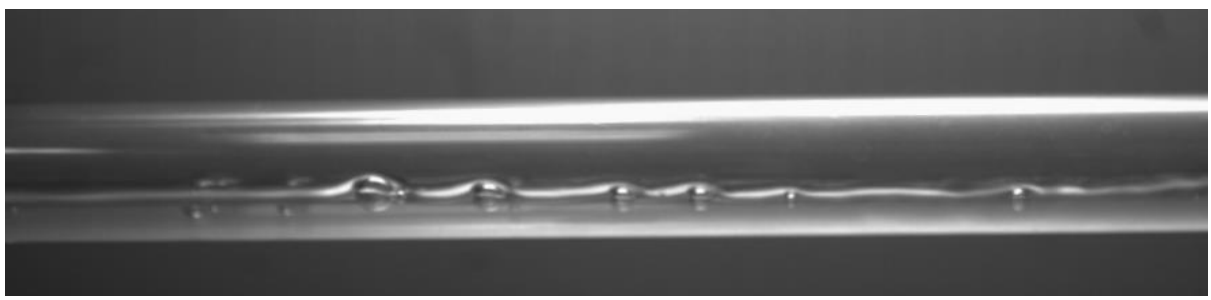

Figure 5.2: Stratified wavy flow observed in air-water flow in a horizontal pipe at U_{SG} = 2.0 m/s and U_{SL} = 0.1 m/s

In this work, the stratified wavy flow was observed in both the horizontal and the inclined pipe flow orientations at different flow conditions depending on the liquid properties. For air-water flow in a horizontal pipe, the stratified wavy flow was the second most dominant flow pattern after slug flow. The flow regime was observed at gas superficial velocities from 1.5 m/s to 4 m/s with various liquid superficial velocities ranging from 0.1 m/s to 0.7 m/s. However, when the flow was changed to an inclined orientation, the stratified wavy flow was only observed at high gas superficial velocity with a corresponding very low liquid loading. Stratified wavy flow was also spotted at different flow orientations with air-surfactant solution flow, and in the horizontal pipe with air-glycerol flow.

Stratified frothy flow: This flow pattern characterised by the coexistence of a continuous liquid phase, a continuous gas phase, and a dispersed phase of small gas bubbles within the liquid phase. There is a distinct interface between the liquid phase which occupies the lower portion of the pipe, and the gas phase which occupies the upper portion of the pipe. The liquid-gas interface is relatively smooth and stable. The presence of the gas bubbles forms a froth layer at the top of the liquid phase, adjacent to the liquid-gas interface. The froth layer

consists of a mixture of gas bubbles and liquid, with a higher gas volume fraction compared to the liquid phase below. The thickness of the froth layer was observed to be affected by the gas flow rate. In this work, the froth was formed mainly due to the presence of surfactants, hence stratified frothy flow was observed with air-surfactant solution multiphase flow in a horizontal pipe at low liquid superficial velocity and medium to high gas superficial velocity.

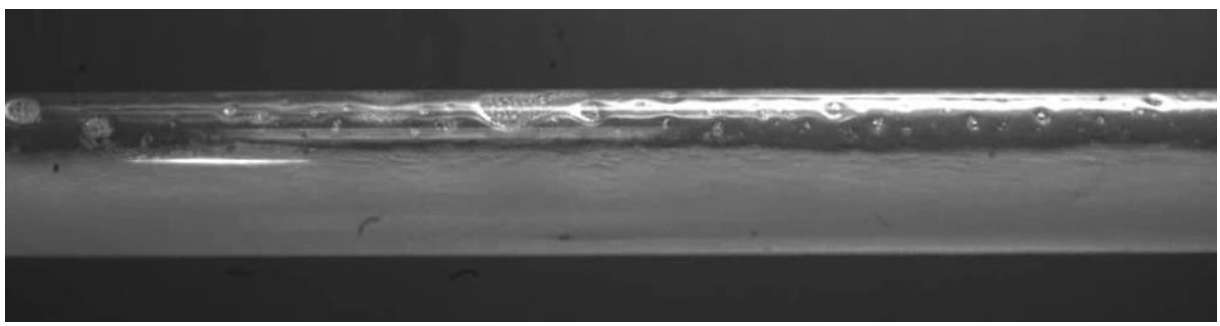

Figure 5.3: Stratified frothy flow observed in air-surfactant solution flow in a horizontal pipe at U_{SG} = 2.0 m/s and U_{SL} = 0.1 m/s

Bubbly flow: In this flow regime, there is a coexistence of small gas bubbles randomly dispersed in a continuous liquid phase. The gas bubbles vary in size and shape depending on the flow conditions. In between the gas bubbles, a thin liquid film is formed, coating the pipe walls or any solid surfaces present. The liquid film separates adjacent gas bubbles and provides a continuous liquid phase. The gas bubbles undergo complex dynamics, deforming, coalescing, break up and moving independently through the liquid phase. The bubbles rise due to buoyancy forces, and their motion creates a slug-like or plug-like flow pattern. The liquid phase flows around and between the bubbles, with intermittent slugs or plugs of gas phase.

Bubbly flow was only observed in two flow orientations, inclined air-water flow, and inclined air-surfactant solution flow at very high liquid superficial velocity, with a corresponding low to medium gas superficial velocity.

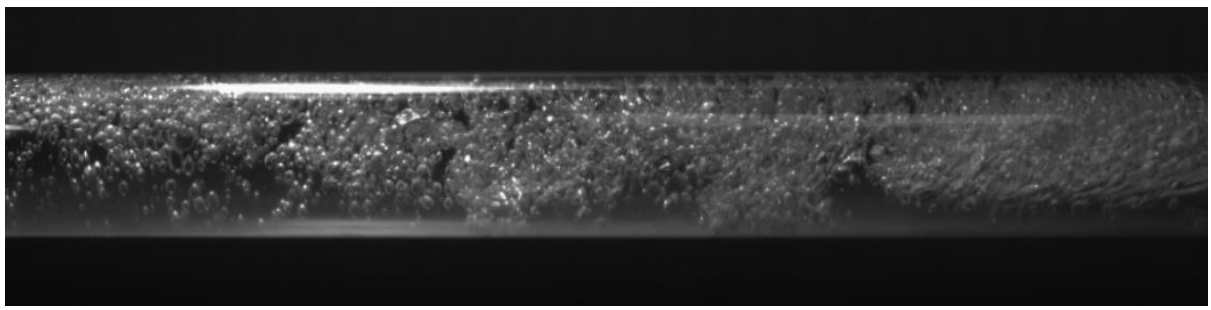

Figure 5.4: Bubbly flow observed in air-water flow in inclined pipe at U_{SG} = 1.0 m/s and U_{SL} = 0.8 m/s

Elongated bubble (EB) flow: This flow regime is characterised by the presence of distinctive elongated or cylindrical-shaped gas bubbles dispersed within a continuous liquid phase. These elongated bubbles arise due to different mechanisms, such as shear forces, and surface tension effects. The behaviour and characteristics of elongated bubble flow depend on factors such as the gas and liquid flow rates, bubble size and shape, and the properties of the fluids involved. Elongated bubble flow shares similarities with both plug flow and slug flow, yet they are distinctly different with respect to their velocities and effects on pressure drop (Hanyang and Liejin, 2016).

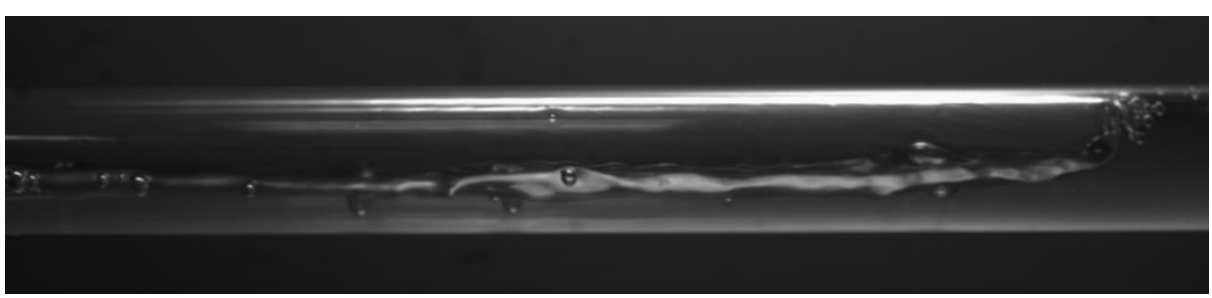

Figure 5.5: Front half of an elongated bubble observed in air-glycerol solution flow in inclined pipe at U_{SG} = 1.0 m/s and U_{SL} = 0.2 m/s

An elongated bubble spreads wider and floats higher above the liquid unlike plug flow where plugs of the dispersed phase cover a large portion of the pipe, also the liquid phase under an elongated bubble is calm, which is in contrast with slug flow where a stream of turbulent and chaotic smaller bubbles are generated within the liquid phase and around the

bubble edges. In this study, the elongated bubble was observed in the inclined pipe at a combination of low gas superficial velocity with low to medium liquid superficial velocity.

Slug flow: This flow pattern is characterised by the presence of distinct large gas pockets (also known as Taylor bubbles), separated by intermittent liquid slugs. The liquid and gas phases are not well-mixed but rather exist as alternating slugs. The liquid slugs occupy most of the cross-sectional area of the pipe, while the gas bubbles are dispersed within the liquid phase. The length and frequency of the liquid slugs and gas bubbles vary depending on the flow conditions, fluid properties, and pipe geometry.

The formation of slug flow typically arises from the difference in densities between the gas and liquid phases, as well as the flow rates of each phase. When the gas flow rate exceeds a certain threshold, it pushes the liquid ahead, forming liquid slugs separated by gas bubbles.

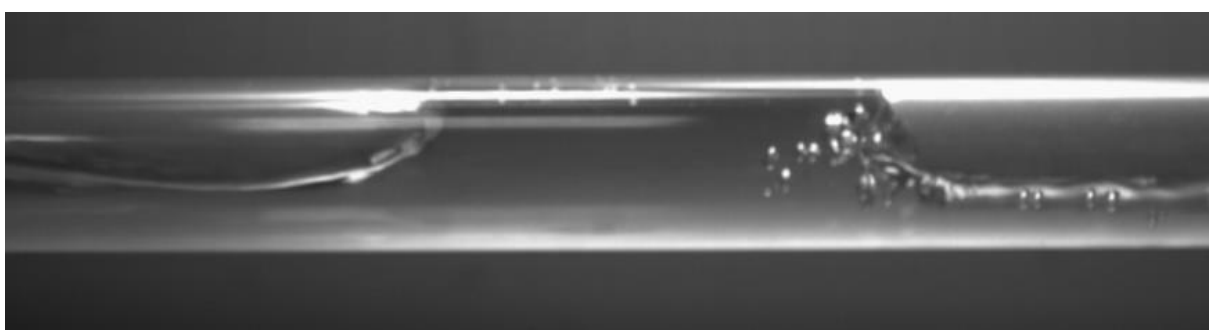

Figure 5.6: Slug flow observed in air-glycerol solution flow in a horizontal at U_{SG} = 2.0 m/s and U_{SL} = 0.3 m/s

In this experimental work, slug flow is one of the most prevalent flow regimes observed. It occurs in all pipe orientations, over a wide range of flow rates. The elongated gas bubbles in horizontal and inclined slug flows are asymmetric, usually travelling at the upper part of the pipe, unlike what happens in a vertical flow where slug flow features an axially symmetrical, bullet-shaped Taylor bubble. In horizontal flow, flow transition follows the following order: stratified smooth to stratified wavy and then onto slug flow.

The length of the gas slugs observed varies depending on gas and liquid flow rates as well as liquid properties. The frequency of slug formation and movement is influenced by the

flow conditions and can vary along the pipe length. The gas slugs in slug flow move at a relatively high velocity compared to the liquid phase. The slug velocity is primarily determined by the gas flow rate, liquid properties, and pipe geometry. The velocity difference between the gas slugs and the surrounding liquid phase contributes to the intermittent flow behaviour.

Churn flow: This flow pattern is characterised by the chaotic and intense mixing of gas and liquid phases. The bubbles are randomly distributed and do not form distinct slugs as in traditional slug flow. Instead, they are dispersed within the liquid phase and move intermittently along with the flow, creating a turbulent and agitated flow regime. The gas and liquid phases form a mixture with no distinct observable gas or liquid regions. The intense mixing leads to a high interfacial area and enhanced mass transfer between the phases. This flow regime was observed when there is a high gas-to-liquid flow rate ratio, the gas bubbles are continuously generated and dispersed within the liquid, creating a heterogeneous mixture. A churn flow regime was observed at a few points with high liquid and gas superficial velocities in inclined air-water flow and inclined air – surfactant solution flow.

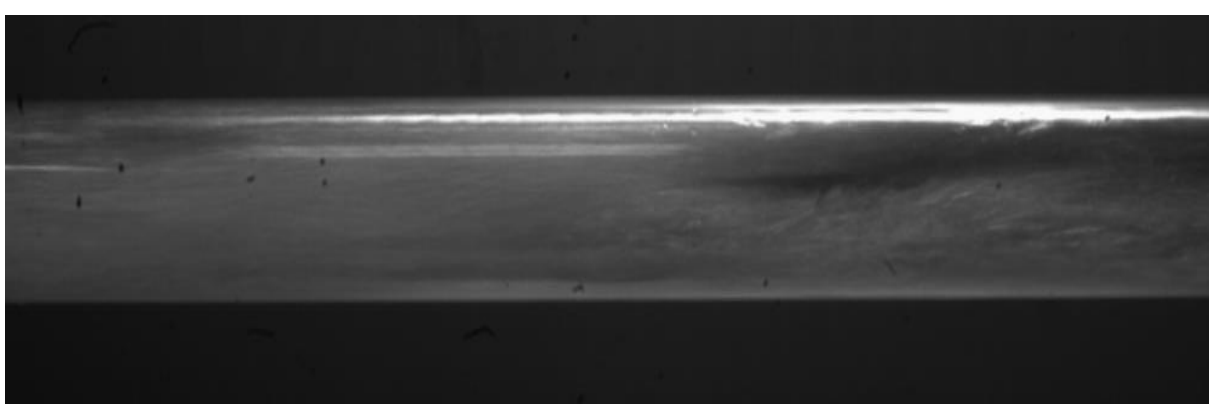

Figure 5.7: Churn flow in air-water flow in inclined pipe at U_{SG} = 4.0 m/s and U_{SL} = 0.8 m/s

5.4 Flow regime mapping

Flow regime mapping is a method used to classify and categorise the different flow patterns or regimes that occur in multiphase flow systems. It involves visually representing the transitions and boundaries between various flow patterns based on certain flow parameters

or characteristics. Flow regime mapping is particularly important in understanding and predicting the behaviour of multiphase flows, as different flow patterns can significantly affect the performance and efficiency of systems. By mapping the flow regimes, engineers and researchers can gain insights into the flow behaviour, pressure drops, heat transfer, and other important aspects of multiphase systems.

The flow regime map provides a visual representation of the different flow patterns that occur within the studied range of operating conditions. It helps identify the transition boundaries between different flow regimes and provides a reference for the expected behaviour of the multiphase flow system under specific conditions. The flow regime maps developed in this work are based on the experimental visual data in the form of videos & still pictures collected for the two-phase gas-liquid flow through a 19 mm diameter pipe at 0^O and 15^O inclinations using three different liquids. The flow regimes appearing at the various flow conditions are a function of the gas and liquid superficial velocities, various other parameters such as pressure drop, liquid holdup, and slug frequency are measured for each data point.

The collected data is then plotted on a flow regime map using a two-dimensional graph. The axes of the graph represent the relevant flow parameters, superficial liquid velocities (U_{SL}) on the vertical axis and superficial gas velocity (U_{SG}) on the horizontal axis. The structure of each flow regime depends on the interaction between various forces, including gravity, buoyancy, friction, inertia, and cohesive forces. These forces act differently at different pipe inclinations. Gravitational forces, for example, increase with increasing pipe inclination, until it eventually attains its highest magnitude at the vertical orientation. Similarly, frictional forces increase with an increase in liquid viscosity, while cohesive forces reduce with the addition of surfactants to the liquid. The changes in these forces led to flow regime transitions and a flow regime map developed as shown in Figure 5.8.

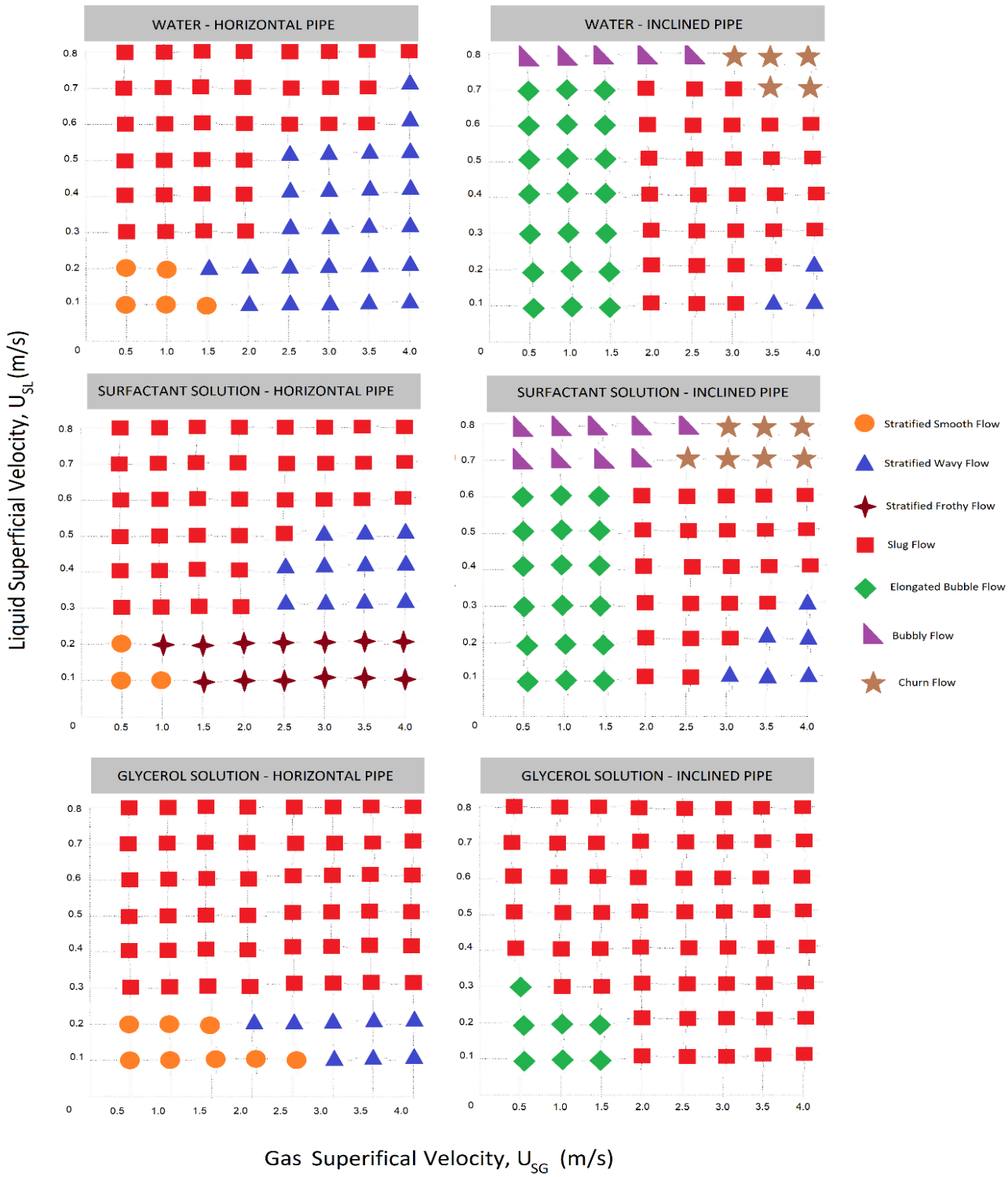

Figure 5.8: Flow regimes observed at different pipe orientations.

The data points examined in present study are compared to the flow regime map of Taitel & Dukler (1976) for air water multiphase flow in a horizontal pip.

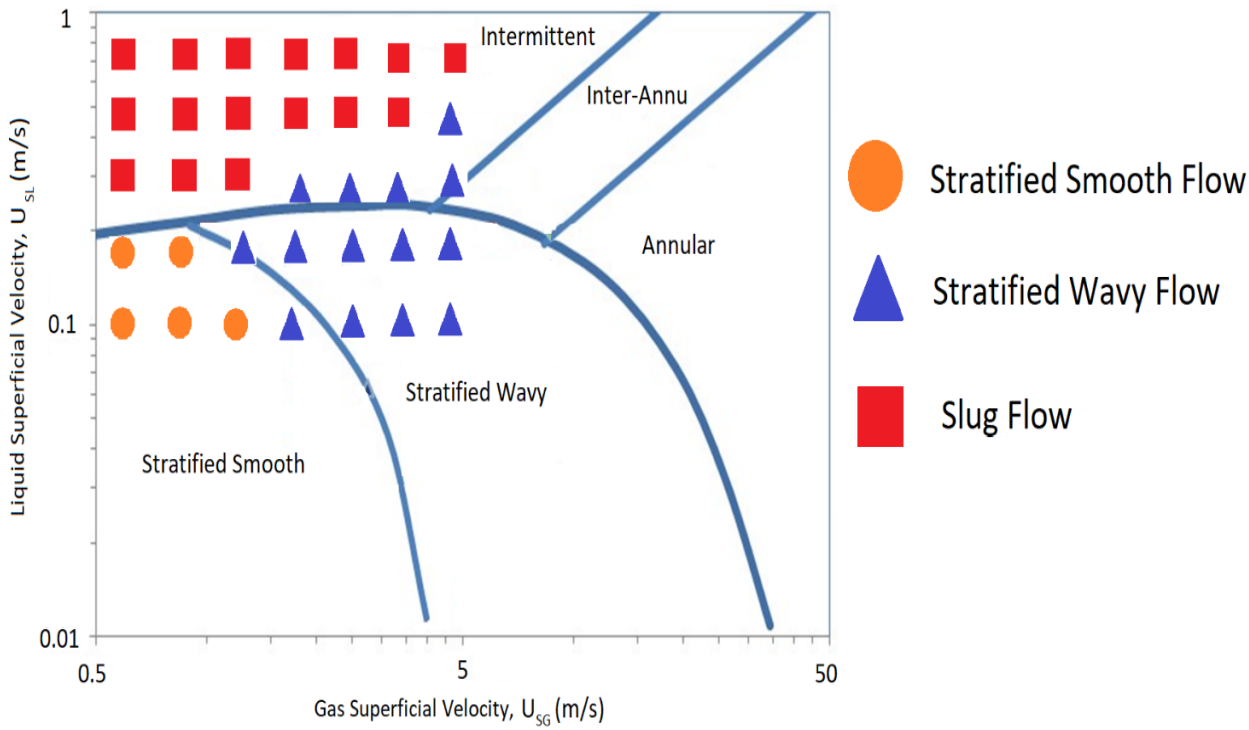

Figure 5.9: Comparison of the Taitel & Dukler (1976) transition map to air-water flow data in a horizontal pipe.

The transition map of Taitel &Dukler (1976) as displayed in Figure 5.9 more successfully captures the data, showing for a constant liquid velocity of 0.1m/s and with increasing gas velocity, the flow regime is smooth stratified flow. Increasing the gas velocity, the flow regime becomes a stratified wavy flow, while increasing the liquid velocity changed the flow regime to slug flow.

5.5 Pressure Drop

Pressure drop is one of the most significant parameters in multiphase flow, understanding and managing pressure drop in multiphase flow systems are critical for efficient operation, equipment reliability, process control, and safety. It simply refers to the decrease in pressure

that occurs as a fluid flow through a pipe, this decrease occurs a result of the resistances encountered by the fluid as it overcomes the flow restrictions and interacts with the walls of the pipe. In this work, gas-liquid pressure data was collected for flow through the 19mm ID pipe at horizontal and 15^{O} upward inclination, for the three different liquids investigated. This section will analyse and discuss on the pressure drop data collected.

5.6 Components of Pressure Drop

Pressure drop in a fluid flow system is typically composed of several components, each contributing to the overall pressure loss. The specific components can vary depending on the flow conditions and the characteristics of the system. In this research, the key components of pressure drop that were encountered include frictional pressure drop, gravitational pressure drop, and acceleration pressure drop.

Frictional pressure losses: Frictional pressure drop in a fluid flow system is primarily caused by the resistance encountered as the fluid interacts with the surface of the pipe. This resistance, known as frictional drag, arises due to the shearing action between the fluid layers as they move at different velocities. When the viscosity of a liquid increases, the fluid has a higher resistance to flow and a greater internal frictional force. The increased viscosity results in higher frictional drag between the fluid and the pipe or walls, leading to an increase in pressure drop along the flow direction.

Gravitational Pressure Drop: Elevation pressure drop, also known as gravitational pressure drop occurs because of a change in the pipe's orientation angle. Theoretically, gravity aids flow in a downhill direction while opposing uphill flow. Gravitational pressure drop is negligible for horizontal flow but becomes one of the dominant causes of pressure loss with increasing pipe inclination angle. Therefore, in an inclined pipe flow with high superficial velocities, the gravitational effect is the dominant cause of pressure drop. As the flow rate increases, the net effect of the increase in frictional losses arising from interfacial shear stress becomes a prominent factor, thus making the frictional pressure gradient more dominant over the gravitational pressure gradient.

5.7 Pressure Drop Measurements

Experimental pressure drop in the test pipe was measured using Omega-Wet/Wet Differential Pressure Transducer, operating in the range of 0-170 mbar. The transducer sensors were connected to the flow inlet and outlet of the test pipe as presented in Chapter 3. The transducer produces a digital output which displays on a computer connected via a USB cable. The total pressure drop across the test pipe is determined by averaging the instantaneous differential pressure transducer measurements over a period of three minutes. The experimental pressure drop data at each of the superficial velocities of liquid, based on the superficial velocities of gas/liquid is graphically presented in Figures 5.10 through 5.17.

5.8 Factors Affecting Pressure Drop

There are several factors that can cause a pressure drop in multiphase flow systems. These factors can vary depending on the specific characteristics of the flow and the properties of the phases involved, such as void fraction, the flow rates of the phases, the gas-liquid ratio, the density difference between the two phases, etc. The roles played by these factors in influencing pressure drop in this study are discussed in the next sub-sections.

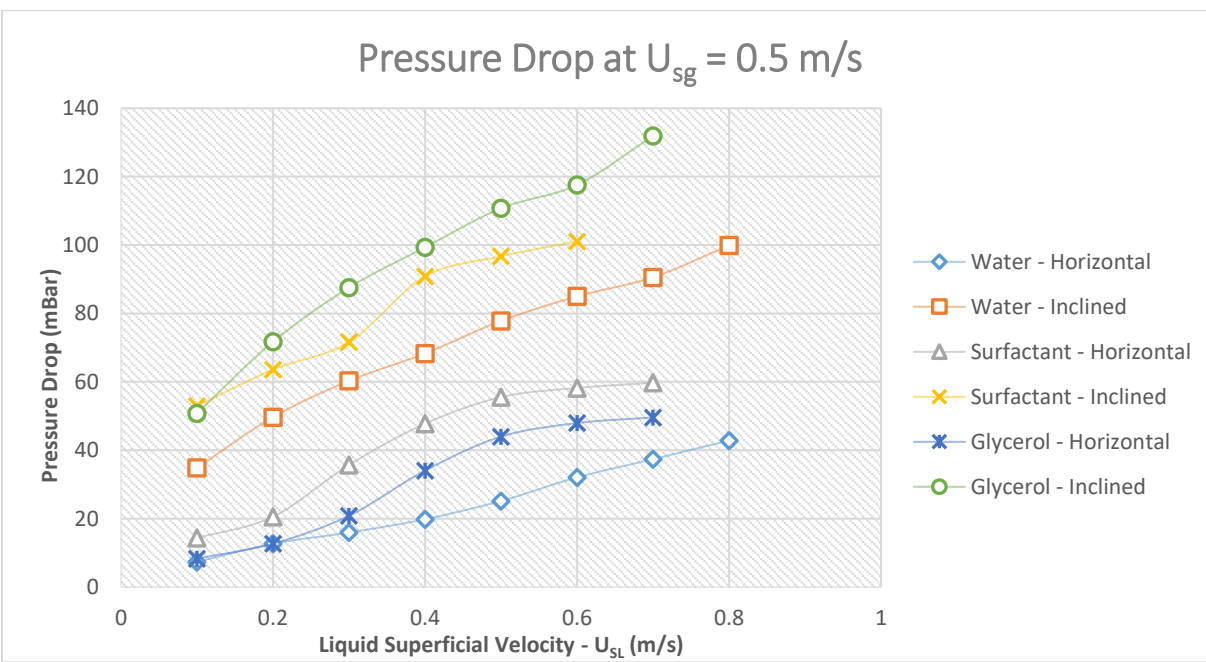

Figure 5.10: Experimental pressure drop, ΔP vs U_{SL}, at U_{SG}= 0.5 m/s

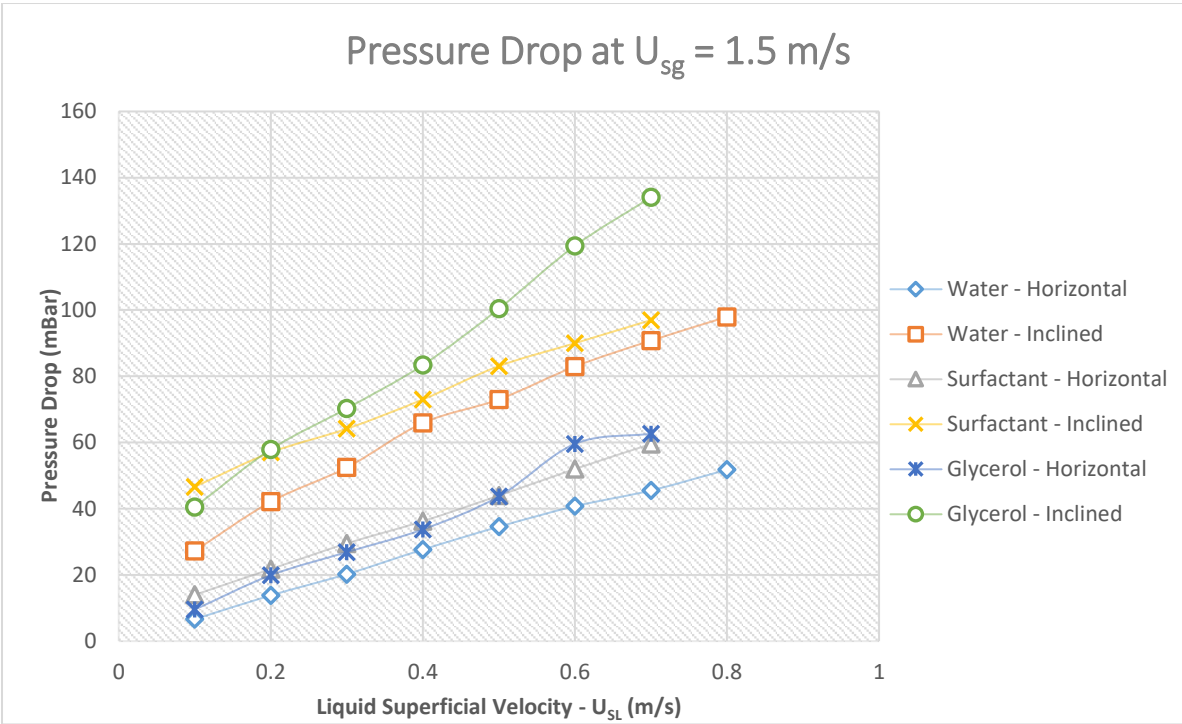

Figure 5.11: Experimental pressure drop, ΔP vs U_{SL}, at U_{SG} = 1.5 m/s

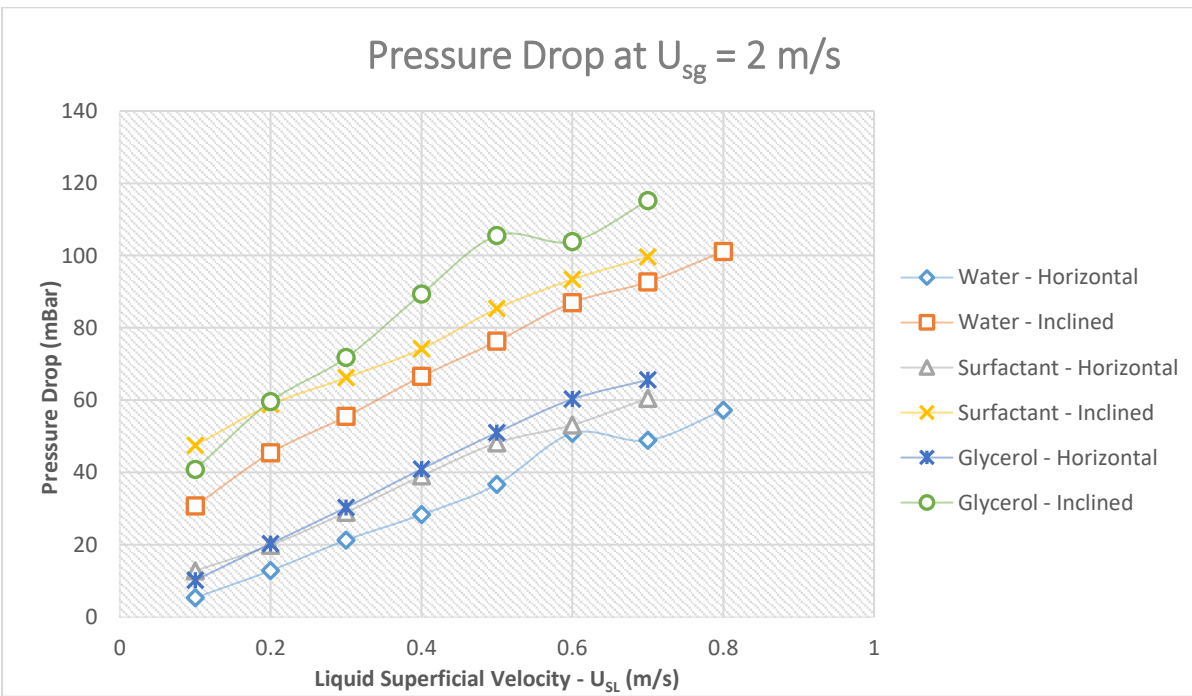

Figure 5.12: Experimental pressure drop, ΔP vs U_{SL}, at U_{SG} = 2 m/s

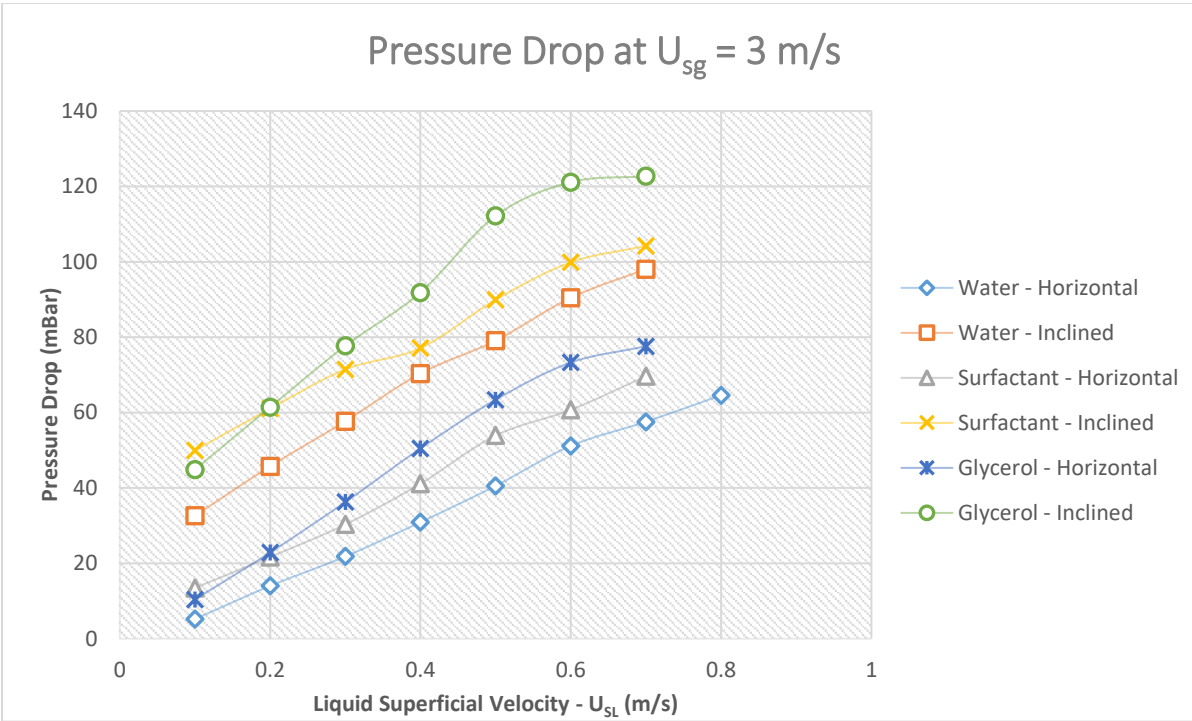

Figure 5.13: Experimental pressure drop, ΔP vs U_{SL}, at U_{SG} = 3 m/s

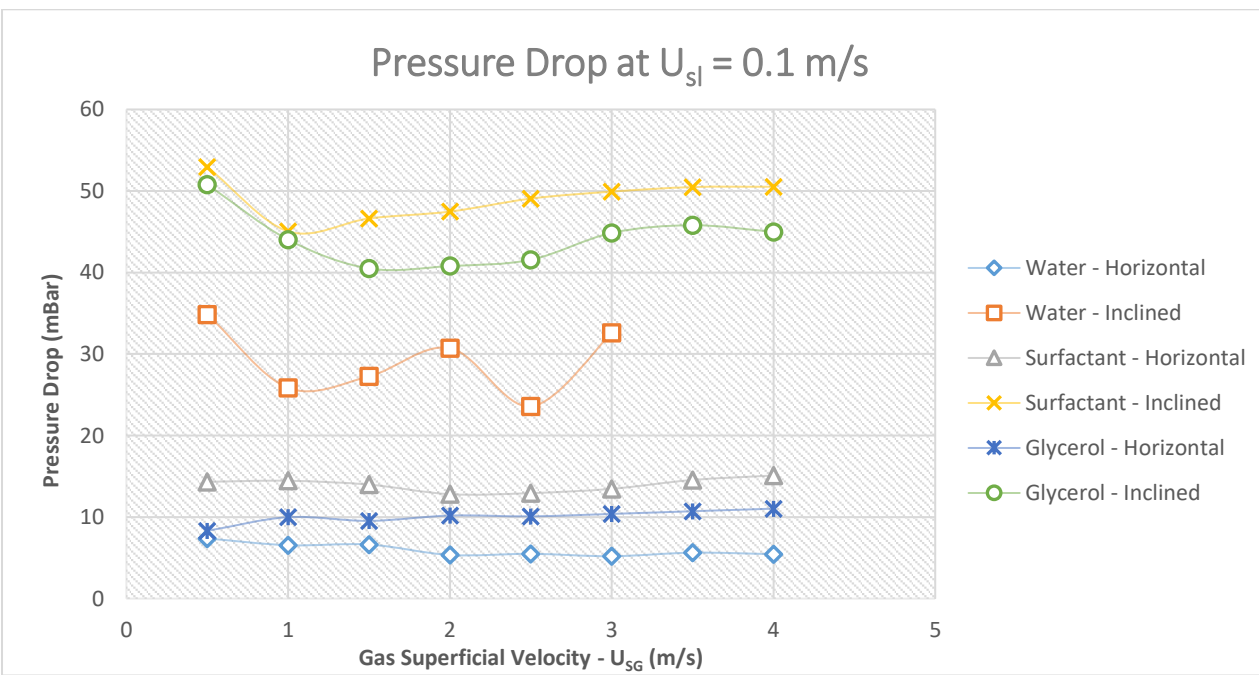

Figure 5.14: Experimental pressure drop, ΔP vs U_{SG}, at U_{SL} =0.1 m/s

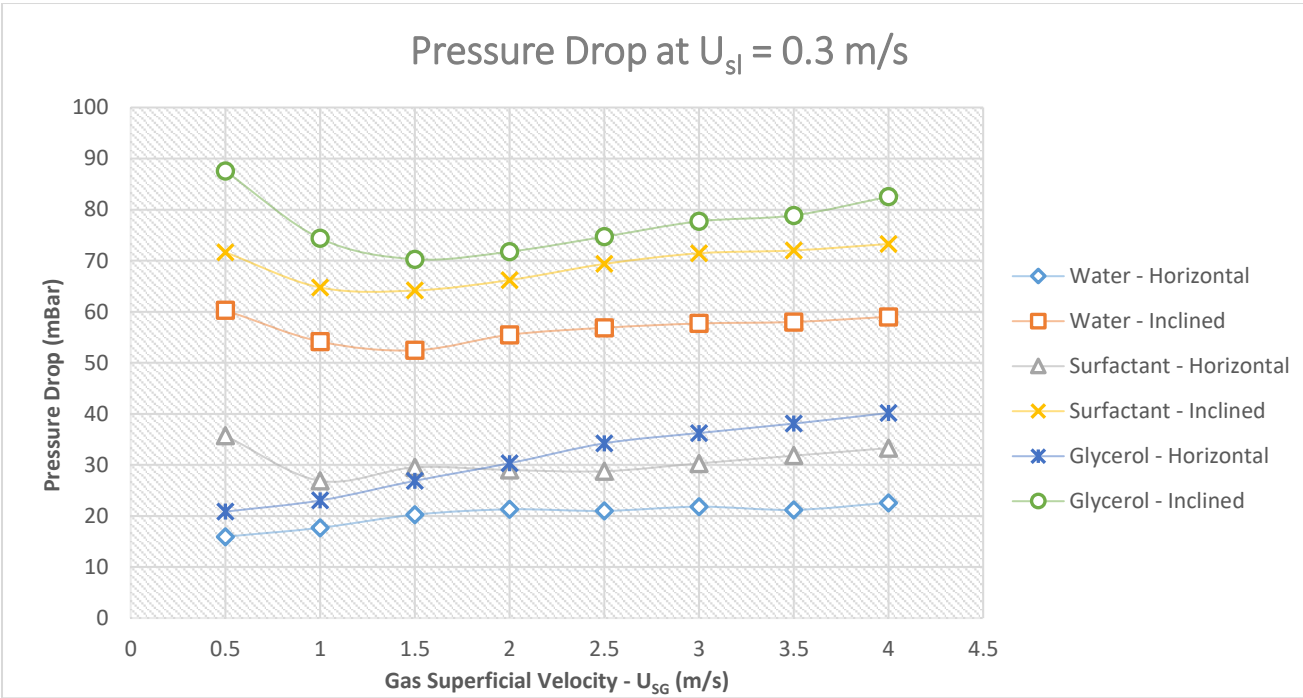

Figure 5.15: Experimental pressure drop, ΔP vs U_{SG}, at U_{SL}=0.3 m/s

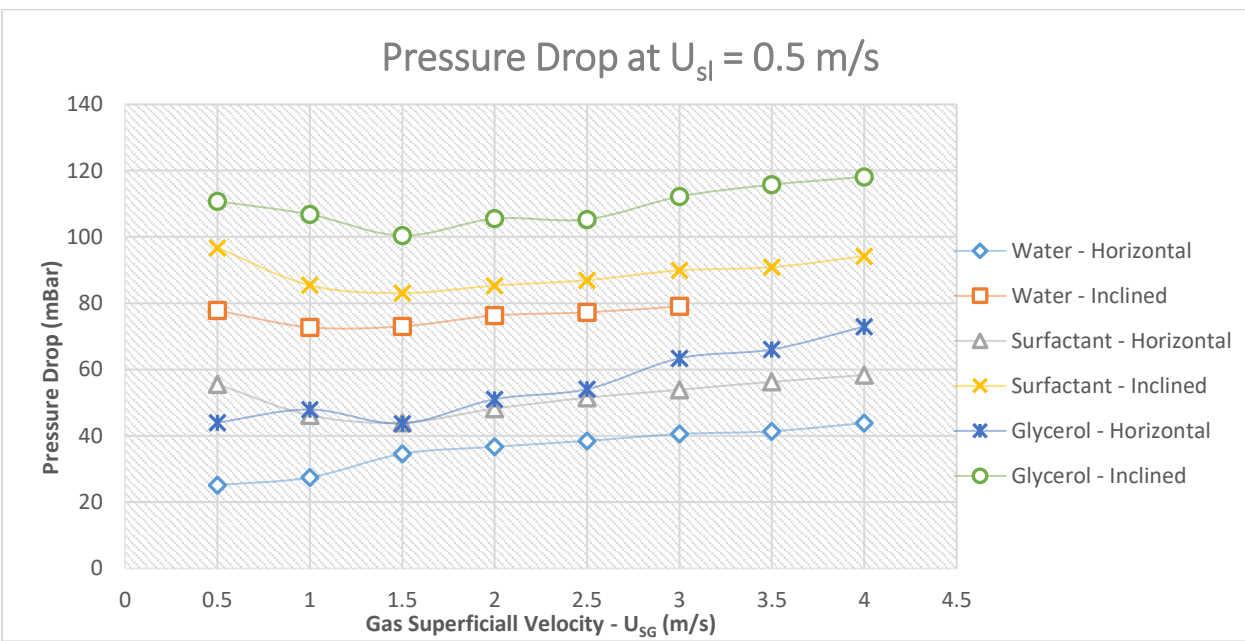

Figure 5.16: Experimental pressure drop, ΔP vs U_{SG}, at U_{SL} =0.5 m/s

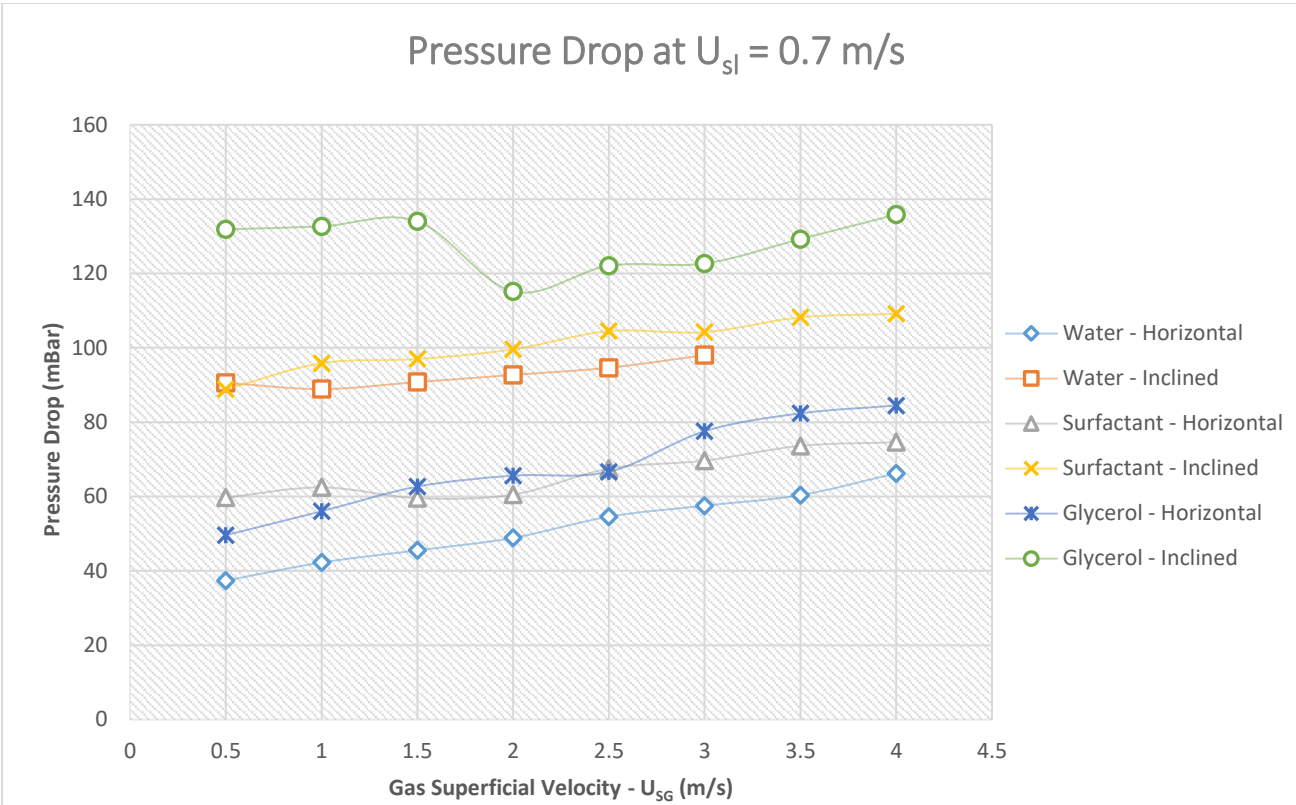

Figure 5.17: Experimental pressure drop, ΔP vs U_{SG}, at U_{SL} =0.7 m/s

Flow Regime Change: The flow regime is a function of void fraction; a high void fraction means there is less of a liquid phase than the gas phase and vice versa. Since pressure drop largely depends on the weight of the fluids in the system, thus the total pressure also changes in magnitude with changes in void fraction. Flow regimes such as slug flow generate high acceleration and deceleration of the liquid structures, this leads to high-pressure fluctuations which occasionally result in sudden pressure changes and instability. Similarly, in bubbly flow, bubbles tend to accumulate at the upper part of the wall, sometimes increasing their packing density with increasing inclination angle. Change in pressure drop due to changing flow regime can be observed in almost all the graphic plots in Figures 5.10 through 5.17, which can be directly related to the flow regime map of Figure 5.8. For example, in the plots of Figure 5.15, the pressure drop curve for air-glycerol flow in an inclined pipe decreases gradually from 90 mBar to 70 mBar between the U_{SG} values of

0.5 to 1.5 m/s at a constant U_{SL} value of 0.3 m/s, and then increases gradually between the U_{SG} values of 1.5 to 4.0. This behaviour can be attributed to a change in flow regime from elongated bubble flow to slug flow as shown in flow regime map of Figure 5.8.

Effects of Liquid Viscosity: Liquid viscosity has a significant impact on pressure drop in fluid flow systems, as the viscosity of the liquid increases, the frictional pressure drop also increases. This is because higher-viscosity fluids have a greater resistance to flow, resulting in more significant frictional forces between the fluid and the pipe walls. The increased viscosity leads to a thicker boundary layer and a higher velocity gradient near the pipe walls, contributing to a higher pressure drop. Higher-viscosity liquids tend to have lower flow velocities compared to lower-viscosity liquids for the same flow rate. This is due to the increased resistance to flow caused by the viscous nature of the fluid. The reduced flow velocity results in a lower momentum of the fluid particles and subsequently a lower kinetic energy, leading to a lower pressure drop. Hence the air-glycerol solution exhibits the highest pressure drop in all the plots.

Effects of Surface Tension: Surface tension can indirectly affect pressure drop through its influence on the flow behaviour and flow regime. Surface tension plays a role in determining the transition between different flow regimes, such as stratified flow, slug flow, annular flow, or bubbly flow. The specific surface tension properties of the liquid can influence the stability and formation of different flow patterns. Each flow regime has its own characteristic pressure drop behaviour, and the transition between these regimes can impact the overall pressure drop in the system. For example, in this work, air - surfactant solution flow exhibits a different flow behaviour as compared to air–water flow at the same experimental matrices, instead of transitioning from stratified smooth flow to stratified wavy flow, surfactant solution transits to stratified frothy flow. This leads to an observable difference in the pressure drop from the two liquids. Surface tension also influences the interfacial shear stress between the liquid and gas phases in multiphase flow. This shear stress at the phase interface can affect the momentum transfer and pressure drop within the

system. The magnitude of interfacial shear stress depends on the surface tension, and the relative velocity between the phases.

Effects of Gas and Liquid Superficial Velocities: The liquid and gas superficial velocities have shown a significant impact on pressure drop within the flow system. Increased liquid velocity leads to higher momentum and kinetic energy of the liquid phase. This results in a higher frictional pressure drop due to increased interaction with the pipe walls. Increased liquid velocity also enhances liquid entrainment or carryover into the gas phase, leading to changes in the flow pattern and potentially leading to increased pressure drop. Similarly, higher gas velocity leads to increased gas momentum and kinetic energy. Furthermore, the effects of increasing gas velocity and low constant liquid superficial velocity was seen to cause the formation of waves, ripples, and disturbances at the liquid-gas interface, changing a stratified smooth flow to a stratified wavy flow leading to a higher pressure drop in the system. Higher gas velocity at a high liquid loading induces more vigorous gas-liquid interactions, such as bubble formation, breakup, or coalescence. These phenomena have influenced the flow regime and altered pressure drop characteristics, such as the plots in Figure 5.13. Additionally, the relative velocity between the liquid and gas phases influences the interfacial shear stress and momentum transfer. Higher relative velocity can enhance momentum exchange between the phases, affecting the pressure drop.

Effects of Pipe Inclination: One of the major components of pressure drop encountered in this study is gravitational pressure drop. This becomes prominent as the flow inclination changes from horizontal. The angle at which a pipe is inclined from the horizontal plane, has a significant impact on pressure drop in fluid flow systems. In upward-inclined pipes, the gravity head acts against the flow direction, resulting in a decrease in pressure and an increased pressure drop. Pipe inclination was seen to influence the flow pattern and regime transition. In a horizontal pipe flow of air-glycerol solution for example, flow patterns that are typically stratified smooth and stratified wavy changes to slug flow or elongated bubble flow when the pipe orientation becomes inclined. This transition to different flow regimes can affect pressure drop as discussed earlier. Furthermore, in upward inclined pipes, the

flow encounters greater resistance against gravity and increased liquid residence time in the system, both phenomena can independently lead to increased pressure drop.

5.9 Liquid Holdup

Liquid holdup, also known as liquid fraction or liquid volume fraction, refers to the fraction or percentage of liquid phase present in a multiphase flow system. It represents the ratio of the volume occupied by the liquid phase to the total volume of the multiphase mixture. The liquid holdup is a key parameter that describes the distribution and behaviour of the liquid phase within the flow system. It is influenced by various factors, including flow regime, flow rate, fluid properties, and geometry of the system.

The liquid holdup can vary along the flow direction and across different sections of the flow system. In some cases, it can be uniform and well-mixed, while in others, it may exhibit variations and stratification. The distribution of liquid holdup affects the overall flow patterns and can impact the performance and operation of the system.

5.10 Liquid Holdup Measurements

Measurement and estimation of liquid holdup are important in the design, analysis, and optimization of multiphase flow systems. Various techniques are used to determine the liquid holdup, such as direct measurements using sensors or visual observations, and indirect methods, such as using pressure drop measurements or electrical capacitance tomography.

In this study, liquid holdup measurements in the test pipe were carried out using the two synchronously working quick-action solenoid valves and a manually operated draining valve to collect the trapped liquid and measure its volume in a measuring cylinder. The liquid hold-up measurements taken were plotted against the superficial velocities of the liquid and of the gas as shown in Figures 5.18 to 5.25.

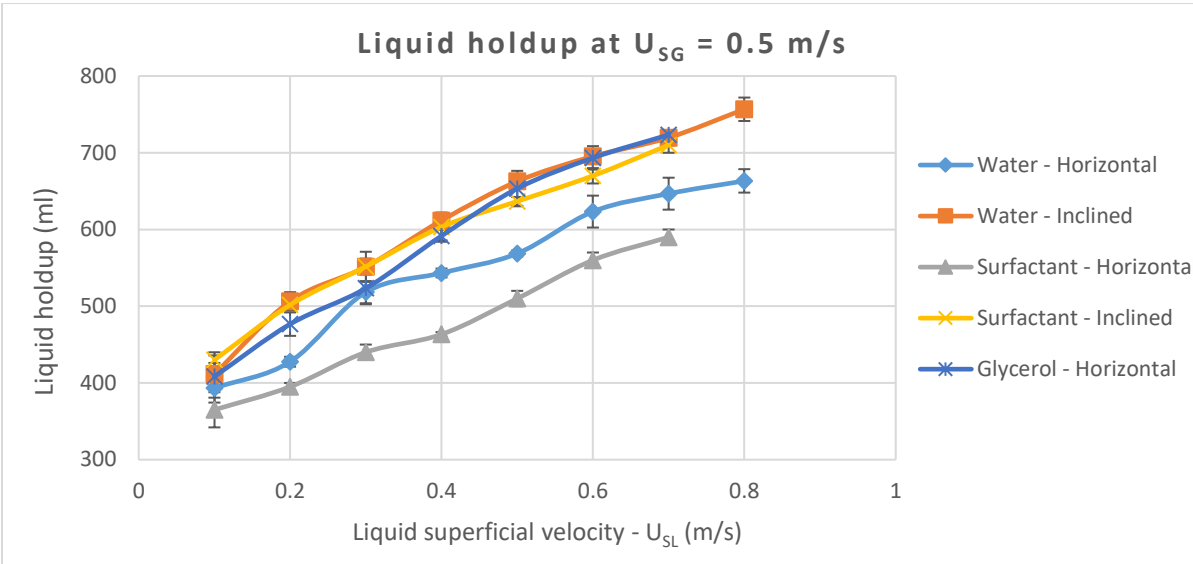

Figure 5.18: Experimental liquid hold-up, H_L vs U_{SL}, at U_{SG} = 0.5 m/s

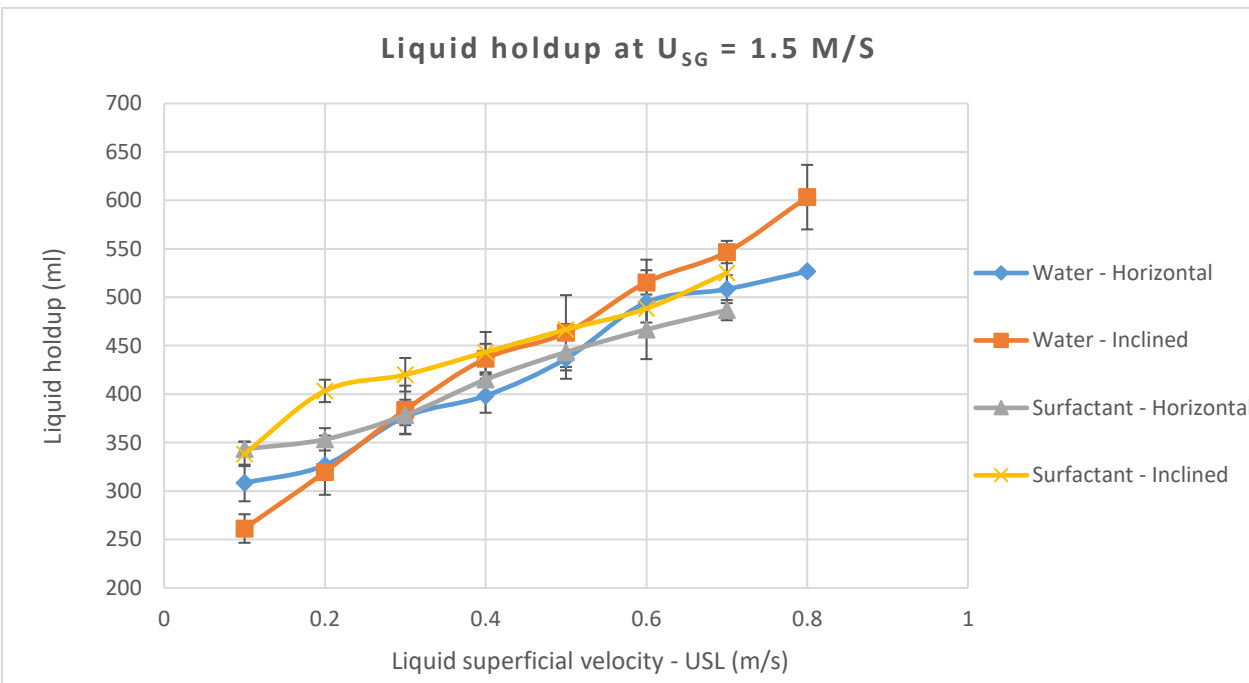

Figure 5.19: Experimental liquid hold-up, H_L vs U_{SL}, at U_{SG} = 1.5 m/s

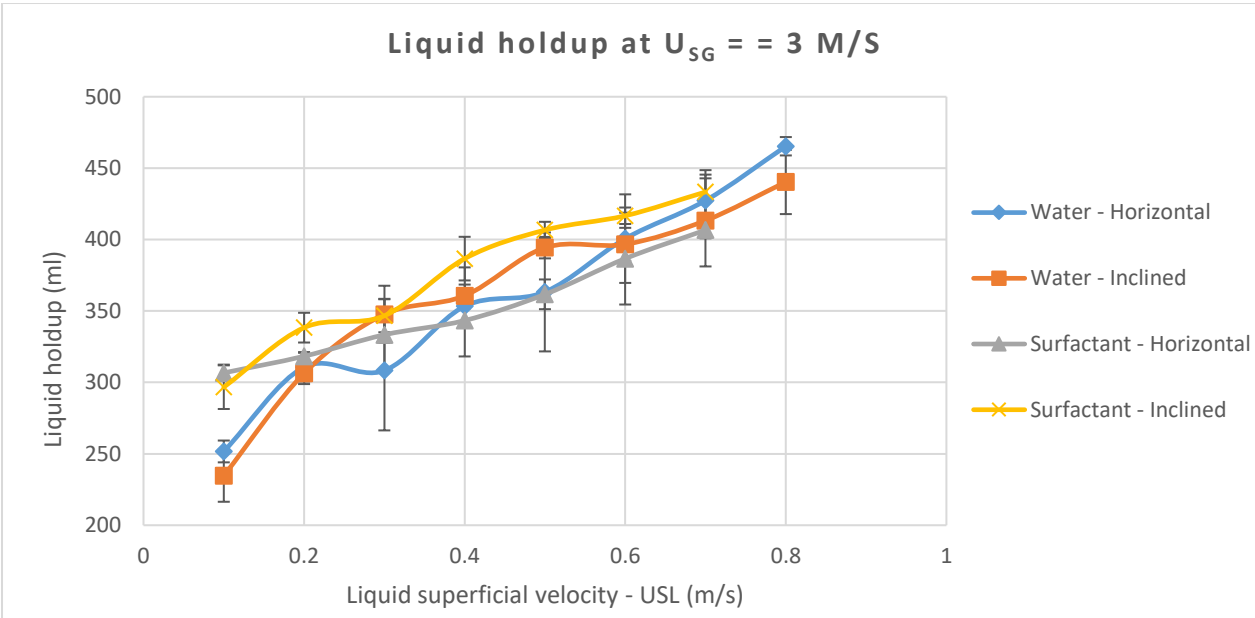

Figure 5.20: Experimental liquid hold-up, H_L vs U_{SL}, at U_{SG} = 3 m/s

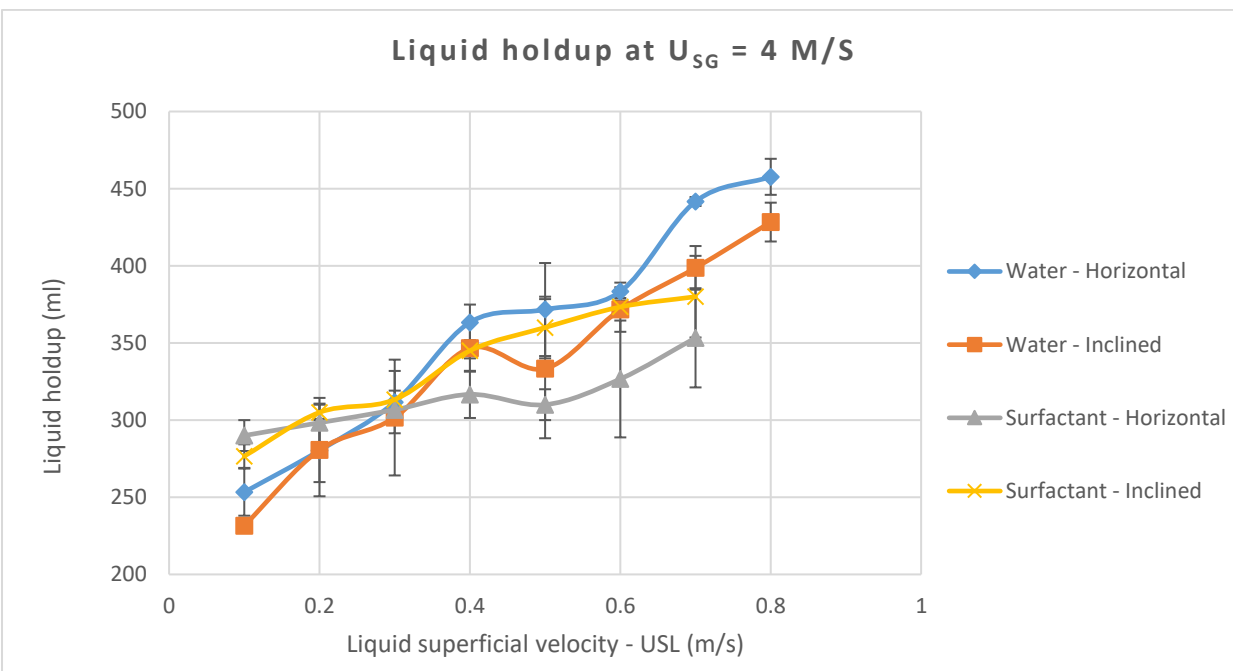

Figure 5.21: Experimental liquid hold-up, H_L vs U_{SL}, at U_{SG} = 4 m/s

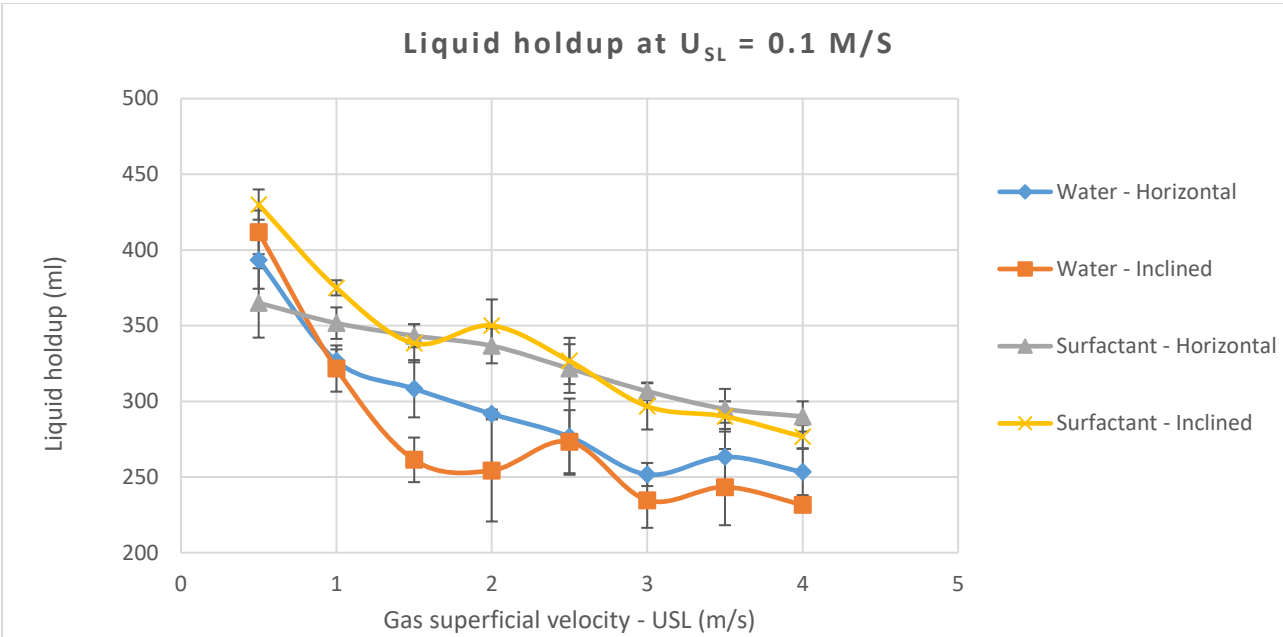

Figure 5.22: Experimental liquid hold-up, H_L vs U_{SG}, at U_{SL} = 0.1 m/s

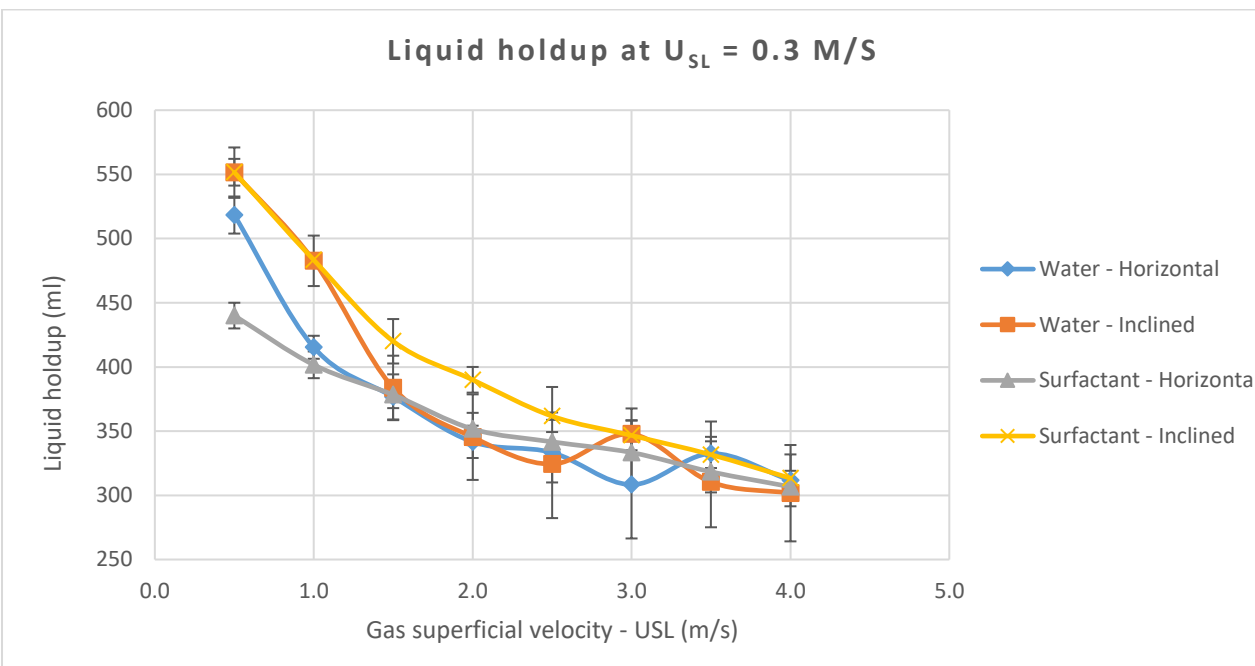

Figure 5.23: Experimental liquid hold-up, H_L vs U_{SG}, at U_{SL} = 0.3 m/s

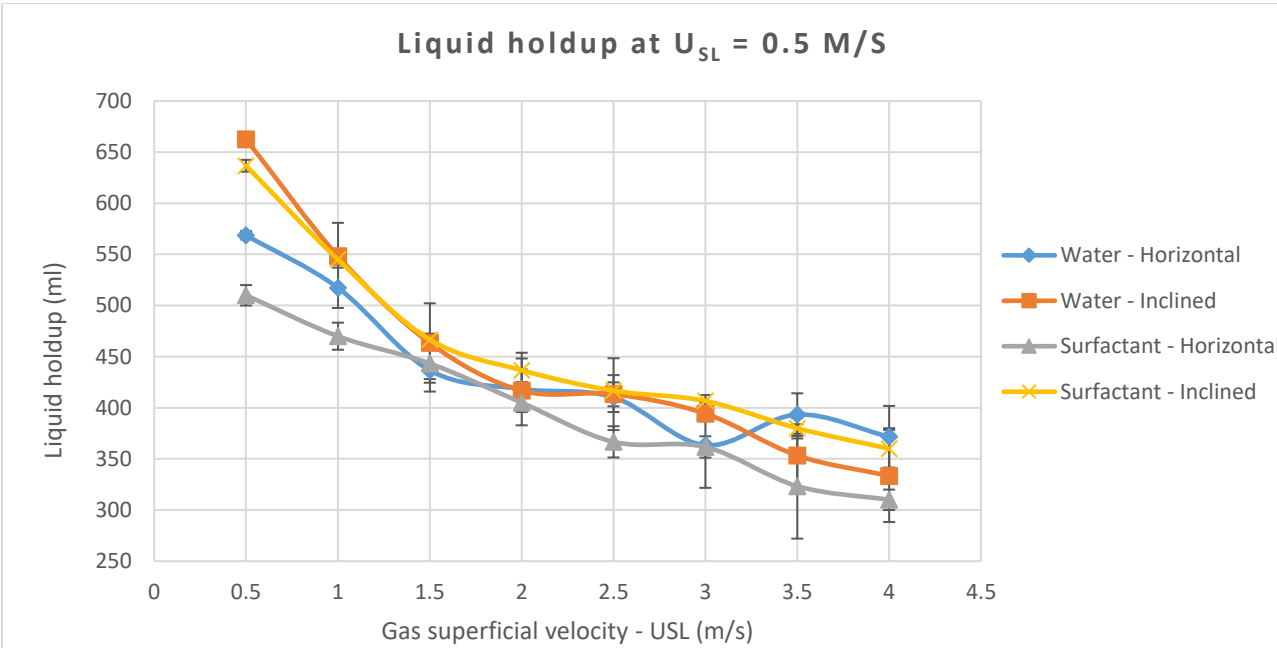

Figure 5.24: Experimental liquid hold-up, H_L vs U_{SG}, at U_{SL} = 0.5 m/s

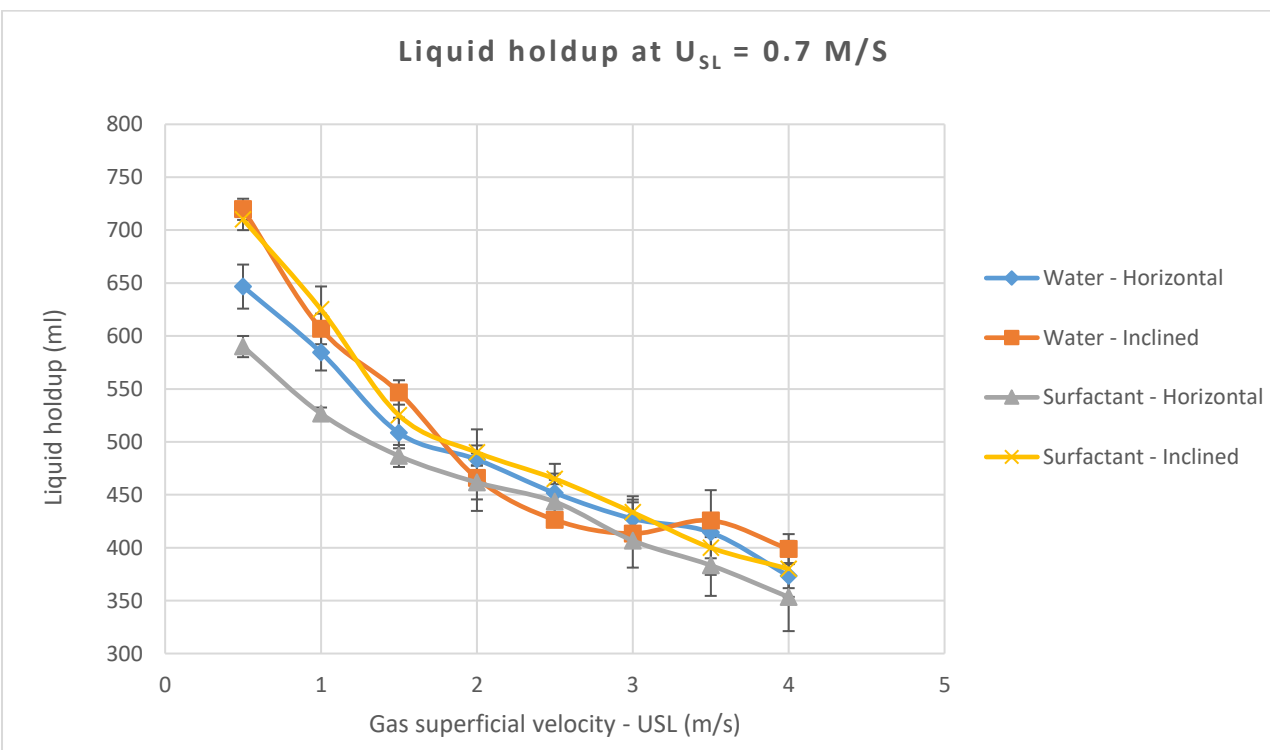

Figure 5.25: Experimental liquid hold-up, H_L vs U_{SG}, at U_{SL} = 0.7 m/s

5.1.1 Factors Affecting Liquid Holdup

There are several factors that influence liquid holdup in a multiphase flow system, some of the key factors observed in this study includes flow regime, fluid properties, flow rate, gas-liquid ratio, pipe inclination, and surface tension.

Effects of Flow Regime: The flow regime, which describes the distribution and interaction of the liquid and gas phases, plays a significant role in determining liquid holdup. Different flow regimes, such as stratified, slug, or bubbly, have distinct liquid holdup characteristics. For example, in slug flow, the liquid holdup is typically higher due to the presence of large liquid slugs separated by gas bubbles. The effects of flow regime change on liquid holdup is seen in all the plots from Figures 5.18 to 5.25.

Effects of Fluid Properties: Physical properties of the liquid, such as density and viscosity, affect liquid holdup. Higher liquid density generally leads to higher liquid holdup, as the denser liquid phase tends to occupy more space in the flow. Similarly, higher liquid viscosity increases the resistance of the liquid phase to flow and influences the transition between different flow regimes thereby promoting higher liquid holdup in both cases.

Effects of Surface Tension: The surface tension between the liquid and gas phases influence liquid holdup, especially in flow regimes where surface tension forces play a significant role. Higher surface tension tends to promote higher liquid holdup by aiding in the stability and formation of liquid films or layers in the flow. Surface tension influences the thickness of the liquid film, higher surface tension tends to promote the formation of thinner liquid films, whereas lower surface tension results in thicker liquid films. Thinner liquid films generally lead to reduced liquid holdup, as the liquid is more concentrated in a thin layer near the walls. The effects of surface tension can be seen in all the liquid holdup plots, where air - surfactant solution flow displays generally lower liquid holdup than air-water flow for the same flow conditions.

Effects of Gas and Liquid Flow Rates: The flow rate of the liquid phase influences liquid holdup. In general, higher liquid flow rates result in higher liquid holdup, as more liquid is introduced into the flow. The ratio of gas to liquid in the flow, often expressed as the void fraction or gas volume fraction, affects liquid holdup. As the gas volume fraction increases, the liquid holdup typically decreases, as more space is occupied by the gas phase. Increasing the gas superficial velocity can lead to a transition from stratified flow to slug flow or other flow regimes. Each flow regime has different characteristics in terms of the liquid holdup. For example, higher gas superficial velocities tend to promote slug flow, resulting in higher liquid holdup near the slug regions. Increasing the gas superficial velocity also enhances the ability of the gas phase to carry liquid droplets or entrain a thin liquid film, leading to increased liquid holdup. This is particularly evident in dispersed flow regimes where the gas phase disperses the liquid phase throughout the pipe cross-section, resulting in higher liquid holdup values.

Similarly, liquid superficial velocity affects the distribution of liquid holdup along the pipe cross-section. Higher liquid superficial velocities tend to promote more uniform liquid holdup distribution, with a more dispersed liquid phase, while lower liquid superficial velocities can result in uneven liquid holdup distribution, with regions of higher liquid holdup near the walls and lower liquid holdup in the core.

Effects of Pipe Inclination: In upward inclined pipes, the liquid phase tends to accumulate at the bottom of the pipe due to the influence of gravity. In this case, the liquid holdup can be higher near the bottom region compared to the upper section of the pipe. Upward inclined pipes also promote slug flow, the liquid slugs tend to accumulate in the lower section of the pipe while the gas bubbles occupy the upper section, this can lead to higher liquid holdup near the bottom region where the liquid slugs are concentrated. Phase separation was also observed in upward inclined flow due to density differences; the denser liquid phase tends to settle towards the bottom of the pipe while the lighter gas phase occupies the upper section. This phase separation can result in localized liquid holdup enhancements near the bottom region of the pipe.

5.12 Slug Frequency Analysis

Slug frequency refers to the rate at which liquid slugs are formed and travel through a pipeline or flow system. In this work, a Photon FASTCAM high-speed camera was used to capture the slug occurrence in each experimental condition for 60 seconds, this technique was adopted the work of Lu (2015). The video recordings were transferred from the camera in a slow-motion format to a high-capacity data storage drive for analysis. The captured video is then played back in slow motion and the number of instances that slug flow occurs is noted to get the total number of slugs formed over the 1-minute period. This gives a fair idea of the slug frequency and how the liquid properties influence this slug frequency. Figures 5.26 through to Figure 5.33 shows plots of the slug frequency per minute as a function of gas and liquid translational velocities.

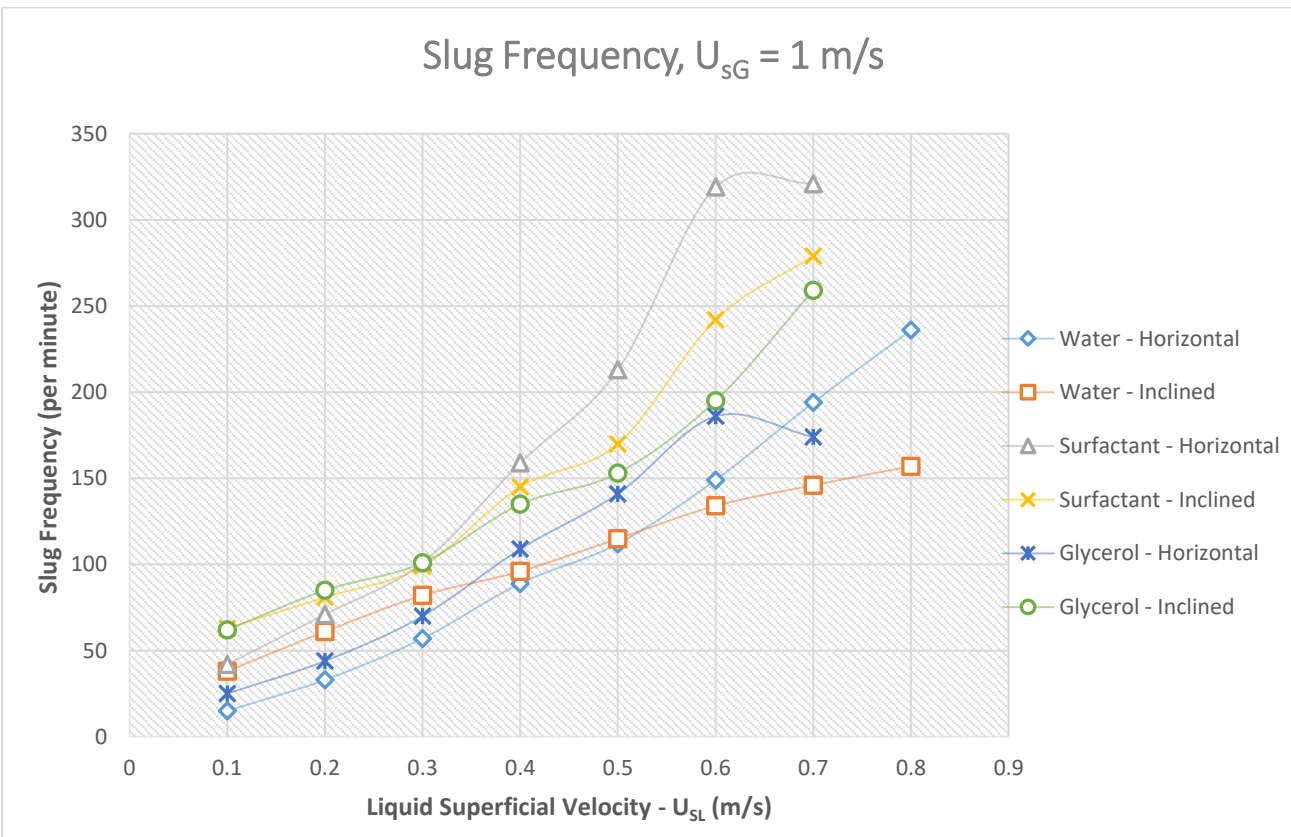

Figure 5.26: Experimental slug frequency, F_S vs U_{SL}, at U_{SG} = 1 m/s

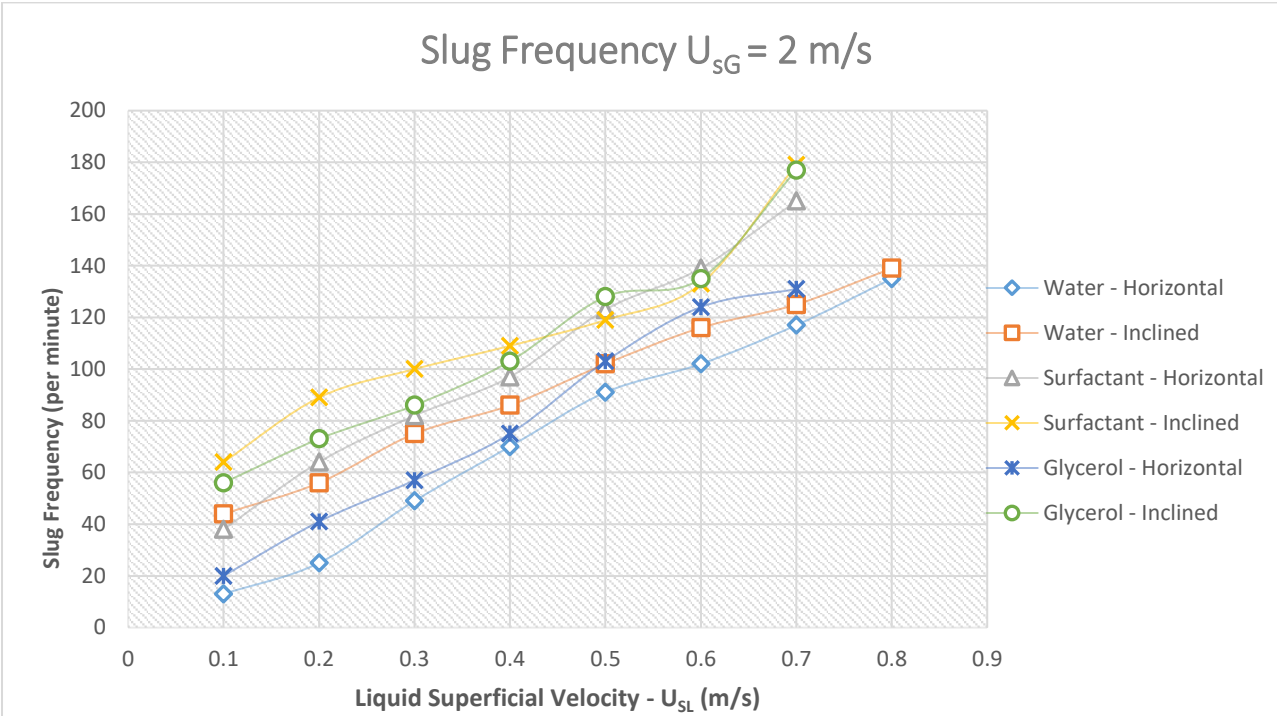

Figure 5.27: Experimental slug frequency, F_S vs U_{SL}, at U_{SG} = 2 m/s

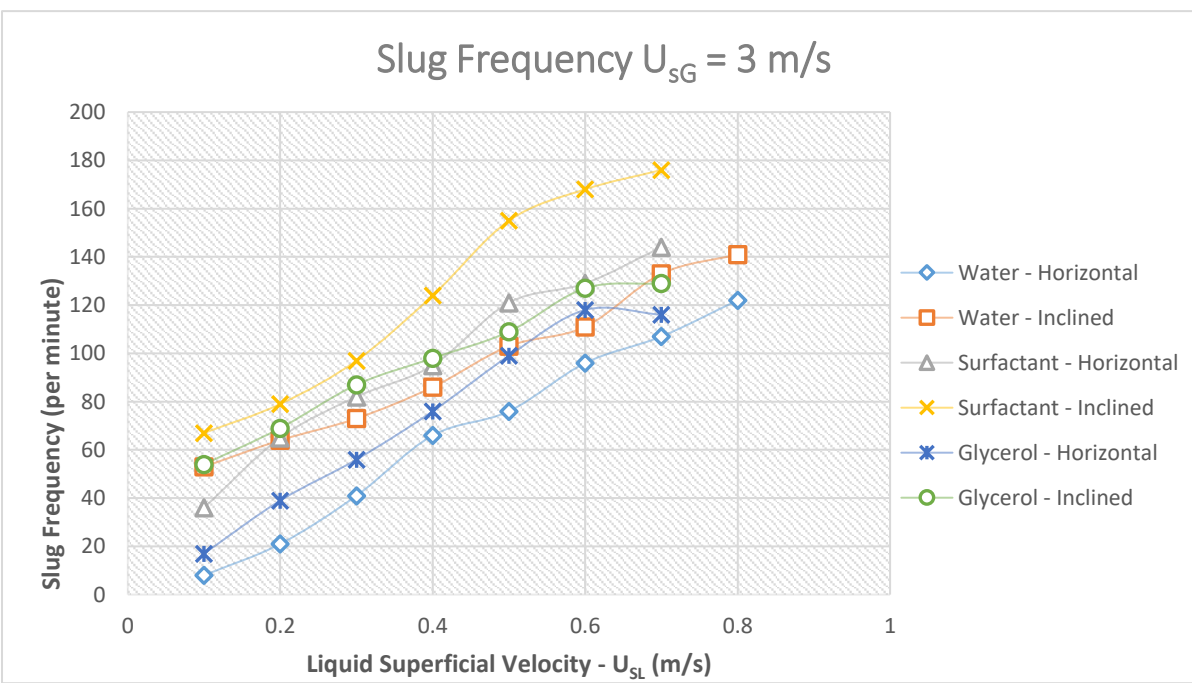

Figure 5.28: Experimental slug frequency, F_S vs U_{SL}, at U_{SG} = 3 m/s

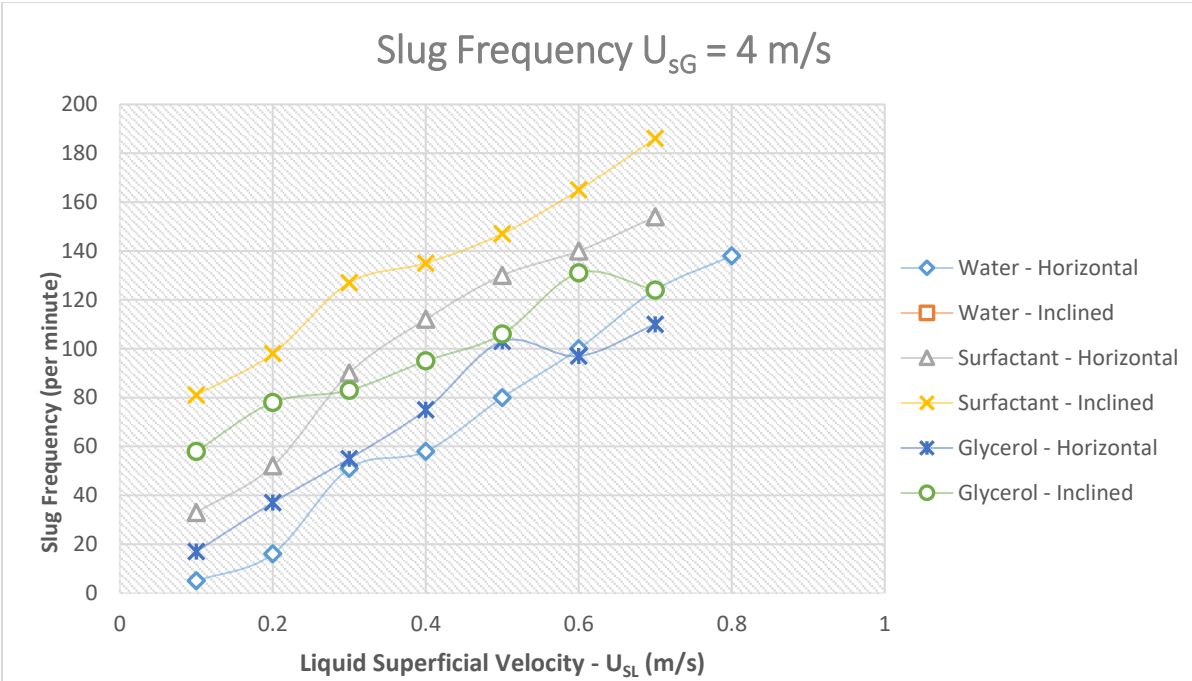

Figure 5.29: Experimental slug frequency, F_S vs U_{SL}, at U_{SG} = 4 m/s

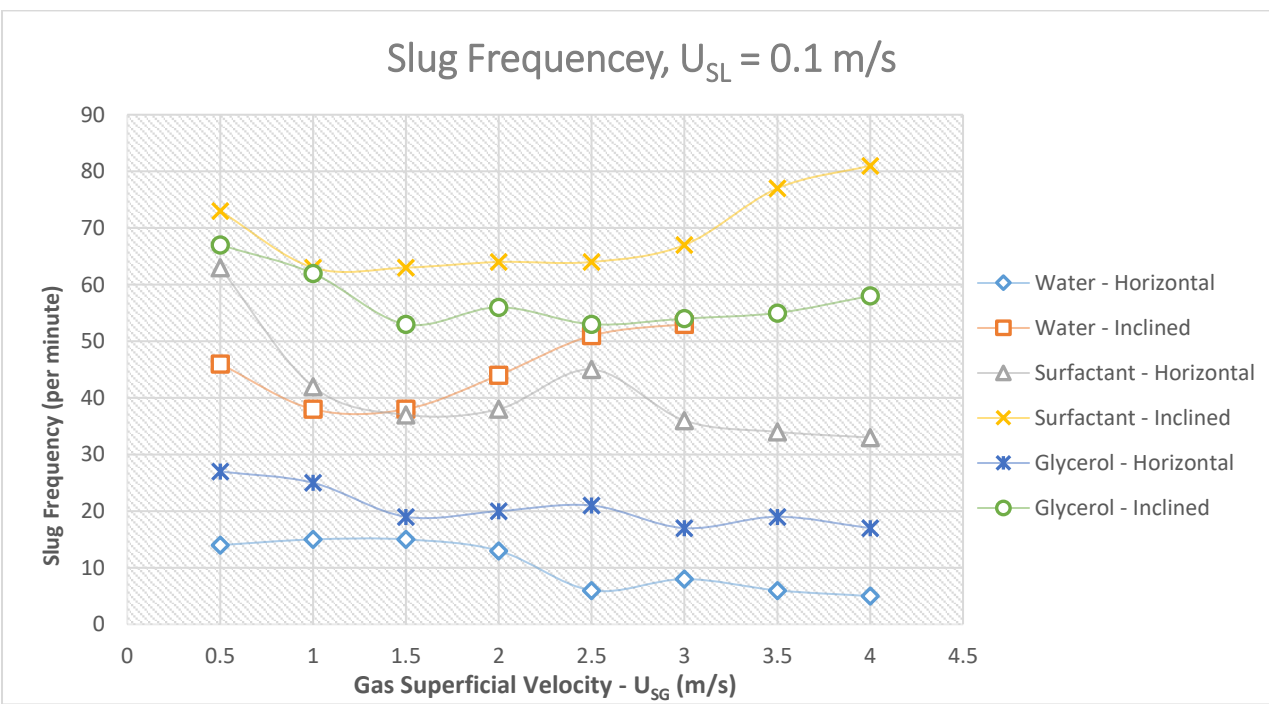

Figure 5.30: Experimental slug frequency, F_S vs U_{SG}, at U_{SL} = 0.1m/s

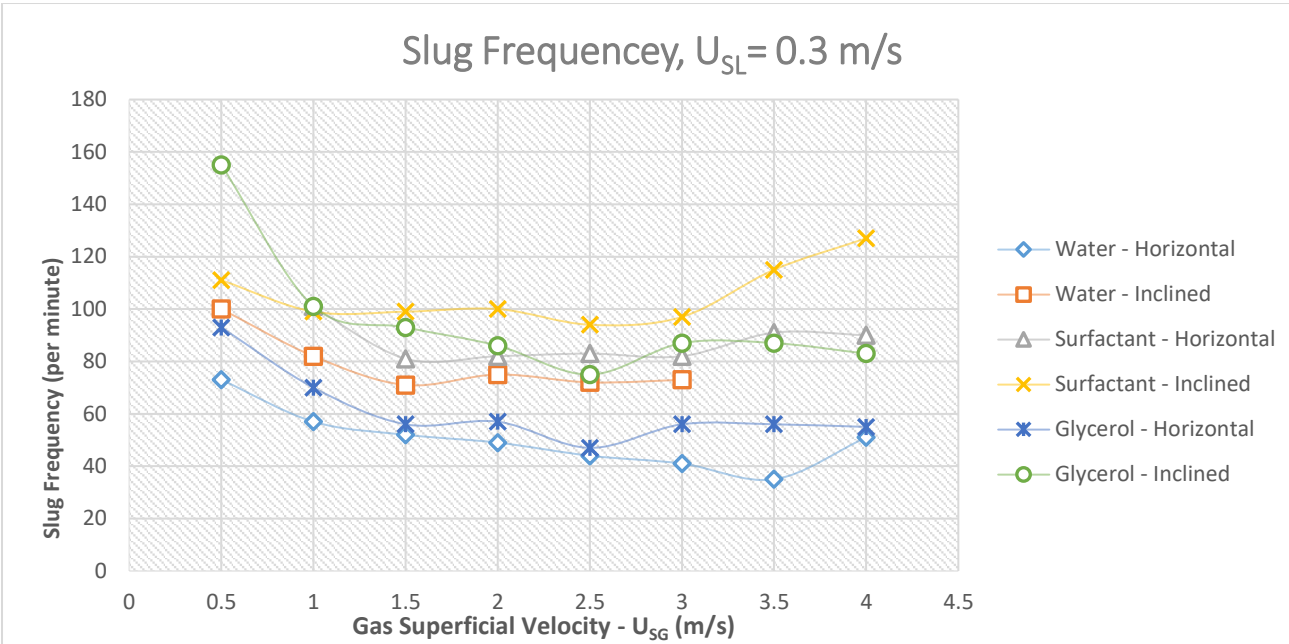

Figure 5.31: Experimental slug frequency, F_S vs U_{SG}, at U_{SL} = 0.3m/s

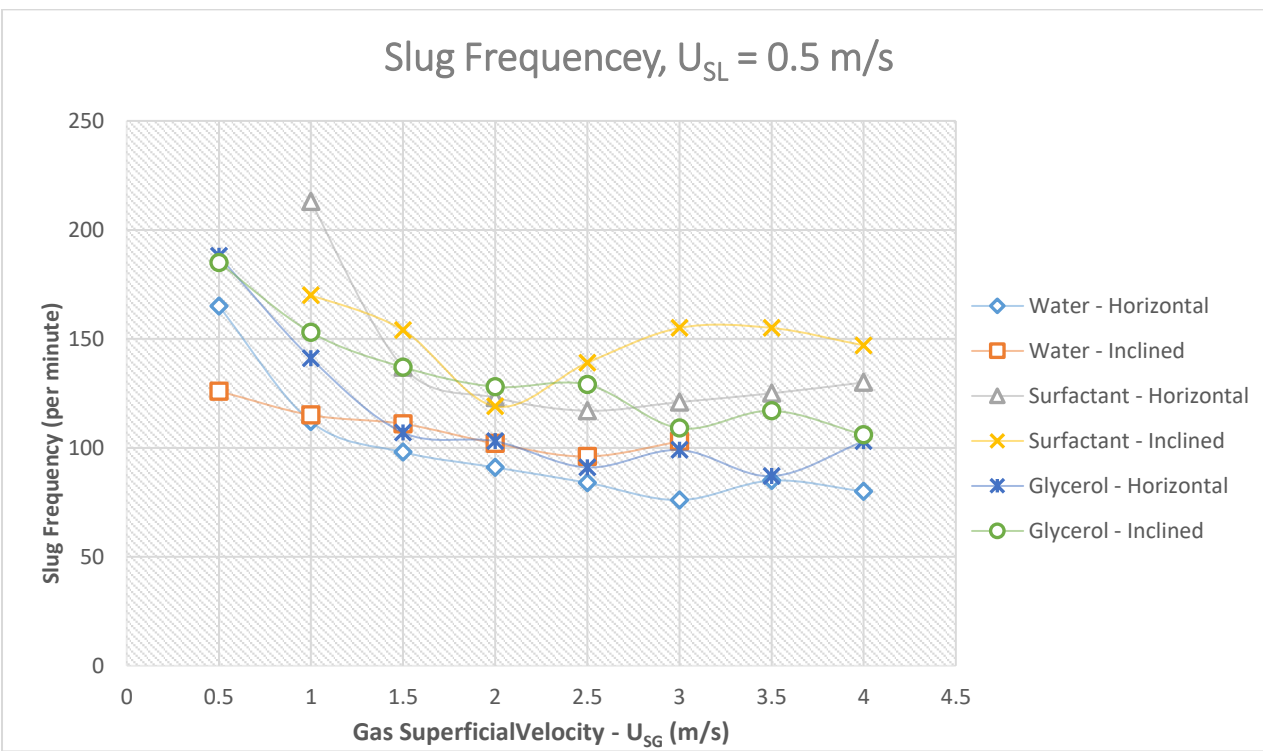

Figure 5.32: Experimental slug frequency, F_S vs U_{SG}, at U_{SL} = 0.5m/s

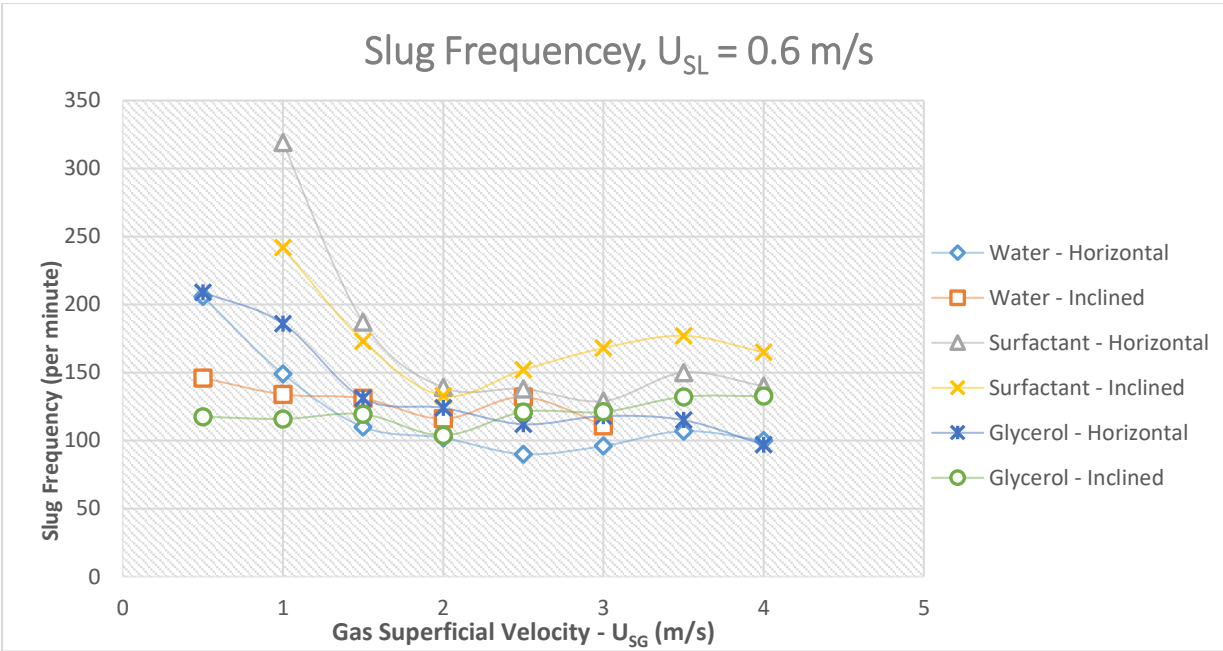

Figure 5.33: Experimental slug frequency, F_S vs U_{SG}, at U_{SL} = 0.6m/s

5.13 Factors Affecting Slug Frequency

The rate at which liquid slugs occur and propagate along the pipe depends on various factors. The key factors affecting slug frequency encountered in this research are flow rate, liquid properties, and pipe orientation (inclination).

Effects of Liquid Superficial Velocity: Generally, increasing the liquid superficial velocity can lead to higher slug frequencies, because higher liquid velocity enhances the liquid momentum and shear forces, contributing to slug formation and propagation. However, the effects of liquid superficial velocity on slug frequency are more complex. At very high liquid velocities, the liquid phase may dominate the flow, suppressing slug formation and leading to a transition to annular or dispersed flow regimes. This can be seen in Figures 5.26, 5.27, and 5.28, when the liquid superficial velocity was increased at a constant gas superficial velocity, the slug frequency curves rise steeply and eventually flattens indicating a decrease in slug frequency. Although slug length data was not captured in this experimental campaign, it was observed that increasing liquid velocity contributes to elongating and stretching the liquid slugs, resulting in larger liquid volumes being carried

between gas pockets. As a result, the slugs become more extended along the pipe length, leading to longer slug lengths.

Effects of gas superficial velocity: Gas superficial velocity also has a significant impact on slug frequency in multiphase flow, increasing the gas superficial velocity leads to a higher slug frequency. Higher gas velocity provides more momentum and shear forces, which promotes the formation and propagation of gas pockets or bubbles. The increased gas velocity enhances the entrainment of liquid into the gas phase, resulting in the formation of larger and more frequent slugs. At higher gas velocities, the slugs exhibit increased stability due to enhanced gas-liquid interaction and better confinement of the liquid phase. This can result to a more organized and persistent slug flow pattern, contributing to a higher slug frequency.

Changes in gas superficial velocity can also induce transitions between different flow patterns, which can impact slug frequency. For example, increasing the gas superficial velocity while keeping the liquid superficial velocity constant may lead to a transition from stratified flow to stratified wavy to slug flow, resulting in an increase in slug frequency. The gas/liquid velocity ratio also plays a crucial role in determining slug frequency. An increase in the gas/liquid velocity ratio tends to increase the slug frequency. When the gas velocity is significantly higher than the liquid velocity, it can create favourable conditions for slug flow patterns to form and propagate.

Effects of viscosity: The liquid's viscosity has a significant impact on slug frequency, as the viscosity of the liquid phase increases, slug frequency tends to decrease. Higher viscosity results in greater resistance to flow and reduces the ability of the liquid to form and propagate as slugs. The increased viscosity hinders the entrainment of liquid into the gas phase, leading to smaller and less frequent slugs. Smaller and shorter slugs were observed with the air-glycerol solution flow. The increased viscosity restricts the stretching and elongation of the liquid slugs, leading to reduced liquid volumes being carried between the gas pockets. Consequently, the slugs become shorter in length and have a smaller liquid holdup. More stable slugs were also observed in air-glycerol solution flow, this is because higher liquid viscosity generally leads to more stable slugs due to increased internal

damping forces and resistance to interfacial deformation. The higher viscosity enhances slug cohesion and reduces slug breakup, resulting in more persistent and less fragmented slug flow patterns.

Effects of surface tension: Surface tension is responsible for the cohesive forces between liquid molecules at the liquid-gas interface. Increased surface tension promotes the formation of smaller liquid slugs and enhances the breakup of liquid films or ligaments, resulting in more frequent slug formation. Lower surface tension generally leads to larger and longer slugs. Reduced surface tension weakens the cohesive forces between liquid molecules, allowing for the formation of larger liquid slugs. The larger slug size and length can result in a higher liquid holdup and more substantial liquid volumes being carried between the gas pockets. Surface tension affects the coalescence of liquid slugs. Higher surface tension inhibits slug coalescence, preventing the merging of adjacent liquid slugs. This can result in more discrete and well-separated slugs, contributing to a higher slug frequency.

Effects of pipe inclination: A notable effect on slug frequency was observed with pipe inclination. As the pipe orientation was changed from horizontal to inclined flow, the gravitational forces acting on the liquid and gas phases also changes. The inclination creates a gravitational component that aids the downward movement of liquid slugs and the upward movement of gas pockets. This enhances slug formation and promotes more frequent slug flow patterns. In inclined pipes, the slugs become elongated along the pipe axis. The liquid slugs tend to stretch and cover a longer length, while the gas pockets become compressed. This can result in longer slugs with a smaller liquid holdup. The gravitational component in the inclined pipes enhances the stability of liquid slugs by providing additional confining forces. This leads to more organized and persistent slug flow patterns with reduced slug breakup and fragmentation.

5.14 Chapter Summary

In this chapter, the hydrodynamic behaviour of multiphase flow was experimentally investigated in a horizontal pipe and a 15^{O} upward inclined pipe. Three different liquids

were used, tap water, surfactant solution, and glycerol solution. The objective is to study the effects of liquid properties on multiphase flow behaviour. Seven main flow regimes were identified, these are stratified smooth flow, stratified wavy flow, stratified frothy flow, elongated bubble flow, slug flow, churn flow, and bubbly flow. The specific flow regimes from different pipe orientations were also determined and a flow regime map was developed to graphically present them.

Pressure drop data along the flow system was also collected using a different pressure transducer. The effects of liquid properties, flow velocities, and pipe inclination on pressure drop were explored. It was seen that the effects of these factors are not always linear. Several mechanisms that drive pressure drop changes were discussed. Gravitational pressure drop dominates with increasing inclination angle at low gas & liquid velocities. Meanwhile, frictional pressure losses result from shear stresses at the interfacial boundaries between the phases and the phases and pipe walls due to an increase in flow velocity and an increase in liquid viscosity.

The liquid holdup is another important multiphase flow parameter studied in this chapter. The liquid holdup was observed to vary depending on the flow regime, fluid properties, flow rates, and pipe inclination. Different flow patterns exhibit different liquid holdup characteristics. For example, stratified flow tends to have a higher liquid holdup compared to dispersed flow or bubbly flow. Higher liquid flow rates generally lead to higher liquid holdup, as there is a larger volume of liquid being transported through the system. While higher-viscosity liquids may have higher viscosity and upward pipe inclination both have higher holdup due to increased residence time

One of the most dominant flow patterns observed in the experimental campaign is slug flow, and the slug frequency data was obtained analysed from the flow video record. The slug frequency was influenced by several factors such as liquid properties, gas/liquid flow rates, and pipe orientation.

Chapter 6

Conclusions and Recommendations

The general aim of the present project was to carry out computational and experimental studies to provide fresh insights into multiphase flow behaviour, with a particular interest in slug flow and the influence of liquid properties and pipe inclination. This chapter summarises the key findings from the work and gives recommendations for future work.

6.1 Key Findings

Effects of Liquid Properties on Taylor Bubble Behaviour: Simulated liquids were used to computationally study the effects of liquid's physical properties (viscosity, density, and surface tension) on Taylor bubbles, a distinguishing feature of slug flow. It was found out that the liquid density has little or no influence on the behaviour of the bubble, while surface tension's effects become prominent with an increase in the pipe's inclination. Viscosity however plays a dominant role at all pipe inclinations.

The Influence of Liquid Properties on Flow Regimes: Liquid properties play a significant role in flow pattern behaviour. determining the flow regime in multiphase flow systems. The viscosity of the liquid phase influences the resistance to flow and the ability of the phases to mix or separate. While surface tension affects the stability of the liquid-gas interface. Higher surface tension tends to promote stratified smooth or stratified wavy flow, while lower surface tension can result in frothy flow or dispersed slug flow. Seven main flow regimes were identified, these include stratified smooth flow, stratified wavy flow, stratified frothy flow, elongated bubble flow, slug flow, churn flow, and bubbly flow.

Effects of Liquid Properties on Pressure Drop: Liquid properties can have a significant impact on pressure drop in a fluid system. Higher-viscosity liquids tend to have higher pressure drops due to increased internal friction between the liquid layers as they move past each other. This results in greater energy losses and requires higher driving pressures to maintain the same flow rate. While surface tension does not directly affect pressure drop in

bulk flow, it can influence flow patterns and liquid distribution in multiphase systems. Variations in surface tension can lead to different flow regimes, interfacial instabilities, and pressure drop changes in two-phase or multiphase flow systems.

Effects of Liquid Properties on Liquid Holdup: Liquid properties show to have an impact on the liquid holdup, the viscosity of the liquid affects the flow behaviour and distribution of phases in a multiphase flow. Higher-viscosity liquids tend to have higher liquid holdup as they offer more resistance to flow and have a greater tendency to accumulate in certain regions of the flow system. This can result in a higher fraction of liquid occupying the cross-sectional area. The interfacial tension between the liquid and gas phases can affect the stability and coalescence of liquid droplets or bubbles. A higher interfacial tension can promote the formation of smaller droplets or bubbles, leading to a larger interfacial area and potentially increasing the liquid holdup.

Effects of Liquid Properties on Slug Frequency: Liquid properties can influence the frequency at which slugs form in a multiphase flow. The viscosity of the liquid plays a crucial role in determining the slug frequency. Higher viscosity liquids tend to form slugs less frequently due to their resistance to flow and reduced ability to disperse into smaller liquid plugs. Instead, they tend to form longer and less frequent slugs. The interfacial tension between the liquid and gas phases affects the stability and coalescence of liquid plugs. Higher interfacial tension tends to inhibit slug formation by promoting the coalescence of liquid plugs into larger slugs. Lower interfacial tension can lead to the formation of smaller, more frequent slugs.

6.2 Key Contributions

Independent effects of liquid properties on slug flow: The simulation work in this research has provided a better understanding of the unique independent effects of liquid properties on slug flow translational velocity. The simulation results have also shown that liquid density has no effect on the drift velocity of a Taylor bubble, at all flow inclinations, while the effects of surface tension become notable only when the flow inclination is at 45^{O} or above, surface tension has no effect on the slug translational velocity when the flow inclination is less than 45^{O} upwards. This feature has never been reported by previous

researchers based on the review done so far, as no previous work has singled out one liquid physical property to study its effect while keeping the other properties constant.

Generated data: One of the most critical contributions of this work is the generation of quality two-phase flow data. Four main flow parameters (flow regime, pressure drop, liquid holdup, & slug frequency) were explored across three different air-liquid (water, surfactant solution and glycerol solution) multiphase flow systems in two pipe orientations, horizontal and 15^{O} up inclined pipe.

Developed flow regime maps: As part of this work, flow regime maps specific to the three liquids studied (water, surfactant solution and glycerol solution) were developed for horizontal and 15^{O} upward inclined pipe. Good agreement was obtained when the flow data was compared with Taitel and Duckler's (1976) air-water flow regime for horizontal pipe.

6.3 Recommendations and future work:

Model development: The simulation result has provided over a terabyte of data for Taylor bubble drift velocities in different liquids and pipe inclinations. Taylor bubble drift velocity is an important parameter in slug flow models which is used in pipeline design and design of separation equipment in oil and gas processing facilities. Most of the drift velocity correlations have low predictive capabilities as they do not adequately account for the effects of fluid properties such as viscosity and surface tension. The simulation data generated will be used in proposing a unified drift velocity model that considers the fluid properties, pipe geometry, and inclination, in terms of dimensionless numbers.

In addition to Taylor bubble drift velocity, the simulation has provided more insight into the effects of liquid properties in the coalescence and breakage of bubbles. It has been believed that coalescence and breakage of bubbles play a crucial role in intermittent flow pattern transition in multiphase systems. A time series plot of the cross-sectional average void

fraction will be used to show how different liquid properties caused coalescence and breakage of bubbles in vertical and inclined multiphase flow.

Experimental work with more pipe orientations: The experimental data collected during this study was for a 19 mm pipe diameter at horizontal and 15^{O} upward inclination. Collecting data of more pipe inclinations and different pipe diameters will enable a comparative study leading to a better understanding of the effects of liquid properties on flow patterns, pressure and void fractions in relative to pipe size and angle of inclination.

List of References

Abdalla (2020); Novel Model for Simulating Performance of Twin Screw Multiphase Pumps Capable Of Handling high (GVF) With Nodal Analysis to study Reservoir/well/pump Interactions; Department of Environment, Land and Infrastructure Engineering,

Abdalellah O. Mohmmed a, Mohammad S. Nasif a, Hussain H. Al-Kayiem a, Rune W. Time Flow Measurement and Instrumentation Volume 50, August 2016, Pages 112-120

Abdul-Majeed, G.H.; (2000) Liquid Slug Holdup In Horizontal And Slightly Inclined **Two-Phase Slug Flow.** *J Pet Sci Eng. 2000;27(1-2):27-32. doi:10.1016/S09204105(99)00056-X.*

Abulencia, J.P; Theodore, L; 2009. **"Fluid Flow for the Practicing Chemical Engineer."** 1st Ed. New Jersey: A John Wiley & Sons, Inc.

Aziz, K. & Govier, G. W. (1972); **The Flow of Complex Mixtures in Pipes** *New York: Van Nostrand Reinhold Company.*

Al-Aweet, F. M; (2008); **The development of capacitance measurement techniques and data processing methods for the characterisation of two-phase flow phenomena in horizontal and inclined pipelines.** *PhD thesis, University of Manchester.*

Baba, Yahaya & Aliyu, Aliyu & Archibong-Eso, A. & Abdulkadir, Mukhtar & Lao, L. & Yeung, Hoi. (2018). Slug length for high viscosity oil-gas flow in horizontal pipes: Experiments and prediction. Journal of Petroleum Science and Engineering. 165. 10.1016/j.petrol.2018.02.003.

Bakker, A., Haidari, A. H. and Oshinowo, L. M.; (2001); **Realize greater benefits from CFD, fluid/solids handling.** *AIChE's CEP magazine*, March, 45-53.

Barnea, D., Shoham, O., and Taitel, Y., (1982), "**Flow pattern transition for downward inclined two phase flow; horizontal to vertical**", *Chemical Engineering Science*, Vol. 37, No. 5, pp. 735-740.

Barnea, D., Brauner, N.; (1985); **Holdup of The Liquid Slug In Two Phase Intermittent Flow;** *Int J Multiph Flow. 1985;11(1):43-49. doi:10.1016/0301-9322(85)90004-7*

Brito R.; (2012); **Effect of Medium Oil Viscosity on Two-Phase Oil-Gas Flow Behavior In Horizontal Pipes.** 2012.

Al-Safran E.; (2016); Investigation and Prediction Of Slug Frequency In Gas/Liquid **Horizontal Pipe Flow.** *J Pet Sci Eng. 2009;69(1-2):143-155. doi:10.1016/j.petrol.2009.08.009.*

Al-Safran E.; (2016); Probabilistic Modelling of Slug Frequency In Gas/Liquid Pipe Flow **Using The Poisson Probability Theory**. *J Pet Sci Eng*. 138:88-96. doi:10.1016/j.petrol.2015.12.008.

Baker, O., (1954), "**Simultaneous flow of oil and gas**", *Oil and Gas J.* Vol. 53, No. 12, pp. 185-195.

Baker, O., (1957), "**Discussion on how uphill and downhill flow affect pressure drop in two-phase pipelines in hilly country**", *Oil and Gas J.*, pp. 150-152.

Beggs, H. D. and Brill, J. P., (1973), "**A Study of Two-Phase Flow in Inclined Pipes**", *J. Pet. Tech.*, pp. 607-617

Bello, A. M., (2006), **"Experimental Studies of Multiphase Flow In Horizontal and Inclined Pipes"**; *Ph.D.* Thesis, *University Of Leeds*

Bendiksen K.H; (1984); An Experimental Investigation Of The Motion Of Long Bubbles In Inclined Tubes. Int J Multiph Flow.;10(4):467-483. doi:10.1016/0301-9322(84)90057-0

Benjamin, T. B., (1968), "**Gravity currents and related phenomena**", *Journal of Fluid Mechanics*, Vol. 31, pp. 209-248.

Bertani, C; Salve, M; 2010; **State-of-Art and Selection of Techniques in Multiphase Flow Measurement**. *Ital Natl Agency*.

Bird, R.B; Stewart, W.E; Lightfoot, E.N.; **Transport Phenomena**; *John Wiley & Sons, 2nd Revised Edition;* 2007

Bilicki, Z. and Kestin, J., (1987), "**Transition criteria for two-phase flow patterns in vertical upward flow**", *International Journal of Multiphase Flow*, Vol. 13, No. 3, pp. 283294.

Bratland, Ove; 2009; **Pipe Flow 1: Single-Phase Flow Assurance;** *drbratland.com*. Bratland, Ove; 2010; **Pipe Flow 2: Multi-Phase Flow Assurance;** *drbratland.com*.

Brill, J.P; 2010; **Modelling Multiphase Flow in Pipes;** *The Way Ahead 06 (02): 16–17. Paper Number: SPE-0210-016-TWA;*

Brill J.P, Schmidt Z, Coberly W.A, Herring J.D, Moore D.W; (1981) **Analysis of Two-Phase Tests in Large-Diameter Flow Lines In Prudhoe Bay Field**. *Soc Pet Eng J.1981;21(3):363378.*

Carrizales M. J; Jaramillo, J. E; and Fuentes. D; 2015 **"Prediction of Multiphase Flow in Pipelines"** *Ing.Cienc., vol. 11, no. 22, pp. 213–233.*

Cook, C.H, Newton, M.B.; (1995); **Experimental Investigtion of Air-Water Slug Flow in Horizontal Pipes and Comparison with Existing Models.** *Twefth Aust Fluids Mech Conf.*

Colmenares, J., Ortega, P., Padrino, J., Trallero. J.L.; (2001); **Slug Flow Model for the Prediction of Pressure Drop for High Viscosity Oils in a Horizontal Pipeline.** *Proc SPE Int Therm Oper Heavy Oil Symp. 2001. doi:10.2523/71111-MS.*

Crawford, T., Weinberger, C. & Weisman, J.; (1985).; **Two-Phase Flow Patterns And Void Fractions In Downward Flow Part I: Steady-State Flow Patterns**. *International Journal of Multiphase Flow, 11, 761-782.*

Davies R.M, Taylor G.I; (1950) **The Mechanics of Large Bubbles Rising through Extended Liquids and through Liquids in Tubes.** Proc R Soc A Math Phys Eng Sci.; 200(1062):375-390. doi:10.1098/rspa.1950.0023.61.

Delnoij, E., Kuipers, J. A. M., and vanSwaaij, W. P. M.; (1999).; **A ThreeDimensional CFD Model For Gas-Liquid Bubble Columns.** *Chemical Engineering Science*, 54,2217-2226.

De Schepper, S. C. K., G.J. Heynderickx and G. B. Marin (2008).; **CFD Modeling Of All Gas Liquid And Vapor Liquid Flow Regimes Predicted By The Baker Chart**. *Chemical Engineering Journal*, 138(13), 349-357.

Drew, D. A; (1983); **Mathematical Modeling of Two-Phase Flow.** *Annual Reviews in Fluid Mechanics*, 15, 261-291.

Dukler, A. E. and Hubbard, M. G., (1975), "**A Model for Gas-Liquid Slug Flow in Horizontal and Near Horizontal Tubes**", *Ind. Eng. Chem. Fundamentals*, Vol. 14, No. 4, pp. 337-347.

Dukler, A. E., Maron D. M., and Brauner N., (1985), "**A Physical Model for Predicting the Minimum Stable Slug Length**", *Chemical Engineering Science*, Vol. 40, pp. 1379.

Domgin, J., Huilier, D. G. F., Burnage, H., and Gardin, P.; (1997); **Coupling Of A Lagrangian Model With A CFD Code: Application To The Numerical Modelling Of The Turbulent Dispersion Of Droplets In A Turbulent Pipe Flow.** *Journal of Hydraulic Research*, 35, 473-488.

Esam M. Abed and Zainab K. Ghoben.; Gas-Liquid Slug Frequency and Slug Unit Length in Horizontal Pipes; The Iraqi Journal for Mechanical and Materials Engineering · January 2015

Fabre, J. and Liné, A., (1992), "**Modelling of Two Phase Slug Flow**", *Annu. Rev. Fluid Mech*, Vol. 24, pp. 21-46.

Ferziger, J. H. and M. Perić (2002); **Computational Models for Fluid Dynamics** (*Third Edition*). Springer, Berlin.

Flanigan, O., (1958), "**Effect of uphill flow on pressure drop in design of two-phase gathering systems**", *Oil and gas journal*, Vol. 56, No. 10, pp. 132.

Fluent; (2018); **19.2 User's Guide;** ANSYS Inc.

Ghajar A.J; 2005; **Non-Boiling Heat Transfer in Gas-Liquid Flow in Pipes;** *Technical Papers, J. Braz. Soc. Mech. Sci. & Eng. 27 (1);* Mar 2005

Gharaibah, E., Read, A., Scheuerer, G. et al. (2015), Overview of cfd multiphase flow simulation tools for subsea oil and gas system design, optimization and operation, in 'OTC Brasil', Offshore Technology Conference.

Gokcal B; 2008; **An Experimental and Theoretical Investigation of Slug Flow for High Oil Viscosity in Horizontal Pipe;** *Thesis/dissertation Ph. D. University of Tulsa 2008* Golan, L. P. 1968. **An Air-Water Study of Vertical Upward and Downward Two-Phase Flow.**

Gomes, T. S; (2016); Multiphase Flow Loop for the Near Horizontal Hydronamics Parameters Measurement: Design, Construction, and Commissioning; *M.Sc*

Dissertation, Texas Tech University

Gould, T. L., Tek, M. R., and Katz, D. L., (1974), "**Two-phase flow through vertical, inclined or curved pipes**", *J. Pet. Tech.*, Vol. 19, pp. 815-828.

Gregory, G. A. and Scott, D. S., (1969), "**Correlation of liquid slug velocity and frequency in horizontal co-current gas-liquid slug flow**", *AIChE Journal* , Vol. 15, pp. 833-835.

Gregory, G. A., (1974), "**Comments on the predictions of liquid holdup for gas-liquid flow in inclined pipes**", *The Canadian Journal of chemical engineering*, Vol. 52, pp. 438-448.

Gregory, G.A., Nicholson, M.K., Aziz, K., (1978); **Correlation Of The Liquid Volume Fraction In The Slug For Horizontal Gas-Liquid Slug Flow.** *Int J Multiph Flow. 1978;4(1):33-39. doi:10.1016/0301-9322(78)90023-X.*

Greskovich, E. J. and Shrier, A. L., (1972), "**Slug frequency in horizontal gas-liquid slug flow**", *Ind. Eng. Chem. Proc. Design Dev.*, Vol. 11, No. 2, pp. 317-318.

Greskovich, E. J., (1973), "**Prediction of gas-liquid hold-up for inclined flows**", *AIChE Journal* , Vol. 19, No. 5, pp. 1060-1061.

Gomez, L. E., Shoham, O., and Taitel, Y., (2000), "**Prediction of slug liquid holdup horizontal to upward vertical flow**", *International Journal of Multiphase Flow*, Vol. 26, pp. 517-521.

Guzhov, A. I., Mamayev, A. A., and Odishariya G.E., (1967), "**A study of transportation in gas-liquid systems**", *10th Intern. Gas Conf. Hamburg Germany*,

Hanyang G. and G. Liejin, "Modeling of bubble shape in horizontal and inclined tubes," Progress in Nuclear Energy, vol. 89, pp. 88–101, 2016. pages 164

Hasan AR, Kabir CS. (1988); **Predicting Multiphase Flow Behviour in a Deviated Well.** *SPE Prod Eng. 3(4):474-482. doi:10.2118/15449-PA.*

Hernandez-Perez, V., Abdulkadir, M., Azzopardi B.J.; (2010) **Slugging Frequency Correlation for Inclined Gas-liquid Flow.** *World Acad Sci, Eng. 2010;2(5):44-51. http://www.waset.ac.nz/journals/waset/v61/v61-8.pdf.*

Hewitt, G.F; 2011; **Gas-Liquid Flow**. http://www.thermopedia.com/content/2/. (Last Accessed: May 25, 2022).

Hewitt, G.F, Manolis, I.G, Mendes-Tatsis M.A, (1995), "**The Effect of Pressure on Slug Frequency on Two-Phase Horizontal Flow**", *The 2nd conference on multiphase flow, Kyoto, Japan, April 3-7, 1995*.

Heywood, N. I. and Richardson, J. F., (1979), "**Slug Flow of Air-Water Mixtures in a Horizontal Pipe: Determination of Liquid Hold-up by -ray Absorption**", *Chemical Engineering Science*, Vol. 34, pp. 17-30.

Hill, T.J, Wood D.G; (1990); **New Approach to the Prediction of Slug Frequency.** *In:*

Proceedings - SPE Annual Technical Conference and Exhibition. Vol Pi. Publ by Soc of Petroleum Engineers of AIME; 1990:141-149.

Hill, T.J, Wood D.G; (1994); **Occurrence, Consequences, and Prediction.** *In: Proceedings of the University of Tulsa Centennial Petroleum Engineering Symposium. Society of Petroleum Engineers (SPE); 1994:53-62.*

Hjertager, L. K., B. H. Hjertager and T. Solberg (2002). CFD modelling of fast chemical reactions in turbulent liquid flows. *Computers & Chemical Engineering*, 26(4-5), 507-515.

Hubbard, M. G., (1965), "**An Analysis of Horizontal Gas-Liquid Slug**", *Ph. D. Thesis, University of Houston, Houston USA.*

Iskandar, F; Dwinanto, E; Abdullah, M; Khairurrijal, K; and Muraza, O; 2016; Viscosity Reduction of Heavy Oil Using Nanocatalyst in Aquathermolysis Reaction *KONA Powder and Particle Journal No. 33 2016005 Review Paper*

Jeyachandra, B.C. (2011); **Effect of Pipe Inclination on Flow Characteristics of High Viscosity Oil-Gas Two-Phase Flow.** 2011.

Jeyachandra, B. C. ; B. Gokcal*1, A. Al-sarkhi2, C. Sarica1, A. K. Sharma1; 2012; Drift

Velocity Closure Relationships for Slug Two-Phase High Viscosity Oil Flow in Pipes; SPE Journal

Jaworski, Z. and P. Pianko-Pprych (2002).; **Two-Phase Laminar Flow Simulations in a Kenics Static Mixer. The Standard Eulerian and**

Lagrangian Approaches; *Transactions IChemE, Chemical Engineering Research and Design*, Part A, 80, 910-916.

Jean Fabre and Bernardo Figueroa-Espinoza2; (2014) Journal of Fluid Mechanics, vol. 755. pp. 485-502. ISSN 0022-1120; Taylor bubble rising in a vertical pipe against laminar or turbulent downward flow: symmetric to asymmetric shape transition.

Jepson, W. P. and Taylor, R. E., (1993), "**Slug flow and its transitions in large-diameter horizontal pipes**", *International Journal of Multiphase Flow*, Vol. 19, No. 3, pp. 411-420.

Kaya, A. S., Sarica, C., and Brill, J. P., (2001), "**Mechanistic modelling of two-phase flow in deviated wells**", *SPEPF*, Vol. 156,

Kolev, N.I; Multiphase Flow Dynamics 4: Turbulence, Gas Adsorption and Release,

Diesel Fuel Properties. *Springer Berlin Heidelberg;39-65. doi:10.1007/978-3-642-207495_2;* 2012

Kora, C., Sarica, C., Zhang, H.Q., Al-Sarkhi, A., Fahd, K., Al-Safran, E.M., (2011); **Effects of High Oil Viscosity on Slug Liquid Holdup in Horizontal Pipes**. *SPE Can Unconvetional Resour Conf 2011. 2011;(November):1-15. doi:10.2118/102727-MS.*

Kordyban, E. S., (1985), "**Some Details of Developing Slugs in Horizontal Two-Phase Flow**", *AIChE J.*, Vol. 31, pp. 802 .

Kouba, G. E., (1987), "**Horizontal slug flow modelling and metering**", *PhD thesis. Dept. of petroleum engineering. University of Tulsa*, Vol.

Kumar S , Chandrasekaran S*,; Flow Pattern and Liquid Holdup Prediction in Multiphase Flow by Machine Learning Approach; Petroleum Engineering Program, Department of Ocean Engineering, IIT-Madras, India

Launder, B. and Spalding, D., (1974), "**The numerical computation of turbulent flows**", *Computer Methods in Applied Mechanics and Engineering* , Vol. 3, pp. 269-289.

Li, J.; (1995); **Piecewise Linear Interface Calculation;** *C. R. Acad. Sci. Paris S´er. II*, 320, 391–396.

Lopez de Bertodano, M., S. -J. Lee, Jr. R. T. Lahey and D. A. Drew; (1990); **The Prediction of Two-Phase Distribution Phenomena Using a Reynolds Stress Model.** *Journal of Fluids Engineering*, 112, 107-113.

Lu M; (2015); Experimental and Computational Study of Two-Phase Slug Flow; *PhD Thesis, Imperial College London*

Mandhane, J. M., Gregory, G. A., and Aziz, K., (1974), "**A flow pattern map for gas-liquid flow in horizontal pipes**", *International Journal of Multiphase Flow*, Vol. 1, pp. 537.

Marcano R, Chen X.T, Sarica C, Brill J.P.; (1998); **Study of Slug Characteristics for TwoPhase Horizontal Flow.** *In: Proceedings of the SPE International Petroleum Conference & Exhibition of Mexico. Soc Pet Eng (SPE); 1998:213-219.*

Mattar, L. and Gregory, G. A., (1974), "**Air-oil slug flow in an upward inclined pipe I, slug velocity, holdup and pressure gradient**", *The Journal of Canadian Petroleum Technology*, pp. 69.

Mukherjee, H. and Brill, J. P., (1985), "**Empirical equations to predict flow patterns in two-phase inclined flow**", *International Journal of Multiphase Flow*, Vol. 11, No. 3, pp. 299315.

Meribout, Mahmoud; Faisal Shehzad, Nabil Kharoua, Lyes Khezzar; 2020; Gas-liquid twophase flow measurement by combining a Coriolis flowmeter with a flow conditioner and analytical models

Nguyen, V. T. & Spedding, P. (1977). **Holdup in Two-Phase, Gas-Liquid Flow—II:**

Experimental Results. *Chemical Engineering Science, 32, 1015-1021.*

Nicholson, M. K., Aziz, K., and Gregory, G. A., (1978), "**Intermittent two-phase flow in horizontal pipes: Predictive models**", *The Canadian Journal of chemical engineering*, Vol. 56, pp. 653-663.

Nicklin, O. J., Wilkes, J. O., and Davison, J. F., (1962), "**Two-phase flow in vertical tubes**", *Transactions of the institute of Chemical Engineers*, Vol. 40, pp. 61-68.

Noh, W. and P. Woodward (1976); **SLIC (simple line interface calculation), in: A. van de Vooren, P. Zandbergen (Editions.)**; *Proceedings of the 5th International Conference on Fluid Dynamics*, 59: Lecture Notes in Physics, Springer, Berlin, 330– 340.

Norris, L.; (1982); **Correlation of Prudhoe Bay Liquid Slug Lengths and Holdups Including Large Diameter Flow Line Tests.;** *Intern Report, Exxon Prod Res Co*. 1982.

Nydal, O. J., (1991), "**An experimental investigation of slug flow**", *PhD thesis, University of Oslo*.

Okezue C.N; (2013) Application Of The Gamma Radiation Method In Analysing The

Effect Of Liquid Viscosity And Flow Variables On Slug Frequency In High Viscosity Oil-Gas Horizontal Flow. *WIT Trans Eng Sci. 2013;79(4):447-461. doi:10.2495/MPF130371.*

Oshinowo, T. & Charles, M.; (1974).; **Vertical Two-Phase Flow: Part II. Holdup and Pressure Drop**. *The Canadian Journal of Chemical Engineering, 52, 438-448.*

Paladino, E, E; Stud of Multiphase Flow in Differential Pressure Type Flow Meters; *PhD*

Thesis - Federal University of Santa Catarina, Technological Centre. Graduate Program in Mechanical Engineering; 2005

Patten, T; **Understanding the Challenges of Two-Phase Flow: Micro Motion White Paper** *Micro Motion Inc.* Available online https://www.emerson.com/documents/automation/whitepaper-understanding-challenges-of-two-phase-flow-micro-motion-en-66308.pdf

Ramdin, M; 2010; **Benchmarking of Computational Fluid Dynamics for Multiphase Flows in Pipelines** *Delft University of Technology.*

Ranade, V.; (2002); **Computational Flow Modeling For Chemical Reactor Engineering.** Academic Press.

Rashmi G. W., T. S. Y. Choong, S. A. Hussain, M. Khalid and T. G. Chuah (2009); **Numerical Study Of Dispersed Oil–Water Turbulent Flow In Horizontal Tube.**
Journal of Petroleum Science and Engineering, 65, 123–128.

Rhee, S. H., Makarov, B. P., Krishnan, H., and Ivanov, I., (2004), "**Assessment of Numerical Techniques in Volume of Fluid Method for Free-Surface Wave Flows**", *9th Symposium on Practical Design of Ships and Other Floating Structures*, Luebeck-Travemuende, Germany.

Rosa, E.; (2004); **Flow Structure in the Horizontal Slug Flow**. *9th BRAZILIAN Congress on Thermal Engineering* 2004;3(2):1-11 .http://www.abcm.org.br/pt/wpcontent/anais/encit/2002/Paper-title/10/CIT02-0143.PDF.

Ribeiro, Joseph & Liao, Ruiquan & Aliyu, Aliyu & Zilong, Liu. (2019). Prediction of Pressure Gradient in Two and Three-Phase Flows in Vertical Pipes Using an Artificial Neural Network Model.

Roitberg, E. D. Barnea, and L. Shemer, "Elongated bubble shape in inclined air-water slug flow," International Journal of Multiphase Flow, vol. 85, pp. 76–85, 2016. pages 164

Shaw, C. T.; (1992); **Using Computational Fluid Dynamics.** Prentice Hall International (UK) Ltd.

Scott, S. L., Shoham, O., and Brill JP.; (1987); **Modelling Slug Growth in Large Pipe Diameter Pipes**. *Pap B2, Present 3rd Int Conf Multiph Flow, Hague*. 1987.

Shoham, O.; Mechanistic Modeling of Gas-Liquid Two-Phase Flow in Pipes; *Society of*

Petroleum Engineers; 2006

Siddiqui M.I., Munir S., Heikal M.R., Rashid Aziz A.A., Dass S.C.; (2015); **Slug Dynamics in a Nearly Horizontal Pipe Using Non-Invasive**

Measurement Techniques. *Mod Appl Sci*. 2015;9(9):50-57. doi:10.5539/mas.v9n9p50.

Spedding, P. L. and Nguyen, V. T., (1976), "**Regime maps for air-water two-phase flow**", *Chemical Engineering Science,* Vol. 35, pp. 779-793.

Sverdrup H.U; Johnson M.W; Fleming R.H; **The Oceans Their Physics, Chemistry, and General Biology**. *New York: Prentice-Hall, Inc.;* 1942.

Taitel, Y. and Dukler, A. E., (1976), "**A Model for Predicting Flow Regime Transition in Horizontal and Near Horizontal Gas-Liquid Flow**", *AIChE. Journal*, Vol. 22, No. 1, pp.
47-55.

Taitel, Y., Lee, N., and Dukler, A. E., (1978), "**Transient Gas-Liquid flow in horizontal pipes: Modelling the flow pattern transitions**", *AIChE Journal*, pp. 920.

Taitel, Y., Barnea, D., and Dukler, A. E., (1980), "**Modelling flow pattern transitions for steady upward gas-liquid flow in vertical tubes**", *AIChE Journal*, Vol. 26 , No. 3, pp. 345354.

Taitel Y, Barnea D. (1990); A Consistent Approach For Calculating Pressure Drop In

Inclined Slug Flow. *Chem Eng Sci. 1990;45(5):1199-1206. doi:10.1016/00092509(90)87113-7.*

Tronconi, E., (1990), "**Prediction of Slug Frequency in Horizontal Two-Phase Slug Flow**", *AIChE Journal*, Vol. 36, No. 5, pp. 701-709.

Ubbink O.; (1997); **Numerical Prediction Of Two Fluid Systems With Sharp Interfaces**; *Ph.D. Thesis, Dept. of Mechanical Engineering, Imperial College of Science, Technology & Medicine.*

Van Wachem, B. G. M. and A. E. Almstedt; (2003); **Methods for Multiphase Computational Fluid Dynamic.** *Chemical Engineering Journal*, 96(1-3), 81-98. Versteeg, H. K. and Malalasekera, W.; (1996); **Introduction to computational fluid dynamics: the finite volume method**; Addison-Wesley.

Weber, M. E., (1981), "**Drift in Intermittent Two-Phase Flow In Horizontal Pipes**", *Canadian Journal of Chemical Engineering*, Vol. 59, pp. 398-399.

Weber M.E, Alarie A, Ryan M.E.; (1986); **Velocities Of Extended Bubbles In Inclined Tubes**; Chem Eng Sci.;41(9):2235-2240. doi:10.1016/0009-2509(86)85073-4.

Weisman, J. and Kang, S. Y., (1981), "**Flow pattern transitions in vertical and upwardly inclined lines**", *International Journal of Multiphase Flow*, Vol. 7, No. 3, pp. 271-291.

Xiao J.J, Shonham O, Brill J.P. ;(1990); **A Comprehensive Mechanistic Model for TwoPhase Flow in Pipelines.** SPE Annu Tech Conf Exhib. 1990:167-180. doi:10.2118/20631MS.

Yahaya D. Baba, Archibong E. Archibong, Aliyu M. Aliyu, Abdulhaqq I. Ameen,Slug frequency in high viscosity oil-gas two-phase flow: Experiment and prediction, Flow

Measurement and Instrumentation, Volume 54, 2017,

Yamazaki, Y. & Yamaguchi, K.; (1979).; **Characteristics of Cocurrent Two-Phase Downflow in Tubes: Flow Pattern, Void Fraction and Pressure Drop.** *Journal of Nuclear Science and Technology, 16, 245-255.*

Zabaras, G. J., (1999), "**Prediction of slug frequency for gas-liquid flows**", *Annual Technical Conference, SPE 56462*, pp. 181-188.

Zaleski, S.; (2005).; **Interface tracking-VOF, in: Lecture Given at Course**:

Industrial two-phase flow CFD, von Karman Institute for Fluid Dynamics,

Belgium.

Zeyad Almutairi Fayez M. Al-Alweet Yusif A. Alghamdi Omar A. Almisned and Othman Y. Al-Othman; Investigating the Characteristics of Two-Phase Flow Using Electrical Capacitance Tomography (ECT) for Three Pipe Orientations; Processes 2020, 8, 51; doi:10.3390/pr8010051

Zhao, Y., Yeung, H., Lao, L.; (2013) **Slug Frequency in High Viscosity Liquid and Gas Flow in Horizontal Pipes**. *2013:105-117.*

Zuber, N. and Findlay, J. A., (1965), "**Average Volumetric Concentration in Two Phase Flow System**", *Journal of Heat Transfer*, Vol. 87, pp. 453-468.

Zukoski E.E; (1966); **Influence of Viscosity, Surface Tension, and Inclination Angle on Motion of Long Bubbles in Closed Tubes**. *J Fluid Mech. 1966;*

Appendix A

Bubble Velocity Data Tables

Drift Velocity @ 0 Degrees													
Pipe Length	**Water**	**D-1**	**D-2**	**D-3**	**ST-1**	**ST-2**	**ST-3**	**ST-4**	**V-1**	**V-2**	**V-3**	**V-4**	**V-5**
1.0	0.184332	0.183486	0.183486	0.185185	0.187793	0.190476	0.190476	0.190476	0.182648	0.180180	0.166251	0.113314	0.044199
1.2	0.186047	0.182648	0.182648	0.186829	0.188679	0.189573	0.191296	0.190476	0.182648	0.180180	0.173160	0.095465	0.034335
1.4	0.184332	0.182648	0.184332	0.184417	0.186916	0.190476	0.189663	0.190476	0.183486	0.179372	0.171674	0.081633	0.028269
1.6	0.186047	0.182648	0.185185	0.186916	0.187793	0.190476	0.191296	0.190476	0.183486	0.178571	0.170213	0.064309	
1.8	0.185185	0.183486	0.183486	0.184332	0.188679	0.189573	0.189663	0.191388	0.184332	0.180180	0.164609		
2	0.183486	0.183486	0.183486	0.186916	0.187793	0.188679	0.191296	0.191388	0.184247	0.179372	0.157480		
2.2	0.186916	0.183486	0.184332	0.185185	0.187793	0.192308	0.190567	0.190476	0.181901	0.178571			
2.4	0.184332	0.184162	0.184332	0.186916	0.187793	0.189573	0.190476	0.190476	0.183486	0.177778			
2.6	0.186047	0.181984	0.183486	0.185185	0.188679	0.189573	0.190476	0.191388	0.183486				
2.8	0.184332	0.181818	0.183486	0.186047	0.186916	0.190476	0.190476	0.189573	0.183486				
3	0.184332	0.183486	0.185185	0.185185	0.187003	0.189573	0.190476	0.192308	0.183486				
3.2	0.186047	0.184332	0.183486	0.186916	0.188590	0.190476	0.190476	0.191388					
3.4	0.185185		0.183402	0.184332	0.188679	0.190476	0.190476	0.189573					

Drift Velocity @ 15 Degrees													
Pipe Length	**Water**	**D-1**	**D-2**	**D-3**	**ST-1**	**ST-2**	**ST-3**	**ST-4**	**V-1**	**V-2**	**V-3**	**V-4**	**V-5**
1	0.20833	0.20725	0.20833	0.20942	0.20942	0.21164	0.2	0.21053	0.20725	0.20000	0.19503	0.15385	0.09524
1.2	0.20833	0.20619	0.20619	0.20833	0.21053	0.20942	0.22222	0.20942	0.20619	0.20202	0.19503	0.15326	0.09569
1.4	0.20833	0.20725	0.20833	0.20833	0.20833	0.20833	0.20833	0.20942	0.20513	0.20000	0.1924	0.1565	0.09592
1.6	0.20833	0.20619	0.20725	0.20942	0.20942	0.21053	0.21053	0.20833	0.20513	0.20202	0.19512	0.15015	0.09547
1.8	0.20725	0.20725	0.20513	0.20833	0.21053	0.21053	0.21008	0.21053	0.20619	0.20101	0.19324	0.15385	0.09569
2	0.20725	0.20619	0.20833	0.20833	0.20833	0.20942	0.20877	0.20833	0.20619	0.20101	0.19417	0.15754	0.09547
2.2	0.20855	0.20619	0.20833	0.20833	0.20942	0.20942	0.21053	0.20942	0.20513	0.20202	0.19417	0.1492	0.09547
2.4	0.20921	0.20833	0.20619	0.20833	0.20942	0.21053	0.20942	0.20725	0.20725	0.20000	0.19417	0.15385	0.09524
2.6	0.20725	0.20619	0.20833	0.20899	0.21053	0.21053	0.21053	0.21053	0.20513	0.20202	0.19417	0.15385	0.09569
2.8	0.20833	0.20619	0.20725	0.20768	0.20833	0.21053	0.20833	0.20833	0.20619	0.20000	0.19417	0.15326	0.09501
3	0.20725	0.20725	0.20619	0.20942	0.21053	0.19802	0.20942	0.21053	0.20619	0.20202	0.19417	0.15385	0.09615
3.2	0.20942	0.20513	0.20725	0.20833	0.21053	0.22222	0.20833	0.20833	0.20619	0.20101	0.19417	0.15385	0.09627
3.4	0.20725	0.20833	0.20833	0.20833	0.20833	0.15038	0.21053	0.21053	0.20513	0.20101	0.19324	0.15267	0.0949

Drift Velocity @ 30 Degrees													
Pipe Length	**Water**	**D-1**	**D-2**	**D-3**	**ST-1**	**ST-2**	**ST-3**	**ST-4**	**V-1**	**V-2**	**V-3**	**V-4**	**V-5**
1.00	0.215054	0.210526	0.215054	0.217391	0.216216	0.214018	0.213904	0.211640	0.214362	0.208333	0.20000	0.153905	0.100000
1.20	0.217391	0.220994	0.217391	0.217391	0.216216	0.217391	0.215054	0.212766	0.212314	0.208442	0.20000	0.153846	0.100000
1.40	0.215054	0.213904	0.210526	0.216216	0.217391	0.213904	0.215054	0.212766	0.215054	0.208333	0.20000	0.155039	0.100000
1.60	0.218460	0.213904	0.220994	0.216216	0.217391	0.215054	0.212766	0.211640	0.213904	0.207254	0.20000	0.155039	0.100000
1.80	0.214018	0.217391	0.214362	0.217391	0.216216	0.215054	0.213904	0.211640	0.212766	0.208333	0.20000	0.155039	0.100000
2.00	0.217391	0.213904	0.216920	0.215054	0.216216	0.216216	0.215054	0.212766	0.212766	0.208333	0.20000	0.155039	0.100000
2.20	0.215054	0.216216	0.215054	0.217391	0.217391	0.215054	0.212766	0.212766	0.215054	0.207254	0.20101	0.155039	0.100000
2.40	0.218460	0.214362	0.216216	0.216216	0.216216	0.213904	0.213904	0.210526	0.214938	0.211640	0.20000	0.153257	0.100000
2.60	0.214018	0.215750	0.215054	0.217391	0.216216	0.216216	0.215054	0.211640	0.211305	0.203978	0.20000	0.153257	0.100000
2.80	0.217391	0.216216	0.215054	0.216216	0.217391	0.213904	0.213904	0.213904	0.214362	0.209534	0.20000	0.160256	0.100000
3.00	0.216216	0.215054	0.216216	0.216216	0.216216	0.216216	0.212766	0.211640	0.215054	0.208333	0.20000	0.153022	0.100000
3.20	0.217273	0.215054	0.215054	0.216216	0.217391	0.214362	0.215054	0.211640	0.212766	0.208333	0.20000	0.154440	0.100000
3.40	0.215169	0.215054	0.217391	0.217391	0.216216	0.215750	0.213904	0.212766	0.212766	0.207254	0.20000	0.155039	0.100000

Drift Velocity @ 45 Degrees													
Pipe Length	**Water**	**D-1**	**D-2**	**D-3**	**ST-1**	**ST-2**	**ST-3**	**ST-4**	**V-1**	**V-2**	**V-3**	**V-4**	**V-5**
1.00	0.215054	0.212766	0.215054	0.216216	0.215054	0.209424	0.206186	0.201005	0.212766	0.205128	0.195122	0.145560	0.096386
1.20	0.215054	0.215054	0.215054	0.213904	0.213904	0.208333	0.206186	0.201005	0.210526	0.205128	0.197044	0.145985	0.096386
1.40	0.216216	0.216216	0.217391	0.215054	0.213904	0.199005	0.205128	0.200000	0.213904	0.205128	0.195122	0.147059	0.097561
1.60	0.215054	0.213904	0.212766	0.216216	0.213904	0.220994	0.205128	0.200000	0.211640	0.206186	0.197922	0.145985	0.096386
1.80	0.215054	0.215054	0.212766	0.213904	0.213904	0.209424	0.208986	0.201005	0.212766	0.204082	0.195217	0.145985	0.096386
2.00	0.213904	0.213904	0.216216	0.217391	0.215054	0.208333	0.201410	0.199005	0.210526	0.206186	0.195122	0.146520	0.097556
2.20	0.215054	0.213904	0.213904	0.212766	0.212766	0.208333	0.207254	0.202020	0.212766	0.204082	0.198020	0.146520	0.096390
2.40	0.215054	0.214938	0.215054	0.216216	0.215054	0.210526	0.205128	0.200000	0.210526	0.207254	0.195122	0.145985	0.096386
2.60	0.215054	0.214018	0.215054	0.216099	0.212766	0.208333	0.205128	0.200000	0.212766	0.205128	0.196947	0.147059	0.097276
2.80	0.213904	0.213904	0.213904	0.212879	0.212766	0.207254	0.205128	0.200000	0.210526	0.205128	0.196175	0.145985	0.096432
3.00	0.213904	0.215054	0.213904	0.215054	0.215054	0.200000	0.206186	0.200000	0.213904	0.205128	0.196078	0.145985	0.096618
3.20	0.217273	0.213904	0.216216	0.215054	0.213904	0.220994	0.204082	0.200000	0.211640	0.205128	0.196078	0.147059	0.097324
3.40	0.212879	0.215054	0.213904	0.213904	0.213904	0.204082	0.206186	0.200000	0.212766	0.205128	0.195122	0.145985	0.096386

Drift Velocity @ 60 Degrees													
Pipe Length	**Water**	**D-1**	**D-2**	**D-3**	**ST-1**	**ST-2**	**ST-3**	**ST-4**	**V-1**	**V-2**	**V-3**	**V-4**	**V-5**
1.00	0.202020	0.192308	0.202020	0.202020	0.202020	0.192308	0.187793	0.181736	0.200000	0.193143	0.181818	0.125392	0.087912
1.20	0.203046	0.202020	0.202020	0.202020	0.200000	0.193237	0.186916	0.177857	0.198020	0.190567	0.181818	0.125000	0.086957
1.40	0.203046	0.203046	0.204082	0.204082	0.200000	0.192308	0.186916	0.179372	0.200000	0.191388	0.181818	0.126582	0.087336
1.60	0.202020	0.203046	0.202020	0.202020	0.199005	0.191388	0.186916	0.180180	0.199005	0.193237	0.182648	0.125392	0.087527
1.80	0.202020	0.202020	0.202020	0.202020	0.200000	0.192308	0.188590	0.178571	0.199005	0.192308	0.181818	0.126183	0.087912
2.00	0.203046	0.202020	0.203046	0.202020	0.201005	0.191388	0.186133	0.178571	0.200000	0.191388	0.182648	0.125786	0.086957
2.20	0.202020	0.203046	0.203046	0.203046	0.200000	0.197239	0.186047	0.180180	0.199005	0.192308	0.181818	0.125000	0.087719
2.40	0.203046	0.203046	0.202020	0.202020	0.199005	0.186741	0.188679	0.179372	0.199005	0.191388	0.181818	0.125786	0.087719
2.60	0.202020	0.202020	0.202020	0.203046	0.200000	0.192308	0.185185	0.179372	0.199005	0.192308	0.181818	0.126183	0.087336
2.80	0.202020	0.202020	0.202020	0.201005	0.199005	0.192308	0.188679	0.178571	0.199005	0.192308	0.183486	0.125000	0.087336
3.00	0.203046	0.202020	0.202020	0.203046	0.200000	0.192215	0.186916	0.179372	0.199005	0.190476	0.180180	0.126582	0.087336
3.20	0.203046	0.204082	0.204082	0.202020	0.200000	0.190567	0.186047	0.179372	0.200000	0.193237	0.181818	0.125392	0.088106
3.40	0.202020	0.202020	0.202020	0.202020	0.200000	0.191388	0.187793	0.179372	0.198020	0.192308	0.183486	0.125786	0.086957

Drift Velocity @ 75 Degrees													
Pipe Length	**Water**	**D-1**	**D-2**	**D-3**	**ST-1**	**ST-2**	**ST-3**	**ST-4**	**V-1**	**V-2**	**V-3**	**V-4**	**V-5**
1.00	0.175439	0.177778	0.178571	0.178571	0.177778	0.166667	0.165289	0.12012	0.175439	0.168067	0.156863	0.088106	0.070671
1.20	0.183402	0.180180	0.180018	0.179372	0.176211	0.165975	0.158103	0.126582	0.175439	0.166667	0.155039	0.087719	0.070922
1.40	0.177069	0.176211	0.177148	0.178571	0.176211	0.165289	0.158730	0.126984	0.174672	0.166667	0.156863	0.087336	0.071429
1.60	0.178571	0.179372	0.178571	0.177778	0.176211	0.166667	0.157480	0.126984	0.174672	0.167364	0.156250	0.088106	0.071429
1.80	0.179372	0.176991	0.178571	0.179372	0.175439	0.165289	0.157480	0.127389	0.175439	0.166667	0.155642	0.087336	0.071174
2.00	0.177778	0.180099	0.177778	0.178571	0.175439	0.165975	0.158103	0.127389	0.174672	0.167364	0.156863	0.088106	0.071174
2.20	0.180099	0.177069	0.179372	0.178571	0.176991	0.165975	0.157480	0.128205	0.174672	0.167364	0.155642	0.087719	0.071174
2.40	0.177069	0.177778	0.177778	0.178571	0.176211	0.165289	0.158103	0.127389	0.173913	0.167364	0.156863	0.087719	0.070922
2.60	0.178571	0.178571	0.178571	0.178571	0.176211	0.165975	0.157480	0.126582	0.174672	0.168067	0.156250	0.087719	0.071429
2.80	0.179372	0.177778	0.177778	0.178571	0.176211	0.165289	0.158103	0.128205	0.174672	0.165975	0.155642	0.087336	0.071429
3.00	0.177778	0.177778	0.178571	0.178571	0.176211	0.165975	0.156863	0.131579	0.174672	0.167364	0.156250	0.087719	0.071429
3.20	0.180099	0.177778	0.179372	0.178571	0.175439	0.165289	0.158730	0.123457	0.174672	0.166667	0.156250	0.088106	0.070671
3.40	0.177069	0.178571	0.177778	0.178571	0.176211	0.165975	0.157480	0.128205	0.173913	0.166667	0.156250	0.087719	0.071429

Drift Velocity													
Angle	**Water**	**D-1**	**D-2**	**D-3**	**ST-1**	**ST-2**	**ST-3**	**ST-4**	**V-1**	**V-2**	**V-3**	**V-4**	**V-5**
0	0.1851	0.1831	0.1839	0.1857	0.1879	0.1901	0.1905	0.1908	0.1833	0.1793	0.1672	0.0887	0.0356
15	0.2081	0.2068	0.2073	0.2086	0.2095	0.2055	0.2098	0.2093	0.2059	0.2011	0.1941	0.1535	0.0956
30	0.2162	0.2153	0.2158	0.2167	0.2167	0.2152	0.2141	0.2122	0.2136	0.2081	0.2001	0.1548	0.1000
45	0.2149	0.2144	0.2147	0.2150	0.2140	0.2088	0.2055	0.2003	0.2121	0.2053	0.1961	0.1463	0.0967
60	0.2025	0.2017	0.2025	0.2023	0.2000	0.1920	0.1871	0.1794	0.1992	0.1920	0.1821	0.1257	0.0875
75	0.1786	0.1782	0.1785	0.1786	0.1762	0.1658	0.1584	0.1269	0.1747	0.1671	0.1562	0.0877	0.0712

Froude Number													
Angle	**Water**	**D-1**	**D-2**	**D-3**	**ST-1**	**ST-2**	**ST-3**	**ST-4**	**V-1**	**V-2**	**V-3**	**V-4**	**V-5**
0	0.418	0.413824	0.415463	0.419604	0.42445	0.429417	0.430524	0.431191	0.41423	0.405057	0.377843	0.200365	0.080437
15	0.47	0.467205	0.468495	0.471265	0.473374	0.464308	0.473959	0.472997	0.46531	0.454336	0.438546	0.346845	0.215897
30	0.489	0.486395	0.487586	0.489529	0.489542	0.486128	0.483702	0.47936	0.482716	0.470192	0.452056	0.349724	0.225941
45	0.486	0.484543	0.485135	0.485698	0.483502	0.471875	0.464415	0.452584	0.479172	0.463841	0.443034	0.330512	0.218549
60	0.458	0.45587	0.457543	0.457149	0.451889	0.433754	0.422789	0.405286	0.449983	0.433869	0.411385	0.284001	0.19763
75	0.404	0.402551	0.403217	0.403594	0.398138	0.37465	0.357929	0.286609	0.394792	0.377541	0.352931	0.198263	0.160814

MORTON NUMBER						
Liquid	**μL**	**ρL**	**ρG**	**σ**	**g**	**Mo**
Water	0.001	998.2	1.225	0.073	9.8065	2.52229E-11
D-1	0.001	870	1.225	0.073	9.8065	2.89344E-11
D-2	0.001	920	1.225	0.073	9.8065	2.7364E-11
D-3	0.001	1,050	1.225	0.073	9.8065	2.398E-11
V-1	0.0021	998.2	1.225	0.073	9.8065	4.90537E-10
V-2	0.0049	998.2	1.225	0.073	9.8065	1.45405E-08
V-3	0.0107	998.2	1.225	0.073	9.8065	3.3062E-07
V-4	0.0886	998.2	1.225	0.073	9.8065	0.001554281
V-5	0.307	998.2	1.225	0.073	9.8065	0.224051621
ST-1	0.001	998.2	1.225	0.054	9.8065	6.23135E-11
ST-2	0.001	998.2	1.225	0.032	9.8065	2.99442E-10
ST-3	0.001	998.2	1.225	0.025	9.8065	6.27976E-10
ST-4	0.001	998.2	1.225	0.018	9.8065	1.68246E-09

EOTVOSS NUMBER						
Liquid	**D**	**ρL**	**ρG**	**σ**	**g**	**Eo**
Water	0.02	998.2	1.225	0.073	9.8065	53.5717
D-1	0.02	870	1.225	0.073	9.8065	46.68297
D-2	0.02	920	1.225	0.073	9.8065	49.36968
D-3	0.02	1,050	1.225	0.073	9.8065	56.35513
V-1	0.02	998.2	1.225	0.073	9.8065	53.5717
V-2	0.02	998.2	1.225	0.073	9.8065	53.5717
V-3	0.02	998.2	1.225	0.073	9.8065	53.5717
V-4	0.02	998.2	1.225	0.073	9.8065	53.5717
V-5	0.02	998.2	1.225	0.073	9.8065	53.5717
ST-1	0.02	998.2	1.225	0.054	9.8065	72.421
ST-2	0.02	998.2	1.225	0.032	9.8065	122.2104
ST-3	0.02	998.2	1.225	0.025	9.8065	156.4294
ST-4	0.02	998.2	1.225	0.018	9.8065	217.263

VISCOSITY NUMBER						
Liquid	**µL**	**D**	**ρL**	**ρG**	**g**	**nVis**
Water	0.001	0.02	998.2	1.225	9.807	0.000113
D-1	0.001	0.02	870	1.225	9.807	0.000130
D-2	0.001	0.02	920	1.225	9.807	0.000123
D-3	0.001	0.02	1,050	1.225	9.807	0.000108
V-1	0.0021	0.02	998.2	1.225	9.807	0.000238
V-2	0.0049	0.02	998.2	1.225	9.807	0.000555
V-3	0.0107	0.02	998.2	1.225	9.807	0.001211
V-4	0.0886	0.02	998.2	1.225	9.807	0.010027
V-5	0.307	0.02	998.2	1.225	9.807	0.034744
ST-1	0.001	0.02	998.2	1.225	9.807	0.000113
ST-2	0.001	0.02	998.2	1.225	9.807	0.000113
ST-3	0.001	0.02	998.2	1.225	9.807	0.000113
ST-4	0.001	0.02	998.2	1.225	9.807	0.000113

FROUDE NUMBER - 0						
Liquid	**uTB**	**ρL**	**ρG**	**g**	**D**	**Fr**
Water	0.1851	998.2	1.225	9.8065	0.02	0.4183
D-1	0.1831	870	1.225	9.8065	0.02	0.4138
D-2	0.1839	920	1.225	9.8065	0.02	0.4155
D-3	0.1857	1,050	1.225	9.8065	0.02	0.4196
V-1	0.1833	998.2	1.225	9.8065	0.02	0.4142
V-2	0.1793	998.2	1.225	9.8065	0.02	0.4051
V-3	0.1672	998.2	1.225	9.8065	0.02	0.3778
V-4	0.0887	998.2	1.225	9.8065	0.02	0.2004
V-5	0.0356	998.2	1.225	9.8065	0.02	0.0804
ST-1	0.1879	998.2	1.225	9.8065	0.02	0.4244
ST-2	0.1901	998.2	1.225	9.8065	0.02	0.4294
ST-3	0.1905	998.2	1.225	9.8065	0.02	0.4305
ST-4	0.1908	998.2	1.225	9.8065	0.02	0.4312

FROUDE NUMBER - 15						
Liquid	**uTB**	**ρL**	**ρG**	**g**	**D**	**Fr**
Water	0.2081	998.2	1.225	9.8065	0.02	0.4702
D-1	0.2068	870	1.225	9.8065	0.02	0.467
D-2	0.2073	920	1.225	9.8065	0.02	0.468
D-3	0.2086	1,050	1.225	9.8065	0.02	0.471
V-1	0.2059	998.2	1.225	9.8065	0.02	0.465
V-2	0.2011	998.2	1.225	9.8065	0.02	0.454
V-3	0.1941	998.2	1.225	9.8065	0.02	0.439
V-4	0.1535	998.2	1.225	9.8065	0.02	0.347
V-5	0.0956	998.2	1.225	9.8065	0.02	0.216
ST-1	0.2095	998.2	1.225	9.8065	0.02	0.473
ST-2	0.2055	998.2	1.225	9.8065	0.02	0.464
ST-3	0.2098	998.2	1.225	9.8065	0.02	0.474
ST-4	0.2093	998.2	1.225	9.8065	0.02	0.473

FROUDE NUMBER - 30						
Liquid	**uTB**	**ρL**	**ρG**	**g**	**D**	**Fr**
Water	0.2162	998.2	1.225	9.8065	0.02	0.4885
D-1	0.2153	870	1.225	9.8065	0.02	0.4864
D-2	0.2158	920	1.225	9.8065	0.02	0.4876
D-3	0.2167	1,050	1.225	9.8065	0.02	0.4895
V-1	0.2136	998.2	1.225	9.8065	0.02	0.4827
V-2	0.2081	998.2	1.225	9.8065	0.02	0.4702
V-3	0.2001	998.2	1.225	9.8065	0.02	0.4521
V-4	0.1548	998.2	1.225	9.8065	0.02	0.3497
V-5	0.1000	998.2	1.225	9.8065	0.02	0.2259
ST-1	0.2167	998.2	1.225	9.8065	0.02	0.4895
ST-2	0.2152	998.2	1.225	9.8065	0.02	0.4861
ST-3	0.2141	998.2	1.225	9.8065	0.02	0.4837
ST-4	0.2122	998.2	1.225	9.8065	0.02	0.4794

FROUDE NUMBER - 45						
Liquid	**uTB**	**ρL**	**ρG**	**g**	**D**	**Fr**
Water	0.2149	998.2	1.225	9.8065	0.02	0.4855
D-1	0.2144	870	1.225	9.8065	0.02	0.4845
D-2	0.2147	920	1.225	9.8065	0.02	0.4851
D-3	0.215	1,050	1.225	9.8065	0.02	0.4857
V-1	0.2121	998.2	1.225	9.8065	0.02	0.4792
V-2	0.2053	998.2	1.225	9.8065	0.02	0.4638
V-3	0.1961	998.2	1.225	9.8065	0.02	0.443
V-4	0.1463	998.2	1.225	9.8065	0.02	0.3305
V-5	0.0967	998.2	1.225	9.8065	0.02	0.2185
ST-1	0.214	998.2	1.225	9.8065	0.02	0.4835
ST-2	0.2088	998.2	1.225	9.8065	0.02	0.4719
ST-3	0.2055	998.2	1.225	9.8065	0.02	0.4644
ST-4	0.2003	998.2	1.225	9.8065	0.02	0.4526

FROUDE NUMBER - 60						
Liquid	**uTB**	**ρL**	**ρG**	**g**	**D**	**Fr**
Water	0.2025	998.2	1.225	9.8065	0.02	0.4575
D-1	0.2017	870	1.225	9.8065	0.02	0.4559
D-2	0.2025	920	1.225	9.8065	0.02	0.4575
D-3	0.2023	1,050	1.225	9.8065	0.02	0.4571
V-1	0.1992	998.2	1.225	9.8065	0.02	0.4500
V-2	0.1920	998.2	1.225	9.8065	0.02	0.4339
V-3	0.1821	998.2	1.225	9.8065	0.02	0.4114
V-4	0.1257	998.2	1.225	9.8065	0.02	0.2840
V-5	0.0875	998.2	1.225	9.8065	0.02	0.1976
ST-1	0.2000	998.2	1.225	9.8065	0.02	0.4519
ST-2	0.1920	998.2	1.225	9.8065	0.02	0.4338
ST-3	0.1871	998.2	1.225	9.8065	0.02	0.4228
ST-4	0.1794	998.2	1.225	9.8065	0.02	0.4053

FROUDE NUMBER - 75						
Liquid	**uTB**	**ρL**	**ρG**	**g**	**D**	**Fr**
Water	0.1786	998.2	1.225	9.8065	0.02	0.4035
D-1	0.1782	870	1.225	9.8065	0.02	0.4026
D-2	0.1785	920	1.225	9.8065	0.02	0.4032
D-3	0.1786	1,050	1.225	9.8065	0.02	0.4036
V-1	0.1747	998.2	1.225	9.8065	0.02	0.3948
V-2	0.1671	998.2	1.225	9.8065	0.02	0.3775
V-3	0.1562	998.2	1.225	9.8065	0.02	0.3529
V-4	0.0877	998.2	1.225	9.8065	0.02	0.1983
V-5	0.0712	998.2	1.225	9.8065	0.02	0.1608
ST-1	0.1762	998.2	1.225	9.8065	0.02	0.3981
ST-2	0.1658	998.2	1.225	9.8065	0.02	0.3746
ST-3	0.1584	998.2	1.225	9.8065	0.02	0.3579
ST-4	0.1269	998.2	1.225	9.8065	0.02	0.2866

Appendix B

Translational Velocity Calculations

U-sl (m/s)	Ap (m2)	Ql (m3/s)	Factor	Ql (l/h)
0.10	0.000284	2.83529E-05	3600000	102.0703
0.20	0.000284	5.67057E-05	3600000	204.1407
0.30	0.000284	8.50586E-05	3600000	306.211
0.40	0.000284	0.000113411	3600000	408.2814
0.50	0.000284	0.000141764	3600000	510.3517
0.60	0.000284	0.000170117	3600000	612.4221
0.70	0.000284	0.00019847	3600000	714.4924
0.80	0.000284	0.000226823	3600000	816.5628
0.90	0.000284	0.000255176	3600000	918.6331
1.00	0.000284	0.000283529	3600000	1020.703

U-sg (m/s)	Ap (m2)	Ql (m3/s)	Factor	Ql (l/m)
0.50	0.000284	0.000142	60000	8.505862
1.00	0.000284	0.000284	60000	17.01172
1.50	0.000284	0.000425	60000	25.51759
2.00	0.000284	0.000567	60000	34.02345
2.50	0.000284	0.000709	60000	42.52931
3.00	0.000284	0.000851	60000	51.03517
3.50	0.000284	0.000992	60000	59.54103
4.00	0.000284	0.001134	60000	68.0469
4.50	0.000284	0.001276	60000	76.55276
5.00	0.000284	0.001418	60000	85.05862

Appendix C

Physical Property Measurements

Time (s)	Volume (ul)	Surface tension (nM/m)
Glycerol/water		
0	9.64617	66.193
1	9.64162	66.059
2	9.64074	66.085
3	9.64144	66.013
4	9.63708	65.968
5	9.63612	66.005
6	9.63202	66.021
7	9.63401	66.059
8	9.63107	66.094
9	9.62539	66.074
Surfactant		
0	5.83608	37.085
1	5.83298	37.093
2	5.82944	36.85
3.016	5.81948	36.866
4	5.81997	36.71
5	5.81508	36.734
6	5.81059	36.693
7	5.8051	36.722
8	5.80408	36.381
9	5.80159	36.457

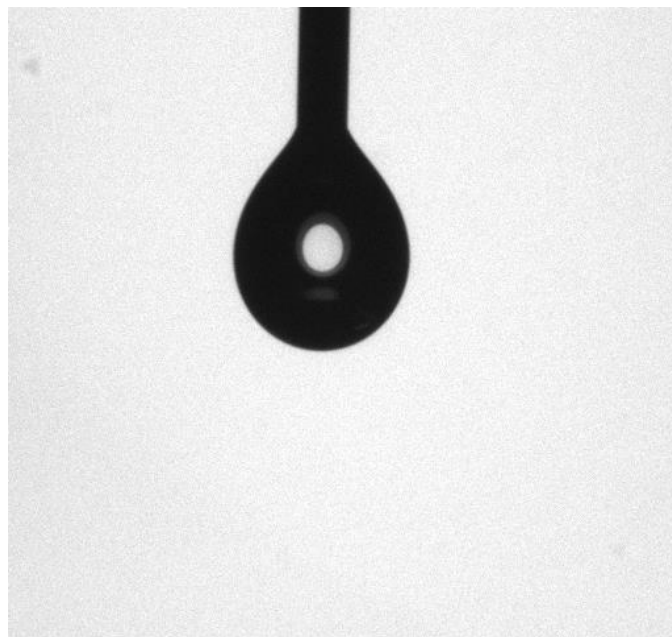

Glycerol

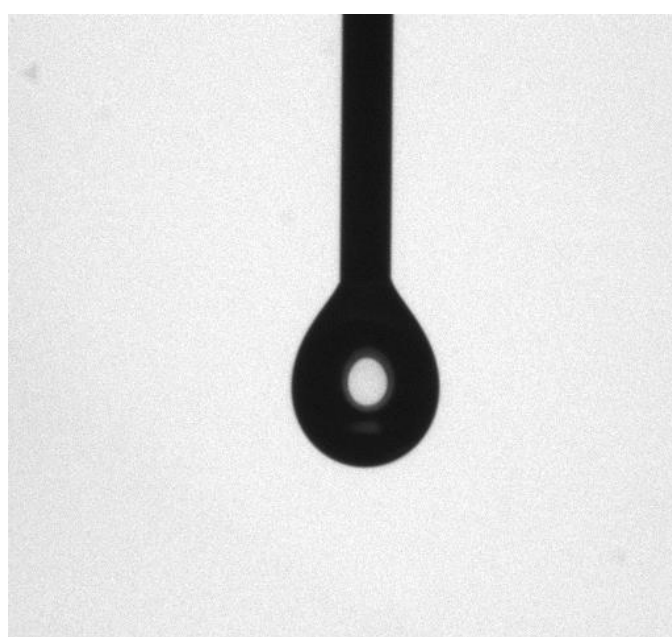

Surfactant

Appendix D

Experimental Data Tables

WATER LIQUID HOLDUP – Horizontal (mL)								
Usl (m/s)	**Usg (m/s)**							
	0.5	**1**	**1.5**	**2**	**2.5**	**3**	**3.5**	**4**
0.1	393	327	308	292	277	252	263	253
0.2	428	352	327	312	308	311	322	280
0.3	518	415	377	342	333	308	333	312
0.4	543	468	398	384	372	353	341	363
0.5	569	517	437	418	410	363	393	372
0.6	623	547	495	438	422	401	408	442
0.7	647	584	508	483	452	427	414	373
0.8	663	603	527	505	488	465	424	458

WATER LIQUID HOLDUP - Inclined (mL)								
Usl (m/s)	**Usg (m/s)**							
	0.5	**1**	**1.5**	**2**	**2.5**	**3**	**3.5**	**4**
0.1	412	322	261	254	273	235	243	232
0.2	506	393	320	300	315	306	295	281
0.3	551	483	384	345	324	348	310	302
0.4	612	512	437	395	380	361	338	347
0.5	663	548	463	417	413	394	353	333
0.6	695	588	515	437	419	397	373	372
0.7	720	607	547	466	426	413	426	399
0.8	757	633	603	488	459	440	433	428

SURFACTANT LIQUID HOLDUP - HORIZONTAL (mL)								
Usl (m/s)	**Usg (m/s)**							
	0.5	**1**	**1.5**	**2**	**2.5**	**3**	**3.5**	**4**
0.1	365	352	343	337	322	307	295	290
0.2	395	367	353	347	335	318	312	298
0.3	440	402	378	352	342	333	318	307
0.4	463	440	415	387	373	343	330	317
0.5	510	470	443	405	367	362	323	310
0.6	560	503	467	423	400	387	353	327
0.7	590	527	487	462	443	407	383	353

SURFACTANT LIQUID HOLDUP – INCLINED (mL)								
Usl (m/s)	**Usg (m/s)**							
	0.5	**1**	**1.5**	**2**	**2.5**	**3**	**3.5**	**4**
0.1	430	375	338	350	327	297	290	277
0.2	502	427	403	367	348	338	323	305
0.3	552	483	420	390	362	347	332	313
0.4	603	527	443	422	403	387	362	345
0.5	637	545	467	437	417	407	380	360
0.6	670	590	488	467	438	417	392	373
0.7	710	625	525	490	465	433	400	380

WATER PRESSURE DROP HORIZONTAL (mbar)								
Usl (m/s)	**Usg (m/s)**							
	0.5	**1**	**1.5**	**2**	**2.5**	**3**	**3.5**	**4**
0.1	7	7	7	5	5	5	6	5
0.2	13	13	14	13	14	14	14	15
0.3	16	18	20	21	21	22	21	23
0.4	20	23	28	28	31	31	32	32
0.5	25	27	35	37	38	41	41	44
0.6	32	32	41	51	48	51	53	54
0.7	37	42	46	49	55	58	60	66
0.8	43	49	52	57	63	65	70	76

WATER PRESSURE DROP INCLINED (mbar)						
Usl (m/s)	**Usg (m/s)**					
	0.5	**1**	**1.5**	**2**	**2.5**	**3**
0.1	35	26	27	31	24	33
0.2	50	44	42	45	39	46
0.3	60	54	52	55	57	58
0.4	68	65	66	67	67	70
0.5	78	73	73	76	77	79
0.6	85	81	83	87	87	90
0.7	91	89	91	93	95	98
0.8	100	97	98	101	101	

SURFACTANT PRESSURE DROP – HORIZONTAL (mbar)								
Usl (m/s)	**Usg (m/s)**							
	0.5	**1**	**1.5**	**2**	**2.5**	**3**	**3.5**	**4**
0.1	14	14	14	13	13	13	15	15
0.2	21	21	22	20	20	22	24	24
0.3	36	27	30	29	29	30	32	33
0.4	48	34	36	39	40	41	43	45
0.5	56	46	44	48	52	54	56	58
0.6	58	54	52	53	59	61	62	66
0.7	60	62	60	61	68	70	74	75

SURFACTANT PRESSURE DROP – INCLINED (mbar)								
Usl (m/s)	**Usg (m/s)**							
	0.5	**1**	**1.5**	**2**	**2.5**	**3**	**3.5**	**4**
0.1	53	45	47	47	49	50	50	51
0.2	64	56	57	59	60	61	62	62
0.3	72	65	64	66	69	71	49	73
0.4	91	74	73	74	76	77	81	82
0.5	97	85	83	85	87	90	91	94
0.6	101	93	90	93	97	100	100	102
0.7	89	96	97	100	104	104	108	109

GLYCEROL PRESSURE DROP – HORIZONTAL (mbar)								
Usl (m/s)	**Usg (m/s)**							
	0.5	**1**	**1.5**	**2**	**2.5**	**3**	**3.5**	**4**
0.1	8	10	10	10	10	10	11	11
0.2	13	16	20	20	23	23	26	26
0.3	21	23	27	30	34	36	38	40
0.4	34	31	34	41	45	50	52	56
0.5	44	48	44	51	54	63	66	73
0.6	48	59	60	60	67	73	78	84
0.7	50	56	63	66	67	78	82	84

GLYCEROL PRESSURE DROP – INCLINED (mbar)								
Usl (m/s)	**Usg (m/s)**							
	0.5	**1**	**1.5**	**2**	**2.5**	**3**	**3.5**	**4**
0.1	51	44	40	41	42	45	46	45
0.2	72	61	58	60	60	61	64	65
0.3	88	74	70	72	75	78	79	83
0.4	99	92	83	89	92	92	96	102
0.5	111	107	100	106	105	112	116	118
0.6	118	116	119	104	121	121	132	133
0.7	132	133	134	115	122	123	129	136

WATER SLUG FREQUENCY – HORIZONTAL (per minute)								
Usl (m/s)	**Usg (m/s)**							
	0.5	**1**	**1.5**	**2**	**2.5**	**3**	**3.5**	**4**
0.1	14	15	15	13	6	8	6	5
0.2	35	33	34	25	30	21	22	16
0.3	73	57	52	49	44	41	35	51
0.4	124	89	76	70	63	66	61	58
0.5	165	112	98	91	84	76	85	80
0.6	206	149	110	102	90	96	107	100
0.7	275	194	138	117	121	107	113	124
0.8	309	236	148	135	133	122	134	138

WATER SLUG FREQUENCY – INCLINED (per minute)						
Usl (m/s)	**Usg (m/s)**					
	0.5	**1**	**1.5**	**2**	**2.5**	**3**
0.1	46	38	38	44	51	53
0.2	74	61	61	56	53	64
0.3	100	82	71	75	72	73
0.4	118	96	95	86	84	86
0.5	126	115	111	102	96	103
0.6	146	134	131	116	132	111
0.7	153	146	144	125	127	133
0.8	160	157	147	139	144	141

SURFACTANT SLUG FREQUENCY – HORIZONTAL (per minute)								
Usl (m/s)	**Usg (m/s)**							
	0.5	**1**	**1.5**	**2**	**2.5**	**3**	**3.5**	**4**
0.1	63	42	37	38	45	36	34	33
0.2	119	71	56	64	69	65	59	52
0.3	***S.W***	101	81	82	83	82	91	90
0.4	***B.W***	159	107	97	91	95	120	112
0.5	***S.B***	213	137	123	117	121	125	130
0.6	***S.B***	319	187	139	138	129	150	140
0.7	***S.B***	321	207	165	164	144	165	154

SURFACTANT SLUG FREQUENCY – INCLINED (per minute)								
Usl (m/s)	**Usg (m/s)**							
	0.5	**1**	**1.5**	**2**	**2.5**	**3**	**3.5**	**4**
0.1	73	63	63	64	64	67	77	81
0.2	95	81	79	89	72	79	91	98
0.3	111	99	99	100	94	97	115	127
0.4	S.B	145	127	109	121	124	151	135
0.5	S.B	170	154	119	139	155	155	147
0.6	S.B	242	173	133	152	168	177	165
0.7	S.B	279	200	179	176	176	180	186

GLYCEROL SLUG FREQUENCY – HORIZONTAL (per minute)								
Usl (m/s)	**Usg (m/s)**							
	0.5	**1**	**1.5**	**2**	**2.5**	**3**	**3.5**	**4**
0.1	27	25	19	20	21	17	19	17
0.2	48	44	41	41	42	39	36	37
0.3	93	70	56	57	47	56	56	55
0.4	124	109	79	75	77	76	77	75
0.5	188	141	107	103	91	99	87	103
0.6	209	186	131	124	112	118	115	97
0.7	217	174	144	131	113	116	107	110

GLYCEROL SLUG FREQUENCY – INCLINED (per minute)								
Usl (m/s)	**Usg (m/s)**							
	0.5	**1**	**1.5**	**2**	**2.5**	**3**	**3.5**	**4**
0.1	67	62	53	56	53	54	55	58
0.2	110	85	76	73	68	69	70	78
0.3	155	101	93	86	75	87	87	83
0.4	170	135	109	103	101	98	96	95
0.5	185	153	137	128	129	109	117	106
0.6	231	195	165	135	136	127	127	131
0.7	347	259	193	177	141	129	136	124

Appendix E

Rotameter Calibration

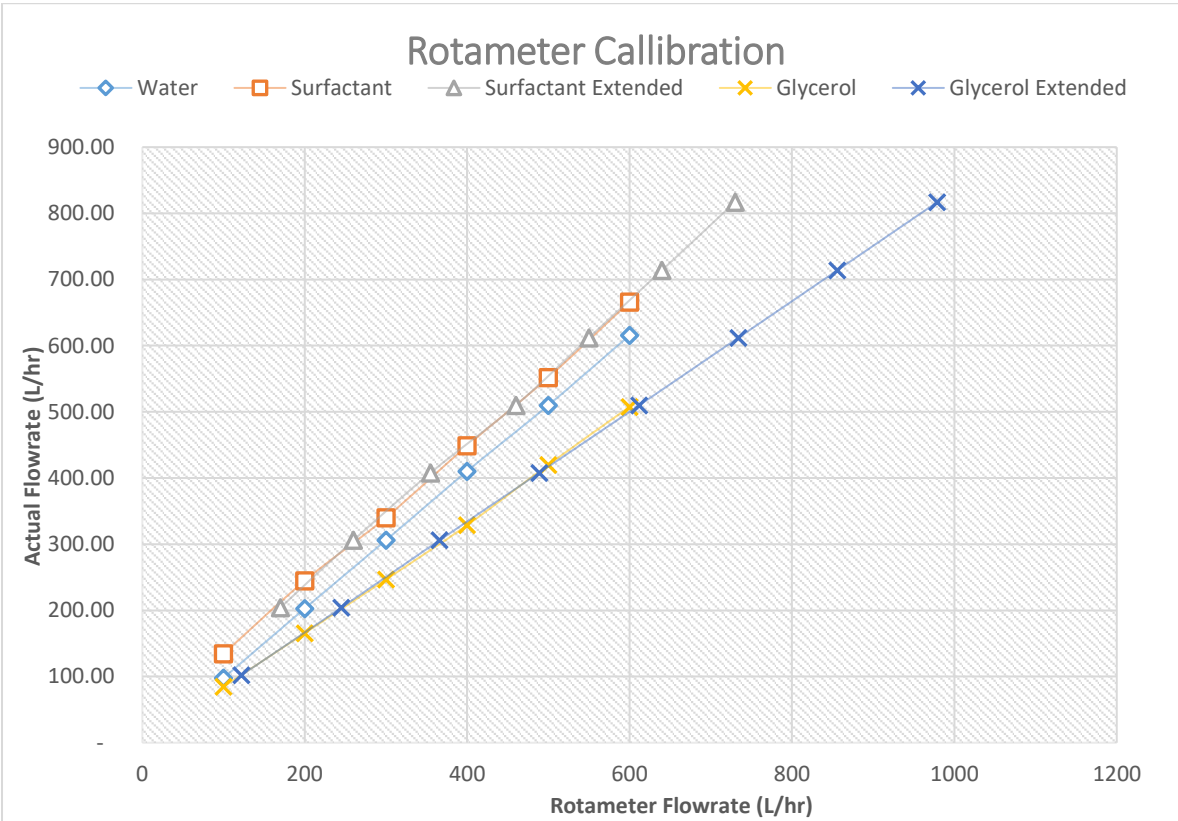

A plot of actual flowrate against rotameter flowrate, showing that actual water flowrate is the same with rotameter flowrate.

Legend Details

Water – Measured water volumetric flowrate values against rotameter indicated flow rate.

Surfactant – Measured surfactant solution volumetric flowrate values against rotameter indicated flow rate.

Surfactant extended – Interpolated (from measured point) surfactant solution volumetric flowrate values against rotameter indicated flow rate.

Glycerol – Measured glycerol solution volumetric flowrate values against rotameter indicated flow rate.

Glycerol extended – Interpolated (from measured point) glycerol solution volumetric flowrate values against rotameter indicated flow rate.